Phase noise of filaments and optical Kerr effect metrology in crystals

Benjamin Maingot

UNIVERSITÉ CÔTE D'AZUR

ÉCOLE DOCTORALE
SCIENCES FONDAMENTALES ET APPLIQUÉES

Bruit de phase des filaments et métrologie de l'effet Kerr dans les cristaux

Benjamin MAINGOT

Institut de Physique de Nice

Présentée en vue de l'obtention du grade de docteur en Physique **de** l'Université Côte d'Azur

Dirigée par : Aurélie Jullien

Soutenue le : 22 Septembre 2023

Devant le jury, composé de :
Marc Hanna, Rapporteur, Directeur de Recherches, Laboratoire Charles Fabry
Aurélien Houard, Rapporteur, Chargé de recherche, Laboratoire d'optique appliquée
Sophie Brasselet, Examinatrice, Directrice de recherche, Institut Fresnel
Caterina Vozzi, Examinatrice, CNR researcher, Politecnico Di Milano
Nicolas Forget, Co-directeur de thèse, Directeur de Recherches, INPHYNI
Aurélie Jullien, Directrice de thèse, Directrice de Recherches, INPHYNI

FASTLITE

MARIE CURIE ACTIONS

INPHYNI
INSTITUT DE PHYSIQUE DE NICE

Résumé

Bruit de phase des filaments et métrologie de l'effet Kerr dans les cristaux

Le développement des sources à XUV utilisables en laboratoire a été motivé par la spectroscopie à rayons X. Ce domaine de la spectroscopie étudie les transitions des électrons près du noyau vers la bande de valence et requiert l'émission de XUV car ils correspondent à l'énergie de ces transitions. Historiquement la spectroscopie à rayons X était réalisée uniquement dans des synchrotrons ou lasers à électrons libres. Le développement récent de l'émission d'harmoniques d'ordre élevé (HHG) a permis aux rayons X d'être émis dans des laboratoires à taille humaine. Le champ électrique requis pour ce type de source à rayon X est typiquement produit par un 'Optical parametric chirped pulse amplifier' (OPCPA). Le processus de HHG est très peu efficace ce qui résulte en une émission de rayon X avec un flux très faible. En conséquence un temps d'intégration de l'ordre de la seconde est nécessaire pour les expériences utilisant ces sources et entraine des temps de mesure complète de l'ordre de quelques heures. La stabilité des OPCPAs en devient d'autant plus critique, et en particulier de leur CEP (ordre zéro de la phase) pour les applications avec des durées d'impulsion de l'ordre du cycle optique. Ce travail se concentre sur deux aspects du développement des OPCPAs : la caractérisation de l'indice de réfraction non linéaire de cristaux utilisés pour le développement d'OPCPAs et le bruit de phase stochastique introduit par la génération de supercontinuum. L'effet Kerr optique est un effet non linéaire d'ordre 3 responsable de l'auto-modulation de phase et de l'auto-focalisation. La caractérisation précise de l'indice de réfraction non linéaire est essentielle pour le design et le développement des OPCPAs étant donné que les nombreux étages de gain qui les composent requièrent des intensités élevées pour atteindre la saturation. Cette thèse présente une nouvelle méthode de caractérisation du tenseur non linéaire d'ordre 3 dans le régime femto-seconde appelée 'Nonlinear chirped interferometry'. Cette méthode est une méthode à trois ondes où une référence est utilisée pour mesurer la variation de délai de groupe d'une sonde sous l'influence d'une pompe de haute énergie dans un matériau non linéaire. La variation de délai de groupe est mesurée avec de l'interférométrie spectrale. Le point fort de cette méthode est son immunité relative aux fluctuations extérieures malgré le fait qu'elle est interférométrique. En effet on atteint des incertitudes au moins aussi bonnes que l'état de l'art sans stabilisation active ou détection hétérodyne. L'interféromètre est utilisé pour caractériser des cristaux liquides ou des cristaux non linéaires (saphir, LBO, KTA, MLN, LGS). La deuxième partie de la thèse est dédiée à la quantification du bruit stochastique de phase de la génération de supercontinuum par filamentation. La filamentation est un effet non linéaire utilisé comme moyen principal d'élargissement spectral employé dans la génération de 'seed' des OPCPAs. Dans ce cas le supercontinuum est typiquement réalisé en focalisant le faisceau de pompe dans un cristal de YAG de quelques millimètres de longueur. Une version modifiée de l'intérféromètre de Bellini et Hänsch avec de la détection spectrale est présentée. Le bruit de phase stochastique est mesuré en utilisant de l'interférométrie spectrale et les paramètres de génération sont caractérisés.

La longueur du cristal de YAG, sa position le long de l'axe de propagation, l'énergie par impulsion et la phase spatiale sont quantifiés individuellement. Une zone optimale de stabilité est identifiée pour chaque paramètre et des coefficients de transfert entre l'énergie et la phase spatiale ainsi qu'entre la phase spatiale et la phase spectrale sont mesurés. Ces coefficients servent de métrique quantifiant l'impact des fluctuations de ces paramètres sur la phase spectrale.

Mots-clés : optique ultra-rapide, optique non linéaire, filamentation, effet Kerr, interférométrie spectrale

Abstract

Phase noise of filaments and optical Kerr effect metrology in crystals

The development of table-top soft X-ray sources has been motivated in the recent years by X-ray spectroscopy. This field of spectroscopy studying the transitions of core electrons to the valence band requires the emission of soft X-ray light as it is the spectral region corresponding to these transitions. Historically this was accomplished in big laser facilities such as synchrotrons or free electron lasers. The development of high order harmonic generation (HHG) in the recent years allowed X-ray spectroscopy to be realized in human-sized optical laboratories. The driving field of these sources is typically generated with an optical parametric chirped pulse amplifier (OPCPA). As the HHG is an inefficient process the soft X-ray yield of a table-top source is very low. This means the experiments require long integration time (of the order of the second per point) leading to hours-long measurements. This means the stability of the OPCPA is critical especially its CEP (order zero of the phase) when it comes to pulse durations close to the optical cycle. This Ph.D. focuses on two aspects of OPCPA development : characterization of the nonlinear refractive index of crystals commonly used for OPCPA in the infrared range and the stochastic phase noise introduced by the supercontinuum generation process. Optical Kerr effect is a third order nonlinear effect responsible for self-phase modulation and self-focusing. The precise knowledge of its metric in materials (the nonlinear refractive index) is essential to calibrate and develop OPCPA as the various OPA stages making an OPCPA require high peak intensity to reach gain saturation. This thesis presents a novel optical Kerr effect spectroscopy method labeled nonlinear chirped interferometry used to characterize the third order nonlinear tensor on the femtosecond time scale. This method is a three-beam experiment where a reference beam is used to monitor the transient group delay variation of a probe beam under the influence of an intense pump beam in a nonlinear crystal. The transient delay shift is measured with spectral interferometry. The strength of the method is its resilience to environmental fluctuations despite being interferometric. It indeed does not require any active stabilization or advance measurement scheme to reach state-of-the-art uncertainty values. This method was used to characterize liquid crystals as well as nonlinear crystals (sapphire, LBO, KTA, MLN, LGS). The thesis's second part is dedicated to quantifying the stochastic phase noise of the supercontinuum generation process. Supercontinuum generation is an extremely nonlinear process used as the main spectral broadening tool in the seed generation of OPCPA. In the case of infrared OPCPA it is typically achieved by focusing the driving beam inside a mm-long YAG crystal. A modified version of the Bellini-Hänsch interferometer with spectral detection is presented. The stochastic phase noise of the supercontinuum is assessed using spectral interferometer and the generation parameters of the supercontinuum are investigated. The YAG crystal length, position along the beam propagation axis, the pulse energy and the spatial phase of the beam are all individually characterized. Stability areas for each parameter are identified and transfer coefficients between energy and spectral phase and spatial phase and spectral phase are extracted. These coefficients are a metric to quantify the impact of the

fluctuations of the parameters on the spectral phase.

Keywords : ultrafast optics, nonlinear optics, filamentation, Kerr effect, spectral interferometry

Aknowledgements

I would like to first acknowledge the two most important contributors to this work who are my two supervisors. Merci beaucoup Aurélie pour tous ces précieux conseils et toutes ces discussions qui m'ont énormément apporté et qui m'ont été indispensables. C'était un plaisir de travailler avec toi pendant ces trois années. Merci beacoup Nicolas là aussi pour de nombreuses discussions scientifiques particulièrement dans les premiers mois de ma thèse durant lesquels ma compréhension était la moins développée.
I would also of course like to thank all my committee members for agreeing to take an interest in my research work. Thank you Marc Hanna and Aurélien Houard for reading this whole thesis thoroughly and for writing very kind reports on your findings. Thank you Sophie Brasselet and Caterina Vozzi for participating in my defense and asking relevant questions even when the topic is not directly related to your field.
I would also like to thank all my colleagues at Fastlite and at Inphyni with a special mention to Ines from Fastlite and Loic from Inphyni who were fellow phd students respectively sharing an office with me. A big thanks to the whole SMART-X network who made this phd even more interesting by introducing me to the field of X-ray spectroscopy and allowing me to travel to many different places in Europe.
And finally a special thanks to Zoey for all your support and care throughout this whole phd.

Table des matières

Introduction

The discovery and the development of the mode-locking of laser cavities [1] and particularly passive mode locking [2] allowed the creation of tabletop pulsed laser sources with a pulse duration shorter than the picosecond. Femtosecond sources are perfect candidates for the generation of optical frequency combs with a resolution in frequency smaller than 10^{-14} [3]. Plenty of applications were then investigated with precise and tunable frequency combs, such as frequency comb spectroscopy [4], optical waveform generation [5] and optical clocks [6]. Femtosecond laser sources are also used for biomedical applications such as laser eye surgery [7], Raman microscopy [8] or two-photon microscopy [9]. In industry femtosecond sources are a manufacturing tool used for metal machining as the short pulse duration allows for material etching with minimal thermal effects [10]. Femtosecond sources are perfect candidates for investigating and using nonlinear optics due to their high peak intensity [11]. With their development came the development of nonlinear optics [12] and its various applications. Nonlinear optics is the field describing the many photon interactions and can be split according to the order of the nonlinearity. Second-order nonlinearity leads to second harmonic generation [13], sum frequency generation, and difference frequency generation [14]. The most notable third-order effect is the optical Kerr effect [15] i.e. the modification of the refractive index with intensity. Higher-order nonlinear effects include high harmonic generation [16] and multiphoton absorption [17]. Nonlinear optics is routinely used for pulse shaping [18], pulse characterization [19] and pulse spectral broadening [20].

One specific category of femtosecond sources that relies on nonlinear optics is called optical parametric chirped pulse amplifiers (so-called third-generation femtosecond sources). OPCPAs are pulse laser sources combining two effects : chirped pulse amplification [21] and optical parametric amplification [22]. Two main pump laser technologies for OPCPA are titanium sapphire and ytterbium YAG. Titanium sapphire has been used for a longer time due to its wide gain bandwidth supporting sub-10 fs pulses [23]. In the later years, Yb :YAG pump lasers are taking over because they can reach higher average powers [24]. Seeding an Optical Parametric Amplifier (OPA) with the pulses generated by such sources [22] can produce few-cycle high-power pulses in the optical and infrared spectral range.

Having access to such ultrashort and broadband pulses opens the door for new applications in attosecond physics as well, such as XUV attosecond pulses generation in gases [25] and more recently in solid state nanostructures [26], the emission and the control of electron wavepackets [27] and the nano tunneling of electrons [28]. All these processes rely on the interaction between the electric field of the light pulse and the Coulomb potential of an electron to bend it and allow a tunnel ionization of the electron. This effect is directly dependent on the electric field value, which is dependent on the Carrier Envelope Phase (CEP) of each pulse.

The Carrier Envelope Phase (CEP) or Carrier Envelope Offset (CEO) is the relative phase difference between the envelope and the carrier wave of a light pulse. Figure 2 shows a typical few-cycle pulse with its CEP.

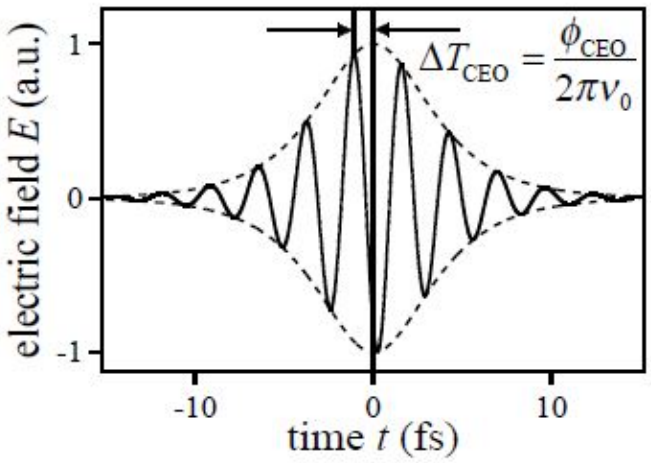

FIGURE 2 – [3] figure 1 :5-fs pulse with sech-shaped field envelope. The pulse-to-pulse carrier-envelope offset phase, Φ_{CEO}, is proportional to the round trip delay of the central fringe, ΔT_{CEO}, and the carrier frequency, ν_0. Φ_{CEO} is defined as the phase angle at the pulse center.

The research on CEP stable sources started in the early 2000s, at this time, the main strategy to achieve CEP stabilization was the control of the oscillator cavity length with thin Silica wedges. Combining an f-2f interferometer with motorized wedges creates an active stabilization method via a feedback loop [29, 30]. The output of the stabilized oscillator can then be amplified to reach hundreds of μJ pulse power [31]. Instead of modifying the laser cavity to compensate for the CEP drift, an acousto-optic frequency shifter (AOFS) can be used at the output of the oscillator along with a feedback loop, this method is called a feed-forward (FF) method [32]. The advantages of the FF method over the FB method are the fact that it only requires simple electronics and that it does not depend on the long-term performance of the system. However, it tends to perform poorly over long periods of time, when the modulation frequency drifts outside of the bandwidth of the AOFS. A solution to compensate for this issue is to combine both feedback and feed-forward methods [33].

Similarly to the mode-locking of a laser cavity, a passive method gives better results [34]. Generating the intrapulse difference frequency, or more generally the difference frequency of a supercontinuum and its seed creates an idler that is CEP stable (figure 9 (b) [34]). To reach the state-of-the-art CEP stable optical amplifiers, the last step is to add a feedback loop with an Acousto-Optic Programmable Dispersive Filter (AOPDF) [35]. Despite passive and active stabilization, noise still remains in the CEP of the OPCPAs. As the amplifiers are complex and long systems, it is difficult to assess the origin of the noise and the contribution of each step to it. However, the most likely suspect of coherence loss is the white light generation. What's more, two supercontinua are generated in a typical CEP stable amplifier, one for the passive stabilization with DFG and one for the measurement setup.

The spectral broadening in supercontinuum generation is caused by two different fundamental nonlinear processes. The first one is Self Phase Modulation (SPM) and is most relevant

for pulses with nJ energy levels. The second one and the most significant in the generation of octave-spanning spectra is filamentation [36]. Filamentation results in a much bigger loss of intrapulse coherence than lone SPM [37] and as a result produces more CEP noise.

This work focuses on two different topics both in service of CEP-stable OPCPA development. The first topic investigated in chapter 2 is optical Kerr effect spectroscopy where nonlinear chirped interferometry is presented and used to characterize crystals used for optical parametric amplification. The next three chapters (chapter 3, 4 and 5) are dedicated to the study of the intrapulse coherence loss due to the WLG process.

Chapitre 1

Introduction

This chapter aims to introduce the necessary concepts to understand the studies developed in this thesis. The first section will define the mathematical formalism used to describe a (continuous or pulsed) light wave and focus on linear optics. The second section will study interferometry. The third section will focus on nonlinear optics by detailing two essential processes for this thesis : difference frequency generation and filamentation.

1.1 Linear optics

1.1.1 Mathematical pulse representation

The first section of this chapter derives the formalism used throughout this chapter to detail the different processes. The formalism derived here was largely inspired from [38]. Light is an electromagnetic wave that can be characterized by its electric field. As the light considered in this thesis is emitted from lasers it is highly directional and will be propagating along the z-axis. The mathematical expression for the electric field is :

$$\vec{E}(r,t) = \hat{e}A(\vec{r},t)e^{i(\vec{k}.\vec{z}-\omega t)} + c.c. \tag{1.1}$$

where k is the wave vector and ω is the frequency of the light. $A(r,t)$ is the wave amplitude and can also be time and space-dependent. $\hat{e}$ is the polarization vector. The polarization is generally elliptical but will be kept linear in this chapter. The transverse spatial profile of the beam will be considered to be homogeneous and can then be expressed only as a function of z and t :

$$\vec{E}(z,t) = \hat{e}A(z,t)e^{i(kz-\omega t)} + c.c. \tag{1.2}$$

A common form of a beam and the only one considered in this thesis is that of a Gaussian beam that takes the form in equation 1.3.

$$\vec{E}(r,t) = \hat{e}A(z,t)\frac{w_0}{w(z)}exp^{i\left(\frac{kr^2}{2q(z)}+kz-\tan^{-1}(\frac{z}{z_R})-\omega t\right)} + c.c. \tag{1.3}$$

where :

$$w(z) = w_0\sqrt{1+\left(\frac{z}{z_R}\right)^2} \tag{1.4}$$

$$q(z) = z - iz_R \tag{1.5}$$

$$z_R = \frac{n\pi w_0^2}{\lambda} \tag{1.6}$$

w_0 is the beam waist and is the beam radius at $z = 0$, $q(z)$ is the complex radius of curvature and z_R is the Rayleigh range.

When simulating or describing a physical phenomenon, the spatial profile is often ignored to simplify the model. In this case, the field can be expressed in the time domain as :

$$\vec{E}(t) = \hat{e}A(t)e^{-i\omega t} + c.c. \tag{1.7}$$

The temporal profile of the wave is described by the temporal wave envelope $A(t)$. The temporal width is defined with the Full Width Half Maximum (FWHM) of the temporal envelope in intensity. Taking the example of a Gaussian beam also in time $A(t)$ takes the form :

$$A(t) = e^{-\sqrt{2ln2}\left(\frac{t}{\tau_{FWHM}}\right)^2} \tag{1.8}$$

The intensity of the pulse is defined as :

$$I(t) = 2n_0\epsilon_0 c|A(z,t)|^2 \tag{1.9}$$

Adding a time-dependent phase to the pulse description gives this mathematical expression along the polarization axis (assuming linear polarization) :

$$E(t) = \sqrt{I(t)}e^{-i(\omega t-\phi(t))} + c.c. \tag{1.10}$$

From this equation, the complex and real amplitudes of the pulse are defined :

$$\tilde{A}(t) = \sqrt{I(t)}e^{-i\phi(t)} \tag{1.11}$$

$$A(t) = \sqrt{I(t)} \tag{1.12}$$

This formalism will be used in section 1.1.2 to describe the Fourier transform properties of a pulse.

1.1.2 Fourier transform

Any square-integrable complex function can be decomposed as the sum of harmonic oscillations with a respective phase and amplitude according to the Fourier theorem. The Fourier transform is the mathematical tool allowing the retrieval of the harmonic decomposition of a complex function. It is expressed as follows taking the electric field as a real function :

$$E(\omega) = \int_{-\infty}^{+\infty} E(t)e^{-i\omega t}dt = \mathcal{FT}(E(t)) \tag{1.13}$$

Similarly the inverse Fourier transform used to go from $E(\omega)$ to $E(t)$ is defined as :

$$E(t) = \frac{1}{2\pi}\int_{-\infty}^{+\infty} E(\omega)e^{i\omega t}d\omega = \mathcal{FT}^{-1}(E(\omega)) \tag{1.14}$$

The field can then be expressed as a function of spectral amplitude and spectral phase as follows :

$$E(\omega) = \sqrt{S(\omega)}e^{-i\varphi(\omega)} \tag{1.15}$$

As examples figures 1.1 and 1.2 show the temporal and spectral profiles of a monochromatic wave and a light pulse respectively.

In the first case (figure 1.1 (a)) the wave is purely monochromatic and written as :

$$E(t) = \sin(-\omega t) \tag{1.16}$$

The Fourier transform is a pure Dirac peak located at the frequency ω as figure 1.1 (b) shows. On the contrary in the second case (figure 1.2 (a)) the wave is a light pulse written as :

$$E(t) = e^{-\sqrt{2ln2}\left(\frac{t}{\tau_{FWHM}}\right)^2}\sin(-\omega t) \tag{1.17}$$

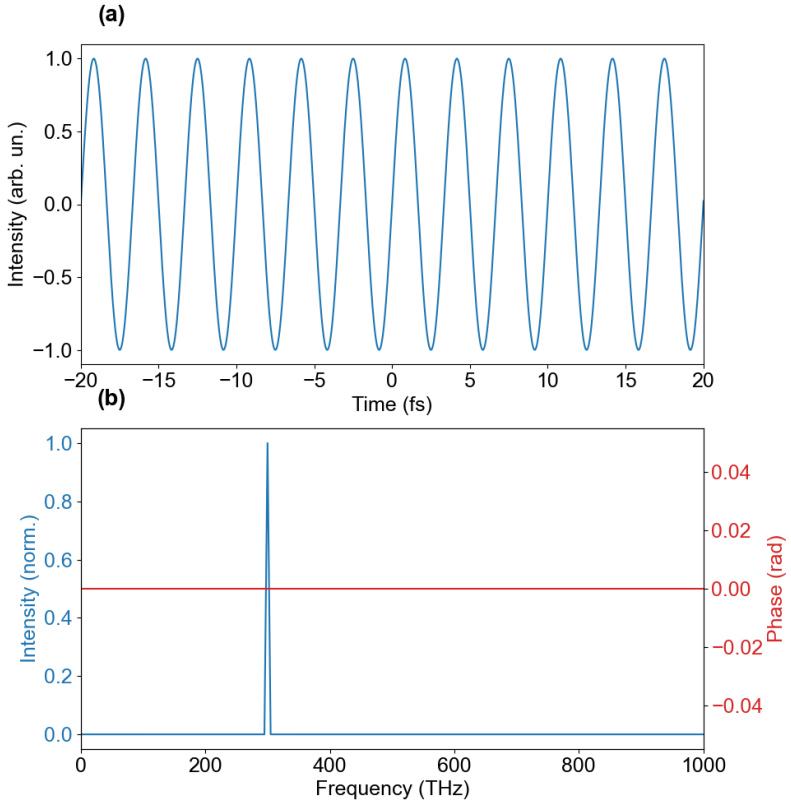

FIGURE 1.1 – (a) : monochromatic wave in the time domain (b) : spectral amplitude of the Fourier transform (blue) and spectral phase of the Fourier transform (red).

The Fourier transform in this case also has a Gaussian shape centered around the frequency as shown in figure 1.2 (b). The product between the temporal duration and the spectral bandwidth is above a given value depending on the shape of the amplitude of the electric field. In the case of Gaussian pulses the time-bandwidth product is as follows :

$$\Delta t \Delta \omega \geq 0.44 \tag{1.18}$$

where Δt and $\Delta \omega$ are the temporal FWHM duration and the FWHM spectral bandwidth respectively. This relationship shows that the larger the spectral bandwidth the shorter the temporal duration. For a given spectrum it gives a minimum duration of a pulse. This is called the Fourier Transform Limit and it is reached as explained in section 1.1.3 for a flat or linear spectral phase.

This concept of Fourier transform was first introduced by Joseph Fourier in the 18th century. It has many applications in mathematics and was the object of many fundamental works [39-42]. Fourier transform is a powerful analysis tool similar to the Laplace transform [43]. It can be used to solve problems in the Fourier domain that would be otherwise difficult to tackle such as differential equations or other problems in mathematical physics [44]. Fourier transform is also routinely used in quantum mechanics. In the same way that it was shown that

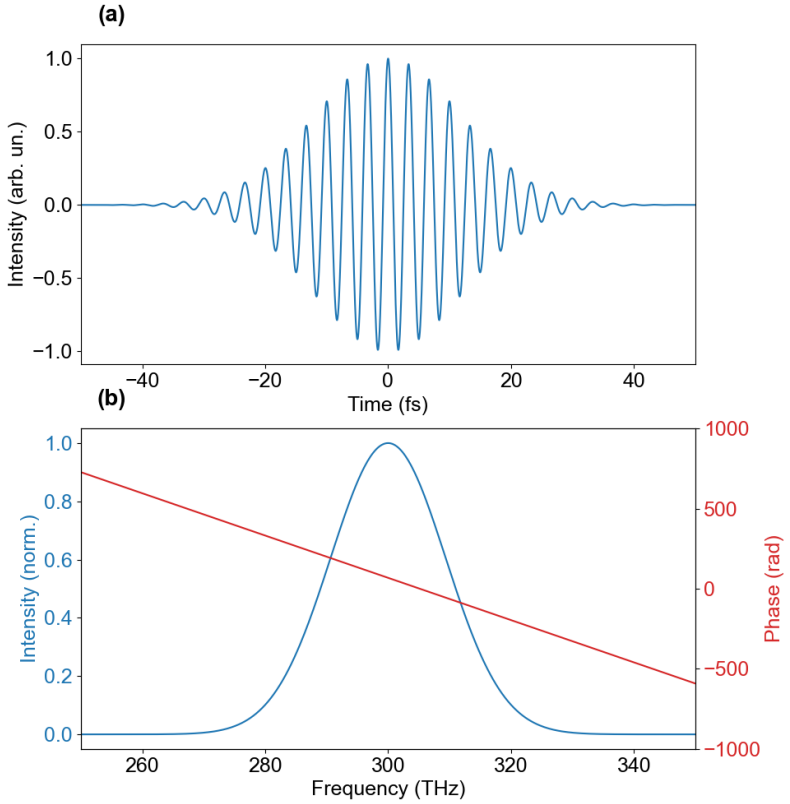

FIGURE 1.2 – (a) : light pulse in the time domain (b) : spectral amplitude of the Fourier transform (blue) and spectral phase of the Fourier transform (red).

Fourier transform can be used to go from temporal representation to frequency representation it can be used to go from a wave function and position representation to wave function and momentum representation [45]. In the field of space optics, Fourier transform is realized [46] simply by the use of a lens for example [47]. The Fourier transform of an object placed before a lens can be observed at the lens focus. Another common device for Fourier transform is the spectrometer used to access the spectral content of an optical pulse [48]. However, only the power spectral density of a pulse or $|E(\omega)|^2$ can be accessed without any phase information. The typical architecture of a spectrometer is a diffracting optics (typically a grating [49]) that diffracts different wavelengths with a different angle and a detection device such as an array of photo-detectors. The use of a diffracting optics gives access to the Fourier plane in numerous shaping systems [50].

1.1.3 Phase description

After the mathematical description of light and the basics of the Fourier transform this subsection takes a look at the phase properties of a light pulse.

Dispersion

Depending on the context the term dispersion has two meanings :

— when discussing the dispersion of a pulse it refers to the description of the spectral phase of the pulse.
— when discussing the dispersion of a material it refers to the effect of a material on the spectral phase of a pulse. This is directly contained in the frequency-dependent refractive index $n(\omega)$.

The spectral phase of a pulse is defined in equation 1.15 as $\varphi(\omega)$. Figure 1.2 shows the Fourier transform of a pulse with a linear spectral phase. This subsection explores the consequences of the spectral phase profile on the temporal shape of the pulse. A Taylor expansion of the spectral phase around a central frequency ω_0 is shown in equation 1.19.

$$\varphi(\omega) = \varphi_0 + \varphi_1(\omega - \omega_0) + \frac{\varphi_2}{2}(\omega - \omega_0)^2 + \frac{\varphi_3}{6}(\omega - \omega_0)^3 + ... \tag{1.19}$$

Figure 1.3 shows the Fourier transform with the different phase orders and their corresponding temporal profiles. The name and consequences of the different orders are detailed below.

— φ_0 is the 0-th order phase or the absolute phase or the Carrier Envelope Phase (CEP). This term is the same in the frequency domain and in the time domain as :

$$\mathcal{FT}[f(t)e^{i\phi_0}] = F(\omega)e^{i\phi_0} \tag{1.20}$$

— φ_1 is the first order of the spectral phase (slope) and corresponds to the group delay (typically expressed in fs). A variation of the group delay does not modify the temporal shape of the pulse but shifts the pulse in the time domain.
— φ_2 is the second order of the spectral phase or Group Delay Dispersion (GDD, typically expressed in fs^2). A non-zero value of GDD causes symmetric temporal stretching of the pulse by creating a time dependence of the instantaneous frequency of the light pulse effectively spreading the arrival time of the different frequency components of the pulse. Adding quadratic spectral phase symmetrically broadens the pulse in the temporal domain (figure1.3 (c)). Additionally, a quadratic phase in the temporal domain is called chirp and the direct consequence of that is a linear dependency of the instantaneous frequency with time. It has the following temporal equation :

$$E(t) = A(t)exp(-i\omega_0 t + \beta t^2) \tag{1.21}$$

where $A(t)$ is the temporal envelope of the pulse and β is the chirp coefficient.
— φ_3 is the third order of the spectral phase or Third Order Dispersion (TOD, typically expressed in fs^3). A non-zero value of TOD also temporally reshapes the pulse but its description is not as simple as with GDD. Adding third-order spectral phase creates a very distinct asymmetric feature in the time domain. There are indeed multiple prepulses visible in figure 1.3 (d) however the FWHM duration of the pulse is almost not

modified.

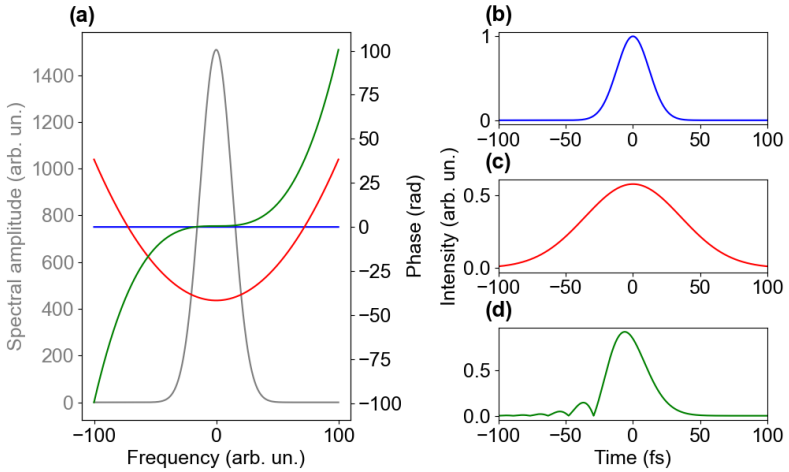

FIGURE 1.3 – (a) : spectral amplitude of the example pulse in grey with three different spectral phases : flat phase in blue, quadratic phase in red and third order phase in green. (b) : temporal envelope of the pulse with a flat phase. (c) : temporal envelope of the pulse with a quadratic phase. (d) : temporal envelope of the pulse with third order phase.

The dispersion analysis is generally limited to these orders of dispersion as the impact of the higher order is not trivial to describe and is not as essential.

As mentioned in the previous subsection accessing the spectral content of a pulse is easily done with a spectrometer. This is only half the information however and to retrieve the complete electric field information spectral phase also has to be known. Determining the spectral phase of a pulse is however much less trivial as the direct measurement of the electric field or of the temporal shape of a femtosecond pulse is not possible with nanosecond response time electronics [51]. Most of the pulse measurement techniques rely on nonlinear optics or interferometry and will be described in the following sections.

The control of the spectral phase of a pulse has been used for numerous applications. One of the most famous ones in ultrafast optics is called chirped pulse amplification (CPA) [52] for which the 2018 Nobel Prize in physics was awarded. In this amplification technique, the pulse is temporally stretched by adding second-order spectral phase before amplification. This drastically reduces the peak intensity resulting in a more effective amplification. The pulse is then re-compressed by compensating for the introduced spectral phase. Spectral phase management is also used in the chirp-managed directly modulated laser [53]. It is a modulation technique used in telecommunication for highly dispersion-tolerant long-distance communication. Long-distance telecommunication is a field requiring dispersion management to transmit information. The typical optical fiber used for telecommunication is called SMF-28 [54, 55]. It is a glass step-index optical fiber with a maximum transmission at the wavelength of 1550 nm (the most common telecommunication wavelength). At this wavelength however and with this core diameter the dispersion inside the fiber (both from the glass dispersion and the waveguide dispersion [56]) is not zero. As a consequence, the temporal shape of a pulse propagating for a

long distance in such a fiber will be stretched. This motivated the development of dispersion compensation techniques [57] or dispersion shifted fibers [58].

All the phase properties considered here were in the time or equivalently in the frequency domain assuming perfect homogeneity in the spatial domain. The next subsection studies the properties of the spatial phase of a light beam.

Spatial phase aberrations

The spatial phase of optical beams describes the phase of the electric field in the transverse plane of propagation. It is a 2-dimensional quantity that is most commonly decomposed using the Zernike polynomials which are mathematically expressed as follows :

$$Z_n^m(\rho,\varphi) = R_n^m(\rho)\cos(m\varphi) \tag{1.22}$$

$$Z_n^{-m}(\rho,\varphi) = R_n^m(\rho)\sin(m\varphi) \tag{1.23}$$

where n and m are positive integers and R_n^m functions are the radials polynomials defined as follows :

$$R_n^m(\rho) = \sum_{k=0}^{\frac{n-m}{2}} \frac{(-1)^k(n-k)!}{k!(\frac{n+m}{2}-k)!(\frac{n-m}{2}-k)!}\rho^{n-2k} \tag{1.24}$$

Figure 1.4 shows the 16 first Zernike polynomials.

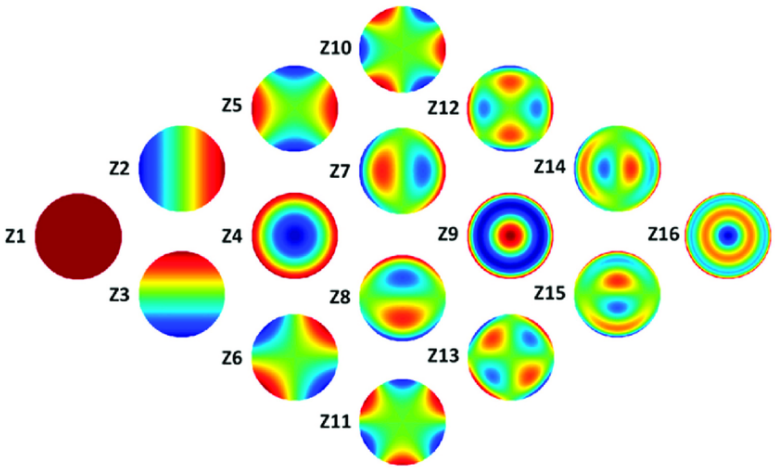

FIGURE 1.4 – 16 lowest order Zernike polynomials. Figure reproduced from [59].

These 2D polynomial functions describe the common optical aberrations. The aberrations are shown with increasing polynomial order. Orders 0 (Z1) and 1 (Z2 and Z3) are an offset and a tilt in the spatial phase and are irrelevant to this thesis. Order 2 is made of the focusing aberration (Z4) and the astigmatism aberration (Z5 and Z6). Order 3 is made of the coma aberration (Z7 and Z8) and the trefoil aberration (Z9 and Z10). Finally, order 4 is made of the spherical

aberration (Z9), the secondary astigmatism aberration (Z12 and Z13), and the quadrafoil aberration (not shown here).

Much like a spectrometer gives no information on the spectral phase, a simple intensity measurement via a camera gives no information on the spatial phase. There are many wavefront measurement techniques available such as Shack-Hartmann wavefront sensor [60], pyramid sensor [61] or shearing interferometry [62] among others [63]. In this work, only the Shack-Hartmann technology will be used as presented in appendix C. Alternatively, analyzing the far field of the beam gives partial information on the wavefront. This is typically achieved by looking at the beam profile at the focal plane of a lens or mirror.

Phase manipulation is also realized in the spatial domain. Its most simple example is the use of focusing optics. More advanced applications exist such as arbitrary wavefront shaping using a spatial light modulator [64-66]. Wavefront shaping is also an essential component of the 4f pulse shaper [67]. Wavefront shaping additionally has a plethora of applications outside of optics in biomedical science for example [68].

1.2 Interferometry

After mathematically describing a single light pulse and its associated phase this section studies the interactions between multiple pulses and specifically the interference phenomenon.

1.2.1 Principle

Let us first consider the most basic example of two monochromatic waves with the same wavelength, whose complex amplitudes are respectively named $E_1(r)$ and $E_2(r)$. The coherent addition is expressed as :

$$E(r) = E_1(r) + E_2(r) \tag{1.25}$$

For the convenience of reading the explicit dependence on r will be omitted in the following equations. The intensity of the total wave is then :

$$I = |E|^2 \tag{1.26}$$

$$I = |E_1|^2 + |E_2|^2 + E_1^* E_2 + E_1 E_2^* \tag{1.27}$$

Substituting the expressions of E_1 and E_2 in equation 1.26 by $E_1 = \sqrt{I_1} e^{i\varphi_1}$ and $E_1 = \sqrt{I_2} e^{i\varphi_2}$ gives this new expression of the total intensity :

$$I = I_1 + I_2 + 2\sqrt{I_1 I_2}\cos(\varphi) \tag{1.28}$$

where φ is the phase difference between the two waves $\varphi = \varphi_2 - \varphi_1$. Assuming waves of the same intensity I_0 the equation writes :

$$I = 2I_0[1 + \cos(\varphi)] \tag{1.29}$$

The intensity is oscillating with the phase difference between the values of 0 and $4I_0$. Now let us consider the particular case of two co-propagating plane waves with a delay distance d such that $E_1 = \sqrt{I_0}e^{-ikz}$ $E_2 = \sqrt{I_0}e^{-ik(z-d)}$. In this case the phase difference is $\varphi = kd = \frac{2\pi nd}{\lambda}$ and the total intensity is :

$$I = 2I_0\left[1 + \cos\left(\frac{2\pi nd}{\lambda}\right)\right] \tag{1.30}$$

Interferometers are based on this principle. In an interferometer, a wave is split into two waves using a beam splitter. The two waves are delayed an unequal distance and then recombined. As the intensity profile depends on the delay d, the refractive index n, and the wavelength λ ; interferometers can be used to measure small variations of all these parameters.

So far only perfect coherence has been studied. Partial coherence is considered by introducing the correlation between the two waves $g_{12} = \frac{<E_1^* E_2>}{\sqrt{I_1 I_2}}$ and the total field becomes :

$$I = I_1 + I_2 + 2\sqrt{I_1 I_2}Re(g_{12}) \tag{1.31}$$

where $\varphi = arg(g_{12})$. In the extreme case where the waves are perfectly correlated $g_{12} = e^{i\varphi}$ which comes back to equation 1.28. In the other extremum of complete decoherence $g_{12} = 0$, there is no interference. Any case in between can be described by introducing the visibility or contrast of the interference. It is defined as :

$$V = \frac{I_{max} - I_{min}}{I_{max} + I_{min}} \tag{1.32}$$

$$I(\tau) = (I_1 + I_2)[1 + Vcos\varphi] \tag{1.33}$$

In the particular case where $I_1 = I_2$ the visibility is :

$$V = |g_{12}| \tag{1.34}$$

$$I(\tau) = 2I_0[1 + Re(g_{12})] \tag{1.35}$$

In the case of two identical delayed waves (delay τ) the correlation can be defined as a function of delay $g_1 = g_2 = g(\tau)$ and the intensity now takes the following form :

$$I(\tau) = 2I_0 \left[1 + |g(\tau)| \cos \varphi(\tau)\right] \tag{1.36}$$

Taking the following coherence function as an example $g(\tau) = g_a(\tau)e^{i\omega_0\tau}$ the temporal coherence τ_c of the wave is defined by the width of $|g_a(\tau)|$. It is linked to the spectral bandwidth of the wave by $\tau_c = \frac{1}{\Delta\omega}$. The direct consequence of this is the lower coherence time for pulsed light compared to monochromatic waves.

When the waves are polychromatic the resulting signal is in this case as derived in [38] :

$$I(\tau) = 2\int_0^{+\infty} S(\omega)(1 + cos(\omega\tau))d\omega \tag{1.37}$$

where $S(\omega)$ is the Fourier transform of the real part of the correlation function $g_a(\tau)$.

This can be interpreted as the superposition of all the interferences between the monochromatic waves of the pulses.

One of the most famous applications of interferometry is the Michelson and Morley experiment in 1887 [69] leading to the theory of special relativity. Michelson interferometer can be used as narrow-band optical filters [70] or to measure the oscillator strengths of atomic transitions in sodium vapor [71]. The latter was accomplished by placing sodium vapor in one of the arms of a Michelson interferometer and studying the interference pattern. Multiple-wave lateral shearing interferometry is used as a sensitive wavefront measurement technique [72].

Interferometry also has applications outside of physics in biomedical fields for example. Optical coherence tomography [73] is a technique based on low coherence interferometry used to visualize internal tissue microstructures. Finally, angle-resolved low coherence interferometry [74] allows the measurement of the size of sub-cellular objects such as the cell nuclei.

1.2.2 FTSI

This section focuses on spectral interference and in particular on Fourier Transform Spectral Interferometry (FTSI) [75]. The purpose of this technique is to access the spectrally-resolved phase difference between two polychromatic waves. Let us consider the interference of two electric fields E_1 and E_2 on a spectrometer. The temporal delay between the two fields is τ. The respective Fourier transforms of these fields are $E_1(\omega)$ and $E_2(\omega)$. The total intensity in the Fourier domain is then :

$$E(t) = E_1(t) + E_2(t - \tau) \tag{1.38}$$

$$I(\omega) = |E_1(\omega) + E_2(\omega)e^{i\omega\tau}|^2 \tag{1.39}$$

$$I(\omega) = |E_1(\omega)|^2 + |E_2(\omega)|^2 + f(\omega)exp(i\omega\tau) + f^*(\omega)e^{-i\omega\tau} \tag{1.40}$$

where $|E_1(\omega)|^2$ and $|E_2(\omega)|^2$ are the spectral intensities of the two electric fields and $f(\omega)$ is the interference term between E_1 and E_2 ($f(\omega) = E_1(\omega)E_2^*(\omega)$). The first step of the FTSI algorithm is to take the inverse Fourier transform of the spectral intensity :

$$\mathcal{FT}^{-1}[I(\omega)] = E_1^*(-t) \otimes E_1(t) + E_2^*(-t) \otimes E_2(t) + f(t-\tau) + f^*(-t-\tau) \tag{1.41}$$

The first two terms are the auto-correlations of the two individual electric fields and are centered around $t = 0$. The two last terms are the cross-correlation functions centered at $t = \tau$ and $t = -\tau$ respectively. As the auto-correlations do not contain any phase information according to the Wiener-Khinchin theorem they are numerically filtered out and only the component at $t = \tau$ is kept. This is only possible if the value of τ is large enough to temporally separate the three components. $f(t-\tau)$ is then Fourier transformed back in the frequency domain to get $f(\omega)e^{i\omega\tau}$. The amplitude and phase of this term are :

$$arg(f(\omega)e^{i\omega\tau}) = \varphi_{E_1} - \varphi_{E_2} + \omega\tau \tag{1.42}$$

$$|f(\omega)e^{i\omega\tau}| = |E_1(\omega)||E_2(\omega)| \tag{1.43}$$

As equation 1.42 shows the phase difference between the two waves is encoded into the interferogram and accessible through the algorithm described here. In the particular case where $E_1(\omega) = E_2(\omega) = E(\omega)$ the equations become :

$$I(\omega) = |E(\omega)(1 + e^{i\omega\tau})|^2 \tag{1.44}$$

$$I(\omega) = |E(\omega)|^2(2 + e^{i\omega\tau} + e^{-i\omega\tau} \tag{1.45}$$

$$\mathcal{FT}^{-1}[I(\omega)] = 2E^*(-t) \otimes E(t) + f(t-\tau) + f^*(-t-\tau) \tag{1.46}$$

$$arg(f(\omega)e^{i\omega\tau}) = \omega\tau \tag{1.47}$$

$$|f(\omega)e^{i\omega\tau}| = |E(\omega)|^2 \tag{1.48}$$

The different steps of the algorithm are presented in this configuration of identical waves in figure 1.5. This is entirely simulated with two spectra centered around the central frequency of 300 THz. The spectral bandwidth of the pulses is 10 THz FWHM and the temporal delay is 1.5 ps [76].

In this example, the two pulses are identical so the phase is as expected purely linear. In the more interesting case where the two electric fields are not identical the phase extracted and shown in figure 1.5 (c) would not be linear but would be the spectrally resolved phase difference between the two waves.

Fourier transform spectral interferometry is part of a family of techniques called spatially and spectrally resolved interferometry (SSRI). It is a technique based on interference with tilted

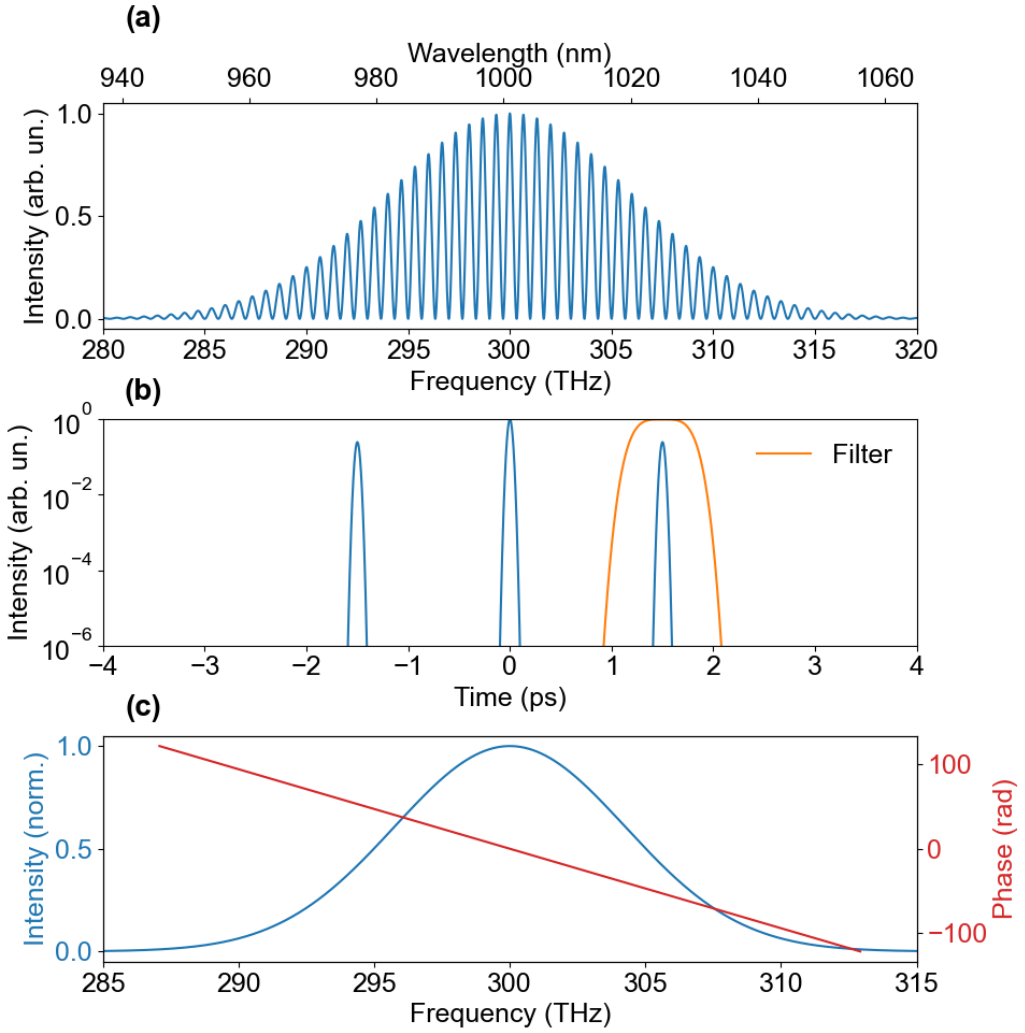

FIGURE 1.5 – (a) : interference pattern around the central frequency of 300 THz. (b) : inverse Fourier transform of the spectrum in figure (a). The central peak is the auto-correlations of the individual waves and the terms at +/-τ are the interference terms. The temporal filter is plotted in orange and selects the component at +τ to Fourier transform back. (c) : Fourier transform of the signal selected in (b). The spectral amplitude is the envelope of the original spectral fringes and the spectral phase is linear with a slope of 1.5 ps matching the temporal delay between the two pulses.

wavefronts and spectral resolution [77]. This technique has been used to determine the dispersion of thin metallic layers [78] or of dispersion compensating laser mirrors [79]. In more recent years SSRI has been used to characterize laser pulses [80] or even to characterize attosecond pulses [81]. The technique can be extended with the use of a broadband light source such as a supercontinuum source [82, 83]. SSRI can also be used in pump-probe experiments as in [84] where a spectral interferometer is coupled to a Sagnac interferometer to take single-shot measurement of both the difference transmission and the difference phase spectra. In [85] spectral interferometry is used to precisely determine the group delay of the pulse stretcher and compressor of a CPA system.

Among this family of techniques is the more specific self-referenced spectral interferometry (SRSI) [86, 87] used for pulse characterization. This is the technique used in the Wizzler (Fastlite). SRSI is a pulse characterization technique based on the generation of a replica of the pulse to characterize with a flat spectral phase. The spectral interferogram resulting from the interference between the original pulse and its replica then yields the spectral phase of the original pulse.

In this thesis, spectral interference is particularly interesting as it will be widely employed for metrology and phase noise analysis of nonlinear processes in chapters 2, 4 and 5.

1.3 Nonlinear optics

So far all the phenomena described were part of linear optics. In other words, it was confined to the interaction verifying the superposition principle. This section focuses on nonlinear optics by studying multi-photon processes such as Difference Frequency Generation (DFG) or the Optical Kerr Effect (OKE). The field of nonlinear optics historically started shortly after the invention of the laser with the discovery of the Second Harmonic Generation (SHG) [88]. It is the interaction of two photons at an identical frequency where a single photon with double the energy is generated.

Most of the formalism derived hereafter was largely inspired by [12].

In linear optics, the polarization vector is directly proportional to the electric field as shown here :

$$P(t) = \epsilon_0 \chi^{(1)} E(t) \tag{1.49}$$

where ϵ_0 is the permittivity of free space and $\chi^{(1)}$ is the linear susceptibility. This equation can be generalized to express the polarization as a power series of the electric field ignoring in this case all the delayed effects :

$$P(t) = \epsilon_0 \sum_k (\chi^{(k)} E^k(t)) \tag{1.50}$$

$$P(t) = \sum_k P^{(k)} \tag{1.51}$$

where $\chi^{(2)}$ is the second order susceptibility and $\chi^{(3)}$ is the third order susceptibility. Equation 1.50 can be written in a vectorial form to be more general. In this case $\chi^{(2)}$ and $\chi^{(3)}$ are second and third order tensors respectively.

Starting from the Maxwell equation the following wave equation can be derived for an electric field at a frequency ω_n :

$$\nabla^2 E_n - \frac{\epsilon_1(\omega_n)}{c^2}\frac{\partial^2 E_n}{\partial t^2} = \frac{1}{\epsilon_0 c^2}\frac{\partial^2 P^{NL}}{\partial t^2} \tag{1.52}$$

Nonlinear optics can be described using the wave equation as well as nonlinear polarization. The derivation will be made for the specific case of Difference Frequency Generation (DFG).

1.3.1 OPA/DFG

Difference frequency generation is a second-order nonlinear effect. In this case, we consider a lossless nonlinear medium and collimated, monochromatic, and continuous waves. The waves propagate on the nonlinear medium with normal incidence so all refraction effects will be ignored. Figure 1.6 shows a diagram of the configuration.

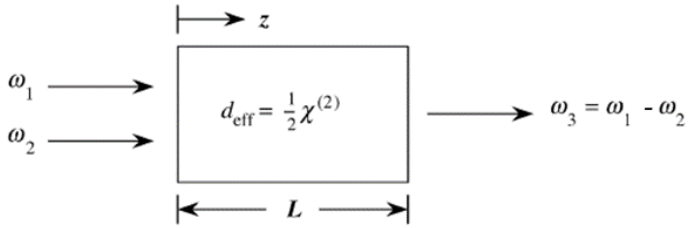

FIGURE 1.6 – Figure modified from 2.2.1 from [12].

All three fields must respect the wave equation 1.3. The electric fields E_i and the nonlinear polarization P_i take the following forms :

$$E_i(z,t) = A_i e^{i(k_i z - \omega_i t)} + c.c. \tag{1.53}$$
$$P_i(z,t) = \tilde{P}_i e^{i(k_i z - \omega_i t)} + c.c. \tag{1.54}$$

where A_i is a constant. This approximation is valid as long as the nonlinear source term ($\tilde{P}_i$) is small. In this case, we assume the wave at frequency ω_3 is a strong wave essentially undepleted by the process. This allows us to consider it a constant for this process. P_2 has the following expression :

$$P_2 = 2\epsilon_0 \chi^{(2)} E_3 E_1^* \tag{1.55}$$

where :

$$E_{1,3} = A_{1,3}e^{ik_{1,3}z} \tag{1.56}$$

Substituting into the amplitude of the polarization gives :

$$P_2 = 2\epsilon_0\chi^{(2)}A_3A_1^*e^{i(k_3-k_1)z} \tag{1.57}$$

Finally substituting this into the wave equation where ∇ is simply the second derivative with position in this particular case gives :

$$\begin{aligned}\left[\frac{\partial^2 A_2}{\partial z^2} + 2ik_2\frac{\partial A_2}{\partial z} - k_2^2A_2 + \frac{\epsilon^{(1)}(\omega_2)\omega_2^2A_2}{c^2}\right]e^{i(k_2z-\omega_2t)} + c.c. \\ = -\frac{2\chi^{(2)}\omega_2^2A_2}{c^2}A_3A_1^*e^{i[(k_3-k_1)z-\omega_2t]} + c.c.\end{aligned} \tag{1.58}$$

After simplification, the equation takes the following form :

$$\frac{\partial^2 A_2}{\partial z^2} + 2ik_2\frac{\partial A_2}{\partial z} = -\frac{2\chi^{(2)}\omega_2^2A_2}{c^2}A_3A_1^*e^{i(k_3-k_1-k_2)z} \tag{1.59}$$

Under the slowly varying envelope approximation the first term vanishes finally giving this wave equation :

$$\frac{\partial A_2}{\partial z} = \frac{i\chi^{(2)}\omega_2^2}{k_2c^2}A_3A_1^*e^{i\Delta kz} \tag{1.60}$$

where $\Delta k = k_3 - k_1 - k_2$ is called the wave vector mismatch. Equation 1.3.1 is called the coupled-wave equation as it describes the amplitude of the E_2 electric field through its coupling with E_1 and E_3. An analog derivation can be done for field 1 by giving the following coupled-wave equation :

$$\frac{\partial A_1}{\partial z} = \frac{i\chi^{(2)}\omega_1^2}{k_1c^2}A_2^*A_3e^{-i\Delta kz} \tag{1.61}$$

If the particular condition of $\Delta k = 0$ the configuration is known as perfect phase matching. The condition for perfect phase matching can be expressed as :

$$\frac{n_1\omega_1}{c} - \frac{n_2\omega_3}{c} = \frac{n_3\omega_3}{c} \tag{1.62}$$

$$n_3 - n_2 = (n_1 - n_2)\frac{\omega_1}{\omega_3} \tag{1.63}$$

In a medium with normal dispersion, the refractive index at frequency ω_2 is higher than at ω_3. The same is true for the frequencies ω_1 and ω_2. This makes equation 1.3.1 impossible in a normal dispersion medium unless the medium is birefringent. Birefringent media have different refractive indices depending on the polarization direction. This allows the phase matching condition to be respected in a normal dispersion medium simply by adjusting the crystal angle and the input beam polarization. One of the most common crystals for second-order nonlinear effects including DFG is β-Barium-Borate (BBO). In perfect phase matching configuration, the coupled-wave equations take this form for ω_2 :

$$\frac{\partial^2 A_2}{\partial z^2} = \frac{2\omega_1^2\omega_2^2(\chi^{(2)})^2}{k_1 k_2 c^4} A_3 A_3^* A_2 \tag{1.64}$$

Introducing $\kappa^2 = \frac{2\omega_1^2\omega_2^2(\chi^{(2)})^2}{k_1 k_2 c^4}|A_3|^2$ gives the new equation :

$$\frac{\partial^2 A_2}{\partial z^2} = \kappa^2 A_2 \tag{1.65}$$

with a solution :

$$A_2(z) = C\sinh(\kappa z) + D\cosh(\kappa z) \tag{1.66}$$

where C and D are integration constants. Finally with the boundary condition of $A_2(0) = 0$ the solution is :

$$A_1(z) = A_1(0)\cosh(\kappa z) \tag{1.67}$$

$$A_2(z) = i\sqrt{\frac{n_1\omega_2}{n_2\omega_1}}\frac{A_3}{|A_3|}A_1^*(0)\sinh(\kappa z) \tag{1.68}$$

Both ω_1 and ω_2 fields show exponential growth with position. The field ω_1 maintains its original phase whereas the phase of the ω_2 field is the phase difference between the field at ω_3 and the field at ω_1. This property is essential when it comes to passive CEP stabilization through the DFG process. The result of this process is an energy transfer between the frequency ω_3 (pump) to the two waves at frequencies ω_1 (signal) and ω_2 (idler). As a result, the signal wave gets amplified by a parametric process (DFG). This is then also called Optical Parametric

Amplification (OPA) and is the base process of the sources called optical parametric amplifiers. A particular category of these sources combining OPA and chirped pulse amplification (CPA) [21] is called Optical Parametric Chirped Pulse Amplification (OPCPA) [89]. An example of such a source will be described extensively in section 3.3.

1.3.2 Quasi-phase-matching

The phase-mismatch Δk was introduced in the previous section as well as the condition of perfect phase matching $\Delta k = 0$ for an efficient OPA process. If the OPA crystal is not birefringent this condition can not be met. When normal phase-matching can not be implemented a technique known as quasi-phase-matching can be implemented. Figure 1.7 shows a periodically poled crystal diagram.

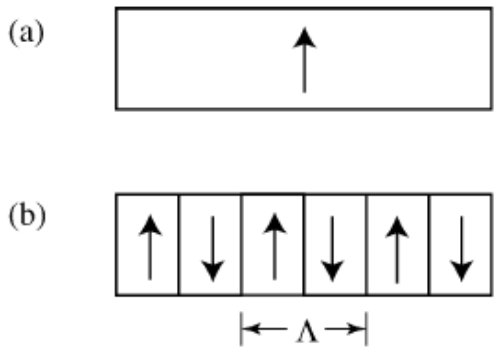

FIGURE 1.7 – Figure from [12]. Schematic representations of a second-order nonlinear optical material in the form of (a) a homogeneous single crystal and (b) a periodically poled material in which the positive c axis alternates in orientation with period Λ.

In a periodically poled crystal, the crystal orientation (c axis) is periodically inverted. As a result, the sign of the nonlinear coupling coefficient d_{eff} is periodically alternated. Figure1.8 compares the field amplitudes in the three cases of perfect phase matching, phase mismatch, and quasi-phase-matching.

The period of the material poling is chosen so that when the field amplitude would decrease (curve (c)) the crystal axis is flipped causing the field amplitude to keep growing.

1.3.3 Sum frequency generation

In an analog fashion to DFG, the process of summing the frequency of two photons is called sum frequency generation (SFG). When the process happens with a single beam it is referred to as second harmonic generation (SHG). The derivation of the coupled wave equations is extremely similar to what was done in section 1.3.1. The expression of the equations is as follows for the SFG process of $\omega_3 = \omega_1 + \omega_2$ (with $\omega_1 \neq \omega_2$) :

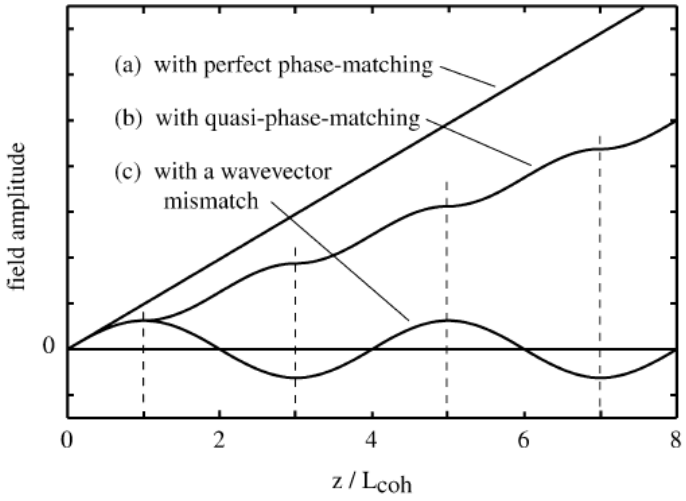

FIGURE 1.8 – Figure from [12]. Comparison of the spatial variation of the field amplitude of the generated wave in a nonlinear optical interaction for three different phase matching conditions. Curve (a) assumes that the phase-matching condition is perfectly satisfied, and consequently, the field amplitude grows linearly with propagation distance. Curve (c) assumes that the wavevector mismatch Δk is nonzero, and consequently, the field amplitude of the generated wave oscillates periodically with distance. Curve (b) assumes the case of a quasi-phase-matched interaction, in which the orientation of the positive c axis is periodically modulated with a period of twice the coherent buildup length L_{coh}, to compensate for the influence of wavevector mismatch. In this case, the field amplitude grows monotonically with propagation distance, although less rapidly than in the case of a perfectly phase-matched interaction.

$$\frac{\partial A_1}{\partial z} = \frac{i\chi^{(2)}\omega_1^2}{k_1 c^2} A_3 A_2^* e^{i\Delta k z} \tag{1.69}$$

$$\frac{\partial A_2}{\partial z} = \frac{i\chi^{(2)}\omega_2^2}{k_2 c^2} A_3 A_1^* e^{i\Delta k z} \tag{1.70}$$

where $\Delta k = k_3 - k_1 - k_2$ is called, the wave vector mismatch. Equation 1.3.1 is called the coupled-wave equation as it describes the amplitude of the E_2 electric field through its coupling with E_1 and E_3. An analog derivation can be done for field 1 by giving the following coupled-wave equation :

$$\frac{\partial A_3}{\partial z} = \frac{i\chi^{(2)}\omega_3^2}{k_3 c^2} A_1 A_2 e^{-i\Delta k z} \tag{1.71}$$

The phase matching considerations are also similar to what was introduced for DFG.

The effects of DFG and OPA presented in this section are second-order nonlinear effects. The most basic second-order effect is second harmonic generation [13]. Second harmonic generation is used in most commercial green laser pointers as well as in high power high beam

quality lasers [90]. The incoherent process analog to second harmonic generation is called two-photon absorption and can be used for high-resolution microscopy [9] for example. An analog effect called sum-frequency generation (SFG) is used in pulse characterization techniques such as auto-correlation [91] or FROG [12]. SFG has a similar principle to SHG using two different pulses. Both these characterization techniques are based on the nonlinear autocorrelation experimentally realized by SFG between two delayed replicas of the original pulse. The only difference between the two techniques is the detection which is a simple photodiode for the autocorrelation and a spectrometer for the FROG. In the case of autocorrelation, only the pulse duration can be retrieved whereas FROG gives complete electric field reconstruction. SFG can also be used to create laser sources mostly in the visible [92] and in the UV [93]. SFG can also be used as a spectroscopy method exploiting the surface SFG [94]. After the description of second-order nonlinear effects, section 1.3.4 describes the main third-order nonlinear effect called Optical Kerr Effect (OKE).

1.3.4 Kerr effect

The refractive index of a material depends on the intensity of the light propagating in the material. This section describes the origin of this effect called the Kerr effect and describes some of its immediate consequences. The third-order non-linear polarization vector is expressed as :

$$P^{NL} = 3\epsilon_0\chi^{(3)}(\omega = \omega + \omega - \omega)|E(\omega)|^2E(\omega) \tag{1.72}$$

Writing the total polarization vector ignoring all the other nonlinear order gives :

$$P^{TOT} = \epsilon_0\chi^{(1)}E(\omega) + 3\epsilon_0\chi^{(3)}|E(\omega)|^2E(\omega) \tag{1.73}$$

$$P^{TOT} = \epsilon_0\chi_{eff}E(\omega) \tag{1.74}$$

where :

$$\chi_{eff} = \chi^{(1)} + 3\chi^{(3)}|E(\omega)|^2 \tag{1.75}$$

The refractive index is generally expressed as :

$$n^2 = 1 + \chi_{eff} \tag{1.76}$$

This gives a dependence of the refractive index on the square of the amplitude of the electric field as follows :

$$n(\omega) = n_0(\omega) + n_2(\omega)|E(\omega)|^2 \tag{1.77}$$

$$n(\omega) = n_0(\omega) + n_2(\omega)I \tag{1.78}$$

where :

$$n_0 = \sqrt{1 + \chi^{(1)}} \tag{1.79}$$

$$n_2 = \frac{3\chi^{(3)}}{4n_0} \tag{1.80}$$

n_0 is then called the linear refractive index and n_2 is the nonlinear refractive index depending on the intensity of the light. This equation is valid when only one field of light is considered. When there are two beams of light $E(\omega)$ and $E(\omega')$ named pump and probe being high and low intensity respectively. In this case, the nonlinear polarization vector for the field ω' has the following form :

$$P^{NL}(\omega') = 6\epsilon_0\chi^{(3)}(\omega' = \omega' + \omega - \omega)|E(\omega)|^2E(\omega') \tag{1.81}$$

The value of the nonlinear refractive index in the case of this cross-coupling effect is :

$$n_2^{(cross)} = \frac{3\chi^{(3)}}{2n_0} \tag{1.82}$$

The magnitude of the nonlinear refractive index, in this case, is twice as high as in the case of the self-induced effect. In this whole section so far the tensor nature of the nonlinear susceptibility has been ignored as the fields considered implicitly always had the same polarization. In reality $\chi^{(3)}$ is an 81 coefficient tensor to account for all the polarization configuration. Naturally, when the nonlinear material has some symmetry properties the associated tensor coefficients will be identical. In the simplest case of an isotropic material for example the diagonal terms are all identical. The intensity dependence of the refractive index has two main consequences in the spatial domain and in the temporal domain : self-focusing and self-phase modulation respectively.

Self-focusing

Let us assume a light pulse with a Gaussian spatial profile in the transverse plane of propagation. If we assume a material with a positive n_2 the refractive index then also has a Gaussian profile in space with a maximum value at the center of the beam. This is exactly analog to the refractive index of a lens causing the beam to focus. The focusing distance in the material z_{sf} can be calculated using Fermat's principle. The refractive index of the material is called n_0 and

is the refractive index value at the edge of the beam. $n_0 + n_2 I$ is the value of the refractive index in the center of the beam. Fermat's principle states that the optical path length of all rays of the same wavefront must be identical. Defining θ_{sf} as the angle between the edge of the beam and the central ray in the material then gives the following relation :

$$(n_0 + n_2 I) z_{sf} = \frac{n_0 z_{sf}}{\cos \theta_{sf}} \tag{1.83}$$

In the small angle approximation $\cos(\theta_{sf}) = 1 - \frac{1}{2}\theta_{sf}^2$ giving :

$$\theta_{sf} = \sqrt{\frac{2n_2 I}{n_0}} \tag{1.84}$$

This is known as the self-focusing angle and allows the calculation of the self-focusing distance $z_{sf} = \frac{\omega_0}{\theta_{sf}}$ which is the distance where the pulse will focus because of self-focusing :

$$z_{sf} = \omega_0 \sqrt{\frac{n_0}{2n_2 I}} \tag{1.85}$$

Self-phase modulation

Let us now ignore all spatial effects and focus on the temporal consequence of the OKE. Let us assume a pulse with the following shape :

$$E(z,t) = A(z,t) e^{i(k_0 z - \omega_0 t)} + c.c. \tag{1.86}$$

The time-dependent refractive index can be expressed as :

$$n(t) = n_0 + n_2 I(t) \tag{1.87}$$

where $I(t) = 2n_0 \epsilon_0 c |A(z,t)|^2$. The consequence of the time-dependent refractive index is a time-dependent phase shift that has the expression :

$$\phi_{NL}(t) = -n_2 I(t) \omega_0 \frac{L}{c} \tag{1.88}$$

As a result of the nonlinear phase shift, the spectral content of the pulse is broadened. This can be mathematically expressed by taking the Fourier transform of the pulse :

$$S(\omega) = |\int A(t)e^{(-i\omega_0 t - i\phi_{NL}(t)}e^{i\omega t}dt|^2 \tag{1.89}$$

This gives a complete description of the spectral content of the pulse. A simpler picture can describe the spectral broadening via the instantaneous frequency of the pulse as a function of time. The frequency of the pulse can be described as :

$$\omega(t) = \omega_0 + \frac{d\phi_{NL}}{dt}(t) \tag{1.90}$$

In the case of a Gaussian pulse in intensity figure 1.9 shows the temporal nonlinear phase and the associated frequency shift.

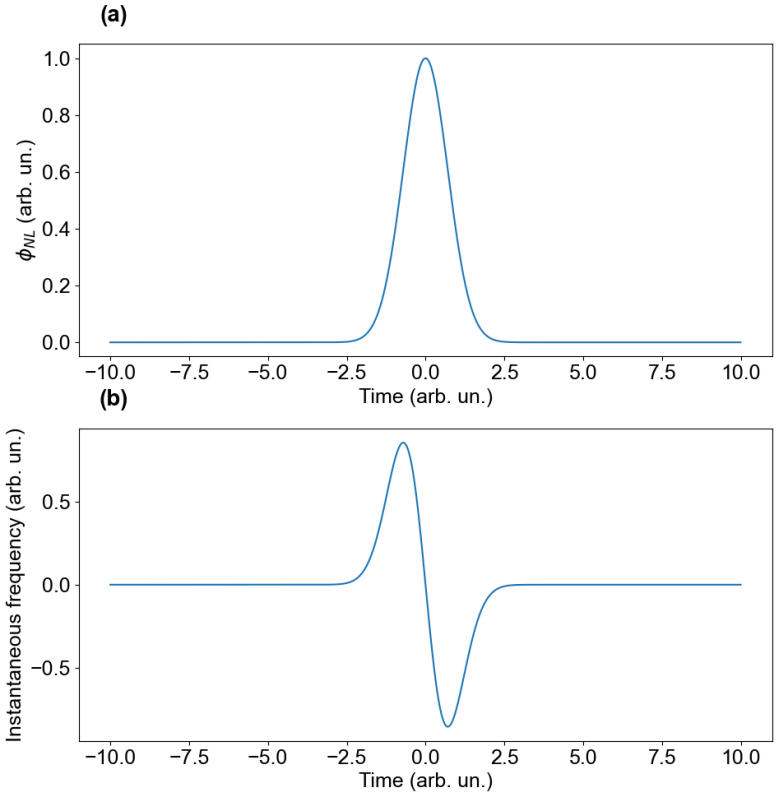

FIGURE 1.9 – (a) : gaussian nonlinear phase shift in time. (b) : associated instantaneous frequency variation.

Self-phase modulation is widely used as a frequency-broadening technique. It is used in pulse post-compression schemes in hollow-core fibers [95] or in multi-pass cells [96]. Self-focusing can be used to fabricate microstructure in materials [97]. Self-focusing is also a limitation to the peak power that can propagate in amplifiers [98]. Above a certain power, the beam collapses leading to the generation of plasma in the medium [99]. These two phenomena are an essential part of the filamentation process [100].

1.3.5 Filamentation

Filamentation is a regime of propagation where the light is confined to a tight effective area over macroscopic distances of propagation [101]. Filamentation can happen in gases [102] or in condensed media [103]. Many processes are involved in the filamentation process. The main one is the Kerr effect described in the previous subsection. When the self-focusing of the beam is stronger than the divergence of the beam the beam size will naturally decrease because of self-focusing. This is defined by the relation :

$$\theta_{diff} = \theta_{sf} \tag{1.91}$$

where θ_{sf} is the self-focusing angle and $\theta_{diff} = 0.61\frac{\lambda}{n_0 d}$ is the diffraction angle. θ_{sf} depends on the beam power which allows the definition of the critical power for which equation 1.91 is met. Injecting the two angle values in the equation gives the following relation :

$$I = \frac{(0.61)^2\lambda^2}{2n_0 n_2 d^2} \tag{1.92}$$

$$P_{crit} = \frac{\pi(0.61)^2\lambda^2}{8n_0 n_2} \tag{1.93}$$

This model only includes self-focusing and diffraction balance. Ignoring every other interaction the beam would collapse to a singularity after the distance z_f defined in equation 1.85. z_f can also be defined as a function of P_{crit} to be [101] :

$$z_f = \frac{0.367 * 2\pi/\lambda * a^2}{\sqrt{(\sqrt{P/P_{crit}} - 0.852)^2 - 0.219}} \tag{1.94}$$

In reality, many mechanisms stop the beam collapse such as multi-photon absorption [104], group velocity dispersion [105], the saturation of the Kerr effect [106], nonlinear absorption [107], nonlocal effects [108], avalanche breakdown [109] and nonparaxial effect [110]. All these processes counteract the self-collapse of the beam. Which mechanism contributes the most depends on the material [111] and the community is not clear cut on the most significant ones [112]. In the bulk case, the significant mechanisms are group velocity dispersion and plasma defocusing [113, 114]. When the beam is focused tightly due to self-focusing the intensity reaches a small fraction of the ionization potential. As a consequence the probability of multi-photon ionization becomes significant and the medium gets ionized generating a plasma. When the field intensity is even higher the main ionization mechanism becomes tunneling ionization. A consequence of the plasma generation is a local reduction of the refractive index according to the law :

$$n = n_0 - \frac{\rho(r,t)}{2\rho_c} \tag{1.95}$$

where $\rho(r,t)$ is the electron density and ρ_c is the density corresponding to the critical plasma density above which the plasma becomes opaque.

The result of the interplay of all these effects is a peculiar structure where the regime of propagation is non-Gaussian without diffraction. This allows the pulse to propagate with peak intensity above the TW/cm^2 over long distances (a few mm in bulk). Despite the highly nonlinear effects at play the beam quality and short pulse duration are conserved. The beam profile during filamentation always has a Townes beam profile [115]. Most of the pulse energy is not contained in the filament itself. 90% of the pulse energy is contained in what is called the photon reservoir around the filament [116]. The reservoir is essential to maintain the filamentation regime [117] and the filaments break down once the energy in the reservoir gets too low. It is decreased by multiphoton absorption or plasma absorption [107]. Another consequence of the filamentation is the intensity clamping [118]. Because filamentation is the result of the self-focusing effect and the various defocusing contribution that all depend on the pulse power the intensity inside the filament is very stable. This specific value depends on the material but is typically of the order of 10^{13} W/cm^2 [100]. The propagation over multiple millimeters with such a small diameter and high pulse energy translates into a high amount of nonlinear effect. One of these effects is called self-steepening. It causes the temporal shape of the pulse to exhibit a steep slope on the front edge of the pulse. This is a consequence of the Kerr effect and the Gaussian temporal profile of the pulse where the central part experiences a higher refractive index. It is illustrated in figure 1.10.

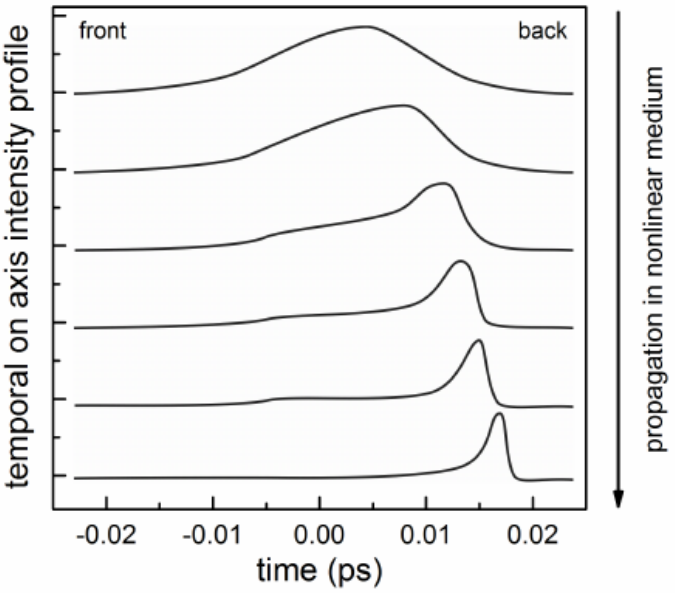

FIGURE 1.10 – Figure from [101].

A third effect after self-focusing and self-steepening arises from the Kerr effect : self-phase modulation. As previously described it causes spectral broadening (so does self-steepening and ionization in a non-symmetrical fashion) and is one of the reasons filamentation can be used as a seed for optical parametric amplification [119].

The structure of a filament looks like the diagram from figure 1.11.

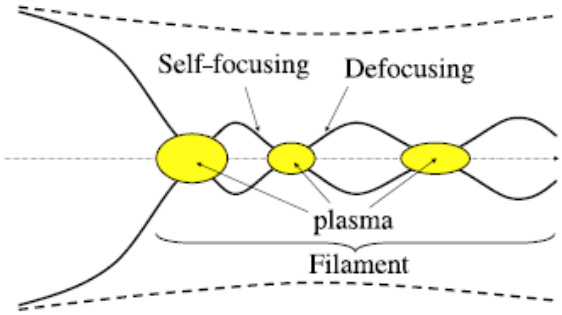

FIGURE 1.11 – Figure 6 from [100].

Filamentation is a complex process where many processes interplay as briefly explained. As such the simulation of all these processes is challenging. Several models were developed to describe filamentation. The non-exhaustive list includes : the moving focus model [116], the slowly varying envelope [120], the soliton description [121], and the nonlinear Schrödinger equation approach [122, 123]. The latter seems to be the most successful approach. Despite many of these simulations focusing on the simulation of filamentation in gases, some work on condensed state media exists [121, 124].

Filamentation is a regime of propagation where the light is effectively collimated at a small effective diameter over relatively long distances. Filament generated in bulk is used as a seed to OPA [35] and will be the main focus of chapters 4 and 5. Filamentation can also be used as an engraving mechanism to write waveguides in glass for example [125].

1.4 Context with SMART-X and Softlite

This Ph.D. is part of the common laboratory "Systèmes organiques pour le Filtrage Temporel des Impulsions Femtosecondes" (Softlite) between the company Fastlite and the institute Institut Physique de Nice (INPHYNI). This laboratory is focused on the study of liquid crystal devices to manipulate femtosecond laser pulses. Thermo-optically addressed liquid crystal spatial light modulators were developed [64] and the current focus of Softlite is the characterization of such devices [126, 127]. The goal of this device is to serve as a flexible shaper for femtosecond optics.

This Ph.D. was funded by the European Union as part of Marie Sklodowska Curie Actions (MSCA). It is part of the Innovative Training Network (ITN) on the Study of carrier transport in MAterials by time-Resolved specTroscopy with ultrashort soft X-ray light (SMART-X). The ITN is focused on X-ray ultrafast spectroscopy with an emphasis on the carrier dynamics of

novel materials for energy supply and storage. The goal of the network is the development of table-top ultrafast X-ray spectroscopy in the condensed phase. The network is made up of 15 early-stage researchers spread throughout 7 European countries. The researchers work in 8 research institutions and two high-tech companies including Max-Born Institut, Stockholm University, Politecnico di Milano, or Greateyes. The research conducted spans various topics around X-ray spectroscopy ranging from source development (this work), sample preparation and characterization [128], X-ray spectroscopy theory [129] and experiments [130]. The Ph.D. thesis aims at pushing the understanding of OPCPA development, particularly as sources for soft X-ray tabletop generation.

1.5 Objectives of the thesis

This thesis has two main topics : the characterization of the nonlinear refractive index (and other terms of the third order nonlinear susceptibility tensor) of crystals relevant for OPCPAs via a novel method and the study of the coherence of the supercontinuum generation in bulk crystals as a potential source of CEP noise. Chapter 2 presents a novel optical Kerr effect spectroscopy method called nonlinearly chirped interferometry. It will be used for the characterization of common crystals used in the optical parametric amplification of near and mid-infrared light with a 1030 nm pump pulse and for the characterization of liquid crystals (previously not done in the femtosecond regime). Chapter 3 will discuss the current state-of-the-art of CEP-stable sources and focus on the optical parametric chirped pulse amplifiers. It will end by presenting a CEP-stable OPCPA and motivating the study of the coherence of bulk supercontinuum generation. Chapters 4 and 5 will study the coherence properties of bulk supercontinuum generation in the experimental conditions of seed generation of near or mid-IR OPCPA. Chapter 4 presents the conditions of WLG as well as the experimental setup used for coherence characterization which is a modified version of the Bellini-Hänsch interferometer [131] with spectral detection. Chapter 5 conducts a parametric study of the WLG process by isolating the generation parameters and studying their influence on the coherence of the WLG process. Among the investigated parameters are the pulse energy, the crystal position, and the spatial phase. The contribution of each parameter to the stochastic phase variations is quantified and optimal generation regimes are identified.

Chapitre 2

Third-order susceptibility metrology

The third-order nonlinear susceptibility tensor $\chi^{(3)}$ quantifies the material response in resonant and non-resonant four-wave mixing processes. This includes the well-known optical Kerr effect (OKE) through the diagonal terms of the tensor as well as some other processes such as cross-polarized wave generation [132]. As the optical Kerr effect appears in all materials regardless of their symmetry properties, they are omnipresent processes. For the specific case of optical parametric amplification, peak intensity in nonlinear crystals can reach or exceed $100\,\mathrm{GW/cm^2}$ [35]. Ignoring third-order nonlinear effects such as self-focusing or self-phase modulation, in this case, is not realistic. Such high peak intensity indeed causes a significant accumulated nonlinear phase (B integral) to the pulses. As a result, their temporal and spatial shapes are significantly modified. Plethora of spectroscopic techniques devoted to $\chi^{(3)}$ terms measurement have been developed in the last decades as detailed in section 2.1. In our group, we have introduced a novel method, "nonlinear chirped interferometry" to characterize the third-order nonlinearity at the femtosecond and picosecond time scale. This method is a three-beam experiment where a reference beam is used to monitor the relative optical group delay of a probe beam under the influence of an intense pump in a given nonlinear medium. Spectral interferometry is used to monitor the transient delay variation of the probe beam inside the nonlinear medium. It will be shown that this transient group delay change is proportional to the nonlinear phase shift under specific chirp conditions of the three involved beams. The method is intrinsically less sensitive to environmental phase drifts although interferometric. It is applied for the characterization of liquid crystals (under the funding "Ultrafast Nonlinear Optics in Liquid Crystals" UNLOC by the Agence Nationale de la recherche) and crystals routinely used for optical parametric amplification. This was a collective work between Elizaveta Neradovskaia, Aurélie Jullien, Nicolas Forget, and me. I was involved in the setup characterization, calibration, and usage to characterize the materials previously mentioned. Two articles were published out of this work. The first one [133] details the principle of the method and the second one [134] gives the results obtained in the characterization of liquid crystals and OPA crystals.

2.1 Third-order susceptibility tensor characterization techniques

Characterizing the $\chi^{(3)}$ tensor of a medium started much before the invention of the Z-scan method [135, 136] in 1989 by Mansoor Sheik-Bahae. The pioneering techniques are based on optical third harmonic generation [137], ellipse rotation [138], photo-acoustics [139], and degenerate four-wave mixing [140]. Z-scan however quickly became the standard characterization method. In this method, the nonlinear sample is moved along the propagation direction of a beam near its focus (+/- Z in figure 2.1). The amount of nonlinear phase and nonlinear absorption experienced by the pulse depends on the peak intensity, hence on the sample position. Monitoring the transmitted power through an aperture as a function of the sample position allows the retrieval of the nonlinear index. If the aperture is completely open, only the imaginary part of the nonlinear refractive index (two-photon absorption, TPA) is measured. Partially closing the aperture gives access to the real part of the nonlinear refractive index, which is responsible for self-focusing or defocusing. This technique involves a single polarization and a single central wavelength, only allowing the retrieval of the diagonal degenerate terms of the $\chi^{(3)}$ tensor. The addition of a half-wave plate before the sample gives access to the anisotropy of the medium [141]. This technique can detect nonlinear phase shifts of 50 mrad.

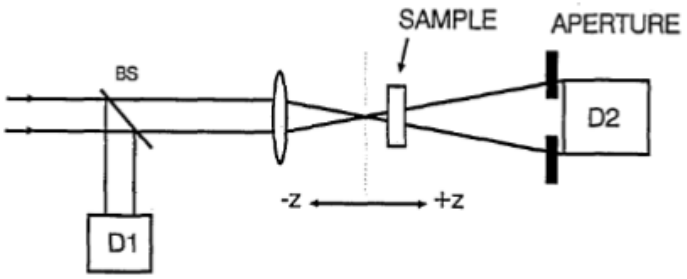

FIGURE 2.1 – Diagram of the Z-scan method where the power ratio $\frac{D2}{D1}$ is recorded as a function of the Z position.

In the next decade, the group of Mansoor Sheik-Bahae came up with some improvements to the original Z-scan method. In the eclipsing Z-scan [142], the aperture is replaced by an obscuration disk that blocks most of the beam and only transmits a thin halo of light. The amount of transmitted power depends again on the self-focusing in the medium. While the standard Z-scan can detect wavefront distortion of the order of $\lambda/300$ with a Signal to Noise Ratio (SNR) of 1, eclipsing Z-scan brings this value down to $\lambda/10000$.

Two-color Z-scan [143] measures non-degenerate nonlinearities. A second harmonic generation crystal and a polarizer are added before the focusing lens. A variable portion of the pump laser is frequency doubled to serve as a probe or a pump. The probe intensity is monitored as a function of the sample position giving access to non-degenerate TPA coefficients and cross-phase modulation effects. The pump and probe pulses can be S or P-polarized independently, measuring diagonal and off-diagonal terms of the tensor. The main drawback of

the two-color Z-scan is the impossibility to discriminate between the instantaneous and the delayed nonlinear response of the media due to a fixed delay.

Time-resolved two-color Z-scan [144] adds an additional adjustable time delay between the second harmonic and the fundamental pump. Performing Z-scan measurements with different pump-probe delays as well as delay scans for different Z positions gives complete information about the instantaneous and delayed nonlinear response of the media.

Other characterization techniques have emerged, such as time-resolved interferometry [145], single shot supercontinuum interferometry (SSSI) [146], spectrally resolved two-beam coupling (SRTBC) [147, 148], cross-phase modulation, frequency shift measurement [149] or chirped spectral holography [150] :

— Time-resolved interferometry is a three-pulse measurement, a standard pump-probe experiment with the addition of a reference pulse sampled from the same driving field. Monitoring the amplitude and phase of the spatial interference pattern between the probe and reference pulses as a function of pump-probe delay gives all the information about the nonlinear refractive index.

— Single-shot supercontinuum interferometry is another three-pulse interferometric experiment. In this case, the probe and reference beams are twin supercontinua generated in air, and instead of detecting a spatial interference pattern, spectral interferometry is studied.

— Spectrally resolved two-beam coupling is a standard pump-probe experiment with the addition of a monochromator to select a narrow part of the probe spectrum. The transmitted probe power is measured in this spectral slice as a function of the pump-probe delay. The addition of the monochromator allows the detection to take place on the edge of the probe spectrum, where the self-phase modulation effects are strongest. Assuming perfect characterization of the probe and pump pulses, one can retrieve real and imaginary parts of n_2. The sensitivity of this method is of the order of 10^{-6} rad using heterodyne detection.

— Chirped spectral holography is a three-beam measurement with a reference, pump, and probe pulse. The pulses go through the sample in this order. The reference and probe pulses are low-energy pulses and the pump is high-energy. The reference propagates in the sample and since it is a low-energy pulse the state of the sample or of the reference pulse itself is unaffected. The sample is then excited by the pump before being probed. This method then uses a spectral holography algorithm to retrieve vibrational information on the sample.

In this non-exhaustive list of methods for OKE, most methods require active stabilization and noise reduction to isolate the contribution of weak nonlinearities. This can be by using heterodyne detection for example or by an active stabilization of the setup mostly in the interferometric measurements. As will be shown in the next section, the biggest advantage of our method is the absence of active stabilization or heterodyne detection while reaching similar or better uncertainty values. The development of this interferometric measurement was motivated by the lack of data on the $\chi^{(3)}$ tensor of materials commonly used in OPAs pumped at the

fundamental wavelength of 1 μm. The typical crystal thickness around the millimeter coupled with the femtosecond to the picosecond time duration of the pulses forces the soft focusing geometry. A hard-focusing geometry would indeed lead to the ionization of the material. As a result, the built interferometer is meter-scale to mimic the experimental conditions of optical parametric amplification. The second motivation was the characterization of liquid crystals that requires high sensitivity to discriminate the contributions of the LC and the substrate. The method proposed here fulfills both these needs. This chapter presents the method by first showing numerical simulations isolating the different effects involved in the measurement, confirming experimentally the method is valid, and finally showing the results obtained in liquid crystals and bulk crystals.

2.2 Principle

Nonlinear chirped interferometry is a frequency degenerated pump-probe experiment with interferometric detection where the probe optical group delay relative to a reference pulse is monitored rather than the nonlinear phase shift. Figure 2.2 illustrates the principle of the experiment with the definition of the three beams : reference, pump, and probe. Two beams are co-propagated in the nonlinear sample with a small angle : the strong pump beam (P) and the weak probe beam (Pr). The different delays will be defined as such : τ_k is the group delay of wave k where k is R for reference, P for pump, and Pr for probe. The two relevant relative delays will be written :

$$\tau_{PPr} = \tau_P - \tau_{Pr} \tag{2.1}$$

$$\tau_{RPr} = \tau_R - \tau_{Pr} \tag{2.2}$$

The latter is the metric of interest. Finally, the relative delay between reference and probe without pump beam will be written as τ^0_{RPr}. As the next section shows $\tau_{RPr} \neq \tau^0_{RPr}$ under the presence of the pump beam and is the monitored experimental parameter. The exact monitored parameter is not strictly the group delay of the probe beam τ_{Pr} but the relative group delay difference between the probe and reference τ_{RPr}. This should be emphasized as the variations of the probe group delay τ_{Pr} will not be identical to the variations of the reference probe relative group delay τ_{RPr} even though τ_R will be kept constant.

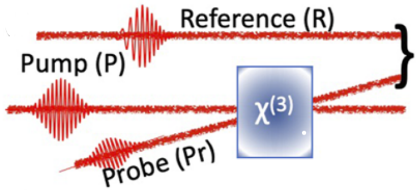

FIGURE 2.2 – Figure from [133]. Principle of nonlinear chirped interferometry.

A simple theoretical model based on the nonlinear Schrödinger equation is sufficient to explain the interactions of the three pulses relevant to the experiment. This model includes the two-beam coupling contribution but excludes diffraction and material dispersion which is justified in this case as the length of the nonlinear medium is much shorter than the dispersion length [151] for the considered pulse duration.

2.2.1 Nonlinear Schrödinger equation

Let $E_P(\omega)$, $E_{Pr}(\omega)$ and $E_R(\omega)$ be the complex amplitude of the pump, probe, and reference respectively. The respective spectral phases are $\varphi_P(\omega)$, $\varphi_{Pr}(\omega)$ and $\varphi_R(\omega)$. The complex amplitudes can then be written as

$$E_k(\omega) = |E_k(\omega)|exp[-i\varphi_k(\omega)] \tag{2.3}$$

with $k \in P, Pr, R$.

To simplify the model, all the spectral phases are assumed to be purely quadratic and can be expressed as :

$$\varphi_k(\omega) = \varphi_k(\omega_0) + \tau_k(\omega_0)(\omega - \omega_0) + \varphi_k^{(2)}(\omega - \omega_0)^2/2 \tag{2.4}$$

where $\tau_k(\omega_0)$ is the group delay and $\varphi_k^{(2)}$ is the chirp coefficient. The formalism shown here was largely developed as a tool for spectrally resolved two-beam coupling [152]. Assuming that the pump and probe pulses are S or P-polarized, that the nonlinear sample is isotropic, and that the excitation wavelength is far away from resonance the propagation equation of the probe pulse amplitude can be written as follows [152] :

$$c\frac{\partial E_{Pr}}{\partial z} + (n_{g,0} + 4\gamma I_P)\frac{\partial E_{Pr}}{\partial t} = 2i\omega_0\gamma I_P E_{Pr} - 4\gamma\frac{\partial I_P}{\partial t}E_{Pr} \tag{2.5}$$

where $n_{g,0}$ is the group index at ω_0, γ is the nonlinear coupling coefficient and I_P is the time dependent pump intensity. With this set of approximations, γ has two different expressions, one for parallel and perpendicular polarization respectively :

$$\gamma_{\parallel} = \frac{3}{4\epsilon_0 n_0^2 c}\chi^{(3)}_{xxxx} = n_2 \tag{2.6}$$

$$\gamma_{\perp} = \frac{1}{4\epsilon_0 n_0^2 c}\chi^{(3)}_{yyyy} \tag{2.7}$$

The three terms containing the pump intensity in equation 2.5 can be separated as follows :

— The left term is an increase of the group index by $4\gamma I_P$ (Kerr effect induced by the pump pulse).

— The second term of the right member is two-beam coupling (2BC) and causes energy exchange between the pump and the probe pulse.

— The first term of the right member is cross-phase modulation (XPM) and causes a frequency shift Ω (figure 2.4).

Let us take a look at each individual term involving the pump intensity and its consequences on the relative group delay τ_{RPr}.

Increase of group index induced by the Kerr effect

The first term on the left of equation 2.5 is :

$$(n_{g,0} + 4\gamma I_P)\frac{\partial E_{Pr}}{\partial t} \tag{2.8}$$

The pump induces a Kerr effect modification of the group index of the probe beam by a term $4\gamma I_P$. This results in a modification of the group delay of the probe. This contribution is however negligible and will be ignored in the numerical model. The group index at the central wavelength of 1030 nm in fused silica is 1.46 [153]. The order of magnitude of the nonlinear term $4\gamma I_P$ for a pulse energy of 1 mJ, a pulse duration of 200 fs, and a beam diameter of 300 μm in fused silica is 0.003. This is three orders of magnitudes below the group index, so this effect will be ignored as it does not contribute significantly to the variation of τ_{RPr}.

Two-beam coupling

The second term in equation 2.5 is :

$$-4\gamma\frac{\partial I_P}{\partial t}E_{Pr} \tag{2.9}$$

This term quantifies the two-beam coupling between pump and probe [152, 154]. Let us consider a pump-probe experiment in a nonlinear sample where the two beams have respective frequencies ω_1 and ω_2. The two beams set up a moving interference grating in the sample. As a result of the Kerr effect, the intensity grating is transcribed into a refractive index grating from which the beams will scatter into each other. The scattered light experiences a phase shift due to the delayed nonlinear response leading to an energy gain or an energy loss. The theoretical coupling equations are derived in [154]. They show that if $\omega_1 < \omega_2$ the probe gains energy from the pulse and vice versa. If the two frequencies are identical no energy exchange happens. For this experiment pump and probe are frequency-degenerated, meaning that no energy exchange should happen between pump and probe. However, this is not true anymore when a chirp is induced in the beams. Let us now consider a frequency-degenerated pump-probe experiment where the pump and probe pulses are chirped.

Figure 2.3 shows the pump and delayed probe with identical chirp values (non-zero) to illustrate the 2BC effect between pump and probe in this case. The Wigner-Ville representation shows the time-frequency distribution of the pump and probe pulses. As a result, a pulse with a flat linear spectral phase will be a vertical line in this representation. Similarly, a chirped pulse will be a slanted line in this representation and the slope of the line is the chirp value of the

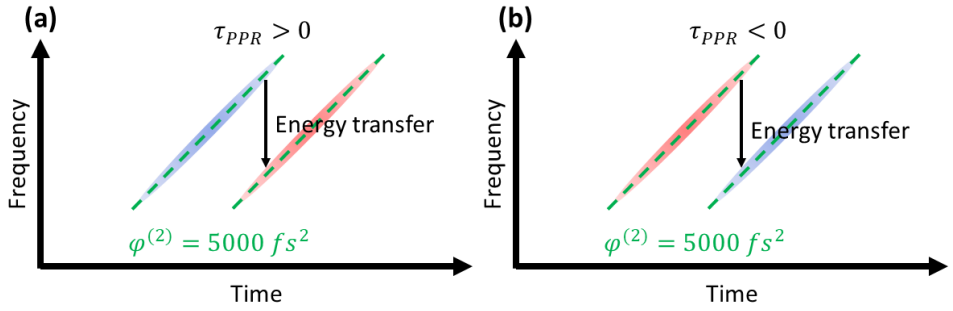

FIGURE 2.3 – Wigner-Ville representations of the probe and pump pulses. The probe pulse is represented in blue and the pump pulse in red. The slope of each pulse is equal to their respective chirp (5000 fs^2). In figure (a) the pump-probe delay is positive resulting in an energy exchange from pump to probe whereas in figure (b) the pump-probe delay is negative resulting in an energy exchange from probe to pump.

pulse. Second-order dispersion creates a time-dependent instantaneous frequency. As the two pulses are delayed their respective instantaneous frequencies are different. This is indicated in the figure by the black arrow. The instantaneous frequency ω_1 is higher than ω_2 which allows energy exchanges between the two pulses via 2BC. Let us assume in figure 2.3 the top pulse is the pump and the bottom pulse is the probe ($\tau_{PPr} < 0$). For this particular delay, the instantaneous frequency of the pump pulse is higher than that of the probe pulse causing energy exchange from the pump to the probe increasing the energy in the leading edge of the probe pulse. This will cause a temporal reshaping of the probe pulse and increase its relative group delay with the reference τ_{PPr}. This means that 2BC contributes to the change of the relative group delay τ_{PPr} if the pump and probe pulses are both chirped.

Cross-phase modulation

The first term of the left side of equation 2.5 is :

$$2i\omega_0\gamma I_P E_{Pr} \tag{2.10}$$

This term corresponds to the cross-phase modulation induced by the pump pulse on the probe pulse. It causes a time-dependent nonlinear phase shift φ_{NL} that results in a transient frequency shift Ω. It should be noted that the frequency shift is much smaller than the carrier frequency. This frequency shift is proportional to the nonlinear phase and as a consequence proportional to the nonlinear tensor coefficients. Figure 2.4 shows the nonlinear phase-shift and its associated probe frequency shift Ω as a function of the pump-probe delay τ_{PPr}.

It should be noted that cross-phase modulation does not affect the probe group delay τ_{Pr}. It will be shown in section 2.2.2 that the interferometric detection method allows transcription of the transient frequency shift Ω to the probe reference delay τ_{RPr}.

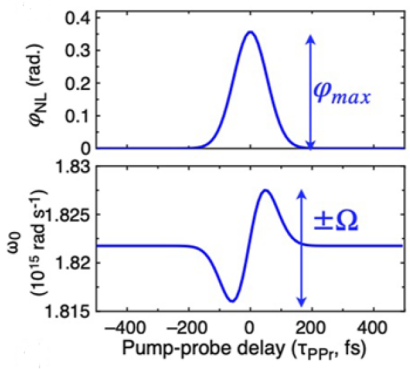

FIGURE 2.4 – Figure from [133]. Nonlinear XPM phase and shift of the carrier frequency of the transmitted probe pulse as a function of the pump-probe delay τ_{PPr}.

2.2.2 Numerical simulations

The model will be used to simulate different chirp configurations and isolate the contributions of the different terms of equation 2.5 to the measured signal. The peak intensity of the pump pulse will be taken to be 300 GW/cm^2 in a 1-mm-thick crystal for an XPM nonlinear phase shift around 300 mrad. The observable is the spectral fringes resulting from the reference-probe interference. The fringes are simulated as a function of τ_{PPr}. From the fringes the probe reference delay τ_{RPr} is extracted by Fourier transform interferometry. The metric used will be the transient delay shift of the probe named $\delta\tau = f(\tau_{PPr})$. It will be shown at the end of this section that $\delta\tau$ is proportional to the nonlinear phase shift φ_{NL} itself proportional to the $\chi^{(3)}$ tensor (the quantity to characterize here). The numerical simulation (supplementary material of [133]) was run using a calculation grid of 8192 points spanning over a 1 PHz-bandwidth centered at 291.3 THz. The equivalent time grid has a time step of 5 fs and spans over 2.05 ps. The simulation results are all displayed in figure 2.6 and are all organized as follows (figure 2.5) :

— The first row of each figure details the chirp parameters of each given configuration.
— The second row of each figure is the reference-probe interferogram scanned over 2.05 ps.
— The third row is the positive AC peak of the Fourier transform located at a time around τ^0_{RPr} (3 ps). This quantity is obtained by following the algorithm of Fourier transform spectral interferometry described in section 1.2.2 on the interferogram of the second row.
— The fourth and last row of each figure is the maximum of the AC peak of the third row. It is extracted by fitting a Gaussian on the AC peak. All these quantities are plotted as a function of the pump-probe delay τ_{PPr}.

4 different configurations are going to be explored. In the first one, the chirp of all three pulses is set to zero giving a reference case for the later configurations. In the second case, the chirp of all pulses is set to an identical quantity (non-zero) to showcase the influence of the 2BC term of equation 2.5. In the third one, the chirp of pump and probe is set to zero while the reference is chirped to showcase the imprint of the transient frequency shift Ω on the transient delay shift $\delta\tau$. Finally, the last configuration shows the combination of both effects previously

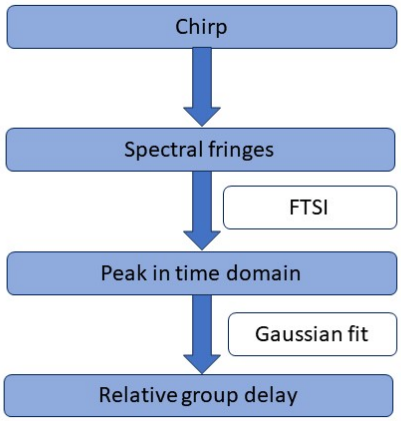

FIGURE 2.5 – Organization of the data presented in figure 2.6

mentioned, the pump and probe are chirped equally, and some additional chirp is added on the reference pulse in this case.

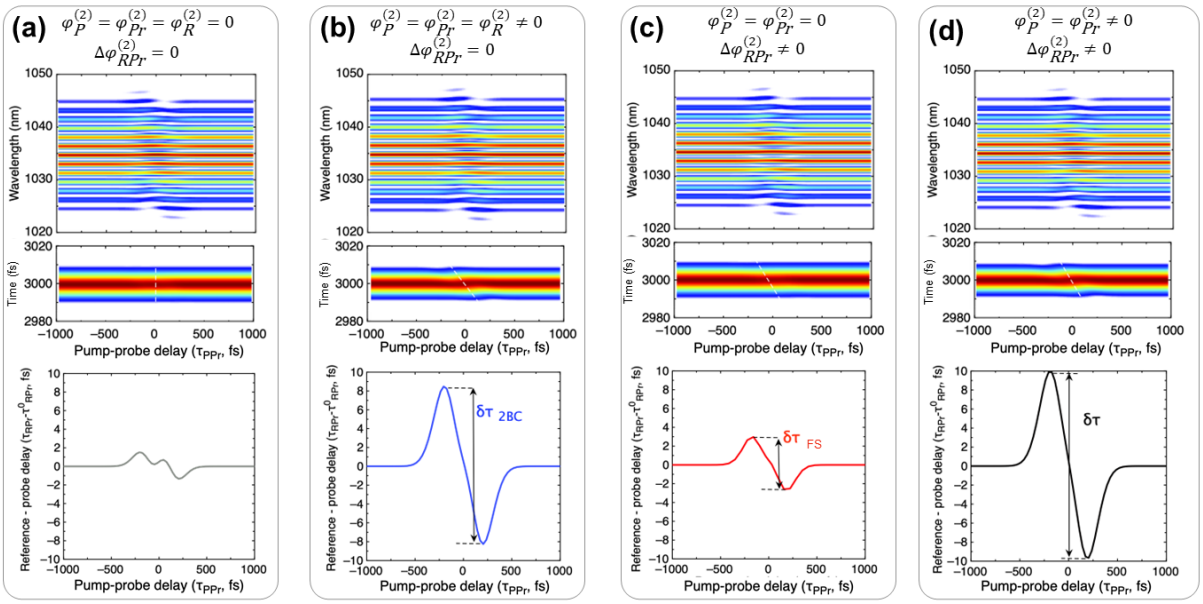

FIGURE 2.6 – Figure from [133]. Numerical illustration for the numerical values indicated in the text. Top row : computed spectral interference S(ω) between the reference and the transmitted probe as a function of τ_{PPr}. Middle row : modulus of the Fourier transform as a function of τ_{PPr}. Bottom row : group delay shift of the transmitted probe $\tau_{RPr} - \tau^0_{RPr}$ as a function of τ_{PPr}. The four columns correspond to the following cases : all three pulses are unchirped (a), all pulses are chirped by the same amount (b), only the reference pulse is chirped (c), and all pulses are chirped with an additional chirp on the reference pulse (d). For all the sub-plots, 2BC stands for two-beam coupling and FS for frequency shift.

Case (a)

Figure (a) describes the first simulated configuration where the second order dispersion of all three pulses is set to zero :

$$\varphi_R^{(2)} = \varphi_P^{(2)} = \varphi_{Pr}^{(2)} = 0 \tag{2.11}$$

$$\Delta\varphi_{RPr}^{(2)} = \varphi_R^{(2)} - \varphi_{Pr}^{(2)} = 0 \tag{2.12}$$

The frequency shift of the probe is clearly visible in the spectrogram as it will be in all the following simulations. In this first case, the reference probe delay is weakly affected by the pump presence. The only effect here is XPM causing mild reshaping of the probe pulse resulting in the minor change in τ_{RPr}. The reference probe delay is constant to the first order with the pump-probe delay when all the pulses are transform limited.

Case (b)

The second case plotted in figure 2.6 (b) adds the same amount of second-order dispersion to all three pulses :

$$\varphi_R^{(2)} = \varphi_P^{(2)} = \varphi_{Pr}^{(2)} = 5000 fs^2 \tag{2.13}$$

$$\Delta\varphi_{RPr}^{(2)} = 0 \tag{2.14}$$

The chirp value added (5000 fs^2) is not significant enough to modify the temporal shape of the pulse as the bandwidth of all pulses is 10 nm (increases temporal duration from 180 fs to 195 fs). Identically to the previous case, a transient frequency shift appears in the spectrogram. However contrary to the previous case the AC peak of the Fourier transform shows a shift made apparent in the reference probe delay plot.

This Z-shaped delay shift is centered around pump-probe temporal overlap and lies within the pump pulse temporal width. It is due to the 2BC between pump and probe. As described in the previous section the probe pulse is reshaped by this effect ultimately affecting the reference probe delay (figure 2.3). When the pump-probe delay is negative the instantaneous frequency of the probe is lower than that of the pump causing energy exchange from probe to pump. When the pump probe delay is positive the opposite effect happens resulting in the characteristic Z shape of the reference probe delay. The transient excursion in τ_{RPr} is labeled $\delta\tau_{2BC} = \tau_{RPr}^{max} - \tau_{RPr}^{min}$. It has an order of magnitude of a dozen of femtoseconds.

Case (c)

In this third case (figure 2.6 (c)) the chirp of the pump and the probe is set back to zero (i.e. there is no 2BC) but the reference still has a positive chirp value :

$$\varphi_P^{(2)} = \varphi_{Pr}^{(2)} = 0fs^2 \tag{2.15}$$

$$\varphi_R^{(2)} = 2000fs^2 \tag{2.16}$$

$$\Delta\varphi_{RPr}^{(2)} = 2000fs^2 \tag{2.17}$$

The same three figures are plotted showing the transient frequency shift and here again a reference probe delay variation with the pump-probe delay. As the pump and probe pulse are both unchirped this variation is not due to 2BC but relies entirely on the difference in chirp between reference and probe. The mechanism is a temporal encoding of the transient frequency shift of the probe via reference-probe relative chirp. The effect is illustrated in figure 2.7.

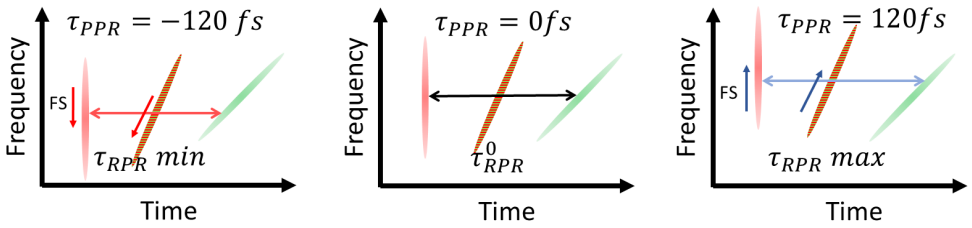

FIGURE 2.7 – Wigner–Ville distribution of the probe-reference electric fields for three different pump–probe delays τ_{PPr}. For each sub-plot, the reference pulse is on the right (green) and the (delayed) probe pulse is on the right (red). The reference pulse is chirped and exhibits a time-dependent instantaneous frequency. The two pulses are chirped differently, and the slopes of the individual representations differ. In between the two pulses appears the interferometric component. The large arrow indicates the reference–probe group delay τ_{RPr}. For $\tau_{PPr} <= 0$, the nonlinear phase induces a red shift of the transmitted probe (red arrow), which increases τ_{RPr}. Symmetrically, for $\tau_{PPr} >= 0$, a blue shift decreases τ_{RPr}. For $\tau_{PPr} = 0$, there is no spectral shift and $\tau_{RPr} = \tau^0_{RPr}$. FS stands for frequency shift.

The Wigner-Ville representation shows the time-frequency distribution of the reference and probe pulses. The interference of the two pulses is displayed in the middle of each figure. The relative delay between probe and reference is also represented with an arrow. The time-frequency slope difference causes encoding of the frequency shift of the probe induced by the probe on the reference probe delay. If the probe is red-shifted (first case) the delay is increased and if the pulse is blue-shifted (third case) the delay is decreased causing the Z shape similar to the 2BC effect. The transient excursion in τ_{RPr} is labeled $\delta\tau_{FS} = \tau_{RPr}^{max} - \tau_{RPr}^{min}$. It has an order of magnitude of a few femtoseconds.

Case (d)

So far two different phenomena have been highlighted : temporal reshaping due to 2BC and temporal encoding of the nonlinear frequency shift due to the reference-probe relative chirp. The Fourier analysis shows that both effects result in a similar transient shift of τ_{RPr} over the same temporal scale and with similar amplitudes. Choosing the chirp parameters adequately

allows the different contributions to add coherently significantly increasing the signal level as simulated in figure 2.6 (case (d)) where :

$$\varphi_P^{(2)} = \varphi_{Pr}^{(2)} = 5000 fs^2 \tag{2.18}$$

$$\varphi_R^{(2)} = 2000 fs^2 \tag{2.19}$$

Figure 2.8 (a) shows another set of Wigner-Ville representations with both pulses chirped. Figure 2.8 (b) presents the evolution of the metric of this experiment ($\delta\tau$) as a function of the nonlinear phase shift induced to the probe. The different contributions detailed before (2BC and frequency shift) are separated in the figure. Remarkably the addition of both components results in a linear dependence of the transient relative group delay excursion $\delta\tau$ on the nonlinear phase in the range of a few hundreds of mrads. It should also be noted that the contribution of 2BC is about twice as significant as the one from the frequency shift encoding. As it will be shown experimentally, using $\delta\tau$ as a metric instead of φ_{NL} makes the detection less sensitive to phase fluctuations and gives additional means to enhance the sensitivity and specificity of the detection.

2.3 Experimental setup

The experimental setup is a pump-probe reference measurement with spectrally resolved interferometric detection.

2.3.1 Driving laser

The driving laser is a Pharos system (PH1-SP-1mJ) from Light-Conversion. It delivers 180 fs Fourier Transform Limit (FTL) pulses with a central wavelength of 1034 nm. The operating frequency can be tuned from 1 kHz to 1 MHz with a maximum average power of 6 W. In this experiment, the frequency was set at 10 kHz or 1 kHz with a pulse energy of 500 μJ. The compressor range can be used to tune the laser chirp.

2.3.2 Interferometer layout

A diagram of the interferometer is shown in figure 2.9. The driving pulse is split into three : a low-energy reference pulse is first sampled with BS1, then the remaining energy is split into a high-energy pump pulse and a low-energy probe pulse (20% of the pump energy) with BS2.

The pump and probe pulse are loosely focused (f=1.5 m) in the sample with a small angle (1°) to spatially separate them. The beam diameter of the pump inside the sample is 550 μm. The pump-probe delay is controlled via a motorized delay line using a Thorlabs controller (Z825B and KDC101). The probe pulse is selected after the interaction and recombined with the delayed reference pulse. As explained before the chirp of all pulses needs to be independently controlled. The laser compressor can change the chirp of all three pulses. The addition of

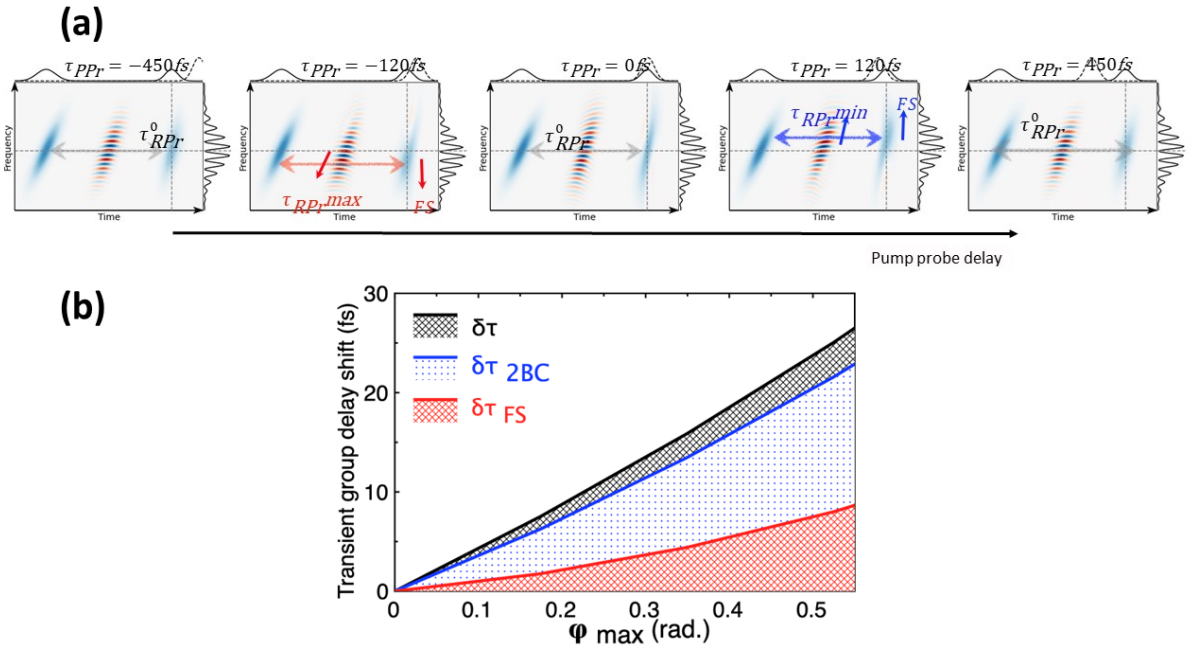

FIGURE 2.8 – (a) : Wigner–Ville distribution of the probe-reference electric fields for five different pump–probe delays τ_{PPr}. For each sub-plot, the reference pulse is on the left and the (delayed) probe pulse is on the right. Both pulses are chirped and exhibit a time-dependent instantaneous frequency. The two pulses are chirped differently, and the slopes of the individual representations differ. In between the two pulses appears the interferometric component. Upper plot : integration of the distribution along the frequency coordinate (temporal intensity, solid line) compared to the cross-section of the pump pulse (dotted line). Right plot : integration of the distribution along the time coordinate [interference spectrum $S(\omega)$]. The large arrow indicates the reference–probe group delay τ_{RPr}. For τ_{PPr} = 450 fs (i.e., no temporal overlap between the pump and probe), $\tau_{RPr} = \tau^0_{RPr}$. For $\tau_{PPr} <= 0$, the nonlinear phase induces a red shift of the transmitted probe (red arrow), which increases τ_{RPr}. Symmetrically, for $\tau_{PPr} >= 0$, a blue shift decreases τ_{RPr}. For $\tau_{PPr} = 0$, there is no spectral shift and $\tau_{RPr} = \tau^0_{RPr}$. FS stands for frequency shift. (b) : Amplitude of the transient shift ($\delta\tau$) of the probe group delay as a function of the XPM nonlinear phase for the three cases.

dispersive material, such as $CaCO_3$, $SF11$, and Al_2O_3, in the reference arm, can further chirp the reference pulse. The polarization of each pulse can be controlled independently with half-wave plates to access diagonal and off-diagonal terms of the $\chi^{(3)}$ tensor. The detection is done on an Avantes spectrometer with a spectral resolution of 0.07 nm with a single-shot detection up to 10 kHz. The signal is the reference-probe spectral interference fringes monitored as a function of the pump-probe delay.

2.4 Experimental characterization

After presenting the principle of the measurement along with its simulation this section presents the experimental characterization of the interferometer.

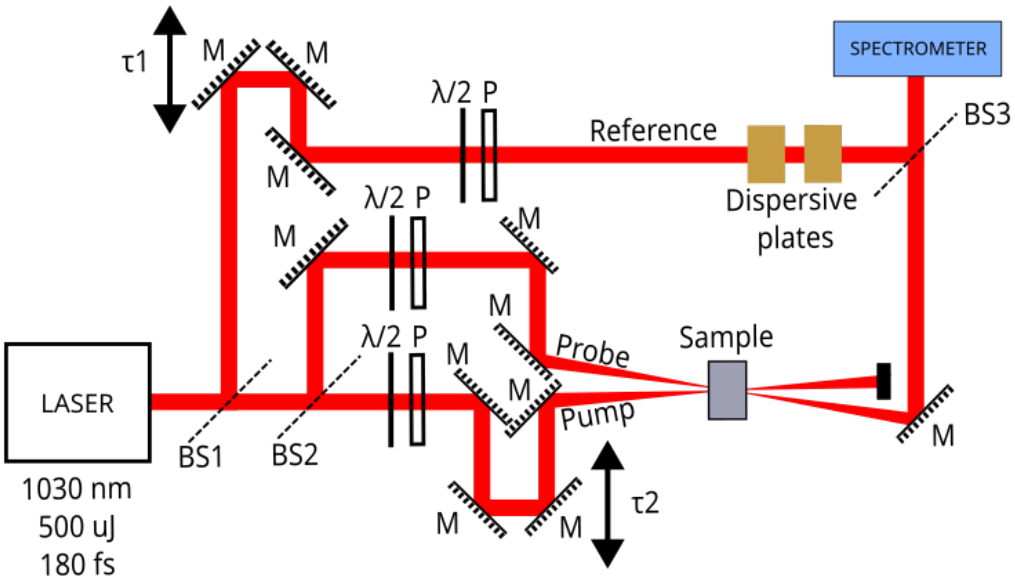

FIGURE 2.9 – Diagram of the interferometer for nonlinear chirped interferometry.

Reference measurement in sapphire

For each acquisition, the pump-probe delay is varied from -2.6 ps to 2.6 ps with temporal steps of 13 fs (400 steps per scan). The integration time of the spectrometer is set to 1 ms (the repetition rate of the laser can be varied to change the number of shots per spectrum) for a total scan time of a few minutes. The nominal reference-probe delay τ^0_{RPr} is set to 3.5 ps. The reference probe delay and relative chirp are measured with the analysis of the AC peak in the Fourier transform out of pump-probe temporal overlap. The delay is the position of the AC peak and the relative chirp can be retrieved by Fourier transforming back the AC peak. The polarization of all three beams is set to horizontal with a pump pulse energy of 40 μJ (peak intensity of 40 GW/cm^2). The chirp coefficients are set to :

$$\varphi^{(2)}_P = \varphi^{(2)}_{Pr} = 5000 fs^2 (\pm 500\, fs^2) \tag{2.20}$$

$$\Delta\varphi^{(2)}_{RPr} = 2000 fs^2 (\pm 100 fs^2) \tag{2.21}$$

which results in pulse durations of 195 fs for the pump and probe pulses and 210 fs for the reference pulse. The pump and probe chirp coefficients (and durations) are measured with a

Wizzler and the reference-probe chirp is measured via spectral interferometry before acquisition. Figure 2.10 shows experimental data with these parameters in a 1-mm-thick sapphire crystal.

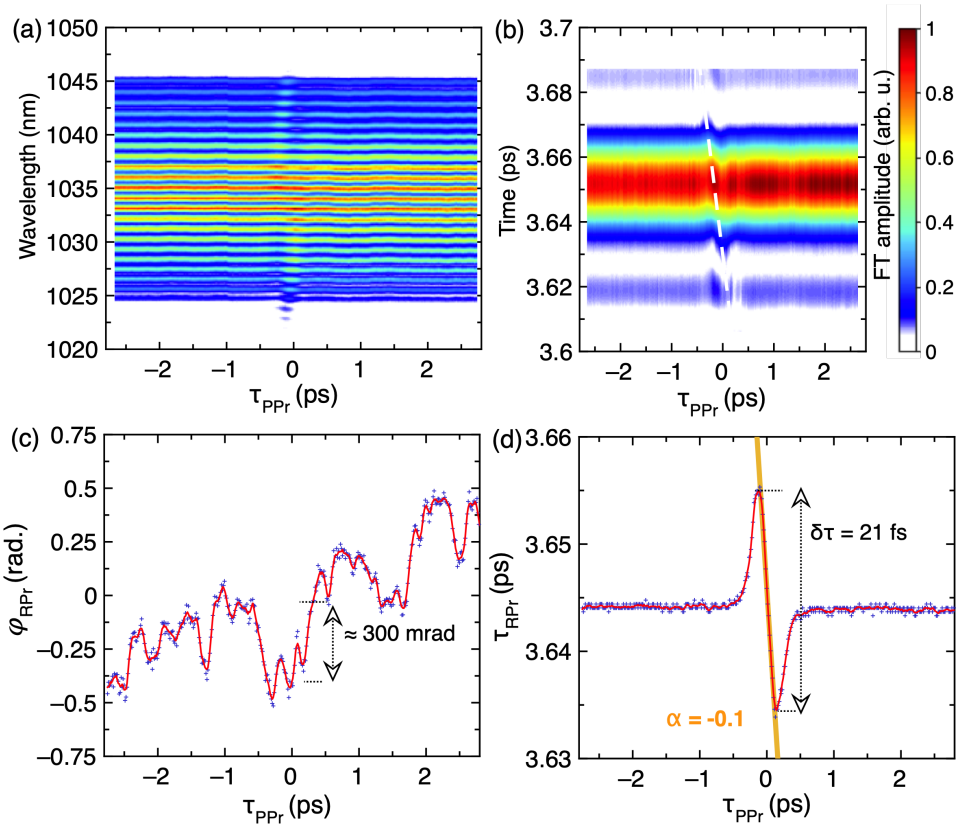

FIGURE 2.10 – Figure from [133]. Typical experimental data for the 1 mm-thick sapphire. The nonlinear phase-shift accumulated by the probe is estimated to be 300 mrad and the normalized frequency-shift is $\Omega/\omega_0 \simeq 10^{-3}$. (a) Interferogram of the probe and reference pulses as a function of pump–probe delay. (b) AC peak of the Fourier transform of the interferograms. The white dashed line highlights the transient swing of the AC peak. (c) The relative phase between reference and probe pulses (φ_{RPr}) as a function of pump–probe delay. (d) τ_{RPr} as a function of pump–probe delay. For sub-plots [(c) and (d)] : raw data (blue), moving average (red), and linear fit (orange).

Figure 2.10 (a) shows the interferogram exhibiting as expected the red shift for slightly negative pump-probe delay and the blue shift for slightly positive pump-probe delay. Additionally, a slight decrease in the signal level is appearing due to self-focusing when the pump and probe overlap which does not influence the measurement. Figure 2.10 (b) shows the AC peak of the Fourier transform where the transient shift of its peak position is clearly visible. It is also emphasized in figure 2.10 (d) plotting the reference probe delay τ_{RPr} as a function of pump-probe delay τ_{PPr} where the characteristic Z shape is visible showing very good agreement with figure 2.6. The total delay excursion is 21 fs with extrema for $\tau_{PPr} = \pm 100 fs$. The delay is varying linearly between the extrema with a slope of -0.1. Figure (c) directly shows the extracted phase difference between reference and probe. This metric is usually the one chosen to determine the

nonlinear phase. In this case, however, without any active stabilization, it is barely distinguishable in the measurement as figure 2.10 (c) illustrates. This shows the relevance of studying the reference probe delay instead and the drastic improvement in SNR this way. In the rest of this study, the delay excursion $\delta\tau$ will be the metric used both for the setup characterization and the nonlinear crystal $\chi^{(3)}$ measurements.

After showcasing an experimental result with a reference sapphire crystal the next step is the characterization of the setup as a function of various experimental parameters. The parameters mentioned above (pump and probe chirp, reference-probe relative chirp, and pump pulse energy) are individually varied while keeping the other experimental parameters identical. The goal of the characterization is to experimentally find the chirp parameters and pulse energy that will maximize $\delta\tau$ for a given φ_{NL}.

2.4.1 Comparison with the numerical model

Pump and probe chirp : 2BC

The first parameter is the pump and probe chirp $\varphi^{(2)}_{PPr}$. The reference-probe relative chirp is kept at 2000 fs^2 with a pump energy of 40 μJ. Figure 2.11 (a) shows the delay excursion $\delta\tau$ and the normalized transient frequency shift measured as a function of $\varphi^{(2)}_{PPr}$ and compares it to the simulated results. The transient frequency shift is retrieved from the interferogram to indicate the amount of nonlinear phase induced on the probe.

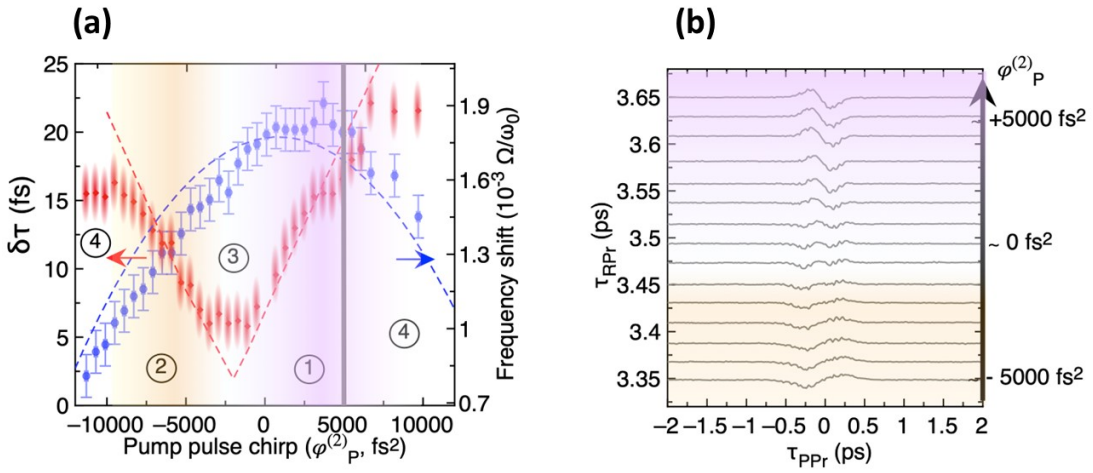

FIGURE 2.11 – Figures from [133]. (a) : experimental data compared to the numerical 1D simulations. The clouds indicate the dispersion of the experimental data. (a) $\delta\tau$ (red) and normalized frequency shift (Ω/ω_0, blue) as a function of input chirp $\varphi^{(2)}_P = \varphi^{(2)}_{Pr}$, for $\Delta\varphi^{(2)}_{RPr} = 2000 \pm 100) fs^2$. The colored area and labels refer to different zones of interest. (b) : τ_{RPr} as a function of τPPr, for various $\varphi^{(2)}_P$ values, indicated on the right y-scale. The curves are artificially shifted for clarity. The colored area correspond to those in figure (a)

The pump and probe are mainly influencing 2BC as explained in section 2.2. The agreement between the numerical simulation is good for both the delay excursion and the frequency shift.

— The normalized frequency shift shows a parabolic variation as pump duration and is naturally maximized for a compressed pump pulse.
— $\delta\tau$ varies mostly linearly with pump and probe chirp and has a V shape with a minimum for a negative chirp value (-2000 fs^2 = -$\Delta\varphi^{(2)}_{RPr}$). Several areas are indicated by numbers (1)-(4).
— (1) is the area with a slightly positive chirp where the frequency shift is mostly constant (meaning so is the nonlinear phase) but $\delta\tau$ increases linearly with the pump chirp. This is the working experimental condition and emphasizes the need for a chirped pump pulse to enhance the 2BC and hence increase the SNR.
— (2) shows a similar linear dependency of $\delta\tau$ with the pump and probe chirp. The Z shape is however reversed in this region as reversing the chirp is equivalent to changing the sign of the energy exchanges of pump and probe explained in section 2.2.
— Area (3) is the area where the delay excursion is minimal. The pump and probe chirp value is -2000 fs^2 and matches exactly the chirp difference between probe and reference. Figure 2.11 (b) shows various experimental delay scans for different pump and probe chirp values. In area (3) the delay is a weak signal with an ill-defined shape that matches exactly the numerical simulation (figure 2.6 (a)). This shape is the result of all the previously explained contribution compensating so it naturally happens when the probe and pump chirp is exactly matching the reference-probe relative chirp. In other words, it was explained in the previous section that choosing the chirp parameters of all three pulses could result in a constructive addition of all the different contributions. Area 3 shows what happens when the chirp parameters are chosen so that the different contributions add destructively resulting in almost no effect on the reference probe delay.
— Area (4) highlights the high chirp values (positive and negative) where the numerical simulations and the experimental result stop matching. This is most likely caused by the higher order of dispersion caused by the gratings compressor that is ignored in the numerical model and can cause temporal reshaping of the pump and probe pulses.

Reference-probe relative chirp : temporal encoding of the transient frequency shift

The second chirp parameter investigated is the reference probe relative chirp by adding various dispersive materials in the reference beam path. In all these measurements the energy and the pump and probe chirp are kept constant and only $\Delta\varphi^{(2)}_{RPr}$ is varied. As the nonlinear phase shift is unaffected by this parameter only the delay excursion is plotted as a function of $\Delta\varphi^{(2)}_{RPr}$ in figure 2.12.

When there is no relative chirp only 2BC is responsible for $\delta\tau$. 2BC is the major contribution to $\delta\tau$. When $\Delta\varphi_{RPr}$ is increased the contribution from spectral shift leads to a linear increase in $\delta\tau$. In figure 2.12 the blue part is the contribution of 2BC while the red part is the added

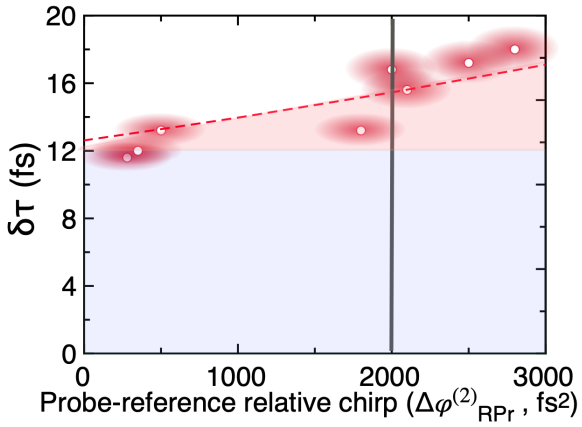

FIGURE 2.12 – τ_{RPr} as a function of the chirp difference between the reference and pump/probe pulses, $\Delta\varphi^{(2)}_{RPr}$, with fixed input chirp $\varphi^{(2)}_{P} = 5000 \pm 500 fs^2$. The colored area refers to 2BC (blue) and frequency-shift (red) contributions.

contribution due to the spectral shift encoding. Additional chirp on the reference pulse is then both improving the SNR and easy to experimentally implement.

Pulse energy : nonlinear phase shift

The last relevant experimental parameter is the pump pulse energy. $\delta\tau$ and the normalized transient frequency shift are plotted as a function of the pump pulse energy in figure 2.13 to show the linear dependence on pump pulse energy of φ_{NL}.

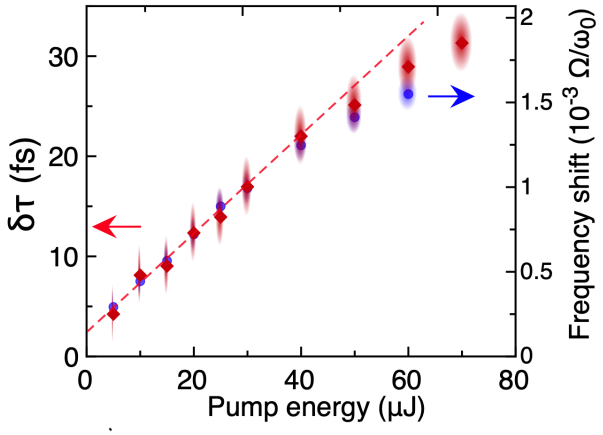

FIGURE 2.13 – Figure from [133]. $\delta\tau$ (red) and normalized frequency shift (Ω/ω_0, blue) as a function of the pump energy for the chirp values indicated by the gray lines in figures 2.11 and 2.12.

The pulse energy is varied from 5 to 80 μJ. Both quantities vary linearly with the pulse energy until 60 μJ where the nonlinear phase shift φ_{NL} is about 600 mrad. This figure showcases the strength of this method which is its sensitivity. Frequency shifts spanning from 30 to 400 GHz (0.01% to 0.2% of the carrier frequency) can be detected with a single scan. This

interferometer is able to detect the effect of phase shifts as low as 10 mrad with single shot detection.

This section showed that the experimental data has a near-perfect agreement with the numerical model presented earlier and identified the optimal experimental working conditions. Additionally, it was shown that within the range of hundred of mrad, the delay excursion $\delta\tau$ (and the slope of the delay Z shape) varies linearly with the nonlinear phase. This allows the relative measurement of the induced nonlinear phase by measuring $\delta\tau$. As this quantity depends on the nonlinear susceptibility the measurement scheme used here will be a relative measurement. A reference crystal (sapphire or fused silica) where the nonlinear tensor was extensively characterized is used to give a reference $\delta\tau$ value. Normalizing the measured delay excursion for an unknown crystal with crystal length and energy and comparing it with the reference value gives a relative measurement of the $\chi^{(3)}$ tensor.

All the results presented until here used all horizontally polarized beams. Independently changing the polarization of the three beams gives access to all the coefficients of the third-order susceptibility tensor. Table 2.14 summarizes the polarization configurations and the associated coefficient.

Pol. config.	Pump	Probe	Ref.	$\chi^{(3)}$ term
(i)	⇔	⇔	⇔	$\chi^{(3)}_{xxxx}$
(ii)	⇕	⇕	⇕	$\chi^{(3)}_{yyyy}$
(iii)	⇔	⇕	⇕	$\chi^{(3)}_{xxyy} + \chi^{(3)}_{xyxy}$
(iv)	⇕	⇔	⇔	$\chi^{(3)}_{yyxx} + \chi^{(3)}_{yxyx}$

FIGURE 2.14 – Polarization configurations and measured components of $\chi^{(3)}$ tensor.

2.4.2 Validation with well-known isotropic samples

In order to validate the method the $\chi^{(3)}$ ratio between the reference sample of fused silica and three different samples (Al_2O_3, BaF_2, and CaF_2) have been measured. Table 2.1 shows that good agreement with the literature was found with similar or lower error intervals.

Sample	$\chi^{(3)}/\chi_0$ (this work)	$\chi^{(3)}_{lit}/\chi_0$ (literature)
Al_2O_3	(1.1 ± 0.2)	(1.3 ± 0.3)
BaF_2	(1.0 ± 0.1)	(1.0 ± 0.1)
CaF_2	(0.5 ± 0.02)	(0.6 ± 0.1)

TABLE 2.1 – $\chi^{(3)}$ ratio between validation set plates, normalized to the fused silica nonlinear term hereafter labeled as χ_0, and compared to the values found in the literature [155-157]. $\chi_0 = (2.0 \pm 0.2)10^{-22} m^2/V^2$, as reported in Ref. [158].

2.5 Characterization of nonlinear crystals

After the presentation and the characterization of the setup, this section describes the results on the characterization of nonlinear optical crystals relevant for OPA development as well as liquid crystals as these measurements were not reported in the literature at the beginning of my Ph.D.

The experimental configuration for all the measurements is as follows : the gratings compressor is detuned to induce 5000 fs^2 of second-order dispersion on the reference, probe, and pump pulses. A 20-mm-long SF11 rod is introduced in the reference beam path to further chirp the reference pulse by 2000 fs^2. The nominal reference probe delay $\tau^0_{R,Pr}$ is set at 3.5 ps.

2.5.1 Characterization of liquid crystals

The first set of measurements presented here is the characterization of liquid crystals. Two different mixtures in the nematic phase are characterized here : MLC2132 and E7 (Merck). The samples are homemade cells where the LC layer is inserted between two 1-mm-thick layers of fused silica. An anchoring layer made of PVA is present between the LC and the fused silica to align the molecules of the LC in a plane parallel to the surface. To discriminate the influence of the anchoring layer and the substrate empty cells are also characterized. The thickness of the liquid crystal layer was measured using spectral interferometry and was found to be around 125 μm in both cases [159]. The laser peak intensity is reduced to 70 GW/cm^2 to work below the damage threshold of the LC [126]. Figure 2.15 shows a detailed measurement in MLC2132. This figure in particular features a piece of additional information this method can retrieve. Figure (d) is a single-shot situ correlation measurement of the pulse duration by integrating the reference-probe delay.

The liquid crystals were oriented in such a way that configuration (i) would give access to the value of the extraordinary nonlinear refractive index and configuration (ii) to the ordinary nonlinear refractive index. Table 2.2 shows the measured $\chi^{(3)}$ values. These are the first reported measurement of the third-order nonlinear susceptibility tensor in liquid crystals in the femtosecond regime.

LC sample	n^e	n^o	n_2^e	n_2^o
E7	1.7	1.51	15.5±0.3	2.44±0.3
MLC2132	1.72	1.49	38.7±0.4	4.4±0.4

TABLE 2.2 – Linear refractive index values from [159] and measured nonlinear index values (x10^{-16} cm^2/W) for nematic E7 and MLC2132, for λ = 1030 nm. The reference sample is fused silica.

Additionally, measurements were performed in different polarization configurations as summarized in table 2.3. It can be noted that the results of the measurements presented here indicate that the magnitude of the nonlinear index could be adjusted by almost an order of magnitude by applying a voltage to orient the LC molecules.

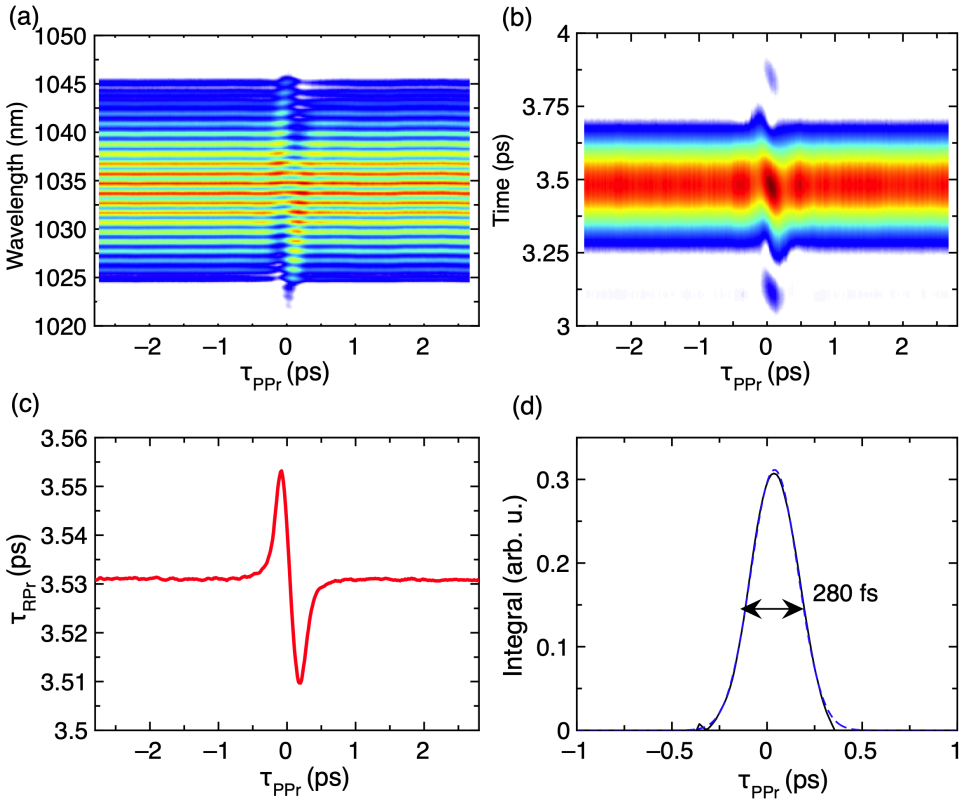

FIGURE 2.15 – Figure from [134]. Typical single-shot experimental data (LC sample). The nonlinear phase shift accumulated by the probe is estimated to be 500 mrad. (a) Interferogram of the probe and reference pulses as a function of pump-probe delay. (b) AC peak of the Fourier transform of the interferograms. (c) Relative optical group delay between reference and probe pulses (τ_{RPr}) as a function of pump-probe delay (τ_{PPr}). (d) Correlation profile of the pump pulse obtained from integration of the signal in (c).

2.5.2 Usual nonlinear bulk crystals for OPA development

After characterizing liquid crystals the interferometer was used to measure the nonlinear refractive index of some usual nonlinear crystals used for optical parametric amplification at Fastlite in particular. The characterized crystals are lithium triborate (LiB_3O_5, LBO), potassium titanyl arsenate ($KTiOAsO_4$, KTA), magnesium doped congruent lithium niobate (5% MgO :$LiNbO_3$, MLN) and lithium gallium sulfide ($LiGaS_2$, LGS). The crystal orientations correspond to the phase matching of amplification of an infrared wave (2-10 μm) with a 1030 nm pump. The measured nonlinear refractive indices are reported in table 2.4 as well as the crystal orientations and lengths.

In addition to all the aforementioned crystals a ZnSe crystal was also characterized to confirm the validity of the method. As the nonlinear response for each crystal is different the pulse energy was adapted to keep the nonlinear phase shift around 500 mrad. The results are in good agreement with the literature for LBO, MLN, and ZnSe. The agreement is not as good for the other crystals. This discrepancy comes from several different factors. The nonlinear index is

$\chi^{(3)}$ term	Sample	$\chi^{(3)}$	φ_{NL} (mrad)
$\chi^{(3)}_{xxxx}$	MLC2132	(17±3) x χ_0	105
$\chi^{(3)}_{yyyy}$	MLC2132	(3.5±0.5) x χ_0	20
$\chi^{(3)}_{xxyy} + \chi^{(3)}_{xyxy}$	MLC2132	(1.3±0.2) x χ_0	9
$\chi^{(3)}_{yyxx} + \chi^{(3)}_{yxyx}$	MLC2132	(2.8±0.5) x χ_0	18
$\chi^{(3)}_{xxxx}$	E7	(7.1±1) x χ_0	40
$\chi^{(3)}_{yyyy}$	E7	(1.08±0.1) x χ_0	5
$\chi^{(3)}_{xxyy} + \chi^{(3)}_{xyxy}$	E7	(4.4±0.8) x χ_0	15
$\chi^{(3)}_{yyxx} + \chi^{(3)}_{yxyx}$	E7	(3.8±0.7) x χ_0	12

TABLE 2.3 – Measured values of some $\chi^{(3)}$ terms for the E7 and MLC2132 mixtures. The values are relative to that of fused silica : $\chi_0 = (2.0 \pm 0.2).10^{-22}$ m^2/V^2 [158]. x refers to the extraordinary axis of the LC cells. The last column gathers the calculated experimental nonlinear phase in the LC layer.

Sample	θ °	ϕ °	L mm	$n_{2,meas}$ 10^{-20}m^2/W	$n_{2,lit}$ 10^{-20}m^2/W
AL_2O_3	0	-	1	-	2.8 ± 0.5 [157]
LBO lo	90	10	2.3	2.24 ± 0.2	
	90	-	5		2.2 ± 0.25* [160]
KTA lo	41.8	0	1.5	10.6 ± 0.2	
	42	0	4		15 [161]
KTA hi	41.8	0	1.5	11.2 ± 0.2	
	42	0	4		15 [161]
MLN lo	45.4	30	2	12.6 ± 0.2	
MLN hi	45.4	30	2	14.3 ± 0.4	
	0	-	2		16.7 ± 2.5* [160]
LGS lo	47	0	1	28.1 ± 0.3	
	48.2	0	5		41 [161]
	90	38.8	7		35 [162]
	90	37.5	2		<64 [163]
LGS hi	47	0	1	31 ± 0.3	
	48.2	0	5		41 [161]
ZnSe	-	-	2	112 ± 1.6	113 ± 12 [164]

TABLE 2.4 – Measured nonlinear refractive indices of LBO, KTA, MLN, LGS and ZnSe at 1030nm for 200 fs pulses. For birefringent crystals, values are given for the fast axis (low index, lo) and/or for the slow axis (high index, hi). θ and ϕ refer to the polar crystallographic orientation. L is the crystal length. All values from the literature were measured near 1030 nm with sub ps pulses, except MgO :LN and LBO, for which the reported values at 800 nm were rescaled (*) to 1030 nm, as described by [165] and references). The reference sample is sapphire.

a sum of several different contributions such as the instantaneous electronic response, the delayed Raman response, and the cascaded quadratic effects. All these effects vary as a function of the pulse wavelength and duration. To the best of my knowledge, this work is the first characterization with these experimental conditions (femtosecond regime with close to mJ pump pulse energy) and the LGS crystal had no characterization in any regime. Figure 2.16 compares the measured nonlinear refractive index of all the materials as a function of their bandgap.

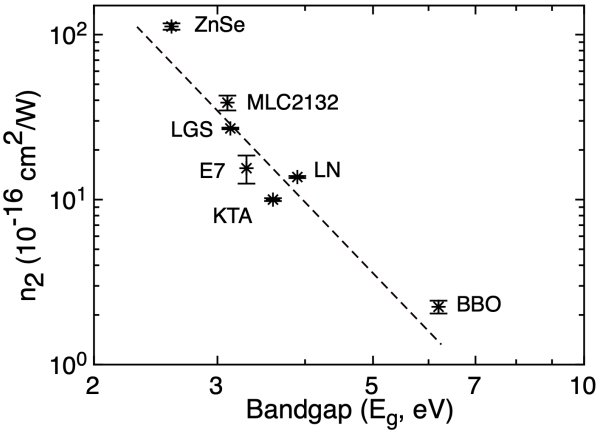

FIGURE 2.16 – Figure from [134]. Nonlinear index dependence versus bandgap for the tested samples in log-log scale. The dashed line indicates a E_g^{-4} dependence.

The plotted dependence of the nonlinear refractive index in a E_g^{-4} [166] (dotted line) fits with the measurement points quite well even for the LC sample.

2.5.3 Phonon detection

The setup can also be used to characterize delayed nonlinear effects. The KTA crystal exhibits a strong Raman ringing at the pulse duration used in this characterization. Figure 2.17 shows a delay scan in KTA with higher pulse energy to emphasize the Raman ringing.

This measurement is outside the range of the nonlinear phase shift previously mentioned (500 mrad) but the intent in this case is not to measure the nonlinear index but to demonstrate the ability of this setup to investigate delayed material response. The pulse energy is increased to 75 μJ (5 times the value used for nonlinear index measurement) and the pump-probe delay range is increased to 5 ps. In this configuration the delay swing is no longer symmetric and a clear oscillation appears after the main delay peak. The oscillation can be decomposed into two vibration modes with wavenumbers of 66 and 75 cm^{-1} corresponding to identified A1 vibrational frequencies in KTA [167].

2.6 Conclusions

Chapter 2 presented a novel OKE spectroscopy method named nonlinear chirped interferometry to characterize the third-order nonlinearity on the femtosecond time scale. The technique

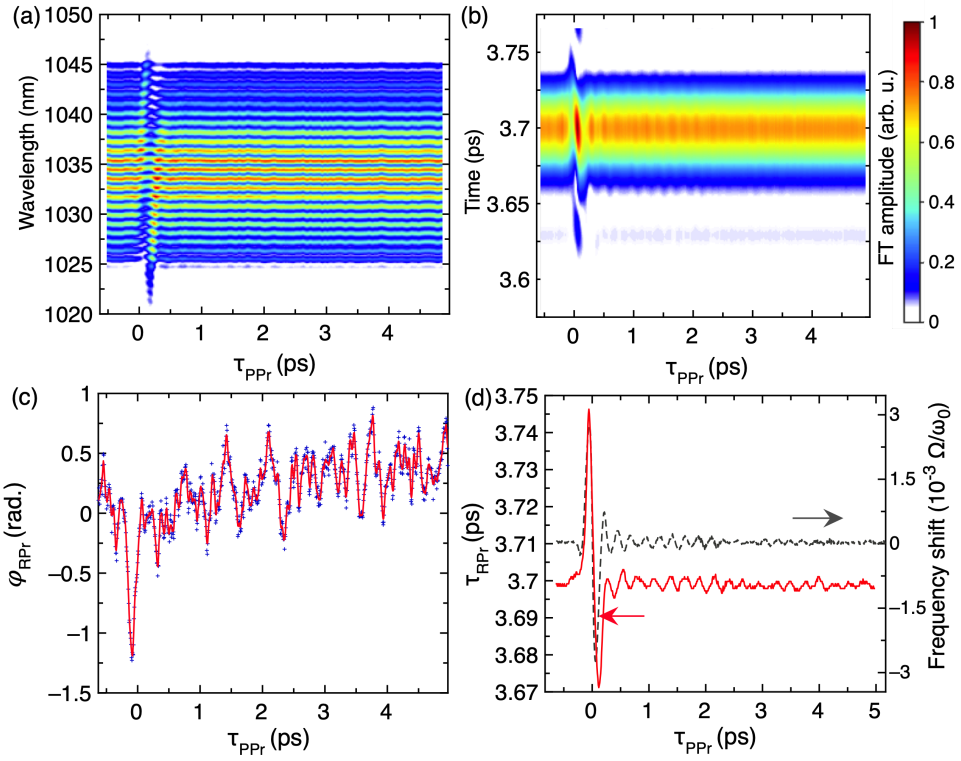

FIGURE 2.17 – Figure from [133]. Experimental data for the KTA crystal on a 6 ps scan range. (a) Interferogram of the probe and reference pulses as a function of pump–probe delay. (b) AC peak of the Fourier transform of the interferograms. (c) Relative phase between reference and probe pulses (φ_{RPr}) as a function of pump–probe delay. Raw data (blue), moving average (red). (d) τ_{RPr} (red) and normalized frequency shift (gray) as a function of pump–probe delay.

consists in monitoring the variation of the first derivative of the nonlinear temporal phase (relative group delay) of a transmitted probe under the effect of a strong pump pulse rather than the nonlinear phase. This is done using spectral interferometry between the probe pulse and a reference pulse sampled upstream. Under the right chirp conditions for all three pulses two distinct mechanisms contribute to the transient delay variation :

— 2BC via energy exchanges between pump and probe induces a temporal reshaping

— the XPM frequency shift is encoded in time by chirping the reference

The experimental working parameters were defined with a 1D numerical model found to be in very good agreement with the experimental data. The main advantage of this technique is the insensitivity to external phase fluctuations even for a meter-scale interferometer. As a consequence, active stabilization or heterodyne detection is not needed to reach a sensitivity of 10 mrad nonlinear phase shift (0.01% of the carrier frequency). The interferometer was used to measure the nonlinear indices of liquid crystals (E7 and MLC2132) in the sub-ps regime (previously unknown). The nonlinear indices of KTA, MLN, and LGS were also measured in the crystal orientations adequate for type I difference frequency generation with a 1030 nm pump. This makes this study relevant for the development of mid-infrared OPCPA sources based on the Yb :YAG technology. The sensitivity and overall performance of the interferometer could

be pushed further by multiple scan acquisition, higher averaging, or extending the involved spectral bandwidth. Additionally, this work is not exhaustive as the phonon presence in KTA was noticed but barely investigated. The work done here was also restricted to the wavelength of 1030 nm. This characterization setup could potentially be used for even shorter pulses however the capability of the method still needs to be proved. Reducing the temporal duration of the pulses would also increase the spectral bandwidth potentially disturbing the spectral phase effects at play here. The characterization could also be extended to phonon detection by increasing the contribution of the frequency shift to enhance the detection capabilities.

Chapitre 3

State of the art CEP-stable sources

3.1 CEP stable sources

Carrier-envelope phase (CEP) is the absolute value of a pulse's spectral (or temporal) phase. It characterizes the phase offset between the carrier of the pulse and its envelope. It is also alternatively named carrier-envelope offset (CEO) as it is linked to the offset of the frequency comb with the zero frequency (named f_{CEO}) as depicted in figure 2. A CEP stable source is a pulsed laser source where the carrier envelope phase of each pulse is identical. It corresponds to an offset frequency f_{CEO} being zero. CEP stabilization is significant for two major fields in optics : frequency comb metrology and spectroscopy and strong field physics and high harmonic generation. Frequency comb metrology and spectroscopy is the use of frequency combs as a metrology tool for precise frequency measurement [168, 169] or as a clock [6, 170] for example. Strong field physics and high harmonic generation are building blocks of current attosecond physics. Attosecond physics tries to put into light the electronic dynamics of gases, molecules, and bulk material using time-resolved spectroscopy [171, 172].

This chapter briefly reviews the past and current advancement of CEP-stable sources. It details the different categories of CEP-stable sources and technologies before precisely describing a CEP-stable OPCPA. This chapter aims at giving an idea of the different options to achieve CEP stability and to motivate the study of phase stability during bulk supercontinuum generation process presented in chapters 4 and 5.4.

3.1.1 Carrier envelope phase measurement

The absolute CEP value can be measured by measuring the photo-electrons emitted left and right compared to the polarization direction by photo-ionization in a noble gas with the pulse to characterize. This is typically done with a stereo ATI setup [173]. This method is an indirect measurement that gives the absolute CEP value. It however requires a pulse with energy high enough to cause photo-ionization and is a costly setup. Alternatively, when the wavelength is high enough (typically in the THz range) electro-optic sampling can be used to retrieve the complete electric field [174].

Although possible as previously mentioned direct CEP measurements are not trivial (at least in the visible and UV range). The standard option is then CEP variation measurements.

The carrier-envelope phase variations are commonly measured via f-2f interferometry. Considering a train of pulses the frequency components in the spectrum are then $f_n = nf_{rep} + f_{CEO}$. If the spectrum of the pulse is not octave-spanning, the first step of the f-2f interferometer is frequency broadening via supercontinuum. Once the spectrum is octave-spanning, the spectrum is frequency doubled to a frequency comb with components $f_2n = 2nf_{rep} + 2f_{CEO}$. The beating then yields the frequency $2f_n - f_{2n} = f_{CEO}$ monitoring the CEP drift of the system as the frequency offset does not give the absolute CEP value but its shot-to-shot variation.

Figure 3.1 shows two examples of possible geometries for an f-2f interferometer.

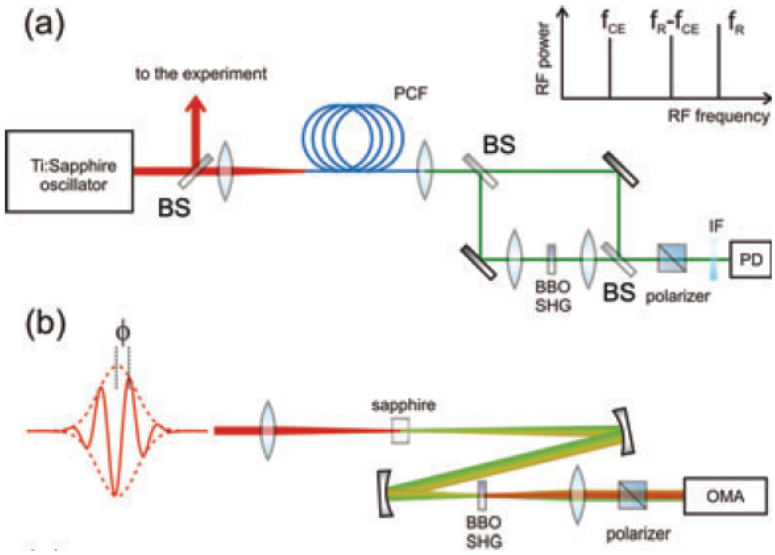

FIGURE 3.1 – Figure from [34]. (a) Inline f -to-2 f interferometer setup for measuring the CE frequency from a femtosecond laser oscillator; (b) f -to-2 f interferometer for measuring the single-shot CEP drift.

In the first case, the broadening is done in a photonics crystal fiber and the geometry is of Mach-Zehnder type. It is the typical choice when the energy of the pulse is in the nJ range as broadening in a bulk crystal is not possible due to the energy being too low. This also forces a Mach-Zehnder geometry which tends to be less stable than the next example. In the second case, the broadening is done in a bulk sapphire crystal and the geometry is inline. This type of interferometer is typical when supercontinuum generation is accomplished in the μJ range as it allows bulk supercontinuum generation. This makes the inline geometry possible and preferred as it is intrinsically more stable (single optical path removing instability). In both cases, the first step of the interferometer is spectral broadening via supercontinuum generation. As a highly nonlinear step, it is likely to add noise to the measured CEP value. The question of the measurement setup then becomes significant if part of the CEP noise measured is not from the source itself but from the measurement device.

3.1.2 Frequency combs

In the field of frequency comb metrology and spectroscopy, the stabilization of the CEO enables the precise measurement of the frequency of light [175]. This quest for frequency measurement started almost as soon as the laser was invented. Some of the early frequency measurements involved the use of harmonic laser frequency chains [176]. Following this precise speed-of-light measurement the definition of the meter was changed in 1983. Many other techniques have been explored until the arrival of optical frequency combs [177-179].

The Fourier transform of a pulse train is a frequency comb as explained in [180] making femtosecond oscillators perfect candidates for frequency comb generators. The frequency spacing of the frequency comb is equal to the repetition rate of the laser f_r. Generally, the electric field of each pulse is not reproducible [181-183] because of the dispersion in the cavity. This phase variation translates in the frequency offset f_{CEO} which then gives this shape for the frequency comb $f = f_{CEO} + nf_r$ where n is an integer. Such a structure is the base for frequency comb metrology. Propagating the output of a mode-locked oscillator in a nonlinear media such as a micro-structure optical fiber allows spectral broadening of the frequency comb [184, 185]. Under the right conditions (no ionization in the fiber) the coherence of the frequency comb is preserved. The measurement of f_{CEO} is simple when the broadening is sufficient to make the spectrum octave spanning via f-2f interferometry. Having access to the precise measurement of the frequency offset allows the design of active CEO stabilization [182, 186]. This is typically done by introducing a controllable amount of dispersive media in the laser cavity. The stabilization of the frequency offset now gives access to precise f_r measurement. As the shape of the frequency comb depends only on these two frequencies that can be controlled and measured independently frequency combs are perfect candidates for optical clocks [187] and frequency synthesizers.

Another adjacent field enabled by the development of frequency combs is frequency comb spectroscopy. The spectral regions of interest for the spectroscopy of molecules are in the ultraviolet (<400 nm), mid-infrared (2-20 μm), far infrared (20-100 μm), and terahertz range (100 μm-1 mm). Frequency combs are available in this range either directly as the output of femtosecond laser or by down-conversion of such a laser [188-192]. Different schemes for frequency comb spectroscopy are available ranging from the simple direct comb spectroscopy [181] to dual-comb spectroscopy [193], with various other techniques such as Ramsey comb spectroscopy [194], dispersive spectroscopy [195] and Michelson based Fourier transform spectroscopy [196]. Among these dual comb spectroscopy is the most widely used. It is analog to Fourier-transform interferometry without any moving parts. In this scheme, the sample is interrogated with a comb with a repetition frequency f_{rep} and this frequency combed creates a beating with a second frequency comb at a slightly different repetition frequency $f_{rep} + \delta f$. The Fourier transform of the temporal signal then reveals the spectrum. The time delay between the two pulses is automatically scanned by the small difference in the repetition frequency up to the time delay of $1/f_{rep}$ [197].

There are multiple options to generate such frequency combs which mostly fall within two

big families : the fiber oscillators and the free space mode-locked oscillators. In the next two sections 3.1.3 and 3.1.4 the two groups of CEP-stable oscillators will be presented.

3.1.3 Fiber oscillator

The first group of CEP stable oscillators is based on fiber optics technologies. Fiber oscillators are a type of laser cavity typically based on the doping of a single-mode fiber with a gain medium such as ytterbium or erbium. The ring geometry is very common for fiber oscillators [198]. Figure 3.2 gives examples of the possible geometries for a fiber laser cavity.

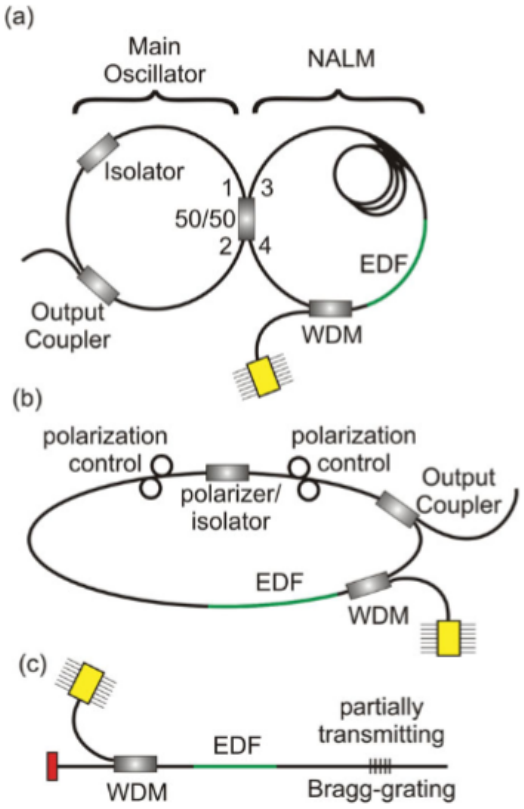

FIGURE 3.2 – Figure from [199]. Different oscillator designs. (a) figure-of-eight laser, (b) ring resonator, and (c) linear oscillator. The mode-locking mechanism in (a) and (b) is usually based on nonlinear phase shift, whereas in (c) a saturable absorber mirror is used. LD : laser diode, WDM : wavelength division multiplexer. EDF : erbium-doped fiber. SMF : standard single mode fiber

The mode-locking of ring cavities was first demonstrated in an Erbium fiber laser using active mode-locking [200]. Nowadays all the laser cavities are passively mode-locked using a figure-eight laser [201], nonlinear polarization evolution [202] or a saturable absorber mirror (the most common type being semiconductor saturable absorber mirror SESAM) [203, 204]. The main advantage of a fiber oscillator is the overall stability and the fact that they are insusceptible to environmental fluctuations. That makes fiber oscillators the best devices in terms of f_{CEO} stability and control. The measurement of the CEP phase (or CEO frequency) is typically done via f-2f interferometry (section 3.1.1) [205]. CEP can then be stabilized inside the

cavity with a feedback loop adjusting its dispersion and can also be directly controlled with an acoustic-optic modulator for example [32]. CEP can also be passively stabilized by intrapulse difference frequency generation within a single frequency comb [206, 207]. All of the previously mentioned tools allow the extreme frequency and phase stabilization down to a precision of 2.10^{-18} Hz [208].

Despite being intrinsically more stable, fiber oscillators have a major drawback. As the guided nature of single-mode optical fiber forces a small effective mode area, the nonlinear effects and damage threshold limit the pulse energy inside the cavity. This makes the energy scaling in fiber oscillators not possible and motivates the development of free-space oscillators.

3.1.4 Free space oscillators

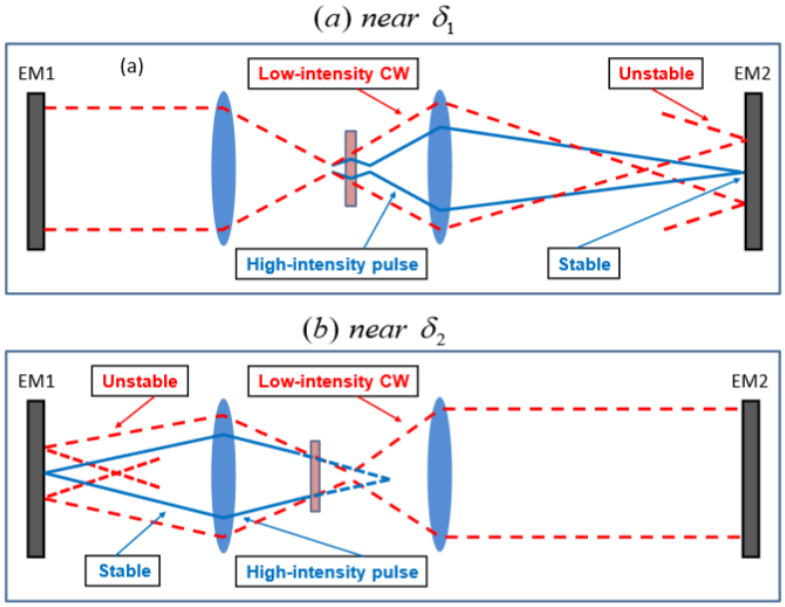

FIGURE 3.3 – Figure from [209]. Illustration of the Kerr lensing effect as a mode-locking stabilizing mechanism in virtual hard aperture technique : (a) increasing δ beyond the stability limit, $\delta 1$, destabilizes CW operation, while ML operation remains stable as the effective distance between f1 and f2 becomes shorter, by the nonlinear forward imaging of the focus point ; (b) decreasing δ below the stability limit, $\delta 2$, destabilizes CW operation, while ML operation remains stable as the effective distance between f1 and f2 becomes larger by nonlinear virtual imaging of the focus point.

Mode-locking is also possible in a free-space oscillator and is typically passively done with Kerr-lens mode-locking [210]. The material of choice for Kerr-lens mode-locking has been Ti :Sa, as it offers a gain bandwidth supporting sub-10-fs pulses around 800 nm. It is pumped with laser sources at a wavelength of around 520 nm. The most common options for pump lasers are argon-ion (514.5 nm) lasers or frequency-doubled Nd :YAG, Nd :YLF or ND :YVO (527-532 nm) [211, 212].

A typical cavity design is shown in figure 3.3. The cavity is made of two converging lenses forming a telescope with the gain (and Kerr) medium in the focal point of the telescope. Two

mirrors confine the beam inside the cavity. The light exits the cavity via one of the mirrors that is partially reflective. δ is the offset in the lens positioning compared to the perfect telescope configuration and $\delta 1$ and $\delta 2$ are the extrema of the range of the lens positioning to maintain stable cavity operation. As depicted the cavity geometry causes CW (blue) operation to be unstable and only high-intensity pulse (red) can propagate due to the Kerr effect. As mentioned without any further actions on the cavity the CEP of the output pulse of an ordinary mode-locked laser is random. The CEP is indeed affected by thermal effects and mechanical vibrations causing optical path variation in the cavity. A typical CEP-stabilized oscillator includes a CEP-measurement setup (f-2f interferometer) associated with a feedback loop adjusting one the cavity parameters influencing CEP such as cavity length, pump power or dispersion inside the cavity [213].

Figure 3.4 shows the diagram of such a cavity.

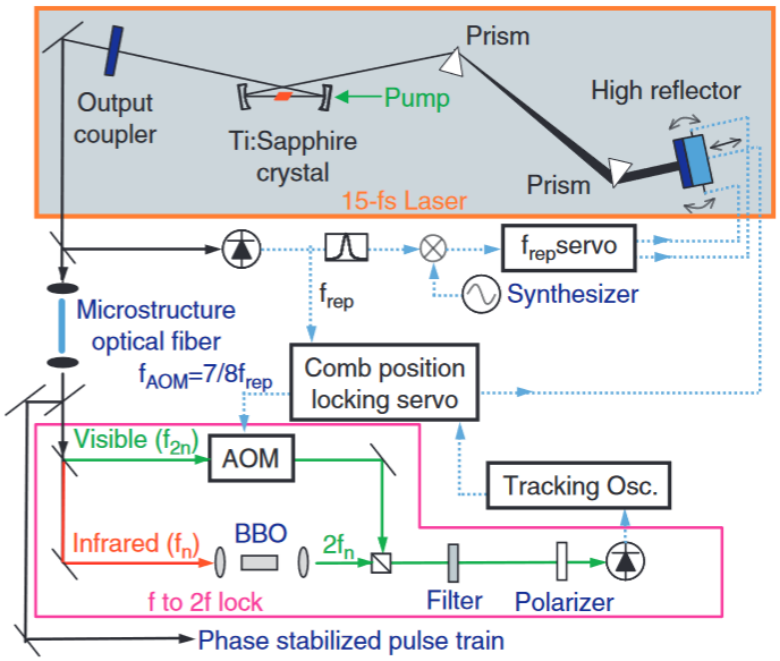

FIGURE 3.4 – Figure from [214]. Experimental setup for locking the carrier–envelope relative phase. The fs laser is located inside the shaded box. Solid lines are optical paths and dashed lines are electrical paths. The high reflector mirror is mounted on a transducer to provide both tilt and translation. AOM—acoustic-optic modulator; APD—avalanche photodiode; BBO—β-barium-borate doubling crystal.

The purple box contains the f-2f interferometer giving the beats that are compared to a reference signal to give the error signal used as feedback inside the laser cavity. The length of the cavity is then adjusted to compensate for the CEP drift and actively stabilize the cavity. Alternatively, to compensate for CEP drift the pump power can be adjusted with an acousto-optic modulator [215]. In addition to the in-loop fast correction scheme, an out-of-loop f-2f interferometer can be added to compensate for the slow CEP drift [216].

Despite Ti :Sa being the material of choice [217, 218] other options are available [215] and

the trend is the development of systems based on Yb :YAG thin-disk lasers [219] as they allow a higher average power.

3.2 OPCPA

Optical parametric chirped pulse amplifiers are common versatile pulsed sources first introduced in 1992 [220]. They have numerous advantages including their availability from the UV to the IR ranges, wavelength tunability, and short pulse duration. OPCPAs combine chirped pulse amplification [21] and optical parametric amplification (section 1.3.1). Contrary to laser amplification, no energy is stored in the amplification medium in the OPA process which makes all thermal effects minimal. The typical architecture of an OPCPA is given in figure 3.5.

FIGURE 3.5 – Diagram of a typical OPCPA

The pulse laser is first used to generate the seed typically through supercontinuum generation either in bulk material [221] or in a hollow-core fiber [222]. The seed and the pump are then temporally stretched using bulk materials or a compressor before the amplification of the seed in the OPA stages. The output pulse is then re-compressed using chirped mirrors or a grating compressor. The two main technologies for the pump laser are Ti :Sa and Yb :YAG systems.

3.2.1 Pump lasers

Ti :Sa lasers

As mentioned in section 3.1.4 Ti :Sa based systems are the reference for ultrashort pulse generation. Such pulses can be used directly for light-matter interaction or metrology [223-225] but can also be used as a seed for a secondary source such as an OPA (section 1.3.1). Development of Ti :Sa OPA sources started in the 1990s [226]. These sources are typically based on kHz Ti :Sa CPA systems [222] but can go up to 250 kHz [227]. However the Ti :Sa technology is limited in terms of average power in the amplifier by thermal effects induced by a large quantum defect and an overlap between emission and absorption spectra (figure 3.6).

Yb :YAG lasers

As a result the development of Yb :YAG based system has taken over in the last decade to reach higher average power. State-of-the-art CEP-stable Yb :YAG based OPCPAs have been pushing the average power to the Watt level [24] slowly replacing the Ti :Sa based systems [228-231]. Some of these systems are hybrid as they are seeded with a Ti :Sa oscillator that offers very

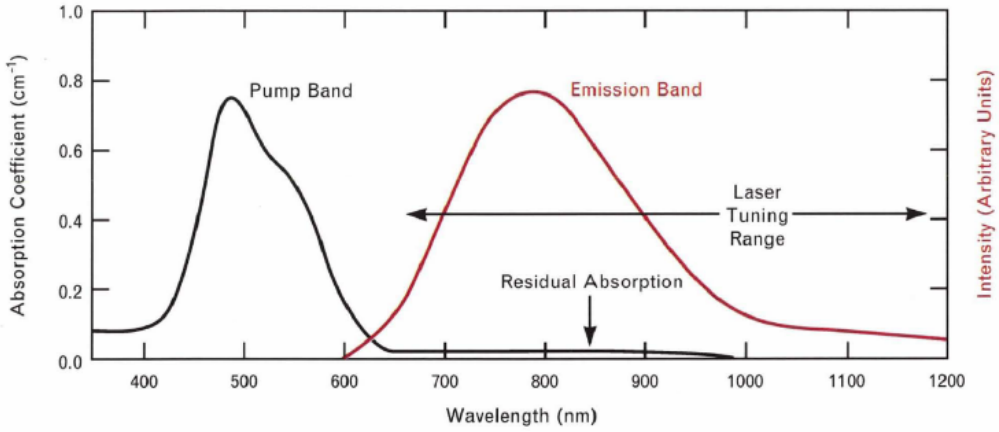

FIGURE 3.6 – Figure from [23]. Emission and absorption bands of Ti :Sa.

wide bandwidth and short pulse duration but are pumped with a Yb-doped system [232]. Another option is to have two different Yb-doped laser systems : one as a seed (a supercontinuum source for example) and one as a pump [233].

One of the options for Yb :YAG pumped OPCPA technology is the thin-disk ytterbium-doped YAG lasers amplifier invented in 1994 [234] with a geometry showed in figure 3.7 for a multipass cell (a) and a regenerative amplifier (b).

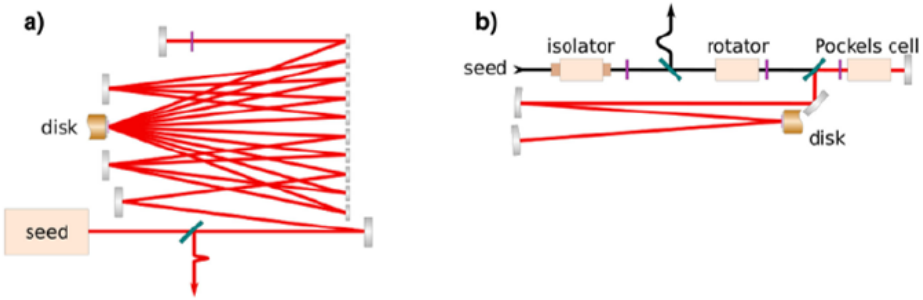

FIGURE 3.7 – Figure from [235]. Schematics of a thin-disk laser amplifier. (a) Multi-pass amplifier and (b) regenerative amplifier.

Compared to Ti :Sa amplifiers limited to dozens of watts of average power, thin-disk Yb :YAG amplifiers can scale up to the kilowatt level with pulse duration around the picosecond [236].

3.2.2 Seed generation and amplification

The first step in an OPCPA is the generation of a seed to be amplified in later OPA stages. It is typically done by generating a supercontinuum (section 1.3.5) with a small fraction of the pump energy. The seed is then later amplified in various optical parametric amplification stages. Figure 3.8 gives an example of an architecture for such a system.

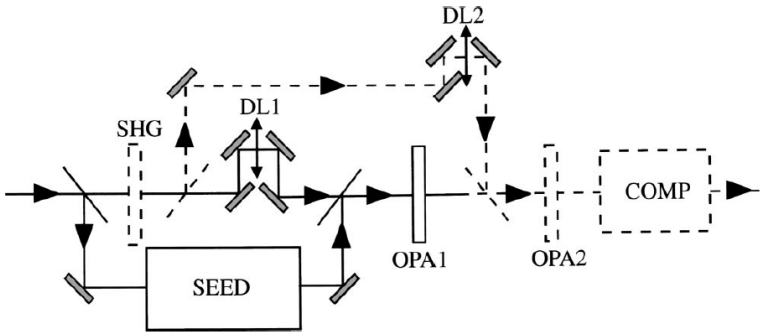

FIGURE 3.8 – Figure from [237]. Scheme of an ultrafast optical parametric amplifier. SEED : seed generation stage ; DL1, DL2 : delay lines ; OPA1, OPA2 parametric amplification stages ; COMP : compressor.

The same architecture can also be employed directly at the output of an oscillator to get a megahertz optical parametric amplifier [238]. Due to the low energy per pulse at the output of an oscillator, spectral broadening in this case is commonly done in photonics crystal fibers.

3.2.3 CEP stabilization

Much like what was introduced in section 3.1.4 without any particular effort the CEP at the output of an OPCPA is random. It can be stabilized in two different ways : with active stabilization or with passive stabilization.

Similarly to the CEP stabilization of oscillators active stabilization is accomplished with a CEP measurement system (typically f-2f interferometer) and a feedback loop to stabilize directly the CEP of the oscillator which in turn stabilizes the CEP of the output [239]. Another advantage of optical parametric amplifiers is the passive CEP stabilization of the idler. The phase of the idler wave in the OPA/DFG process is given by [34] :

$$\phi_i = \phi_p - \phi_s - \pi/2 \tag{3.1}$$

where ϕ_i is the phase of the idler, ϕ_p the phase of the pump, and ϕ_s the phase of the signal. If the pump and signal share the same CEP variations or in terms of frequency if they share the same f_{CEO} the CEP of the idler is automatically a constant. This idea was first proposed in [240]. This condition is met in the architecture shown in figure 3.8 making the idler intrinsically passively CEP stable. In this case, the architecture is called interpulse DFG as the difference frequency generation involves two different pulses. Intrapulse DFG follows the same principle but the difference frequency generation happens between the blue edge and the red edge of the same pulse [222]. The main advantage of intrapulse DFG is its intrinsic geometric stability. As a single pulse is involved in the DFG process all the instability coming from the optical path variations between signal and pump are nullified as they are the same pulse. Both active and passive CEP stabilization schemes can be implemented in the same source.

3.3 Seeder 800 nm

This section presents a CEP-stable OPCPA based on a Yb :YAG CPA system. It was commissioned by Fastlite to Amplitude group and my task on this system was to take part in its building and characterization. As a CEP-stable system with a modern architecture based on a Yb :YAG CPA amplifier I (under the guidance and supervision of Simone Bux and later Yoann Pertot) built and characterized, it is a perfect example to illustrate the key parameters and hurdles of modern high-average-power CEP-stabilization. The system will be reviewed here along with the measurement of its CEP stability.

The OPCPA has two CEP-stable outputs : 1600 nm and 800 nm. The 1600 nm is generated first and then frequency-double to 800 nm. The 800 nm is used for seeding a Ti :Sa based amplifier. The system is made of four parts : the first part of the system is the pump laser, the second part is the DFG where the passively CEP-stabilized seed is generated, the third part is made of the various OPA stages as well as the frequency doubling crystal. The fourth and last stage is the compression and characterization of the output beams. A diagram of the OPCPA is shown in figure 3.9

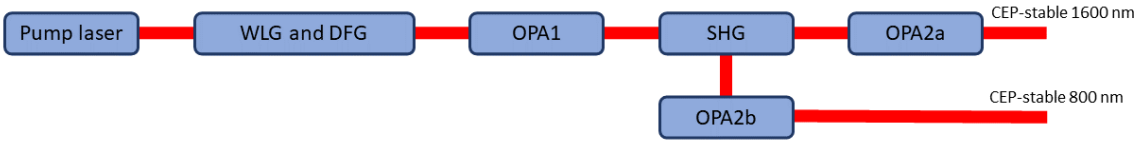

FIGURE 3.9 – Diagram of the OPCPA.

3.3.1 Pump laser and pointing stabilization

The pump laser is a Tangerine laser from Amplitude group. Its operating frequency is 100 kHz with a pulse energy of 200 μJ for a total average power of 20 W. The FTL pulse duration is 350 fs and the power stability of the pulse is below 1.5% rms. The beam polarization is vertical.

3.3.2 Passive CEP stabilization

The seed generation is done with an inline geometry (patented by Fastlite) [241] according to the diagram displayed in figure 3.10.

The first step in the seed generation is the slight rotation of the polarization of the input beam (vertically polarized). The beam is then sent to a calcite plate. Calcite is a birefringent material placed so that the fast axis is aligned with the horizontal direction and the slow axis is aligned with the vertical direction. As a result, the polarization of the input beam is projected on both crystal axes. The output of the calcite plate is a low-energy horizontally polarized pulse followed by a delayed high-energy vertically polarized pulse. Both pulses are then sent into a

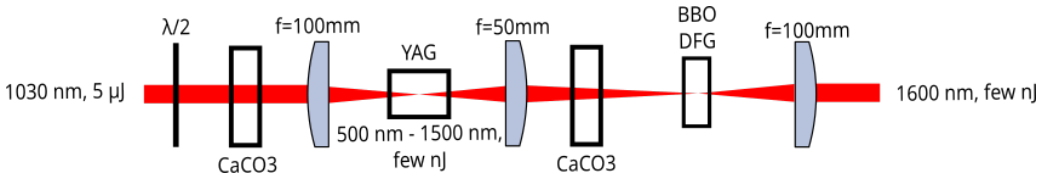

FIGURE 3.10 – Diagram of the seed generation box. L/2 is a half-wave plate, CaCO3 are calcite plates, YAG is the WLG crystal and BBO DFG is the DFG crystal.

6-mm long YAG crystal for supercontinuum generation. As the energy of the first pulse is too low for any significant nonlinearities to happen it propagates in the YAG mostly unchanged. The delayed higher energy pulse however is energetic to generate a WL in the target region of 625 nm. Both beams are then recombined temporally with a second calcite plate in the reverse crystal orientation and focused into a BBO crystal where the DFG takes place. The target region of 1600 nm is generated by difference frequency between the 625 nm part of the spectrum and the 1030 nm. The WL and the 1030 nm share the same CEP fluctuations making the output of the DFG passively CEP-stable. The spectrum after DFG is displayed in figure 3.11. The energy of the pulse at this point is below the detection range of the power meter estimated at the nJ level.

3.3.3 Amplification stages

The seed pulse is then amplified in three different OPAs. OPA 1 amplifies the DFG spectrum using the second harmonic of the driving laser (515 nm) as a pump and the resulting spectrum is shown in figure 3.11 (b).

This pulse is then frequency doubled to the desired wavelength at 800 nm. Both the remaining 1600 nm and the 800 nm are amplified in separate additional OPAs (OPA 2a and OPA 2b). Figure 3.11 (c) and (d) show the spectrum of the frequency-doubled output of OPA 1 and the final output both at the central wavelength of 800 nm (OPA 2a).

The output energy is 9 μJ and the FTL duration is 12.4 fs with a central wavelength of 802 nm. The remaining pulse at 1600 nm is amplified in OPA 2b in a periodically poled lithium niobate (PPLN) crystal [242]. The final output is shown in figure 3.12.

The FTL duration at the output at 1600 nm is 26 fs at a central wavelength of 1614 nm. The pulse energy is around 7.5 μJ.

To summarize the OPCPA is pumped with 200 μJ of 1030 nm (20 W) that are converted into two passively CEP-stabilized outputs : the first one with a central wavelength of 1614 nm and a spectral bandwidth of 220 nm for a pulse energy of 7.5 μJ (750 mW), the second one with a central wavelength of 802 nm, a spectral bandwidth of 108 nm for a pulse energy of 9 μJ. In total 16.5 μJ out of the 200 μJ of the pump are converted at the output of the system for a total efficiency slightly higher than 8% which is typical for this kind of systems [35, 221, 241, 243]. The compression of the output of OPA 2b was done using chirped mirrors to reach a measured duration of 12.5 fs (FTL of 12.4 fs).

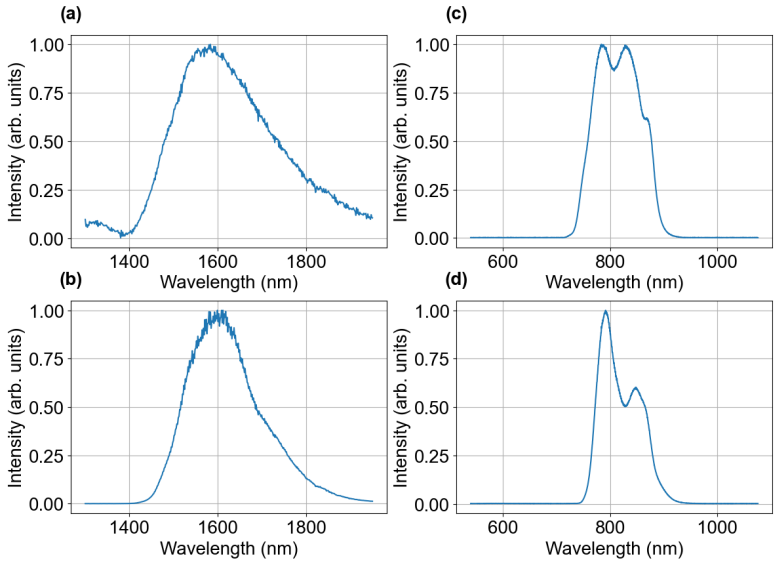

FIGURE 3.11 – a : spectrum after DFG. b : spectrum after OPA1. c : spectrum at the output of the BiBO crystal. d : Spectrum after OPA 2b.

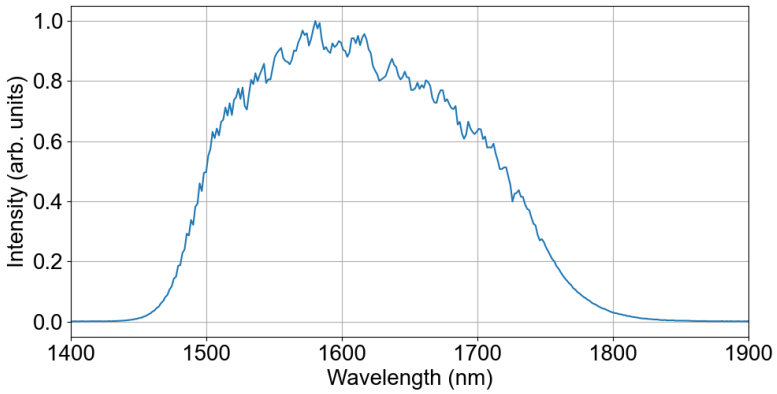

FIGURE 3.12 – Spectrum at the output of OPA 2a.

3.3.4 CEP measurements

The CEP of both outputs was measured and as an illustration, the CEP measurement of the output of OPA 2b will be shown here. The setup to measure the CEP drift of the system is a f-2f interferometer. As the energy of the output is in the μJ range the broadening is done in a bulk YAG crystal. Figure 3.13 shows a diagram of the interferometer.

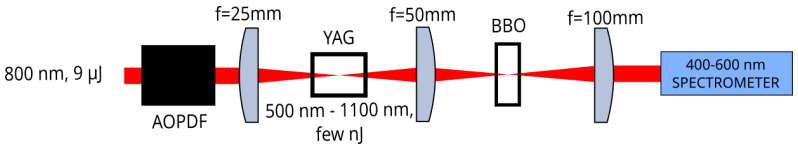

FIGURE 3.13 – Diagram of the f-2f interferometer.

The first step of the interferometer is the propagation through an acousto-optic programmable dispersion filter (AOPDF) [244]. This step fulfills two roles : the first one is the fine-tuning

of the compression of the pulse which will be shown to have a high impact on the CEP measurement, and the second one is the possibility to implement a feedback loop on the CEP to achieve a better measurement of the fast CEP fluctuations. After compression by the AOPDF, the pulse is spectrally broadened via filamentation in a 2 mm-thick YAG crystal. The conditions of filamentation are very different compared to the supercontinuum used in the seed generation (section 3.3.2). The focal length of the lens is much smaller meaning the filament is shorter. The pulse duration is shorter and the wavelength is different (800 nm vs 1030 nm). The spectral broadening of the pulse results in a supercontinuum spanning between 500 and 1100 nm. This spectrum is octave-spanning allowing frequency doubling of the 1050 nm part of the spectrum on the 525 nm by imaging the focus of the YAG crystal in a 0.5 mm-thick BBO crystal. As the group velocity of the blue and red parts of the supercontinuum are different due to the propagation in the YAG crystal and the imaging lens, they are delayed inside the BBO crystal (around 300 fs). The polarization of the second harmonic is perpendicular to the one of the supercontinuum. A polarizer at 45° orientation (not on the diagram) is added after the BBO crystal to project everything on the diagonal polarization allowing interference on the spectrometer.

The spectrum shows spectral fringes around 525 nm and as explained in section 3.1.1 the phase variations of these spectral fringes are directly linked with the variations of the CEP of the pulse. This phase is monitored by a Fringeezz (from Fastlite) which is a device analog to a fast spectrometer directly processing the phase value. The acquisition is single shot at the frequency of 10 kHz (1 out of 10 shots), and the CEP is plotted in figure 3.14.

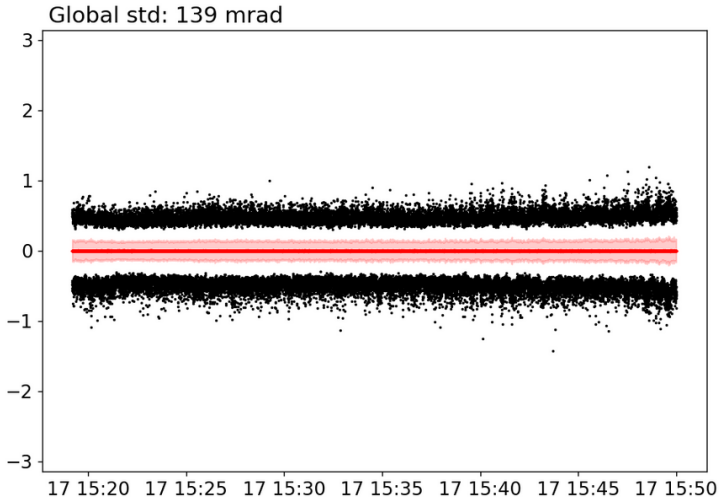

FIGURE 3.14 – CEP of output 2b over 30 seconds with active stabilization.

The overall stability value of the CEP is 139 mrad rms when the feedback loop with the AOPDF is active. This value highly depends on the parameters of the f-2f interferometer. As mentioned before the input pulse duration has a huge impact on the measured CEP variations. For example a variation of the GDD as low as 100 fs/s^2 can degrade the CEP rms by 100 mrad. It is similarly very sensitive to the YAG crystal position along the propagation direction and to the pulse energy. To finish this setup presentation figure 3.15 gives another CEP measurement where the active stabilization loop is turned off to show the slow variations compensation.

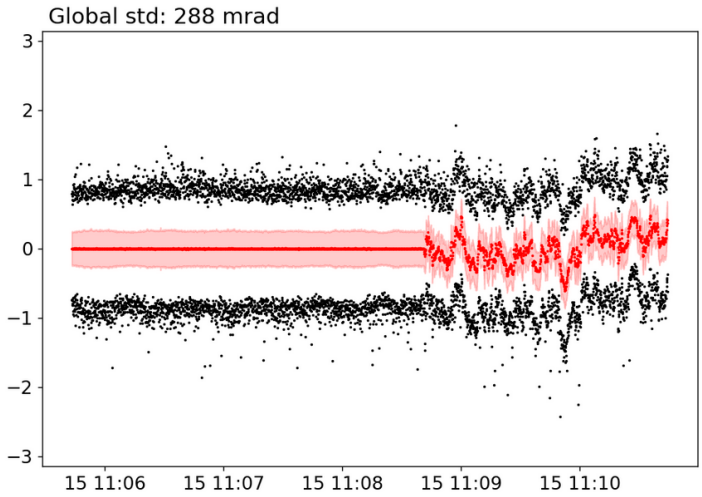

FIGURE 3.15 – CEP of output 2b with the feedback stabilization loop turned off in the middle of the measurement.

The purpose of the stabilization loop is made obvious with such a picture. The rms is much worse with an rms value of 288 mrad, and clear variations appear when the loop is turned off. The slow drifts in the CEP noise are most likely due to mechanical fluctuations and airflow inside the system. The origin of the fast CEP fluctuations is however a more open and significant question as it is not possible to compensate for these fluctuations with an active feedback loop. The investigation and the quantification of the CEP noise introduced by the WLG process is the objective of the next two chapters.

3.4 Role of the WLG in the CEP noise

Despite having both active and passive CEP-stabilization the CEP of state-of-the-art OPCPA still exhibits fast phase fluctuations below the hundred-mrad rms range [35, 221, 243] and their origin is still unknown. As a highly nonlinear process in both the generation and characterization steps, supercontinuum generation is likely to be responsible for fast CEP fluctuations. Some experimental work was accomplished to assess the coherence of the supercontinuum generation process by Bellini and Hänsch [131] using spatial interferometry. Some further investigation was conducted in [29] using spectral interferometry. Alongside experimental work, some more recent theoretical work also showed plasma broadening could be responsible for CEP fluctuations [37, 245]. This particular relationship between the supercontinuum generation and the CEP fluctuations is the motivation for chapters 4 and 5.

Chapitre 4

Spectral coherence in filamentation in bulk crystals

4.1 Motivation

As showcased in chapter 3, state-of-the-art CEP-stable OPCPAs exhibit CEP noise down to a level of dozens of mrad. The origin of this phase noise remains an open question and isolating the noise contribution of the different parts of the OPCPA is not trivial. Since CEP is order zero of the phase it is coupled to practically any of the pulse properties such as its energy, spatial profile, or spatial phase. This means that if any of these parameters are fluctuating then the CEP might follow these fluctuations making CEP stability experimentally challenging to achieve. This also implies that sources of energy noise or spatial profile variations will have a direct impact on the CEP noise.

4.1.1 Noise sources in OPCPA

A major source of noise in any OPCPA is the pump laser itself. Naturally, the stability of the pump laser will be degraded by the OPCPA. As the gain in the first amplification stages of an OPCPA is exponential, the energy variations of the pump will greatly impact the energy stability of the OPCPA. The amplified spontaneous emission (ASE) of the pump laser will directly translate on the signal via the CPA. This is especially true for nanosecond OPCPAs. This has been studied for the temporal contrast for example. In [246] the poor temporal contrast of the pump pulse causes fluctuations in the spectral amplitude of the generated signal and also degrades its contrast by generating a ps pedestal. This effect can be seen as the analog to amplified spontaneous emission in lasers (ASE) for the optical parametric amplification process. This was also numerically modeled in [247] where Ross et al. identify three stages of noise. The first stage is the ASE of the pump laser, and the second stage is the transfer of the pump beam noise on the signal beam during parametric amplification. As the signal is chirped in an OPCPA the temporal noise due to ASE is converted into spectral noise. The third stage is the re-compression of the spectral phase transforming the spectral noise into a pedestal around the signal pulse exactly as observed in [246]. Although these two studies show that the pump ASE

is directly transcribed on the signal in some cases optical parametric amplification can mitigate a noisy pump laser by saturating the gain. This was especially observed in gain-saturated fiber-based systems [248-250]. In the case of fiber-based systems, four sources of noise are identified [250]. The first one is amplified quantum noise (AQN) and is fundamental quantum noise resulting from quantum vacuum fluctuations. The second source of noise is Raman phonon-seeded excess noise which comes from the delayed nonlinear response in optical fibers. The third source of noise is pump-transferred noise which turns the pump noise into signal fluctuations instantly in the optical parametric amplification process. The last noise source is residual pump noise resulting from poor filtering of the pump combined with the signal at the input of the amplifier.

As an extremely nonlinear process at the beginning of the amplification chain, supercontinuum generation is another natural suspect as a contributor to the phase noise (section 3.4). Furthermore, WLG is commonly used in the CEP measurement as it is the starting block of f-2f interferometers when the spectrum of the pulse to characterize is not octave-spanning [251]. In the case of OPCPA, the supercontinuum generation is done via filamentation in bulk crystals [36]. In fiber-generated supercontinua, the spectral broadening mechanism is pure SPM [252-254]. CEP stabilization of completely fiber-based sources is commonly realized in the frequency comb community [255-257]. The plasma contribution is the main difference between the continua generated in bulk through filamentation and the fiber-generated supercontinua. This additional spectral broadening mechanism makes the stabilization and compressibility of the supercontinuum more challenging than in the fiber case [100, 258-260].

To look at the CEP-noise specifically, the notion of intrapulse coherence introduced in section 1.3.5 is used. This term is first introduced in [37] where it is used to quantify the coherence of the different spectral components of a single pulse. This particular study focuses on the f-2f interferometry however the conclusions are relevant for the passive CEP-stabilization scheme. It was shown that intrapulse coherence is maintained through spectral broadening when the broadening mechanism is pure SPM but whenever plasma generation is involved the coherence is decreased. The phase fluctuations due to the broadening mechanism were numerically simulated in the f-2f configuration and reached π rms when plasma broadening is the broadening mechanism as illustrated in figure 4.1.

Outside of the f-2f measurement, intrapulse coherence is relevant for passive CEP stabilization. The link is especially clear when considering intrapulse DFG. As presented in section 3.2.3 a possible CEP-stabilization scheme involves difference frequency generation of two spectral components of the same pulse [262-264]. In this case, the intrapulse coherence or lack thereof will have a direct impact on the CEP fluctuations. However, this argument is also true when it comes to interpulse DFG. In the architecture presented in section 3.3 (inline DFG) the driving laser pulse is split into two replicas using one of them to generate a supercontinuum. The intrapulse coherence of the supercontinuum is linked in the same way as it is for f-2f interferometry in this case. The same argument can be made when the DFG geometry is of the Mach-Zehnder type. In this case, however, the CEP fluctuations will also be due to the typical interferometer instabilities such as mechanical vibrations.

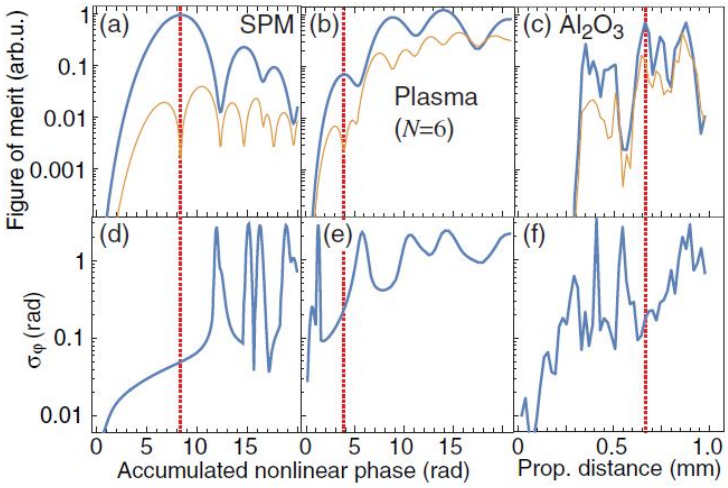

FIGURE 4.1 – Numerical simulations of the intrapulse coherence of supercontinuum pulses. Simulations are based on an ensemble of 1000 input pulses with 10 fs duration and 1% energy standard deviation. (a)–(c) Mean value (thick blue line) and standard deviation (thin orange line) of the FOM. The first maximum of the FOM has been marked by a dashed red line. (d)–(f) Standard deviation of $\Delta\varphi$. (a), (d) Symmetric spectral broadening due to self-phase modulation. (b), (e) Asymmetric spectral broadening due to plasma generation driven by a multiphoton process of the order of 6. (c), (f) Full simulation of nonlinear propagation in sapphire according to [261].

Additionally to the intrapulse coherence one still has to consider the phase noise introduced by the pump and seed pulse recombination in the DFG process [265].

Even though the quantitative link between the shot-to-shot phase noise of the WLG and the CEP noise has not been established yet, a quick preliminary study conducted in appendix E shows similarities between the power spectral densities. The absence of experimental correlation is most likely due to the poor quality of the CEP stabilization in the source used.

The approach employed here is to assess the intrapulse decoherence added by the filamentation process and to compare it with the noise floor of the state-of-the-art CEP-stable systems. This chapter presents a simple experimental setup to measure the spectrally resolved shot-to-shot phase fluctuations of a supercontinuum generated in a bulk crystal. This will be used to measure the stochastic phase noise introduced by the filamentation and to confirm empirical knowledge on the optimal conditions of WLG as well as the ability of different pump lasers to be used as drivers for CEP-stable OPCPA. In the next chapter, a more systematic approach will be employed to study the influence of key parameters on the WLG process and their fluctuations.

4.2 Guidelines for supercontinuum generation

Before getting into the spectral coherence measurements, this section introduces guidelines and general properties of supercontinua generated in bulk crystals. The principle of filamentation and the mechanisms at play are described in section 1.3.5. The spectral broadening is

mainly caused by two phenomena. The first one is self-phase modulation (section1.3.4) causing symmetrical spectral broadening and is the main contribution to the generation of the infrared part of the spectrum. When the power is above the critical power P_{crit} the crystal is ionized creating a plasma (section1.3.5) and generating the blue edge of the supercontinuum. The filament structure is created by the balance of the self-focusing and plasma defocusing occurring above the critical power. Filamentation has been extensively studied both experimentally and theoretically [36, 100, 101, 261, 266-269]. Most of these studies are experimental especially when the filamentation takes place in bulk due to the complexity of the simulation.

4.2.1 Experimental conditions for generation

This study is limited to the generation of a supercontinuum used for Yb :YAG driven OPCPAs. The energy level is of the order of the μJ to the dozen of μJ with a YAG crystal about a dozen mm in length [35, 243]. This section takes a look at the spectral shape of the generated WL as a function of the pulse energy and the crystal position. Numerical aperture will not be covered here, as it was done extensively by Anne-Laure Calendron et al. in [266]. They showed that the optimal numerical aperture to reach the broadest spectrum is obtained for a numerical aperture of 0.015 which will be the one used here. They tried numerical apertures ranging from 0.015 to 0.3 showing that the bandwidth of the visible side of the supercontinuum is mostly unaffected while the infrared broadens with decreasing NA.

The driving laser is a regenerative Yb :YAG CPA system (Pharos PH1-SP-1mJ) from Light-Conversion. It was described in section 2.3. It delivers 180 fs Fourier Transform Limit (FTL) pulses with a central wavelength of 1034 nm. The operating frequency can be tuned from 1 kHz to 1 MHz with a maximum average power of 6 W. In this experiment, the frequency was set at 1 kHz with a pulse energy of 1 mJ. The beam quality is excellent with an M^2 value of 1.1. A compressor can be used to adjust the laser chirp. 9 μJ are sampled from the available pump laser energy. The setup used for the characterization is shown in figure 4.2.

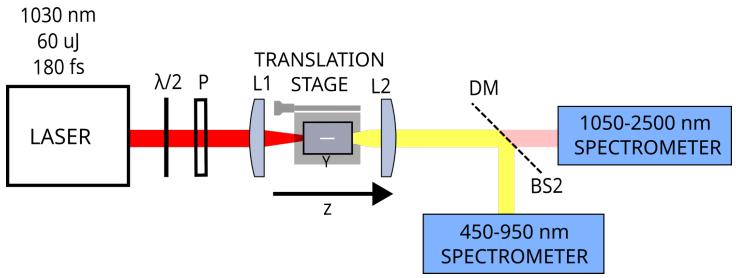

FIGURE 4.2 – Diagram of the WLG characterization setup. The z-axis is indicated below the YAG crystal. The origin of the axis is defined when the interface of the YAG crystal is placed at the driving beam waist. z is negative if the crystal is placed before the beam waist and positive after.

4.2.2 Spectral shape as a function of crystal position and pulse energy

Moving the YAG crystal along the beam propagation direction (z) around the focal point has a strong effect on the spectral shape of the supercontinuum.

Let us first take a look at the intensity dependence of the spectrum in two particular cases.

z = -1.5 mm

The first one is when the input face of the YAG is placed slightly before the focal point of the driving pulse ($z = -1.5\,\text{mm}$).

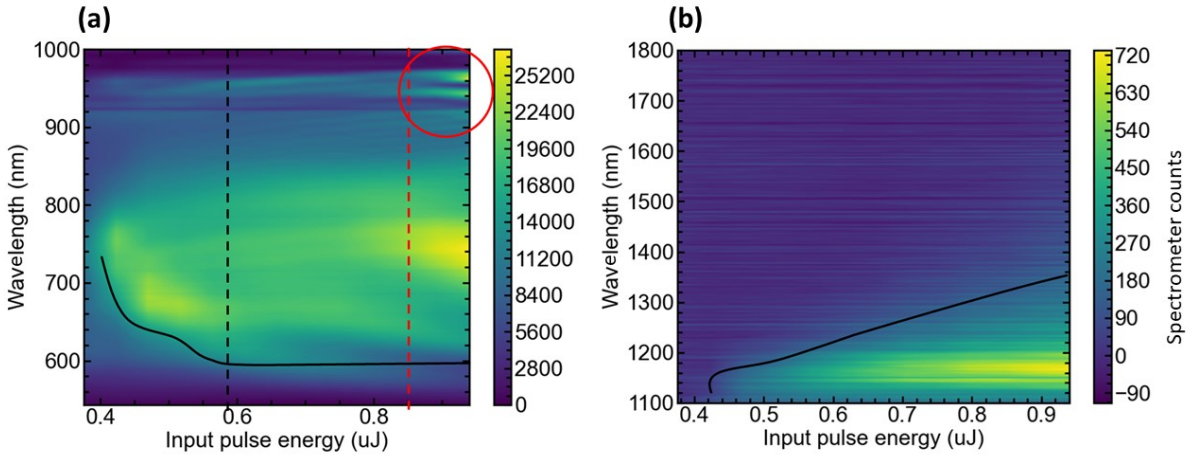

FIGURE 4.3 – (a) : Colormap of the WLG spectra as a function of pulse energy when the input interface of the YAG crystal is before the beam waist ($z = -1.5\,\text{mm}$) in the short-wavelength range. The color bar is in spectrometer counts. The continuous black line shows the spectral broadening by following the low wavelength edge of the continuum as a function of energy. The black vertical dotted line shows the energy at which the broadening stops. The red vertical dotted line shows the double filamentation threshold. The red circle shows the interference between the two filaments after the onset of double filamentation. (b) : Colormap of the WLG spectra as a function of pulse energy when the input interface of the YAG crystal is before the beam waist ($z = -1.5\,\text{mm}$) in the long-wavelength range. The color bar is in spectrometer counts. The continuous black line shows the spectral broadening by following the high wavelength edge of the continuum as a function of energy.

Figure 4.3 (a) shows a colormap of the acquired spectra in the short wavelength range as a function of energy in this configuration. The first thing that comes to light is the critical power. The spectral broadening only appears after this threshold ($0.4\,\mu$J). It is visible in the plot at the start of the black line that indicates the low wavelength edge of the spectrum as a function of energy. It is distinguishable from pure SPM as the spectral broadening is not decreasing from the pump laser wavelength but shows a maximum in this case around 750 nm. One can also see in this plot the onset of double filamentation as indicated by the red vertical line. Double filamentation happens when a second filament is generated after the first one in the propagation direction. When the pulse energy reaches a second threshold ($2 * P_{crit}$) [101], the remaining intensity after the first filament is strong enough to cause a second Kerr focus and ionize the

YAG again generating a second filament. This threshold is easy to detect as the temporal delay between the two filaments creates interferences, as indicated in the red circle. In between these energies, two different regions are identified (separated by the black dotted line). In the lower energy one, energy increase leads to a significant broadening of the supercontinuum. In the higher energy one, the spectral shape remains unchanged with added pulse energy. To obtain the broadest spectrum and the highest amount of energy in the supercontinuum the optimal working conditions are with an energy just below the double filamentation threshold. Figure 4.3 (b) shows a similar colormap for the long-wavelength range. Contrary to the other side of the continuum, only SPM is responsible for the broadening on this side. Here again, the black line shows the amount of broadening by following the long wavelength edge of the continuum as a function of energy. In this case, the spectrum only shows monotonous decreasing in power with increasing in wavelength as would be expected from pure SPM broadening.

z = 1.5 mm

Let us now take a look at the second position of the YAG crystal. Figures 4.4 (a) and 4.4 (b) show similar colormaps when the YAG is placed after the beam focus ($z = 1.5\,\mathrm{mm}$).

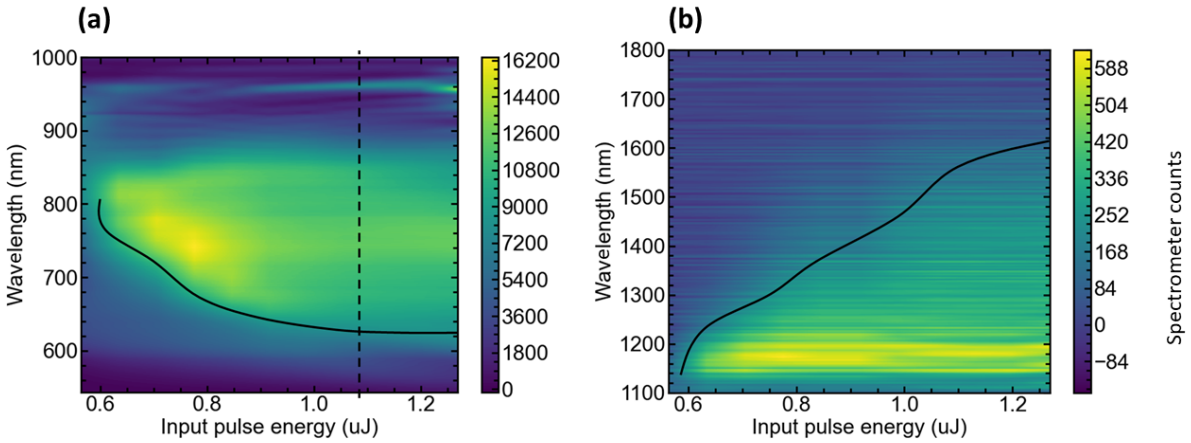

FIGURE 4.4 – (a) : Colormap of the WLG spectra as a function of pulse energy when the input interface of the YAG crystal is after the beam waist ($z = 1.5\,\mathrm{mm}$) in the short-wavelength range. The color bar is in spectrometer counts. The continuous black line shows the spectral broadening by following the low wavelength edge of the continuum as a function of energy. The black vertical dotted line shows the energy at which the broadening stops. (b) : Colormap of the WLG spectra as a function of pulse energy when the input interface of the YAG crystal is after the beam waist ($z = 1.5\,\mathrm{mm}$) in the long-wavelength range. The color bar is in spectrometer counts. The continuous black line shows the spectral broadening by following the high wavelength edge of the continuum as a function of energy.

In this second configuration, the behavior is qualitatively the same with the onset of filamentation around $0.6\,\mu$J, and the increase of broadening with energy. The broadening stops at the energy of $1.1\,\mu$J which is significantly higher than in the previous case. The double filamentation is however not visible here. The main difference is the broadening of the infrared part

of the continuum. It reaches 1650 nm at its broadest against 1400 nm in the previous configuration. On the other side of the spectrum, however, the broadening is lesser and requires more energy for a similar result. This second configuration seems more appropriate to generate the IR part of the spectrum and the previous one is more suitable for the visible side.

z = -3, 0 and 3 mm

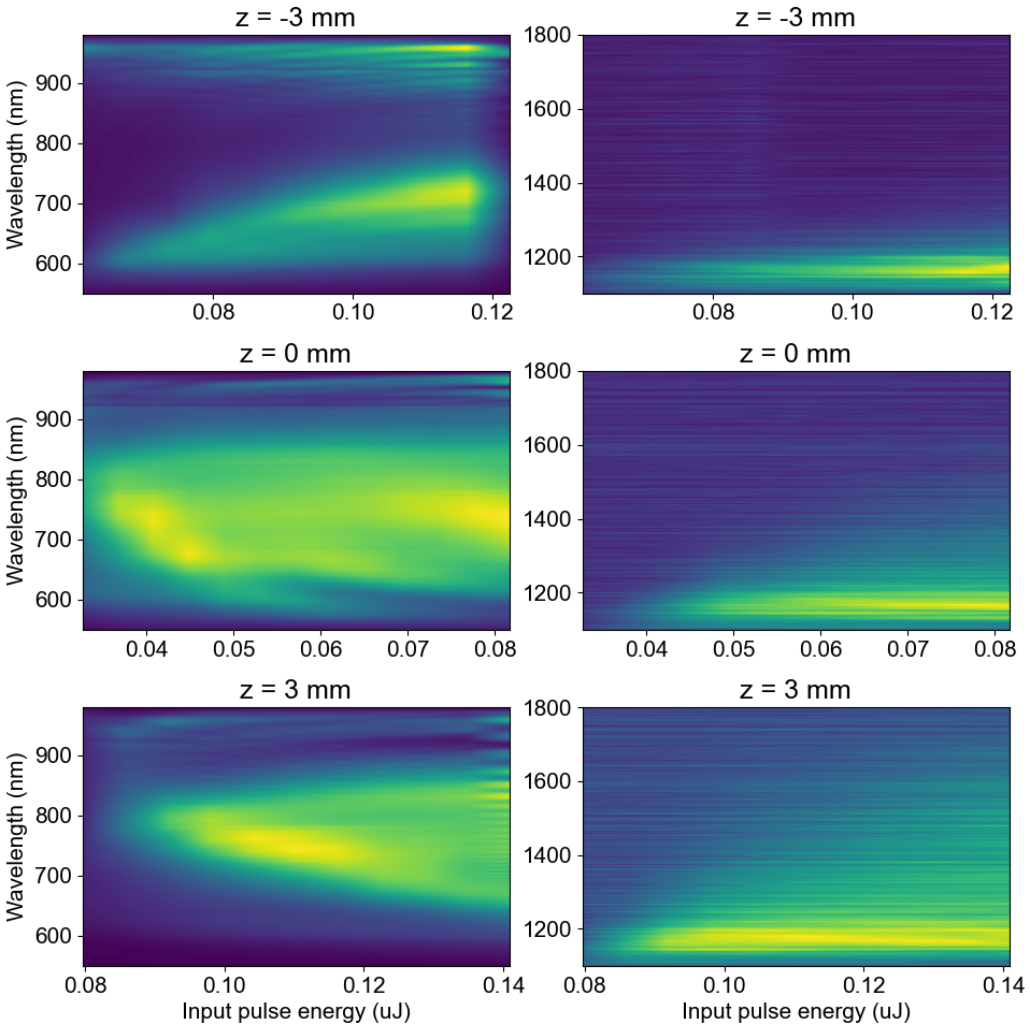

FIGURE 4.5 – Colormap of the WLG spectra as a function of pulse energy at three different crystal positions (z = -3, 0 and 3 mm) in both wavelength ranges.

Figure 4.5 shows colormaps at additional positions for both sides of the supercontinuum. The spectral shape heavily depends on the crystal z position. For the long wavelength range, the dependence is the most obvious. The broadening is indeed much more pronounced if the crystal is placed after the beam waist ($z > 0$ mm). This is due to geometric reasons. If the YAG crystal is placed after the driving beam waist, the beam is defocusing when entering the crystal. In this configuration, the resulting filament will be longer. As the infrared side of the supercontinuum is driven purely by SPM, increasing the size of the filament increases the amount of

SPM and thus spectral broadening. The short-wavelength range offers more flexibility, as the plasma broadening is always present. The visible side of the supercontinuum is caused by plasma generation mostly, thus not as affected by the focusing geometry. Plasma generation happens as long as the power is above P_{crit}. The spectral intensity is however different for different crystal positions. Placing the crystal far before the focal point gives a very structured spectrum with a maximum in the higher energy part of the spectrum (around 650 nm) but almost no energy conversion to the 700-900 nm region. On the contrary, placing the YAG crystal at the beam waist (z=0 mm) gives a flat spectrum on the whole 600-950 nm spectral range. Placing the crystal after the beam waist (z=3 mm) gives yet another different result. The spectrum is not as structured as with z=3 mm but also not as broad as with z=0 mm (cut-off wavelength around 580 nm) with a cut-off wavelength at the double filamentation threshold of 600 nm.

This study shows that optimizing the crystal position for the short wavelengths and for the long ones is contradictory. Two optimal positions are identified : at z = -1.5 mm the generation is more favorable to a broad and flat visible part of the spectrum ; at z = 1.5 mm the generation is more favorable to a broad infrared spectrum. In both cases, the energy is optimal just below the double filamentation threshold to achieve the broadest and most intense supercontinuum.

4.3 Spectral coherence measurement : double WL interferometer

The objective consists in measuring the spectral coherence of the supercontinuum generation via filamentation in bulk YAG crystal. To measure coherence a phase measurement is necessary. To measure the shot-to-shot phase fluctuations over the full spectral bandwidth a double white light interferometer is used. The interferometer is a variant of the Bellini-Hänsch interferometer [131] where a similar interferometer is presented. It was pioneering work on the study of the coherence of the supercontinuum generation process. Bellini and Hänsch showed via spatial interferometry between two supercontinua that coherence is maintained through filamentation and showed the dispersion properties of the generated white lights. This work is also similar to the interferometer presented in [29] where Baltuska et al. studied spectral interference between the remaining pump of a supercontinuum and a reference. Their work identified an energy region ideal for f-2f interferometry as shown in figure 4.6. As expected by the experimental knowledge the region labeled 'stable single filament' is where the energy is above the onset of single filamentation and below the onset of double filamentation labeled 'breakdown of single filament'.

This thesis combines both ideas and presents a similar interferometer where the phase measurement is quantitative and spectrally resolved over the whole supercontinuum bandwidth. Figure 4.7 shows a diagram of the interferometer.

The interferometer has a Mach-Zehnder geometry with two identical arms. The relative delay between the two arms τ is controlled via a manual reflective delay line. Each arm includes a half wave-plate and a polarizer to control the pulse energies independently. Two f=150 mm lenses focus the beam inside 6 mm long YAG crystals. The NA of the beam is 0.015, as indicated above. A pair of f=50 mm achromatic lenses collimate the supercontinua. After the second

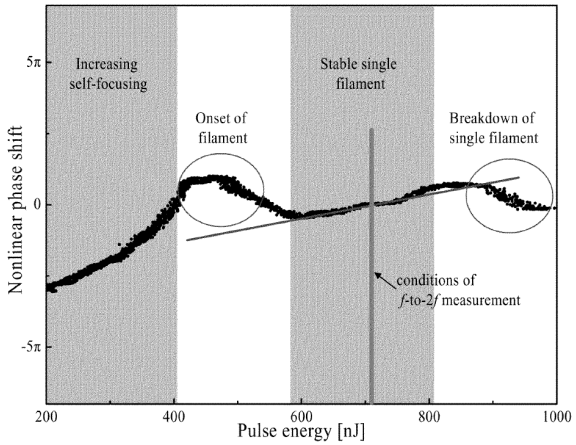

FIGURE 4.6 – Figure from [29] coupling of the white-light generation in bulk sapphire. Solid dots depict phase changes extracted from single-shot interferograms. The straight line shows a linear fit marking the slope of phase intensity-dependent variation in the vicinity of the pulse energy used for f-to-2f characterization.

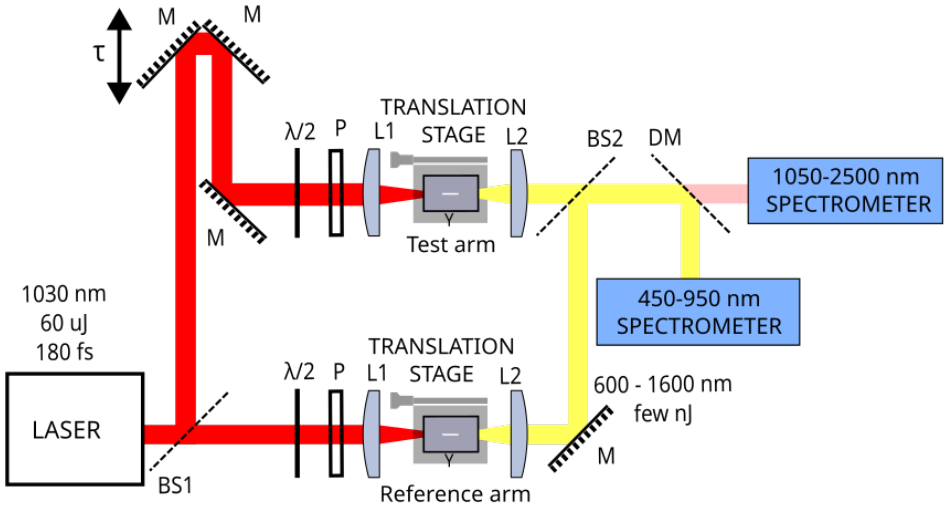

FIGURE 4.7 – Diagram of the double white light interferometer. BS1 : 50/50 beam splitter at 1030 nm, M : mirror, $\lambda/2$: half wave-plate, P : polarizer, L1 : 150 mm BK7 focusing lens, Y : YAG crystal, L2 : 50 mm achromatic collimating lens, BS2 : 500-1700 nm 50/50 beam splitter, DM : 950 nm long-pass dichroic mirror.

beam splitter BS2 (500-1700 nm) recombines the two beams they are split into two different spectrometers using a 950 nm long-pass dichroic mirror. The short-wavelength range is defined by the lower bound of the operating bandwidth of BS2 and by the cutoff wavelength of DM (figure 4.7) which are 500 and 950 nm respectively. The long-wavelength range is defined by the cutoff wavelength of the silicon filter used to remove the driving beam from the supercontinuum (1100 nm) and by the signal level on the spectrometer. It is numerically set to keep a fringe contrast above 1% of the maximum contrast. The short wavelength range is sent to a Si spectrometer (resolution of 0.26 nm, integration time of 1.1 ms) and the long wavelength range (1100-1700 nm) is sent to an InGaAs spectrometer (resolution of 3.27 nm, integration time

of 1 ms). With an appropriate group delay τ between the two arms (around 300 fs) the spectrometers show spectral fringes (figure 4.10). The value of τ is chosen to reach a fringe spacing of 15 nm which gives 60 sampling points per fringe period with the spectrometer resolution in the short-wavelength range. The phase of these spectral fringes is the phase difference between the test and the reference arm. The relative phase stability is studied by acquiring 1000 consecutive single-shot spectra and extracting the phase via an FTSI algorithm, as explained in the next sections.

4.4 Phase retrieval algorithm and intrinsic setup stability

The setup is first characterized without any nonlinear effect. This is done by removing the YAG crystals and replacing the spectrometers by a spectrometer around 1035 nm (resolution of 0.24 nm and integration time of 1 ms). This simpler case will be used to present the phase retrieval and data processing algorithms which follow the algorithm explained in section 1.2.2. Figure 4.8 (a) shows a typical interference spectrum acquired in this configuration. As the spectral bandwidth of the pump laser is much narrower than the one of the supercontinuum the temporal delay is increased to 1.5 ps. The inverse Fourier transform of the spectrum in figure 4.8 (a) yields the temporal signal depicted in figure 4.8 (b).

As expected from section 1.2.2, the inverse Fourier transform yields three components. At delay zero is the sum of the two fundamental terms and two interferometric terms are found at delays $+/-\tau$. The component at delay $+\tau$ is numerically selected and Fourier transformed back to the frequency domain. The spectral amplitude and phase of the resulting signal are displayed in figure 4.8 (c).

The spectral amplitude corresponds to the envelope of the fringes acquired in figure 4.8 (a). The spectral phase is the phase of the fringes acquired in 4.8 (a). The slope is the relative delay.

All these steps are now repeated for an acquisition over 1000 consecutive laser shots and the spectrogram and extracted phase as a function of acquisition time at two different wavelengths are plotted in figure 4.9 (a) and (b).

Without any nonlinear effect, the noise of the interferometer itself is characterized. The origin of this noise is the shot-to-shot variation of the optical delay difference caused by mechanical vibrations for instance. Figure 4.9 (c) shows the spectrally resolved standard deviation of the noise extracted from the spectrogram in figure 4.9 (a). This quantity is used throughout this work as a metric to quantify phase noise measured by this interferometer. The order of magnitude for the phase noise measured in this case is below 6 mrad on the whole spectrum of the driving laser. This is the same order of magnitude obtained when taking a single spectrum and adding 1000 shots of random background noise. This shows that the interferometer's intrinsic stability is close to the detection threshold of the spectrometer. This also explains the shape of the measured noise which is simply inversely proportional to the spectral intensity of the driving laser and hence inversely proportional to the signal-to-noise ratio. This measurement gives a ground stability level for forthcoming WLG measurements. This will be used as

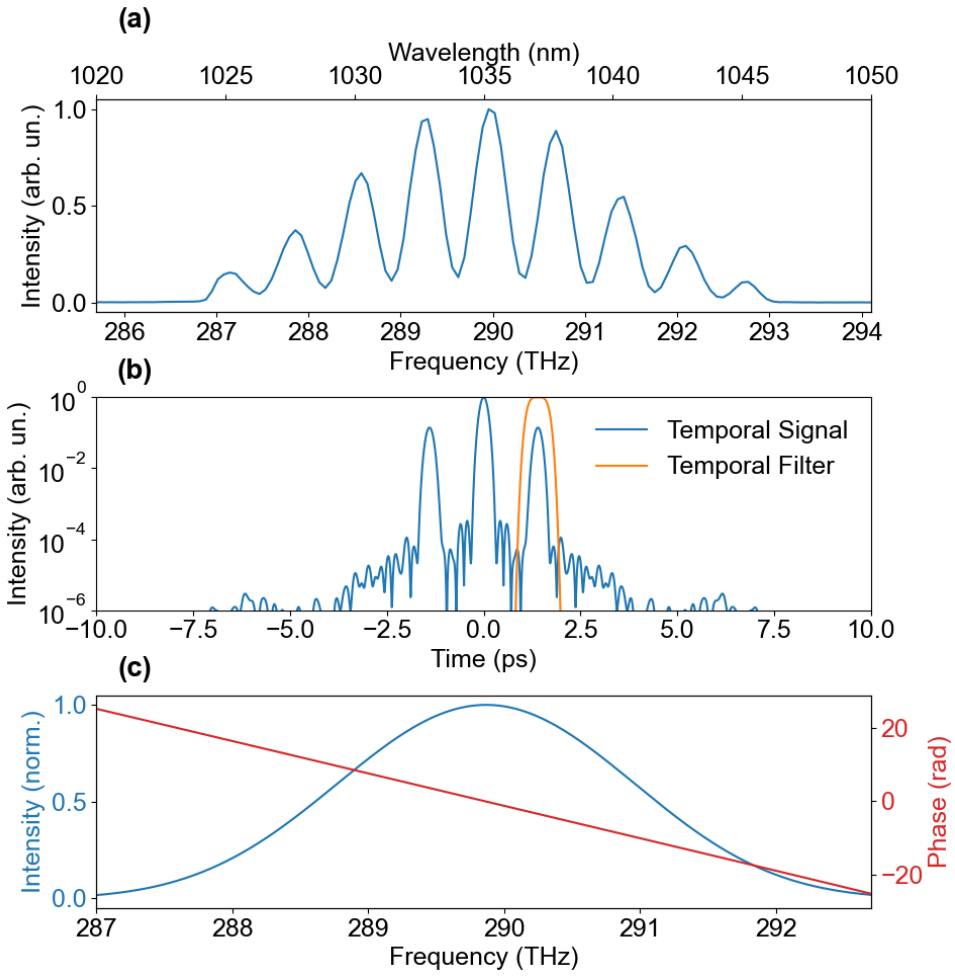

FIGURE 4.8 – (a) : interference spectrum of the pump laser with a wavelength axis and frequency axis. (b) : temporal signal computed with inverse Fourier transform. The orange curve shows the Hypergaussian temporal filter used to filter one of the delayed components. (c) : spectral amplitude of the Fourier transform (blue) and spectral phase of the Fourier transform (red) with a slope of 1.5 ps.

a reference value throughout the next measurements and gives us the ground stability of the interferometer itself.

4.5 Balanced setup stability

After this preliminary setup characterization, the same measurement can be reproduced with the WLG in each arm of the interferometer. Although the generation conditions in both arms are made identical by directly looking at the filament position in the YAG crystal and looking at the spectrum shape, obtaining perfectly identical spectra is not possible because of the recombining beam-splitter imperfections. As a consequence, two indistinguishable contributions to the phase noise are measured. On the one hand, the two arms cannot be made perfectly identical making the pump laser instability not perfectly identical in each arm. On the

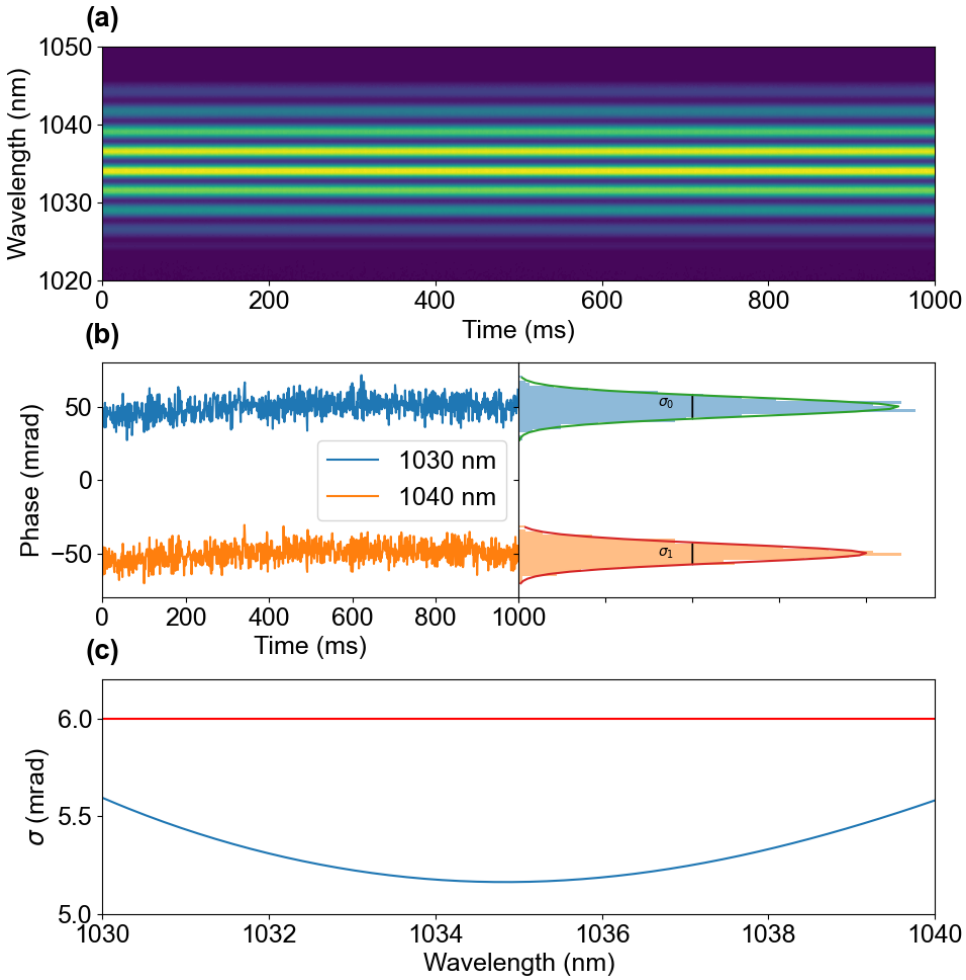

FIGURE 4.9 – (a) : Spectrogram over 1000 laser shots without the YAG crystals. (b) : Extracted spectral phase at 1030 nm and 1040 nm in blue and orange respectively in the left part of the plot. The right part shows a histogram of the phase values for both wavelengths with a Gaussian fit. The standard deviations σ_0 (σ_1 respectively) are displayed in the fit. (c) : Standard deviation of the spectral phase with no nonlinear effect. The red line is the 6 mrad threshold used as interferometer intrinsic stability.

other hand, the purely stochastic fluctuations added by the supercontinuum process itself are also measured.

Two crystal positions were identified in section 4.2 : z = -1.5 mm and z = 1.5 mm to give the broadest and flattest visible and infrared spectrum respectively.

In the first one the YAG crystals are placed at z = -1.5 mm and the energy is set just below the double filamentation threshold.

4.5.1 z = -1.5 mm

Figures 4.10 (a) and 4.10 (b) show a spectrogram in the short-wavelength range and long-wavelength range respectively.

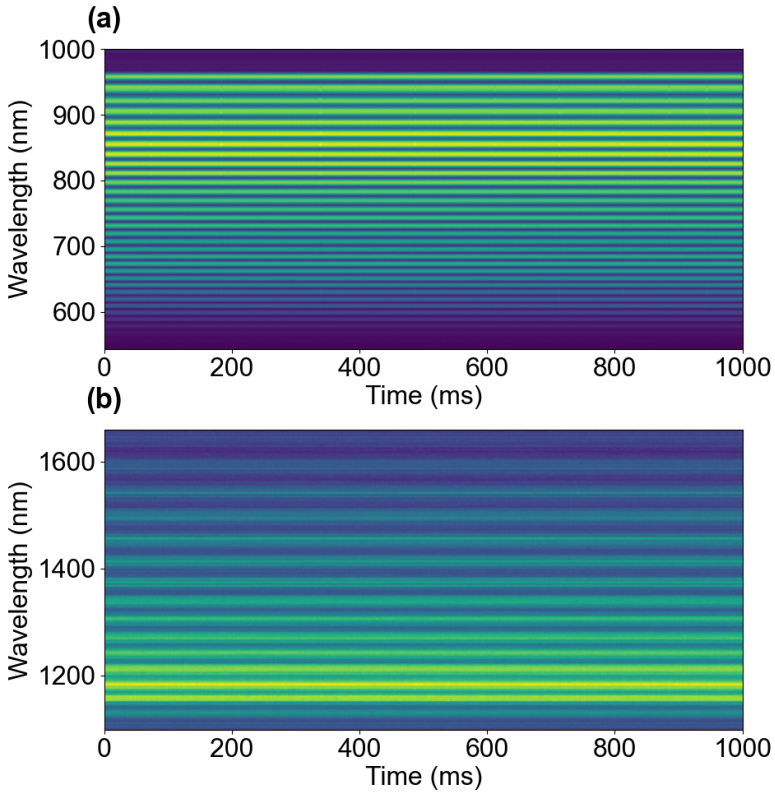

FIGURE 4.10 – Spectrograms in the short-wavelength range (a) and long-wavelength range (b) over 1000 single shot acquisitions when the WLG is optimized for the short-wavelength range.

An additional step is added to the data processing here. The slow phase drifts below the frequency of 5 Hz are numerically filtered out. This is motivated by the presence of an active feedback loop in most CEP stable systems. The 5 Hz threshold is typically slower than the response time of the CEP feedback loops.

As expected, the slow phase drift present in the unfiltered phase is removed by numerical filtering. This allows the study to focus on the shot-to-shot CEP fluctuations or two-sample Allan variance [270] which can not be compensated by a feedback loop. The spectrally resolved standard deviation of the phase for the two wavelength ranges is plotted in this case in figure 4.11.

The first information to extract from this figure is that the phase noise level always stays above the interferometer intrinsic noise of 6 mrad and spans from 35 mrad at 640 nm to 8 mrad at 950 nm which is not a significant increase of the phase noise. This shows that the WLG process alone contributes to the decrease of intrapulse coherence. In both wavelength ranges the wavelengths further from the pump wavelength exhibit a higher phase noise. This is intuitive as the further away from the pump, the more accumulated nonlinear phase. The effect of high-pass filtering is showcased here, as the unfiltered beam in the short-wavelength range has a noise figure twice as high as the filtered one. Its impact is almost zero in the other wavelength range.

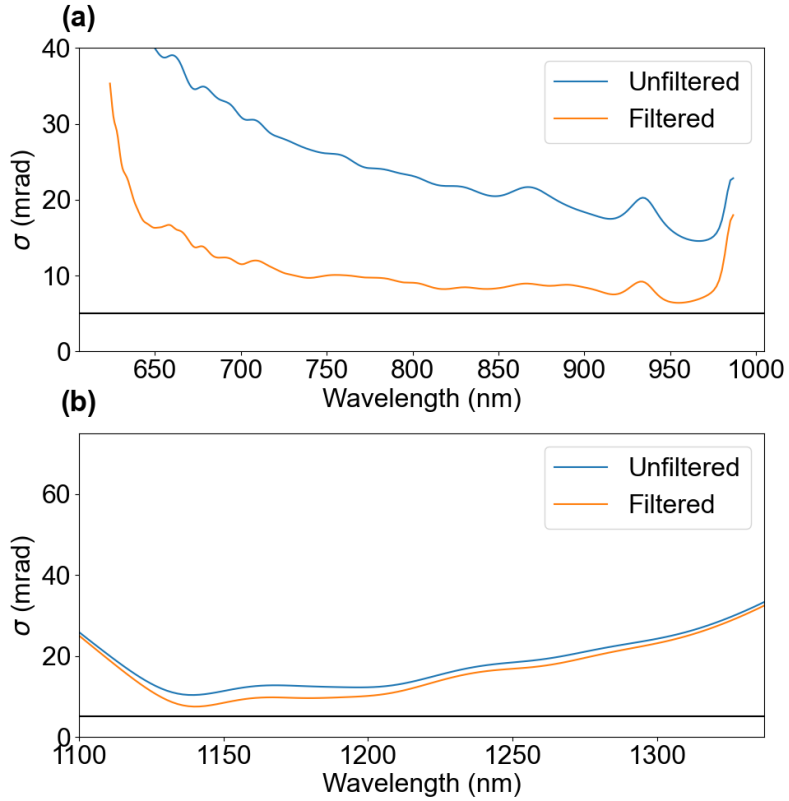

FIGURE 4.11 – Standard deviation of the phase with a YAG crystal placed slightly before the beam waist in the short-wavelength range (a) and long-wavelength range (b) for z = -1.5 mm. The blue lines are the standard deviations computed from the directly extracted phase and the orange ones with the additional step of high-pass filtering. The horizontal black line is the 6 mrad intrinsic interferometer stability.

4.5.2 z = 1.5 mm

The same measurement can be done with an optimization for the IR side of the WL. In this case, the YAG crystal is placed slightly after the pump beam focal point. The results are shown in figure 4.12.

The quantitative behavior is the same as in the previous configuration. The noise increases as the wavelength gets further away from the pump laser wavelength. In the short-wavelength range, the standard deviation is of the same order of magnitude as before although it is slightly lower. In the long-wavelength range, however, the behavior is opposite. The phase noise is lower in this configuration and as expected from 4.2 the spectrum is much wider. It cuts off around 1700 nm whereas it cuts off at 1350 nm in the previous configuration. Contrary to the previous case frequency filtering reduces the noise by a factor of 2 in both spectral ranges.

These first balanced results give a reference value for the stability of the WLG process. In both configurations explored so far the phase noise stays below 20 mrad for most of the spectral range. This will be used as a reference value for all the next measurements in chapter 5 and in section 4.6. Table 4.1 presents the minimal phase jitter obtained in both configurations presented in section 4.5 and compares it to the interferometer stability.

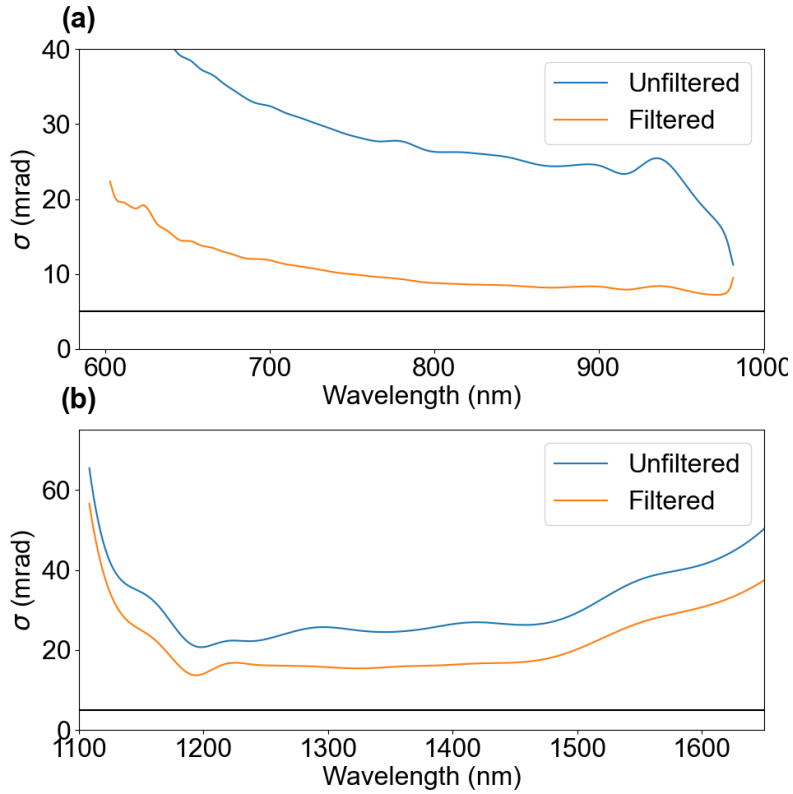

FIGURE 4.12 – Standard deviation of the phase with a YAG crystal placed slightly after the beam waist in the short-wavelength range (a) and long-wavelength range (b) for z = 1.5 mm. The blue lines are the standard deviations computed from the directly extracted phase and the orange ones with the additional step of high-pass filtering. The horizontal black line is the 6 mrad intrinsic interferometer stability.

All the results showed up to this point were acquired using the Pharos PH1-SP-1mJ as a pump laser showing a minor increase of the stochastic phase noise (20 mrad) compared to the intrinsic noise value of the interferometer (6 mrad). This value is expected to depend on the characteristics of the pump laser (energy stability or beam quality for example). Using a different driving laser should however affect the noise level measured by the interferometer. The next section takes a look at the results obtained using different driving lasers.

4.6 Comparison of different pump lasers

This section puts the previous results in perspective by taking a look at different pump lasers to run the same experiment. Three additional pump lasers with a pulse duration of around 1 ps are used : Amphos®3102, Trumpf Scientific Lasers®(TSL) DIRA200-1, and TSL DIRA500-10. These pump lasers were destined for OPCPAs in the groups of Nirit Dudovich at the Weizmann Institute of Science, the group of Paul Corkum at the National Research Council, and the group of Albert Stolow at the National Research Council respectively. The Amphos®3102 was

	Pump	VIS	IR
Interferometer	5 mrad	NA	NA
z = -1.5 mm	NA	6 mrad	8 mrad
z = 1.5 mm	NA	8 mrad	14 mrad

TABLE 4.1 – Minimal phase jitter in both configurations and wavelength ranges compared to the interferometer stability.

characterized in Faslite and both TSL lasers were characterized in the National Research Council of Ottawa. As the repetition rate of all these pump lasers is above 1 kHz, the data acquisition scheme is not simply a commercial spectrometer but the homemade (by me) one presented in appendix B (resolution of 0.3 nm). As the short-wavelength range generally shows higher noise values and more precise results, the infrared part of the continuum is ignored for now. Table 4.2 gives the relevant parameters of the studied pump lasers. As the pulse duration of these three pump lasers is similar so are the conditions of the WLG, which justifies studying them together. Unfortunately, the technologies used in the pump lasers are proprietary and can not be discussed here.

Laser	3102	DIRA500	DIRA200
Rep. rate (kHz)	50	10	1
Energy (mJ)	4	50	200
Power (W)	200	500	200
Duration (fs)	800	900	800
M^2	<1.3	<1.33	<1.41
Energy stability (%)	<1	<0.3	<0.3

TABLE 4.2 – Characteristics of the different pump lasers.

In this whole section, the setup used to characterize the different lasers is the same as presented in section 4.3. Due to the longer pulse duration, the filamentation threshold is higher (around 10 μJ with the same NA). This is expected to change the filamentation dynamics and influence the noise figure. One of the reasons for this is the transition from multi-photon ionization (under 500 fs) to avalanche ionization (above 500 fs) as explained in [266]. A simple filtering of the spatial profile of the beam through an aperture was also added to improve the stability of the WLG. The purpose of this section is to compare the optimal performance of each pump laser and try to find a correlation between the noise floor and the characteristics of the different lasers. In this context, only the best results obtained with each laser will be displayed here. The different lasers will be presented in order of pulse energy, starting with the 3102.

4.6.1 Amphos®3102

The 3102 has an average power of 200 W and power stability of 1% rms measured over 8 hours. The pulse energy is 4 mJ with a repetition rate of 50 kHz. The shot-to-shot energy stability is below 2% measured over 1000 laser shots. The pulse duration is 800 fs with a central wavelength of 1030 nm and a bandwidth of 1.8 nm. The spatial properties of the beam are as follows : the M^2 value of the beam is below 1.3 for a beam diameter of 5 mm at $1/e^2$. Figure 4.13 shows the spectrum of a WL generated in this configuration.

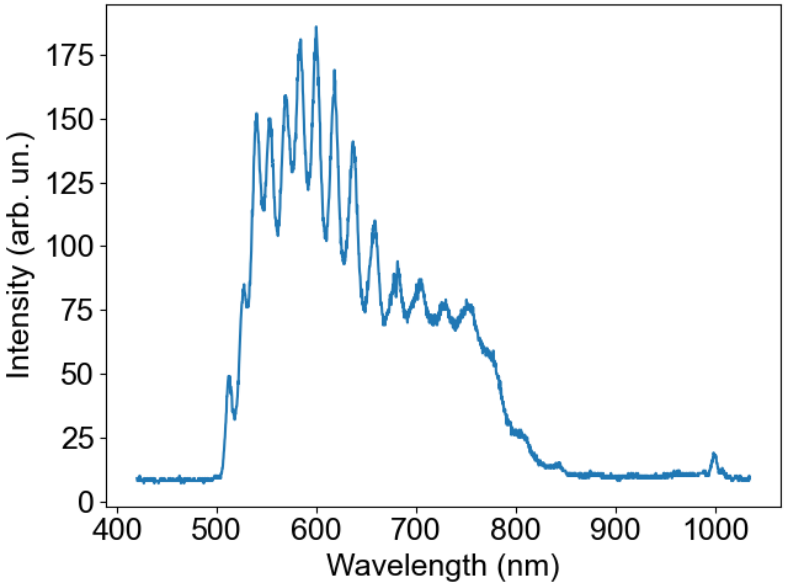

FIGURE 4.13 – Spectrum of a WL generated with the 3102 pump laser.

The shape of this spectrum shows some differences compared to the ones in the previous section. The first thing to notice is the complete absence of light in the 800 to 950 nm region. The lower wavelength part of the spectrum is more intense and starts at 500 nm. The lower wavelength cutoff will be observed in all the lasers with a pulse duration of around 1 ps.

Figure 4.14 shows the interference spectrogram and the associated phase noise.

The noise of the 3102 is always above the 20 mrad reference with a value of around 40 mrad over most of the measured spectral range. There is also no increase in the noise as the wavelength gets lower. Instead, the noise has a minimum at the wavelength of 690 nm. The shape of the noise curve might simply be explained by the shape of the spectrum. It could be a decrease of the SNR causing the higher noise in the 750-800 nm region.

4.6.2 TSL DIRA500

The second pump laser studied here is the DIRA 500 from TSL. The average power is 500 W for a pulse energy of 50 mJ and a repetition rate of 10 kHz. The beam has an M^2 value below 1.5. Figure 4.15 shows the spectrum of a WL generated in this configuration.

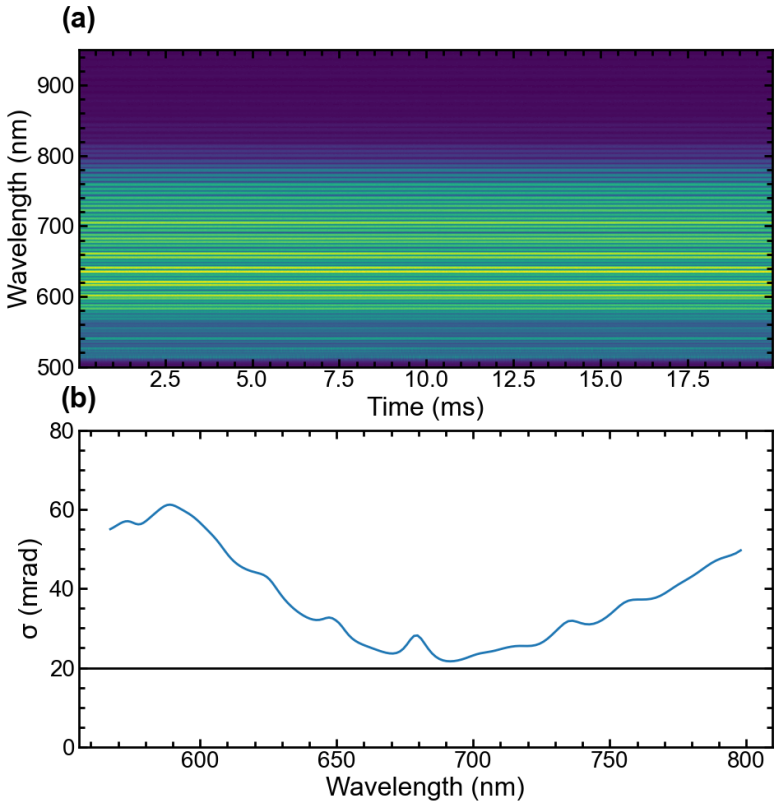

FIGURE 4.14 – Spectrogram acquired with the Amphos®3102 laser (a) and the associated phase noise (b). The black line is the reference stability of the Pharos laser at 20 mrad rms.

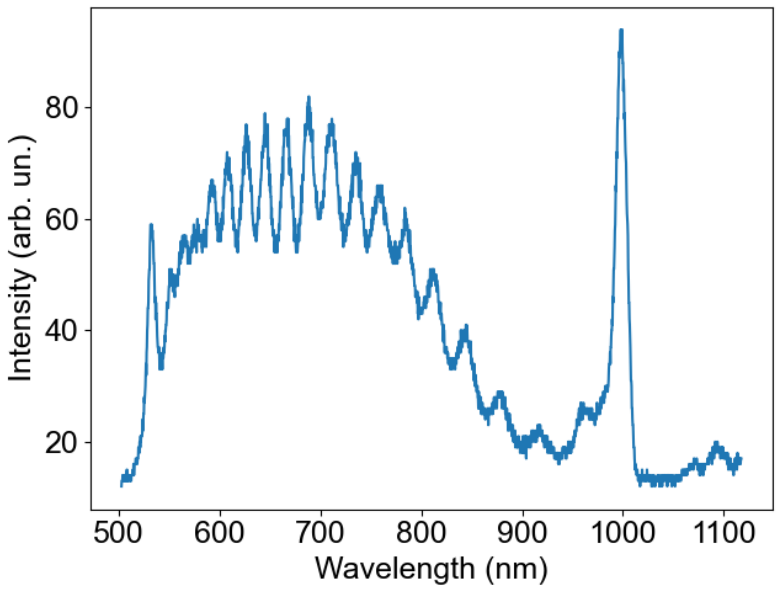

FIGURE 4.15 – Spectrum of a single WL generated with the DIRA500 pump laser.

In this case, again the intensity of the continuum is not flat and the same gap around 850 nm is present, although not as pronounced as in the previous case. The strong peak at 1 μm wavelength is caused by some residual light from the fundamental beam transmitted inside the

spectrometer. Figure 4.16 shows the interference spectrogram and the associated phase noise.

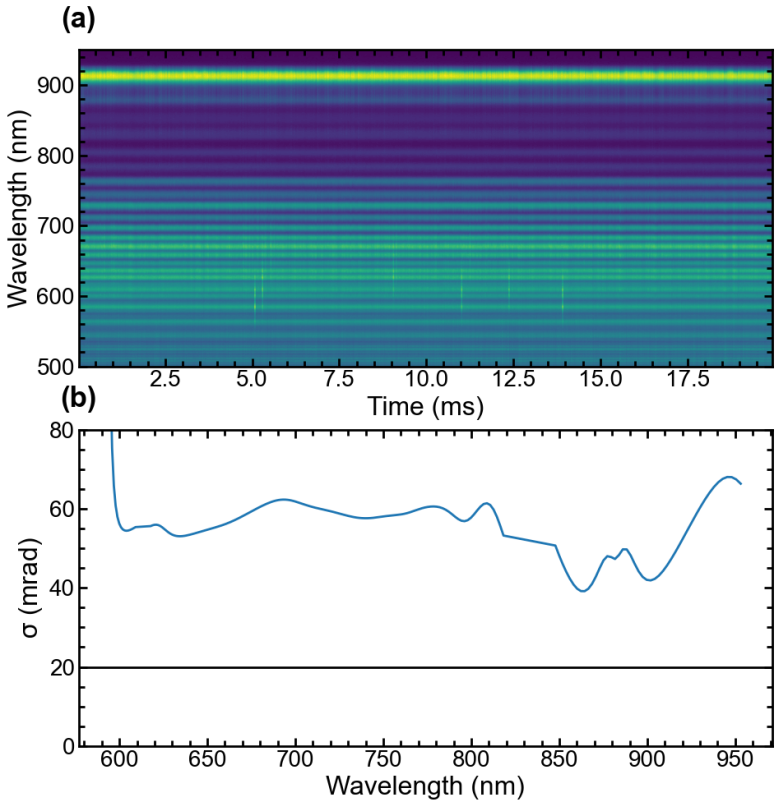

FIGURE 4.16 – Spectrogram acquired with the DIRA500 laser (a) and the associated phase noise (b). The black line is the reference stability of the Pharos-driven WLG at 20 mrad rms.

The phase noise, in this case, is once more slightly above the previous two cases (Pharos at 20 mrad, 3102 at 40 mrad) with a value close to 60 mrad on the measured spectral range. Contrary to the 3102 case, the noise curve is mostly flat as a function of wavelength.

4.6.3 TSL DIRA200

The third pump laser studied here is the DIRA 200 from TSL. The average power is 200 W for a pulse energy of 200 mJ and a repetition rate of 1 kHz. The beam has an M^2 value below 1.5.

Although basic filtering through an aperture improves the shot-to-shot phase stability of the WLG, far-field spatial filtering was used in this case to achieve the best results. The beam was propagated through a telescope with a magnification of 1 (two f=50 mm lenses). An 80 μm diameter pinhole was inserted at the focal point of the telescope. Figure 4.17 shows the spectrum of a WL generated in this configuration.

This continuum has a similar spectral shape to the one generated with the 3102. There is almost no energy conversion above 800 nm and the cut-off wavelength in the lower wavelength part is around 500 nm. Figure 4.18 shows the interference spectrogram and the associated phase noise.

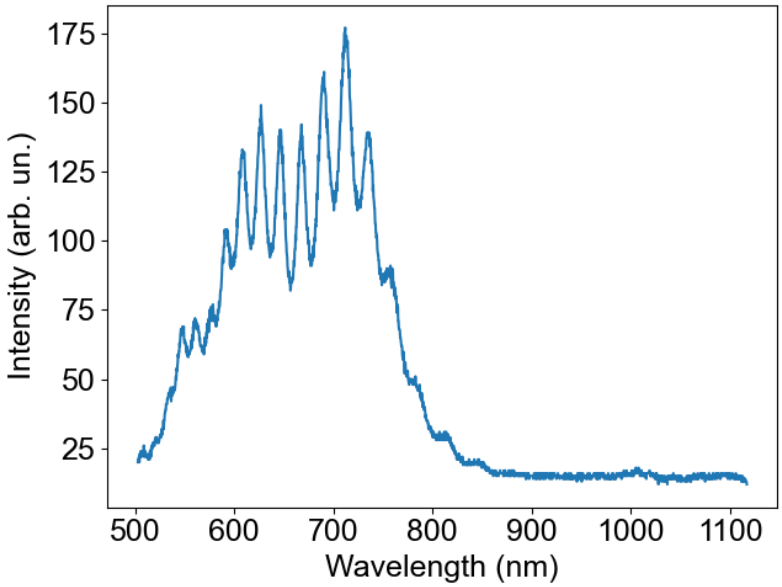

FIGURE 4.17 – Spectrum of a single WL generated with the DIRA200 pump laser.

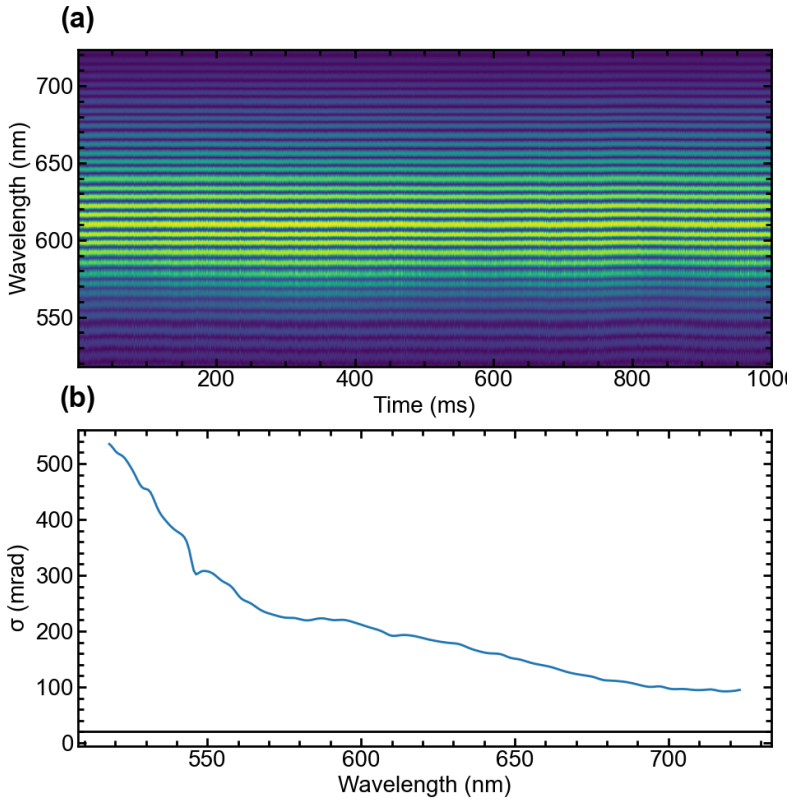

FIGURE 4.18 – Spectrogram acquired with the DIRA200 laser (a) and the associated phase noise (b). The black line is the reference stability of the Pharos laser at 20 mrad rms.

The phase noise is clearly above all the other lasers. The noise is in this case always above 100 mrad rms. The increase of the phase noise with decreasing wavelength is also present here.

4.6.4 Discussion

To get a better idea of the comparison of the phase noise of each pump laser, figure 4.19 shows the phase noise of all pump lasers in the same spectral range.

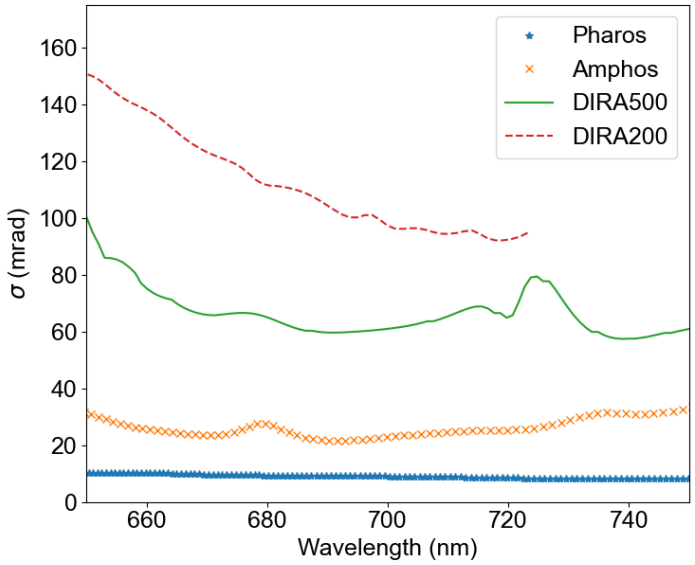

FIGURE 4.19 – Comparison of the phase noise of all four studied pump laser in the 650 to 750 nm spectral region. The blue starred line is the Pharos stability, the orange cross line is the Amphos stability, the green line is the DIRA500 stability and the red dotted line is the DIRA200 stability.

The comparison shows a clear dependence of the noise on the pump laser used. The noise increases with pulse energy but not with average power. It also does increases with the inverse of the repetition rate. The reasons behind this dependence can be multiple. Some hypotheses involve quantum noise in the oscillator [271]. From a more experimental point of view, having more energy per pulse could also mean having more hot spots in the beam inside the amplifiers or oscillator or more shot-to-shot energy variations. All of these can be seen as a consequence of a higher B-integral value. This indicates that going towards high pulse energy for OPCPA development would decrease the CEP stability of the sources but still requires further investigation.

The end of this chapter comes back to Pharos-driven WLG and studies the modification of the laser operating mode.

4.7 Driving laser (Pharos) operating mode

This section uses the Pharos pump laser with a duration of around 200 fs to conduct a study on the dependence of the coherence of the WLG on the operating mode of the driving laser. The Pharos laser has a nominal maximum average power of 6 W. Within this limit, the operating repetition rate can be tuned from 1 MHz (pulse energy of 6 μJ) to 1 kHz (pulse energy of 1 mJ). The repetition rate can be further reduced by the pulse picker at the output of the amplifier

and an arbitrary amount of the pulse energy can be picked using wedges and the combination of half-wave plate and polarizer. The available operating energies of the laser are 6, 60, 600, and 900 μJ with respective repetition rates of 1000, 100, 10, and 1 kHz. These configurations are given by the laser manufacturer as optimal operating conditions and they correspond to the maximum pulse energy available for each repetition rate. For each of these sets of parameters, the phase stability in the visible range is assessed keeping the generation conditions identical (section 4.3). This is achieved by reproducing the same WLG spectrum for each output pulse energy of the driving laser by adjusting the positions of the YAG crystals and the pulse energies. For the same reasons as explained in section 4.6 only the short-wavelength range is studied in this section.

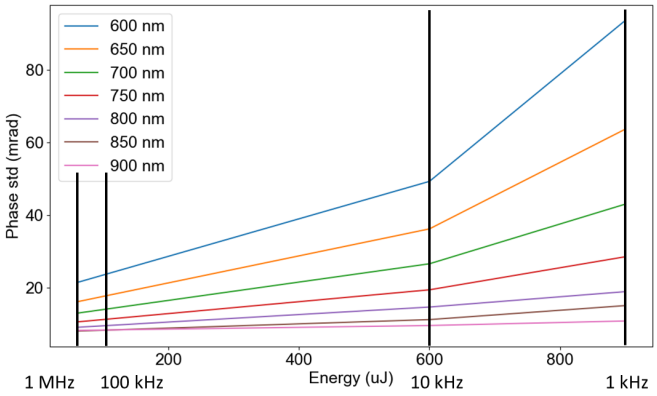

FIGURE 4.20 – Phase stability of the WLG over 1000 laser shots at 7 wavelengths as a function of the pulse energy at the output of the driving laser for the company defined optimal working conditions (i.e. repetition rate is changed).

Figure 4.20 shows the measured stability at 7 different wavelengths as a function of the pulse energy at the output of the driving laser. It could be expected from section 4.6 that increasing the pulse energy increases the phase noise. The trend here is clear and the stability curves are strictly monotonous at all wavelengths even though there are only 4 measurement points. At the lowest energy (6 μJ) the noise is comparable to what was shown in section 4.5 (below 20 mrad). It goes up to 30 mrad at 750 nm with a pulse energy of 900 μJ. As the average power is kept constant, the noise increases with the decrease of the repetition rate as well.

In addition to these configurations, the pulse energy can be reduced to work below the maximum average power of the driving laser by reducing the pumping in the amplifier. This is investigated with the operating repetition rate of 1 kHz. Pulse energies between 400 and 850 μJ are studied and the results are plotted in figure 4.21.

The stability is strictly worse than what was shown in figure 4.20. At the wavelength of 750 nm the noise figure goes from 19 mrad in the previous configuration (600 μJ, 10 kHz) to 28 mrad in this configuration (600 μJ, 1 kHz). Here again, the noise level increases with the energy although not as clearly as in figure 4.20. At 750 nm the noise goes from 35 mrad at 400 μJ to 63 mrad at 850 μJ. The noise goes down at 900 μJ which could be the indication of a saturation effect in the amplifier. This would explain why working below the maximum energy for a given

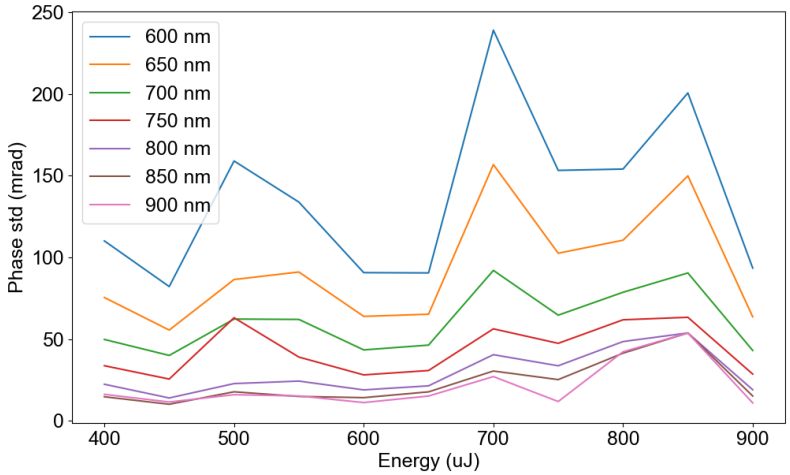

FIGURE 4.21 – Phase stability of the WLG over 1000 laser shots at 7 wavelengths as a function of the pulse energy at the output of the driving laser with an operating repetition rate of 1kHz.

repetition rate gives a higher noise value. These results also seem to indicate a dependence of the noise on the repetition rate of the laser for a given energy. The noise at 600 μJ is indeed higher for a repetition rate of 1 kHz than for 10 kHz.

Figure 4.22 shows a plot of the phase noise as a function of the pulse energy for a repetition rate of 10 kHz for energy values between 400 and 600 μJ.

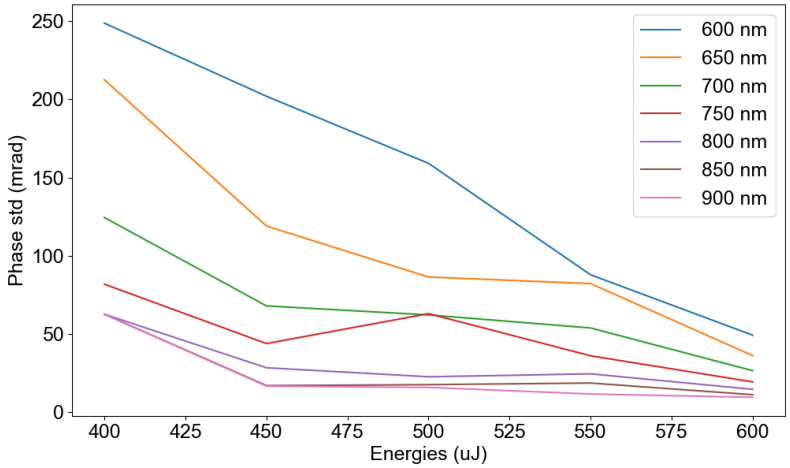

FIGURE 4.22 – Phase stability of the WLG over 1000 laser shots at 7 wavelengths as a function of the pulse energy at the output of the driving laser with an operating repetition rate of 10kHz.

The tendency is the opposite here. The noise is purely going down with increasing pulse energy. The reason for this decrease is not clear but it could again be explained by a saturation effect in the amplifier. As the energy range displayed here was investigated for both 1 and 10 kHz repetition rate table 4.3 summarizes the noise values at 750 nm as a function of energy for both operating frequencies.

There does not seem to be any clear dependence on the repetition rate on the measured

Energy (μJ)	400	450	500	550	600
1 kHz	34	25	63	39	28
10 kHz	82	44	63	36	19

TABLE 4.3 – Noise value (mrad) at 750 nm as a function of pulse energy for a repetition rate of 1 and 10 kHz.

noise. For energies below 500 μJ the noise is higher at 10 kHz but for higher energies, it is higher at 1 kHz. The conclusion to be drawn from these measurements is that whenever the laser parameters are modified away from the manufacturer's optimum the stability decreases. This indicates that the amplifier is designed to work under certain conditions of average power to achieve the best stability. It was further confirmed with LightConversion that straying away from the designed experimental configurations changes the thermal lensing inside the amplifier and decreases the overall performance of the laser system. Unfortunately, I do not have access to the exact parameters modified in this study (diode current, power stability in each preset...) or to the exact amplifier architecture making it difficult to draw more relevant conclusions.

This section shows that the WL generated in the operating modes with a high energy and a low repetition rate seems to have a lower coherence overall. The thermal effects in the amplifier and the B integral (studied in appendix D) also seem to be detrimental as they have an impact on the pulse quality. However, no clear dependence on either pulse energy or repetition rate is established here. Comparing these results with section 4.6 puts the noise level of the Pharos laser used at a repetition rate of 10 kHz and pulse energy of 600 μJ just below the Amphos 3102.

4.8 Conclusion

This chapter presented a new phase characterization setup measuring the intrapulse coherence of the WLG process through spectral interferometry. The objective of this setup is to quantify the shot-to-shot stochastic phase noise introduced by the white light generation process. It requires a single-shot interferometric measurement over 4 octaves of spectral bandwidth ideally able to detect phase shifts of the order of the mrad. In order to accomplish this task the double WL interferometer was developed. It is an upgraded version of two existing setups :

— The Bellini-Hänsch interferometer [131] realizing spatial interference between two supercontinua showing for the first time that this light is coherent.

— The interferometer presented in [29] where the remaining driver of a supercontinuum interferes with a reference to assess the nonlinear phase shift accumulated by the driving laser during supercontinuum generation.

The double WL interferometer combines both ideas by measuring the single-shot spectrally-resolved phase variations between two supercontinua via spectral interferometry. The metric to quantify the spectral phase noise is the standard deviation of the spectral phase variations over 1000 single-shot acquisition σ. The baseline stability of the interferometer was

shown to be under 6 mrad by measuring σ without any nonlinear effect. The noise floor is raised to above the dozen of mrad when the WLG process occurs. The comparison of different pump lasers shows a decrease in the coherence with the increase in the energy of the driving pulse. Characterizing the different operating modes using the Pharos laser shows the dependency on the energy is not that simple and can be affected by B integral or thermal effects. The next chapter will study the systematic influence of multiple generation parameters on the intrapulse coherence of the WLG process. The influence of the energy fluctuations, the focusing conditions, and the spatial phase of the driving laser will be quantified in the next chapter.

Chapitre 5

Parametric study of the phase coherence of the WLG process

5.1 Motivation

The previous chapter presented the interferometer used to characterize the random phase noise added by the WLG process. The analysis was focused on a balanced interferometer with identical configurations for both WLGs. The properties of the driving laser were modified. This chapter is a parametric study of the WLG process conducted with the Pharos laser exclusively. The impact of key parameters on the phase noise is independently quantified by moving away from the balanced interferometer. Disturbing the generation in one of the arms (test arm) while the other arm (reference arm) remains unchanged allows the extraction of two quantities. The first one is the decoherence through the standard deviation of the phase difference σ. The second one quantifies the impact of the fluctuations through the extraction of the transfer coefficient κ between a given parameter and the spectral phase.

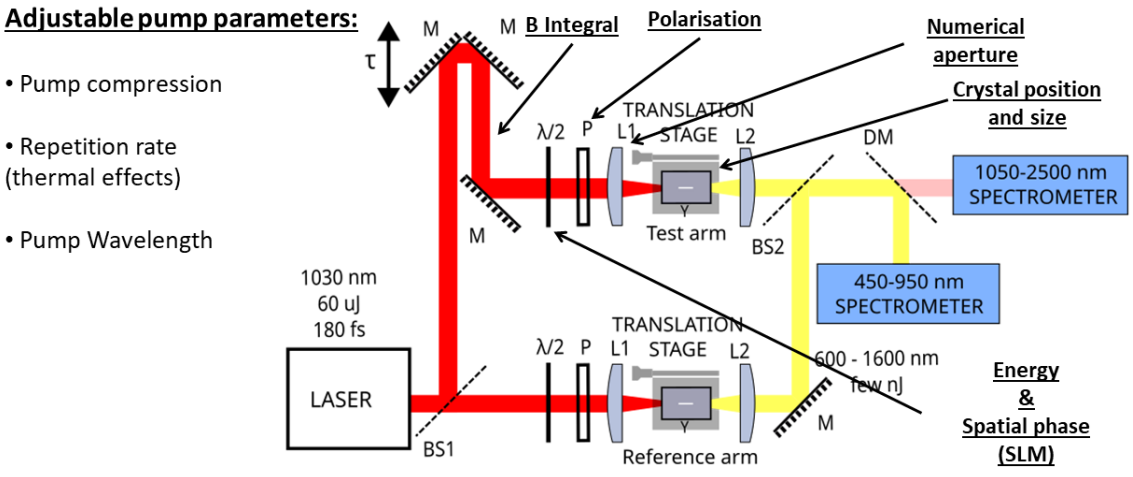

FIGURE 5.1 – Interferometer layout with an array of possible parameters to investigate for the WLG. Parameters to be tuned on the pump laser itself are indicated on the left. Parameters to be tuned on the beam on the test arm itself are underlined around the interferometer.

Figure 5.1 shows a diagram of the interferometer with an array of parameters to explore. These parameters can be split into three categories. The first category was covered in the previous chapter and includes the modifications on the driving laser itself. The second category is the quality of the pulse which can be affected by the duration of the pulse, its phase properties (spatial and spectral), polarization, energy, and the stability of all these parameters. The final category is the configuration including the focusing geometry (NA), the crystal position, and its size. Among the mentioned parameters : section 5.2 investigates the position and length of the YAG crystal, and section 5.3 investigates the pulse energy. Finally, section 5.4 investigates the spatial phase of the driving beam. All these parameters will be modified in the arm labeled test arm in figure 5.1 while the reference arm will never be modified.

5.2 Crystal position and length

As was shown in section 4.2 the crystal position along the propagation axis has a major influence on the shape of the supercontinuum spectrum. This section investigates the influence of the crystal position on the intrapulse coherence of the WLG process. Furthermore, two crystal lengths are studied here : a 6 mm-long YAG and a 10 mm-long YAG. These experimental configurations will be referred to as configurations (I) and (II). The main difference between the two crystal lengths is the width of the infrared spectrum as shown in figure 5.2.

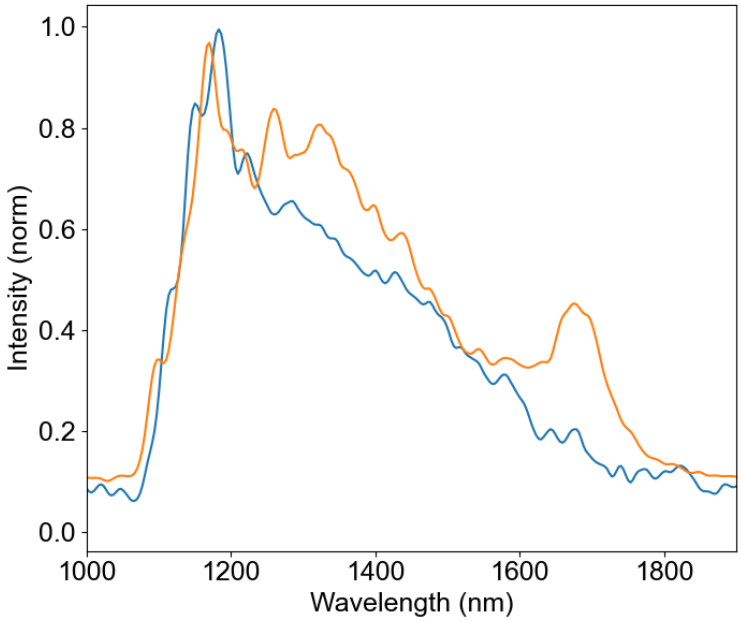

FIGURE 5.2 – Comparison of the infrared spectra of the WL generated in 6 mm-long (blue curve) and 10 mm-long (orange curve) YAG crystals. The 10 mm crystal shows a broader spectrum with a cutoff wavelength at 20% of the maximum intensity of 1720 nm compared to 1580 nm for the 6 mm-long crystal.

As mentioned in section 4.2 the broadening in the infrared part of the spectrum is purely caused by SPM. Increasing the length of the nonlinear media increases the amount of SPM and hence increases the spectral broadening. The metric used is identical to the one presented in

chapter 4. It is the spectrally resolved standard deviation σ of the interference fringes over 1000 consecutive laser shots. In this section and the next both wavelength ranges are studied as the long-wavelength range is heavily influenced by the crystal position.

5.2.1 Phase noise variations

The crystal in the test arm is placed before the beam focus to improve the width and shape of the visible spectrum and the intensity is set slightly below the double filamentation threshold. The crystal in the test arm is then moved along the propagation direction around the beam focus. The resulting phase noise as a function of the crystal position for 3 wavelengths in the visible and the infrared is plotted in figure 5.3.

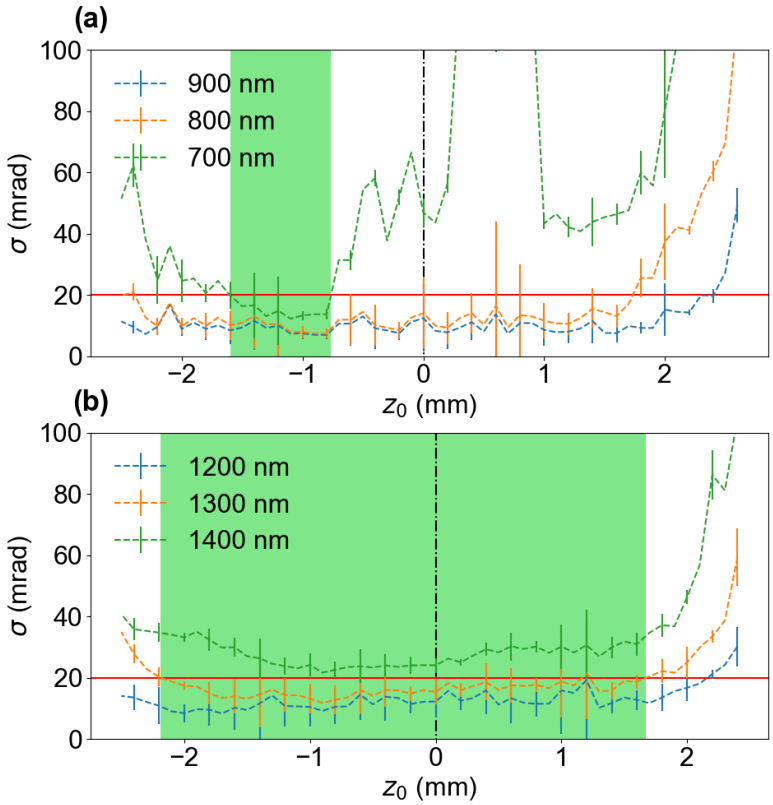

FIGURE 5.3 – Phase standard deviation as a function of crystal position in the short (a) and long (b) wavelengths range with a 6 mm-long YAG crystal. The focus (z = 3.2 mm) is indicated with a dashed line. Lower z-values values get the YAG closer to the focusing lens while higher z-values are further away from the lens. The red line indicates the balanced stability of the interferometer. The green areas refer to the stable operating zone.

From this graph, we can define the stability ranges delimited by the positions where the phase noise goes above the threshold value of 20 mrad on the whole spectral range for the short-wavelength range and at 1300 nm for the long-wavelength range. In the long-wavelength range, the stability range spans from z = -2.2 to z = 1.7 mm. As a comparison, the Rayleigh range of the focused beam is around 0.5 mm and the crystal length is 6 mm. Although moving the crystal changes the spectral shape the position has little influence on the coherence on this side

of the spectrum and the stability range is lenient. In the other wavelengths range the stability range is much narrower (from z = -1.6 to z = -0.75 mm). This confirms what was investigated in section 4.2 and further shows that positioning the crystal before the beam focus yields more phase-stable visible part of the supercontinuum. In both wavelength ranges the stability is strongly degraded when the crystal is placed far from the beam waist (above z = 2 mm).

The same study of the influence of the crystal position was conducted with a longer YAG crystal (10 mm-long). The results are plotted in figure 5.4.

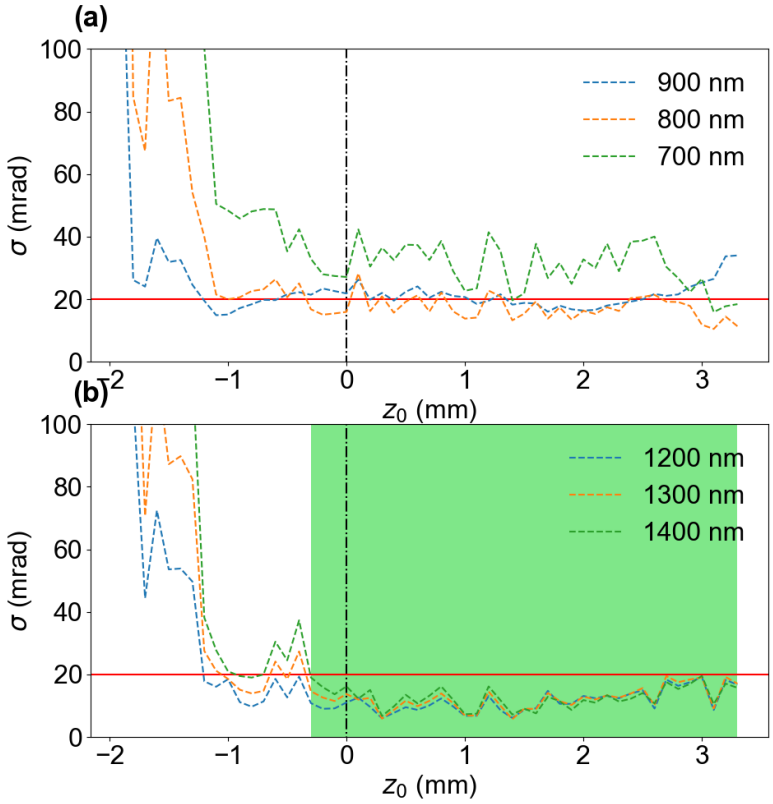

FIGURE 5.4 – Phase standard deviation as a function of crystal position in the short (a) and long (b) wavelengths range with a 10 mm-long YAG crystal. The focus (z = 0 mm) is indicated with a dashed line. Negative positions get the YAG closer to the focusing lens while positive positions are further away from the lens. The red line indicates the balanced stability of the interferometer. The green areas refer to the stable operating zone.

The quantitative behavior is similar to the previous case. The stability in the short-wavelength range is worse and never gets below the 20 mrad threshold. The phase of the long-wavelength range is on the other hand improved. The stability range is wider and the minimal phase jitter is lower. This indicates that using a longer nonlinear crystal is more suited to a phase-stable and spectrally wider long-wavelength range. It is however detrimental to the coherence of the short-wavelength range.

5.2.2 Higher orders of the spectral phase

Delay

The interferometer gives access to the spectral phase difference between the reference arm and the test arm. So far this thesis has only looked at the spectrally resolved shot-to-shot variations of this phase difference. However, more information is encoded in the phase, such as the delay between the two pulses. This can simply be obtained with the slope of the spectral phase. This subsection takes the dataset presented in the previous subsection 5.2.1 and extends the analysis to extract the delay between the two arms as a function of the crystal position. As the results with the two crystal lengths are extremely similar only the length of 6 mm is shown here. The evolution of the delay with crystal position is plotted in figure 5.5 (a) and (b) for both wavelength ranges.

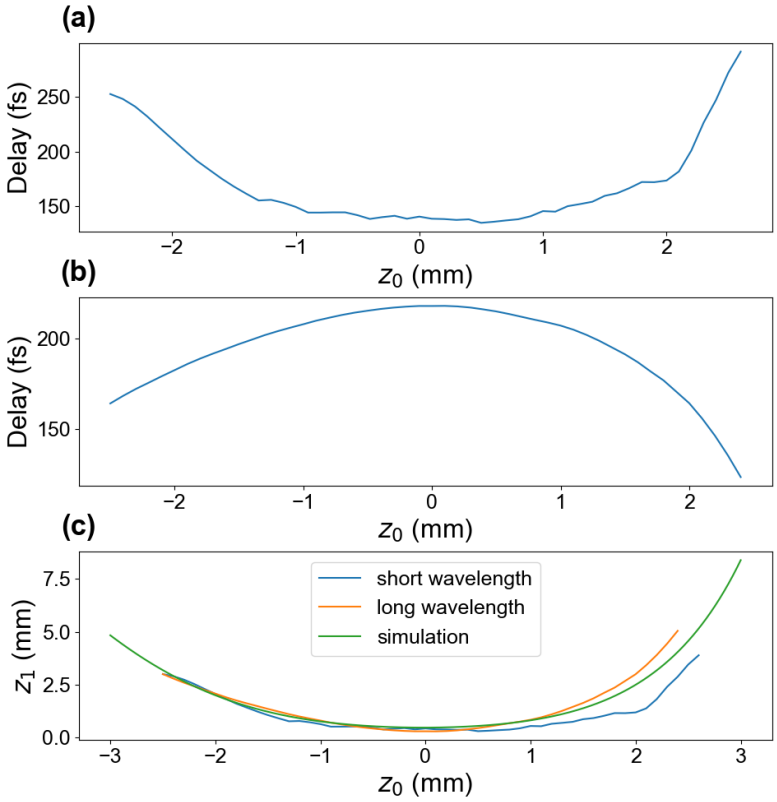

FIGURE 5.5 – Delay between the two arms as a function of the crystal position in the (a) short-wavelength range and (b) long-wavelength range. (c) : Calculation of the z_1 position as a function of the z_0 position from the delay curve in figure (a) in the (blue) short-wavelength range and (orange) long-wavelength range. Simulation of the z_1 position as a function of the z_0 position using ABCD matrix formalism (green curve).

The delays have an opposite behavior in both wavelength ranges. It decreases with position and reaches a minimum before increasing in the short-wavelength range whereas it increases and reaches a maximum before decreasing in the long-wavelength range. The extremum is

reached for a crystal position of z = 0 mm which corresponds to the front face of the YAG crystal being at the focal position.

The shape of the delay curve can be explained by the variation of the starting point of the filament in the YAG crystal. The group delay in YAG is higher in the visible than at the driving wavelength and lower in the infrared than at the driving wavelength so displacement of this point can cause such a delay shift. Figure 5.6 shows a diagram of the Kerr focus inside the YAG crystal.

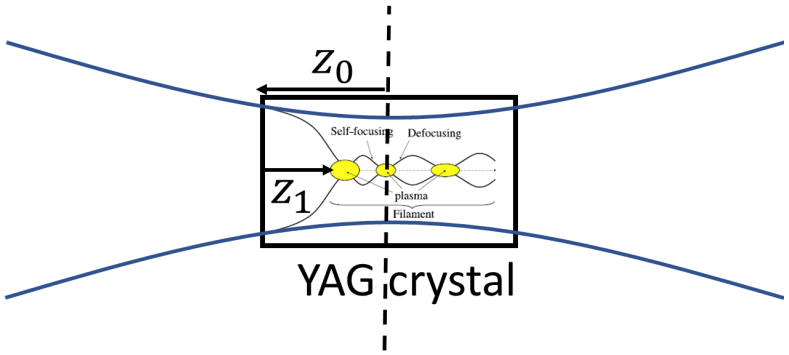

FIGURE 5.6 – Diagram of the Kerr focus inside the YAG crystal. The blue Gaussian beam is the focused driving laser. The dotted red line shows the focus inside the YAG crystal caused by self-focusing. The distance z_0 (positive in this diagram) is the distance between the input face of the YAG crystal and the beam waist of the driving laser ignoring any interaction with the YAG crystal. The distance z_1 is the distance between the Kerr focus inside the crystal and the YAG interface (always positive).

The group delay in YAG at the driving wavelength is $GD_{1030} = 2790\,\mathrm{fs/mm}$. Taking 700 and 1400 nm as the central wavelengths for both wavelengths ranges gives the following respective group delays $GD_{700} = 2834\,\mathrm{fs/mm}$ and $GD_{1400} = 2770\,\mathrm{fs/mm}$. The moving of the Kerr focus can be calculated from the delay simply by dividing the delay by the difference in group index between the driving laser and the considered wavelength range. The calculation of the Kerr focal in the crystal (z_1) deduced from the experimental delay curves is shown in figure 5.5 (c).

The retrieved starting point of the filament is indeed the same in both wavelength ranges with a symmetrical excursion around z = 0 mm of a few mm.

The starting point of the filament can be simulated using a simple numerical model based on ABCD matrices. The YAG is considered as a second lens and the combined focus position is simulated. The focal length of the YAG crystal can be defined in multiple ways [272]. The choice here was to follow the derivation done by J. H. Marburger in 1975 in [273]. The focal length of the Kerr medium is then :

$$f = \frac{0.367 * 2\pi * a^2}{\lambda\sqrt{(\sqrt{\frac{P}{P_{crit}}} - 0.852)^2 - 0.219}} \tag{5.1}$$

where a is the beam radius, P is the peak power and P_{crit} is the critical power as defined in section 4.2. Simulating the z_1 position as a function of the z_0 position gives the results shown in figure 5.5 (c). The evolution of the delay follows exactly the one of the Kerr focus position. The delay caused by the change in focusing position can be calculated from the curve in figure 5.5.

The simulated value of z_1 and the value retrieved through the experiment have a perfect qualitative agreement and the order of magnitude is the same. The model fits very well despite its simplicity and the fact that material dispersion is ignored and the group index of the YAG is kept constant even though the spectral shape changes with z_0. The retrieval of the delay can then be used to determine the starting point of the filament inside the crystal [101].

NL phase orders

After investigating the global delay between the two arms as a function of the crystal position z_0 the next step in the analysis is to apply a similar treatment with a wavelength dependence. The delay can be retrieved at different wavelengths by looking at the slope of the spectral phase at specific wavelengths. In figure 5.7 the wavelength-dependent delays are plotted for three different wavelengths in both wavelength ranges on top of a color map of the first delay peak of the Fourier transform of the spectrum.

The individual delay curves are computed by taking a window of the original fringed spectrum and processing it with the same algorithm. For the delay curve at 800 nm for example the original spectrum is numerically filtered between 750 and 850 nm and the slope of the retrieved phase is plotted as a function of z_0. In other terms, this wavelength-dependent study is a way to look at the dispersion properties of the generated WL. The temporal profile of the interference term is given by the delayed peak. The wavelength-dependent delay peaks follow the delay curves plotted in figure 5.5 (a) and (b) e. g. parabolic dependence. In the short wavelengths, two singular points are identified at z_0 = -1.5 mm and z_0 = 1.5 mm. At these points, the delays for the three wavelengths are the same (185 and 215 fs respectively). The temporal width of the delayed peak is also at a minimum. This can be explained by the material dispersion induced by the YAG crystal. The reference arm is placed at z_0 = 1.5 mm hence the first singular point for the same position of the test arm crystal. The second point at z_0 = 5.5 can be explained by the fact that the position of the Kerr focus z_1 in the crystal is the same as that for z_0 = 1.5. The material dispersion caused by the propagation in the YAG is then the same. At the point where the pulse is most dispersed the delay difference between 700 and 900 nm is 80 fs. The group indices at these respective wavelengths in YAG are 2810 and 2870 fs/mm. The corresponding YAG thickness to reach an 80 fs delay is then 1.3 mm which matches exactly the value obtained by subtracting the values in figure 5.5 (c) at z_0 = 1.5 and z_0 = -1.5 mm.

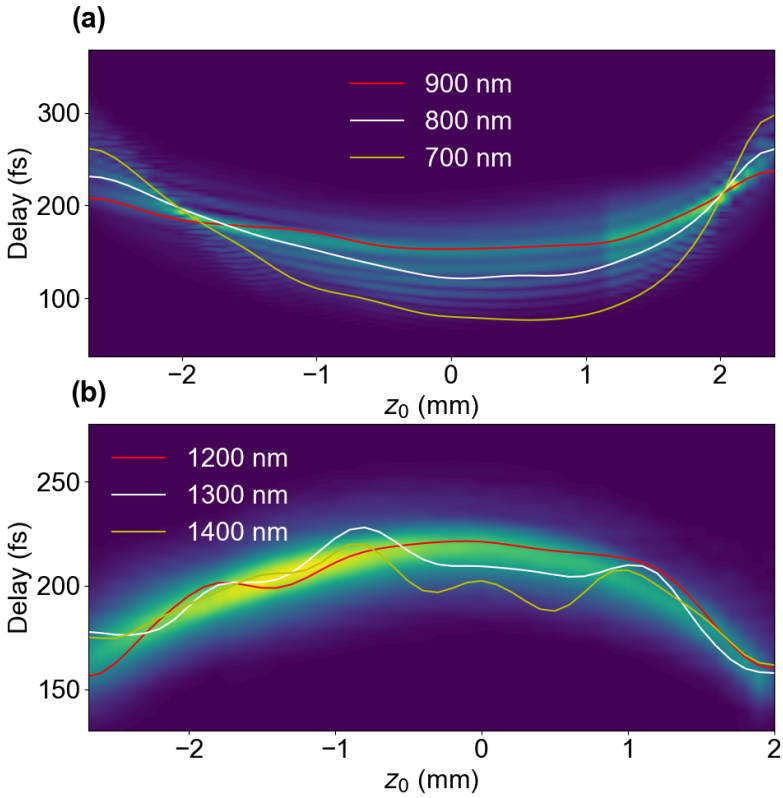

FIGURE 5.7 – Delay curves for three different wavelengths in the (a) short-wavelengths range and in the (b) long-wavelengths range as a function of the crystal position. The delay curves are plotted on top of a color map representing the first delay peak of the Fourier transform (remaining signal after filtering in figure 4.8 (b)).

In this section, the influence of the crystal position was studied. Three quantities were extracted :

— A stability range where σ stays below the target value of 20 mrad over the whole spectrum (spanning more than a mm).
— The evolution of the group delay difference between the two arms. This is explained by the evolution of the starting point in the filament in the YAG crystal and is compared to numerical simulations.
— The variations of the wavelength-dependent group delay explained by the dispersion in the YAG crystal.

5.3 Pump laser energy

It was identified in sections 4.6 and 4.7 that the pulse energy at the output of the laser amplifier has a significant impact on the intrapulse coherence and section D.1 indicated that this dependence is not entirely due to the B integral of the driving pulse. Furthermore, the typical fluctuations of the energy of the output pulse of an OPCPA are typically of the order of the percent. The transfer between energy and carrier-envelope phase is also used as a control tool

to modify the absolute value of the CEP [274] making energy an essential generation parameter. It is quantified by the transfer coefficient $\kappa(\lambda)$ reflecting the amount of spectral phase (at the wavelength λ) added by an increase in pulse energy.

This section further investigates the influence of pump energy on the generation process. Two distinct quantities are studied here. The first one is the influence on the coherence of a change in the pulse energy (section 5.3.2) and the second one is the impact of the energy fluctuations (section 5.3.3).

Three experimental configurations are explored here. In the first two, the YAG crystals are 6 mm-long. In the first one, both crystals are placed at position $z = -1.5$ mm, and in the second one at position $z = 1.5$ mm. These experimental configurations will be referred to as configurations (III) and (IV). In the last configuration, the crystals are 10 mm long and are placed at $z = 1.5$ mm. This is configuration (V). In all configurations, the energy in the reference arm is set just below the double filamentation threshold. Table 5.1 summarizes all the different configurations.

Exp. config.	YAG length	Position	Scan
I	6 mm		z-scan
II	10 mm		z-scan
III	6 mm	-1.5 mm	E-scan
IV	6 mm	1.5 mm	E-scan
V	10 mm	1.5 mm	E-scan

TABLE 5.1 – Different experimental configurations and parameter-scans performed in this study. z-scan (resp. E-scan) refers to a controlled change of the YAG position (reps. seed energy) in the test arm.

5.3.1 Data processing

In this section, the data processing has an additional step due to the laser behavior in this specific configuration. The attenuator of the laser was set at a minimum transmission of 15%. This causes 1% peak-to-peak fluctuations followed by relaxation over a few laser shots of the pulse energy. Figure 5.8 shows the energy stability of the Pharos laser measured with a photodiode.

Figure 5.9 shows a typical phase profile acquired with the intensity profile of figure 5.8. The intensity spikes are perfectly reproduced in the spectral phase.

The raw phase data is separated into two sets : the first one is made of all the points where the phase is below the blue dashed line and is used to extract the standard deviation in the same manner as the previous sections. The second data set is made of the points where the phase is above the blue dashed line and they are used to quantify the impact of the 1% energy fluctuations on the phase and extract a spectrally resolved intensity to phase transfer coefficient.

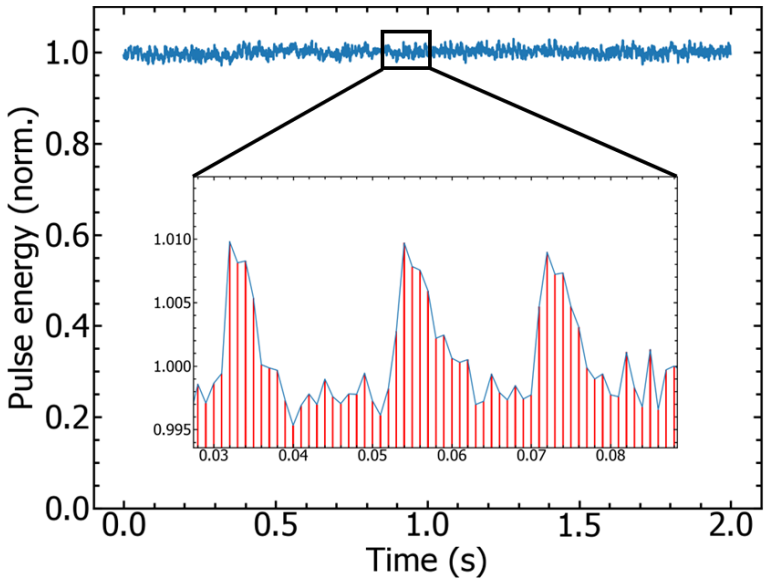

FIGURE 5.8 – Pulse-to-pulse energy stability of the driving laser with an enclosed zoom over 100 ms (each red bar is a laser shot).

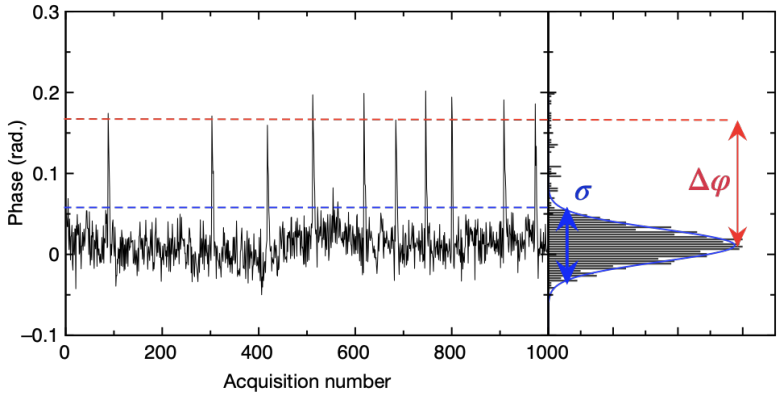

FIGURE 5.9 – Illustration of the significant quantities extracted from the acquisitions : the phase is calculated by Fourier transform for an arbitrarily chosen wavelength as a function of acquisition time for each acquired spectrum. The blue dashed line indicates the threshold applied to filter out the effect of laser overshoots. σ is the standard deviation of the measured phase noise, and $\Delta\varphi$ is the phase jump induced by laser overshoots. The process is repeated for each wavelength.

5.3.2 Phase stability

In this subsection, the two measurements (III and IV) with 6 mm-long crystals are studied. In configuration (III) the crystal in both arms are placed at $z = 2$ mm to favor the generation of the visible side of the spectrum as shown in section 5.2. The energy in the test arm is varied between 0.35 and 1.57 μJ with steps of 20 nJ. This range goes from the onset of filamentation at the lowest energy to above the double filamentation threshold (1.13 μJ). The threshold is identified by the modulation of the spectrum appearing close to the pump wavelength as mentioned in section 4.2. Figure 5.10 shows the phase noise at three different wavelengths in both

wavelength ranges as a function of the pulse energy in the test arm.

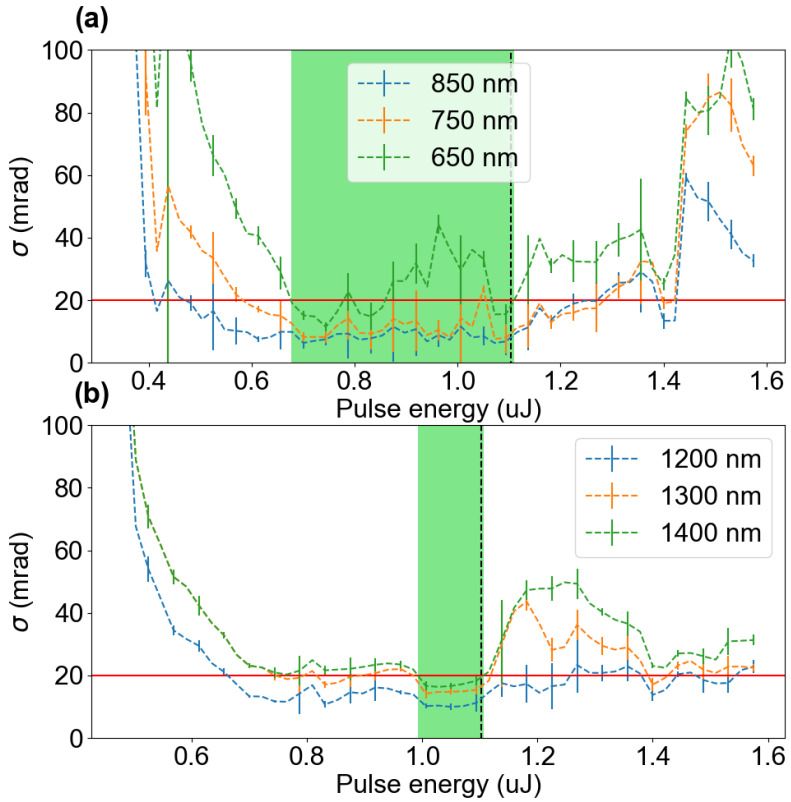

FIGURE 5.10 – Phase standard deviation as a function of seed pulse energy in the short (a) and long (b) wavelength ranges for z = -1.5 mm. The energy axis starts at the onset of filamentation. The dotted black line refers to the onset of double-filamentation. The green areas refer to the stable operating zone.

The qualitative behavior is identical in both wavelength ranges. The phase noise starts at a value above 400 mrad at 750 nm and above 150 mrad at 1300 nm. The phase noise then decreases with energy until it reaches a plateau and then increases with energy again. At the onset of the single filamentation, the energy is not sufficient to ensure a well-established filament, and intensity fluctuations have a high impact on the phase noise. When the energy reaches a higher value the energy fluctuations have a lower impact on the phase noise until the energy reaches the threshold for double filamentation. As expected from [245] the phase noise is minimal when the single filament is stable. The stability ranges are defined as the range where the phase noise is under the stability value of 20 mrad and extend from 0.68 μJ to 1.11 μJ in the short-wavelengths range and from 0.992 μJ to 1.11 μJ in the long-wavelengths range.

In configuration (IV) the YAG crystals are placed after the beam focus at $z = 1.5$ mm to favor the infrared wing of the supercontinua. The energy was varied from 0.5 to 1.23 μJ with steps of 15 nJ. Figure 5.11 shows the phase noise at three different wavelengths in both wavelength ranges as a function of the pulse energy in the test arm.

The qualitative behavior is identical to the previous configuration. However, the stability ranges are different. In the short-wavelengths range it spans from 0.91 to 1.09 μJ, and in the long-wavelengths range from 0.91 to 1.1 μJ. As the results obtained from the 10 mm-long crystal

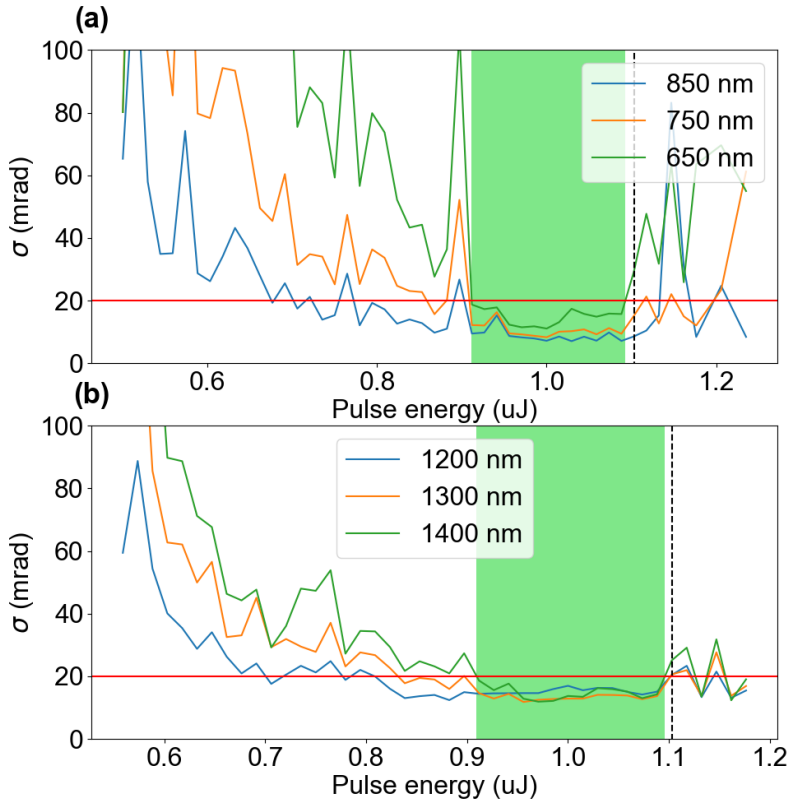

FIGURE 5.11 – Phase standard deviation as a function of seed pulse energy in the short (a) and long (b) wavelength ranges for z = 1.5 mm. The energy axis starts at the onset of filamentation. The dotted black line refers to the onset of double-filamentation. The green areas refer to the stable operating zone.

show an identical behavior the curves are not shown here. Instead table 5.2 summarizes the stability ranges in all 5 configurations.

	I	II	III	IV	V
Stab. range (short λ)	1.5 - 2.5 mm	above 20 mrad	0.68 - 1.1 µJ	0.91 - 1.09 µJ	above 20 mrad
Stab. range (long λ)	1 - 4.3 mm	0.5 - 4.8 mm	0.99 - 1.1 µJ	0.91 - 1.1 µJ	0.83 - 1.3 µJ
min jitter @750 nm	12 mrad	21 mrad	9 mrad	9.5 mrad	28 mrad
min jitter @1300 nm	12 mrad	7 mrad	14 mrad	12 mrad	5 mrad

TABLE 5.2 – Significant phase stability values for the different experimental configurations : phase stability ranges for the two spectral bands (two first rows) ; minimum phase noise for two wavelengths (two last rows).

The stability range in the long-wavelength range is significantly smaller (2.5 times smaller) in the configuration where the crystals are placed before the beam focus (III). On the other hand, this configuration gives the broadest stability range (2 times bigger) in the other wavelength range. Using a longer YAG crystal increases the stability of the long-wavelength range both in minimal phase jitter and stability range but the coherence in the short-wavelength range is much worse.

5.3.3 Transfer coefficient

The second quantity extracted from these measurements is the spectrally resolved transfer coefficient between intensity and spectral phase. As shown in figure 5.9 the 1% pulse energy fluctuations cause a phase jump $\Delta\varphi$. The value of $\Delta\varphi$ is energy and wavelength dependent. A transfer coefficient $\kappa(\lambda)$ between intensity and spectral phase can then be extracted. Figure 5.12 shows κ values for different wavelengths in configurations (III) and (IV).

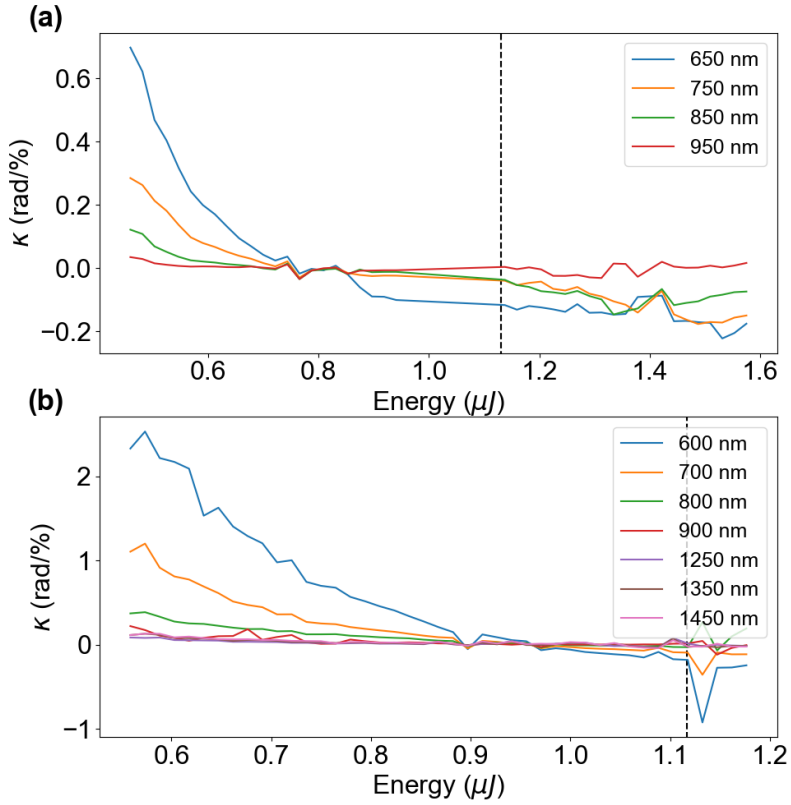

FIGURE 5.12 – Amplitude-to-phase coupling coefficient for experimental configurations III (a) and IV (b). The dashed black line refers to the onset of double-filamentation.

In both cases the intensity fluctuations have little to no effect on the phase in the long-wavelengths range hence the low κ value. On the other side of the spectrum, the transfer coefficient is larger for lower energies or when the energy is close to the onset of double filamentation. It is also larger for lower wavelengths. It is however smaller in configuration (III) (0.6 rad/% vs 2 rad/%) further confirming this configuration as a favorable configuration to generate the visible part of the WL. Surprisingly there is a stationary point for both configurations where the transfer coefficient crosses zero for all wavelengths at 0.785±0.085 μJ for configuration (III) and at 0.955±0.015 μJ for configuration (IV). In configuration (IV) the stationary point is right below the double filamentation threshold and is counter-intuitively larger than in configuration (III). The presence of this stationary point gives a remarkable generation point to minimize the impact of the energy fluctuations. The extraction of the $\kappa(\lambda)$ is also relevant for the use of the pulse energy as a CEP control tool.

5.3.4 Higher orders of the spectral phase

Similarly to section 5.2.2 a study on the dependence of the starting point of the filament on the energy is performed. The behavior in configurations (III) and (IV) is qualitatively the same so configuration (III) will be shown as an example. Figure 5.13 shows the evolution of the delay τ as a function of the pulse energy in the test arm in both wavelength ranges with the associated experimental and simulated starting point of the filament. The delay shows a monotonous variation increasing with energy in the visible and decreasing in the infrared with pulse energy. This variation is also explained by a variation of the starting point of the filament inside the YAG crystal. The starting point of the filament (experimental z_1) can once again be retrieved from the delay in both wavelength ranges and is plotted in figure 5.13 (c).

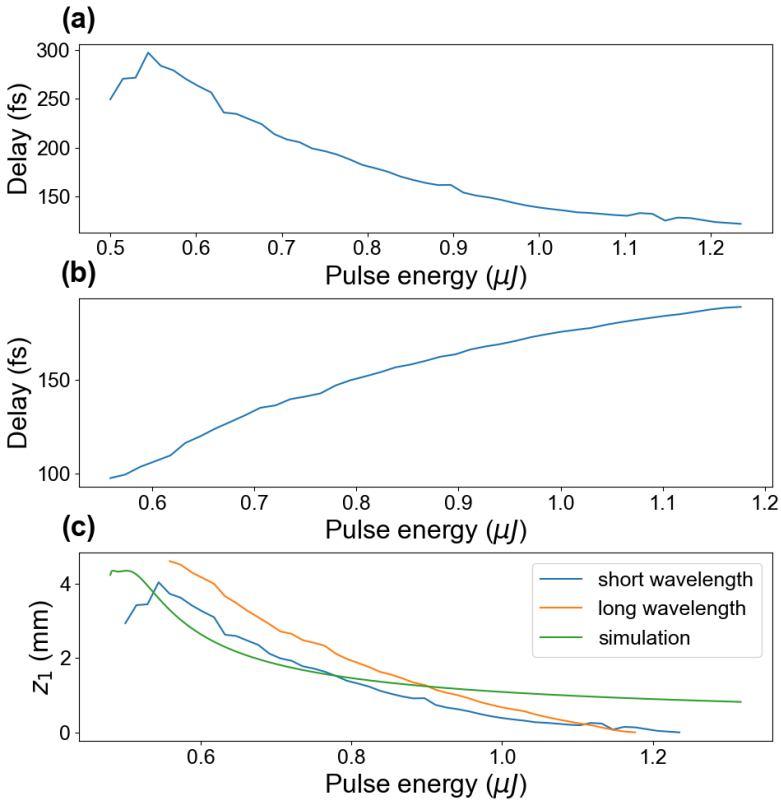

FIGURE 5.13 – Experimental delay in the short-wavelengths range (a) and long-wavelengths range (b) as a function of the pulse energy. (c) : Calculation of the z1 position as a function of the energy from the delay curve in the short-wavelength (blue) and long-wavelength (orange) range. Simulation of the z_1 position as a function of the pulse energy using ABCD matrix formalism (green).

In this case, again the focal point in the YAG is simulated and shown in figure 5.13 (c) as a function of the pulse energy. The conclusion is the same as in the previous section. Finally, figure 5.14 shows a colormap of the delay peak in the Fourier domain with a wavelength-dependent delay analysis.

This section quantified the impact of the energy of the driving pulse on the coherence of the WLG process. It was shown that the range of generation is lenient (up to 40% of the pulse

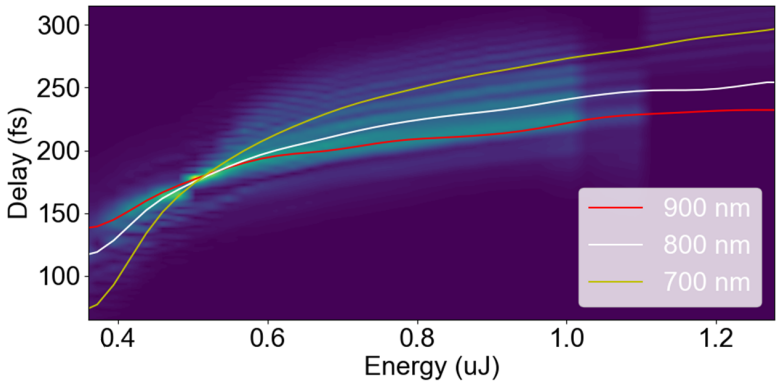

FIGURE 5.14 – Delay curves for three different wavelengths in the short-wavelength range as a function of the pulse energy. The delay curves are plotted on top of a color map representing the first delay peak of the Fourier transform.

energy) in both wavelength ranges. The influence of energy fluctuations has also been quantified through the transfer coefficient $\kappa(\lambda)$ that has been shown to reach values of the order of 1 rad/%. Furthermore, this section confirmed the tendencies from section 5.2 where positions favorable for each wavelength range were identified.

5.4 Spatial phase

The last parameter investigated in this chapter is the spatial phase of the driving laser. Spatio-temporal couplings [275-278] have been extensively studied in the case of the propagation of a light pulse. When it comes to filamentation the relationship between the spatial phase of the driving laser and the spectral phase of the supercontinuum has not been studied to the best of my knowledge. It can however be expected that the spatial phase would alter the filamentation dynamics. The spatial phase of the beam is indeed directly imprinted in the properties of the beam focus. As filamentation happens at the ionization threshold the focusing geometry and properties have a direct impact on the WLG process [266]. Wavefront manipulation has been shown to impact different nonlinear effects such as high harmonic generation [279] among others [280]. It has been shown however that basic spatial filtering can improve the overall performances of OPCPA systems. Section 4.6 also showed that spatial filtering improves the intrapulse coherence of the WLG process. The spatial phase is indeed likely to be one of the parameters that are not perfect and that shows shot-to-shot fluctuations because of thermal effects or defects in the materials. This section conducts a more extensive study on the influence of the wavefront shape of the driving beam and takes a look at the lowest-order optical defects.

The interferometer is modified to control and measure the spatial phase in the test arm as illustrated in figure 5.15.

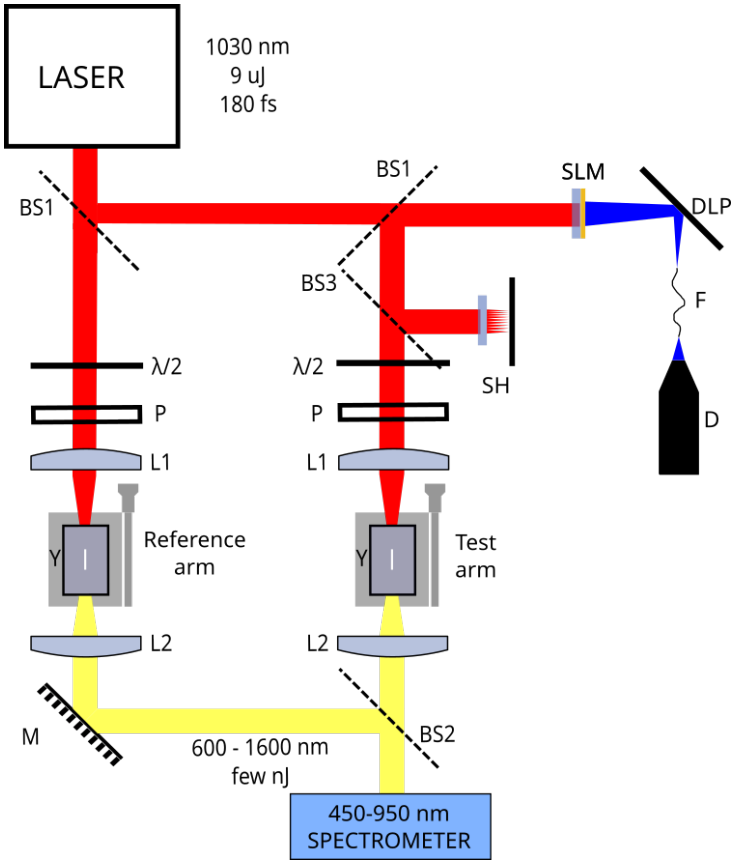

FIGURE 5.15 – Diagram of the interferometer with the addition of SLM : Spatial Light Modulator, DLP : Digital Light Processing unit, F : Square multimode optical fiber at 1030 nm, D : Blue laser diode, BS3 : 1030 nm 99/1% beam splitter, SH : Shack-Hartmann wavefront sensor.

5.4.1 Wavefront modification and characterization

The spatial phase control is accomplished with a homemade thermo-optically addressed Spatial Light Modulator (SLM) [64] and its measurement by relay-imaging the plane of the SLM on an Imagine Optic HASO4 Shack-Hartmann wavefront sensor (phase resolution of 0.01λ). Enough is to say that the SLM exploits the thermotropic character of liquid crystals and enables phase control through the absorption of a blue laser diode. Here the spatial phase is proportional to the blue light intensity. The SLM and blue diode shaping are described in appendix C. The aberrations studied here are picked from the lower-order Zernike polynomials. Figure 1.4 in section 1.1.3 shows representations of the Zernike polynomials. The polynomials with an index number under 3 (offset and tilt) are not relevant hence they are not studied here. The polynomials with indices between 4 and 11 are the ones picked for this study. Z4 is the focus, Z5 and Z6 are the astigmatism (0° and 45°), Z7 and Z8 are the coma (0° and 90°), Z9 is spherical and Z10 and Z11 are trefoil (0° and 90°). These aberrations were picked as they are the dominant aberrations in the wavefronts of actual laser systems and they are expected to have the highest impact on the phase stability. The five experimental configurations are named after their dominant aberrations and will be designated by : (i) focus, (ii) astigmatism, (iii) coma, (iv)

trefoil, and (v) spherical. The wavefronts used for the experiments are presented in figure 5.16. It is clear from the measured wavefronts that they are each not purely decomposed in a single aberration as the control of the SLM is "hand-made". It can however be improved as shown in [127]. The discrepancy between the Zernike polynomials and the experimental configurations is however not a problem as the wavefront of actual laser systems is not made of a single optical aberration. Figure 5.17 shows a decomposition in Zernike polynomials of the 5 experimental wavefronts and figure 5.18 shows the far field in each experimental configuration.

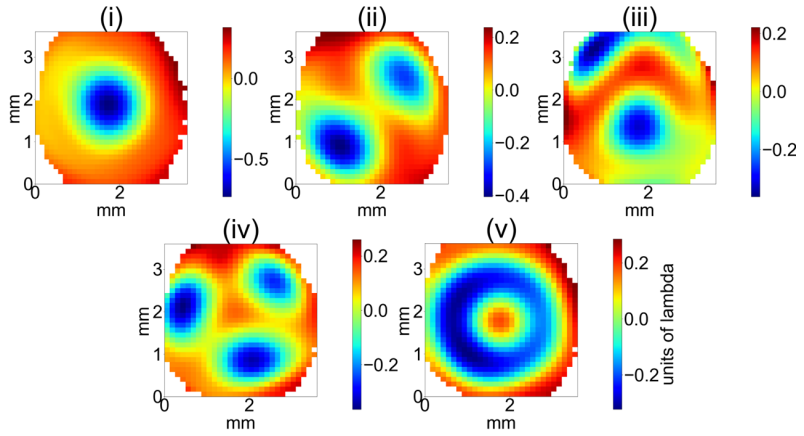

FIGURE 5.16 – Experimental wavefronts measured with the Shack-Hartmann wavefront sensor for the five aberrations.

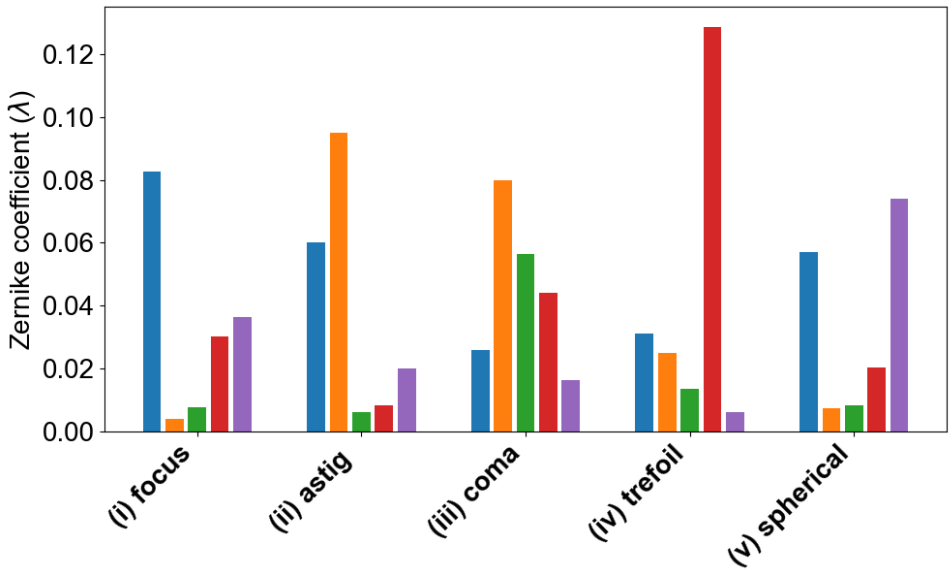

FIGURE 5.17 – Histogram showing the Zernike decomposition of each wavefront. Each wavefront is indicated by its dominant aberration name. The blue bars are the focus coefficient, the orange ones astigmatism, the green ones coma, the red ones trefoil, and the purple ones spherical. Each wavefront is taken at the maximum of the measurement range of table 5.3

The metric used to quantify the amount of spatial phase induced to beam in the test arm is the peak-to-valley of the wavefront. The PtV is the maximum value of the wavefront minus the

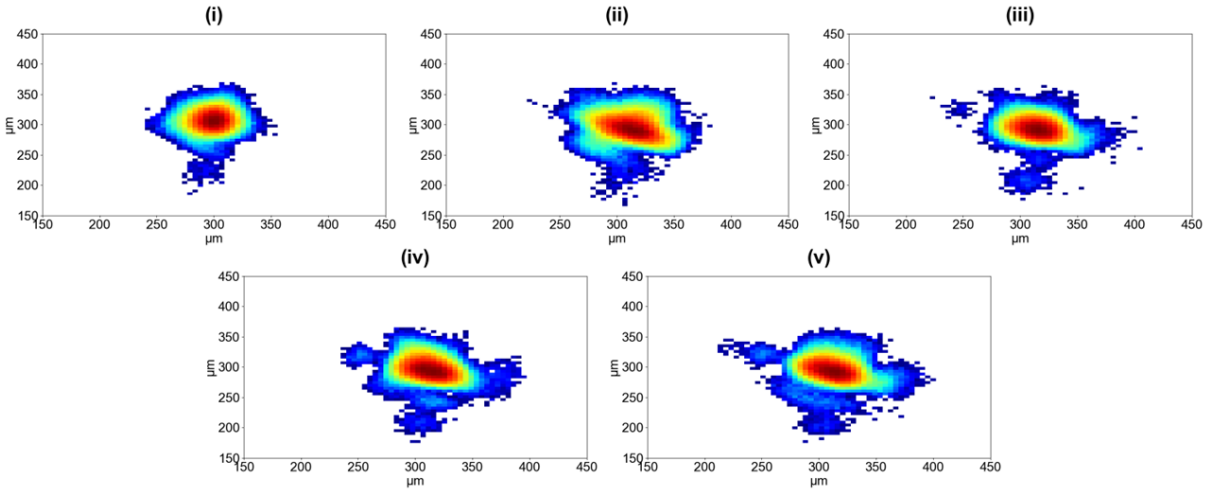

FIGURE 5.18 – Experimental far fields in the center of the measurement range measured with a camera for the five aberrations in logarithmic scale.

minimum value of the wavefront. It can be controlled experimentally in the typical range 0.1-0.6 λ. As the shape of the wavefront is not modified for a given aberration the PtV is a relevant metric.

Similarly to section 5.3 two separate investigations are going to be pursued from the spatial phase study. The first one is the coherence of the WLG process with a given wavefront aberration in the test arm to simulate a degraded driving laser. The second one is the quantification of the impact of the wavefront fluctuations to simulate a fluctuating driving laser. This is achieved by measuring the transfer coefficient between the spatial phase and the spectral phase. Only the short wavelength range will be studied here as the tendency from all previous measurements show that the dynamics in both wavelength ranges are identical and more pronounced in the short wavelength range.

Simply introducing the SLM into the setup degrades the phase stability as figure 5.19 shows. This noise increase is not due to the SLM itself but to the addressing system and more specifically the fan of the blue laser diode.

5.4.2 Phase stability : effect of wavefront constant degradation

To assess the coherence of the WLG process for a given aberration level a programmable spatial phase with a constant shape and a variable PtV is induced in the test arm. The measurement range for each aberration is given in table 5.3 and the spatial phase increment is around 0.05 λ in all the cases. To give an idea of the focal point perturbation the far field measurements of figure 5.18 are compared to 2D Gaussian fits and the remaining error (in % of total energy) is added to table 5.3. The fit is done with a 2D Gaussian function along the axes x and y. There is no account for the rotation of the far field profile in this rough fit also explaining the relatively high error values obtained. This quantity is an estimate of the deformation of the far field profile of the beam (it includes the far field shape as well as the energy in the feet) at the center of the measurement range for each aberration.

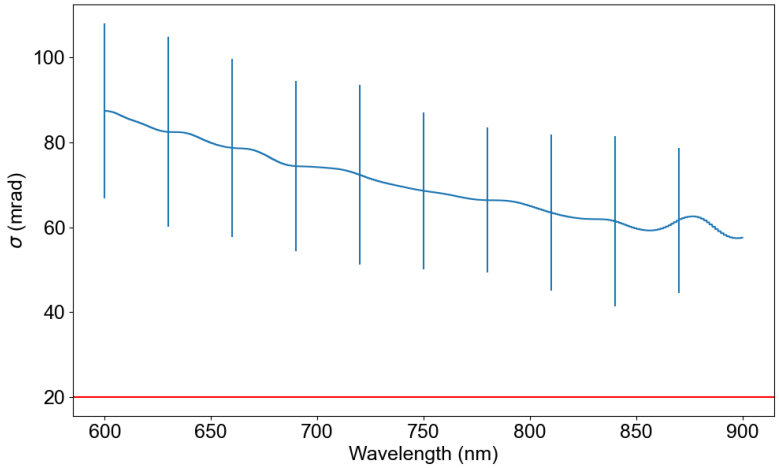

FIGURE 5.19 – Phase standard deviation as a function of wavelength in the short-wavelengths range when the SLM is not addressed. The red line indicates the 20 mrad stability value defined in section 4.5

Experimental wavefront	(i)	(ii)	(iii)	(iv)	(v)
PtV range (units of λ)	0.12-0.35	0.14-0.64	0.27-0.58	0.39-0.61	0.44-0.62
Fit error (%)	15	35	17	32	36

TABLE 5.3 – PtV measurement ranges for section 5.4.2

For each experimental configuration corresponding to an aberration, the PtV of the wavefront is modified within the measurement range. The parameters for the WLG are optimized in the middle of the measurement range. The energy is then set right below the double filamentation onset and the crystal is placed at z = -1.5 mm. Keeping these parameters constant the spatial phase is incremented from the lowest value to the highest value of the measurement range. At each increment, the coherence of the WL is measured thus quantifying the effect of a spatial phase degradation. The data acquired in configuration (ii) are taken as an example and figure 5.20 shows the rms phase stability as a function of the PtV spatial phase induced.

The phase noise is almost constant over the whole measurement range (very slight decrease) so in this configuration (ii) introducing a spatial aberration to the test arm has no consequence on the coherence of the WLG process. This tendency is verified for all the investigated configurations and figure 5.21 summarizes the stability values measured at the edges of the measurement range for the five experimental configurations.

Much like the example of aberration (ii) in all 5 cases there is no clear variation of the standard deviations at the extrema of the measurement ranges. Configuration (ii) shows the highest variation of 27 mrad (20% variation). Configuration (iii) is the only one where the phase noise is higher at the maximum than at the minimum of the measurement range. Finally, no aberration shows stability values significantly higher than the base setup stability. There is unexpectedly no clear impact of a constant aberration induced in the beam of the test arm on the coherence of the WLG process. The wavefront perturbation is likely affecting the filamentation dynamics and the properties of the WL. These properties include the spectral shape and bandwidth, the

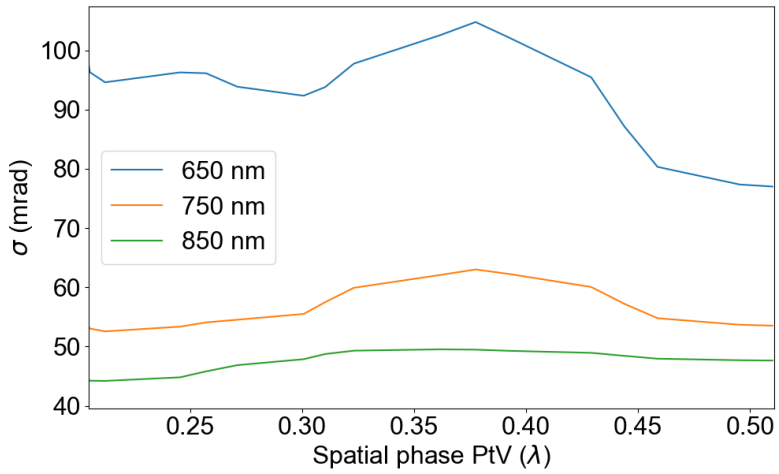

FIGURE 5.20 – Phase standard deviation at 4 different wavelengths in configuration (ii) as a function of the spatial phase PtV.

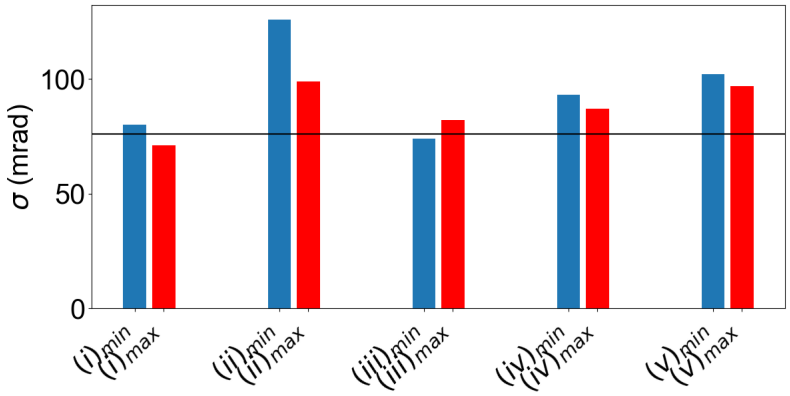

FIGURE 5.21 – Phase rms at 750 nm for the extrema of the measurement range for all 5 optical aberrations. The black line is the reference value of the stability when the SLM is not addressed.

spectral intensity, and the wavefront of the emitted white light but they are not measured here. The quantity studied here (the spectral phase variations) is however surprisingly not affected.

5.4.3 Spatial phase to spectral phase transfer coefficient

Similarly to section 5.3.3 this section quantifies the impact of weak fluctuations of the spatial phase on the spectral phase. A transfer coefficient between the spatial phase and the spectral phase is extracted with the following experimental protocol. The induced spatial phase is incremented every 350 ms over 10 s of measurement using the DLP unit (appendix C). The measurement range, in this case, is given in table 5.4 and is much smaller than in the previous study.

The measurement range was chosen to ensure the spectral phase shifts induced by the spatial phase shifts stay under 2π (for each increment, not for the whole range) so that the retrieval algorithm can unwrap the phase correctly. Because each spatial phase increment is below the

Experimental wavefront	(i)	(ii)	(iii)	(iv)	(v)
PtV range (lambda)	0.019-0.058	0.056-0.17	0.05-0.15	0.062-0.22	0.029-0.25

TABLE 5.4 – PtV measurement ranges for section 5.4.3

resolution of the HASO4 sensor (0.01 λ) a direct wavefront measurement is not possible. Instead, the wavefront is measured at the edges of the measurement range. As the SLM is used in the range where the induced phase is proportional to the flux of the blue writing beam (between 0.38 and 5.3 W/cm^2) a photodiode measurement of the blue writing beam gives access to the full wavefront information at each experimental increment. Figure 5.22 shows such a photodiode measurement of the blue writing beam for aberration (ii).

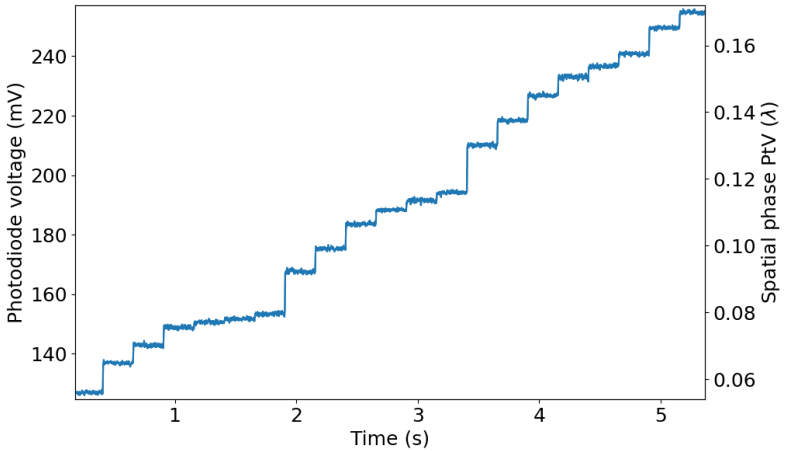

FIGURE 5.22 – Photodiode measurement of the blue writing beam as a function of time showing the increments performed by the DLP unit. The right axis shows the corresponding spatial phase PtV in configuration (ii).

The increments of the intensity of the blue writing beam are clearly visible in the plot. They are however not homogeneous due to the DLP unit.

To give some perspective on the spatial phase variations, figure 5.23 shows the far field measurements of the test arm beam at the extrema of the measurement range and at two consecutive points in the center of the measurement range in the case of configuration (ii). Although slight differences are visible in the far field profile between the maximum and minimum of the measurement range (variations around 5% of the maximum intensity) the profiles at the center of the measurement range are identical (variations lower than 1% of the peak intensity).

Figure 5.24 (a) shows the spectrogram associated with the spatial phase variation shown in figure 5.22. The spatial phase PtV is varied from 0.056 to 0.17 λ with increments around 0.006 λ. (right scale of figure 5.22) 12 increments indicated by a vertical black dotted line for a total excursion of 0.076 λ are shown. The spectral phase retrieved from figure 5.24 (a) at 750 nm is plotted in figure 5.24 (b). The total excursion of the spectral phase is above 20 rad for a spatial phase excursion of 0.48 rad. As depicted on figure 5.24 (b) a spatial phase shift of 0.005 λ (30 mrad) causes a spectral phase shift of 1.4 rad. The transfer coefficient $\kappa(\lambda)$ between the spatial phase and spectral phase is the ratio between the two phase shifts and is 50 for aberration

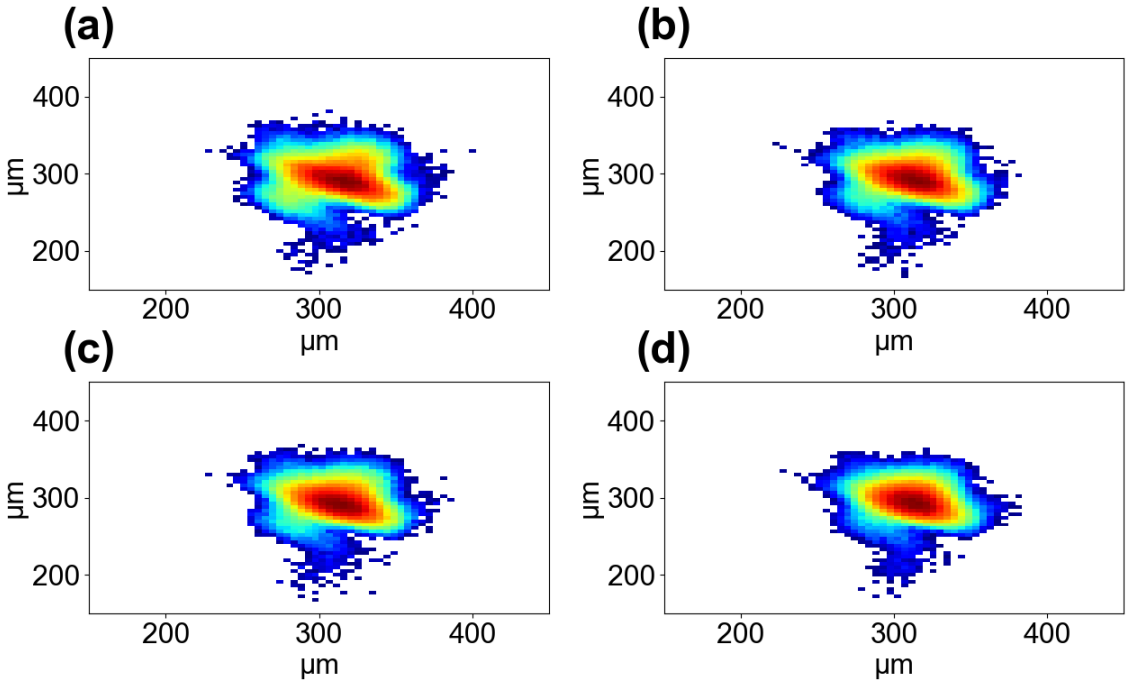

FIGURE 5.23 – Far field profile of the beam in the test arm at the minimum (a), maximum (b) and center (c) and (d) of the measurement range with respective PtV phases of 0.056, 0.17, 0.113 and 0.119 λ in logarithmic scale for aberration (ii).

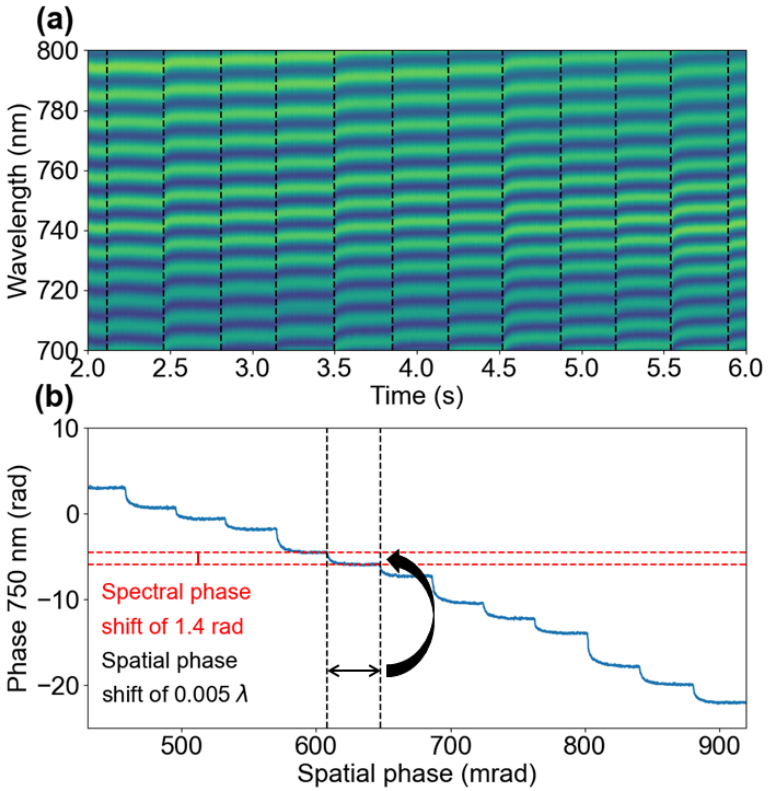

FIGURE 5.24 – a : Spectrogram around 750 nm in the case of aberration (ii). The vertical dashed black lines represent an increment in the spatial phase (see text). b : Extracted phase at 750 nm from figure (a).

(ii) at 750 nm. Disturbing the wavefront with a perturbation one order of magnitude below the resolution of the HASO4 (i. e. undetectable) results in a spectral phase shift above 1 rad. This magnitude of fluctuations is highly detrimental to any subsequent phase-sensitive process such as compression or CEP. Peak-to-peak phase fluctuations can also be detrimental to the overall stability of the WL. The same experimental protocol was conducted for all 4 other aberrations (i, iii, iv and v). Figure 5.25 shows the spectrograms for each aberration.

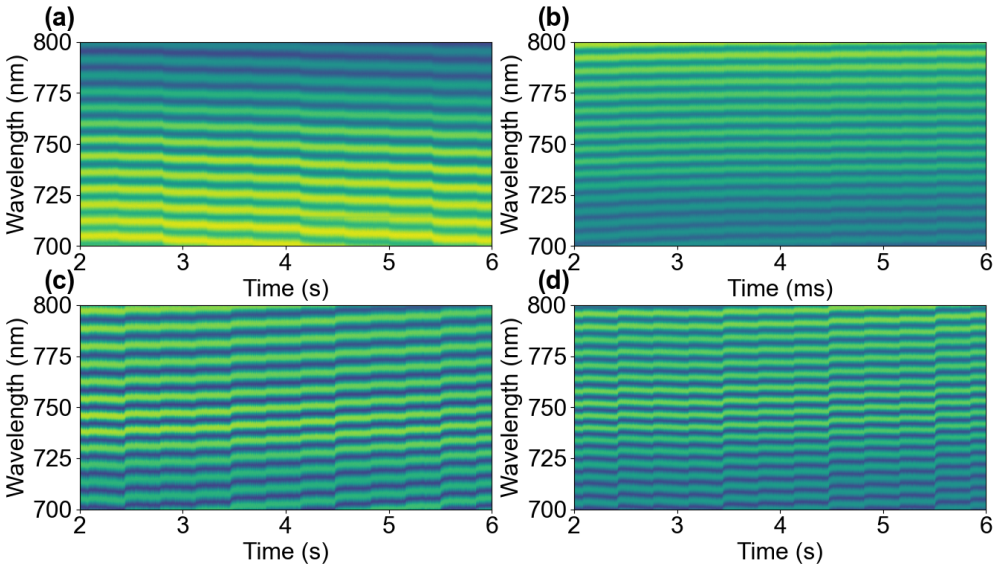

FIGURE 5.25 – a : Spectrogram around 750 nm in the case of aberration (i). b : Spectrogram around 750 nm in the case of aberration (iii). c : Spectrogram around 750 nm in the case of aberration (iv). d : Spectrogram around 750 nm in the case of aberration (v).

Figure 5.26 shows the transfer coefficients for all 5 aberrations as a function of wavelengths. obtained from the spectrograms of figure 5.25.

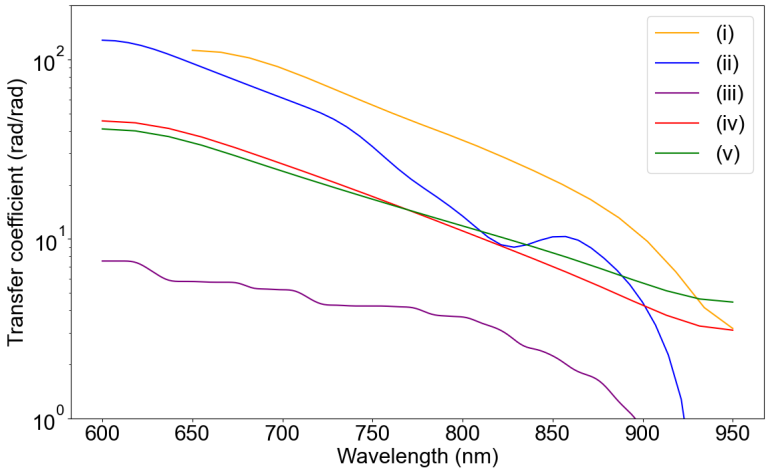

FIGURE 5.26 – Retrieved transfer coefficient $\kappa(\lambda)$ for the 5 aberrations as a function of wavelength plot in log scale. The dip in the κ value for aberration (ii) is unexplained at this time and most likely a measurement artifact.

As expected the lower wavelengths show a larger transfer coefficient. The two lowest order (third order) aberrations (i) and (ii) show the two biggest transfer coefficients. Among the two the focus aberration shows a value about 1.5 times higher than the astigmatism. Spherical (iv) and trefoil (v) show similar transfer coefficients despite trefoil (v) being fourth-order and spherical (iv) being fifth-order aberrations. Coma (iii) shows a much smaller κ value (10 times less than focus (i)) than all the other aberrations even though it is a fourth-order aberration. The transfer coefficient overall decreases with aberration order and it seems to be higher for centrosymmetric aberrations. The absolute value of the transfer coefficient is much higher than expected especially knowing that the ranges for stability are bigger than expected. The reasons behind this value are not explained yet. One of the possible explanations would be similar to what was explored in sections 5.2 and 5.3 through the movement of the filament starting position. A model of the beam profile after the focusing lens would be necessary to get a full understanding of the focal point modification induced by each wavefront.

5.5 Conclusion

In this chapter, a parametric study of the coherence of the WLG process was conducted. Three major parameters were explored : the crystal position, the pulse energy, and finally the spatial phase. Additionally, the transfer coefficients between energy and the spectral phase were derived as well as the transfer coefficient between the spatial phase and the spectral phase. In section 5.2 two particular positions of the YAG crystal along the propagation axis were identified. If the crystal is placed 1.5 mm before the beam focus the generation favors the short-wavelength range with a better coherence. The range of crystal positions allowing phase-stable WLG is larger than a mm. If the crystal is placed 1.5 mm after the focus the generation favors the long-wavelength range with a broader spectrum and a better coherence. The range of crystal positions allowing phase-stable WLG completely vanishes for the short-wavelength side of the spectrum. This confirms the preliminary study of section 4.2. In both of these positions, the impact of the pulse energy was quantified in section 5.3 showing that the range of pulse energy leading to a minimum loss of intrapulse coherence is lenient. It reaches up to 40% of the maximum pulse energy in the short-wavelength range if the crystal is placed before the beam focus and gets reduced to half the size when the crystal is placed after the beam focus. However, the fluctuations of energy can be directly transcribed into spectral phase fluctuations as the extraction of the spectrally resolved intensity to phase transfer coefficient. These coefficients are below 1 rad/% for z = -1.5 mm but can reach values as high as 2 rad/% for z = 1.5 mm at the wavelength of 600 nm. This is the last evidence of the discrepancies between the two particular crystal positions further confirming that generating phase-stable visible and infrared parts of the supercontinuum are contradictory. Section 5.4 shows that the results on the pulse energy are similar when it comes to the spatial phase. The wavefront of the driving beam can indeed have a high aberration (close to λ PtV) without any decrease in coherence. This further confirms the lenient crystal positions for a phase-stable generation as a variation of the focus aberration is analog to moving the YAG crystal along the propagation direction.

Shot-to-shot wavefront variations are however very detrimental to the spectral phase stability of the resulting supercontinuum. It was shown by the extraction of spectrally resolved spatial phase to spectral phase transfer coefficients that are of the order of dozens of rad/rad. One of the missing studies for this thesis is the extraction of crystal position to spectral phase transfer coefficients. They could be compared to the spatial phase to spectral phase transfer coefficients for the focusing aberration. This conclusion highly motivates the development of wavefront sensors capable of measuring phase variations one order of magnitude more accurately than state-of-the-art sensors ideally at the laser repetition rate. Having access to such a wavefront sensor would allow the correlation of the wavefront variations with the phase rms of the WLG and more interestingly with the CEP of an OPCPA. The retrieval of the spatial phase to spectral phase transfer coefficients gives an alternative solution for the control of the absolute CEP value. Introducing an SLM in the WLG arm of an OPCPA would allow fine control of the CEP and could also be used in a stabilization feedback loop.

Additionally to what was shown in this chapter, appendix D shows the study of two other parameters : polarization and B integral. As the results are inconclusive they were not included in the main text.

Chapitre 6

Conclusion

This thesis uses spectral interferometry to study two key phenomena in OPCPA systems : the optical Kerr effect and supercontinuum generation in bulk crystals. The measurement of the nonlinear refractive index using the novel nonlinear chirped interferometry is detailed. Nonlinear crystals and liquid crystals are characterized in the femtosecond regime with a precision competing with state-of-the-art measurements. A review of the state-of-the-art OPCPA sources is then drawn as well as a more in-depth example of a Ti :Sa seeder stressing the significance of studying the phase properties of the supercontinuum generation process. This study is conducted in the next part of the thesis where a modified version of the Bellini-Hänsch interferometer is presented. It is used as a phase measurement setup to quantify the intrapulse coherence of the supercontinuum generation. The measurement principle is introduced first before studying the coherence in the case of various driving lasers as well as their operating parameters. Finally, a parametric study of the WLG process is conducted to quantify the decoherence as a function of three key generation parameters : the crystal position, the pulse energy, and the spatial phase of the driving beam. The effect of a static perturbation is assessed and transfer coefficients are extracted.

6.1 Linear and nonlinear optics

First, the involved processes involved in spectral interferometry and supercontinuum generation are presented in detail. The phase description of a light pulse is essential for this work both in the spectral domain to describe the temporal shape of the pulse and in the spatial domain to quantify the wavefront of the pulse. The most popular method to measure such a phase is through interferometry which principle is described. In particular, the principle of spectral interferometry is discussed as it is the main measurement tool used throughout the thesis. The optical Kerr effect describes the dependence of the refractive index on the intensity. It has two main consequences in self-focusing and self-phase modulation. The regime where self-focusing, multi-photon ionization, and plasma-defocusing balance over macroscopic distances of propagation is called filamentation. As a result, the pulse can propagate over mm-long distances with high intensity, causing significant spectral broadening

due to self-phase modulation, ionization, and self-steepening.

6.2 Third-order susceptibility metrology

6.2.1 Summary

A novel optical Kerr effect spectroscopy method is presented. The method is named nonlinear chirped interferometry and is used to characterize the third-order nonlinearity on the femtosecond time scale. The technique consists in monitoring the variation of the first derivative of the nonlinear temporal phase (group delay) of a transmitted probe under the effect of a strong pump pulse rather than the nonlinear phase. This is done using spectral interferometry between the probe pulse and a reference pulse sampled upstream. Under the right chirp conditions for all three pulses two distinct mechanisms contribute to the transient delay variation :

— 2BC via energy exchanges between the pump and probe a temporal reshaping

— the XPM frequency shift is encoded in time by chirping the reference

A 1D numerical model was used to further confirm the validity of the experiment and was found to be in very good agreement with the experimental data. Although interferometric the method is relatively insensitive to external fluctuations and can reach a sensitivity of 10 mrad phase variations. The interferometer was used to measure the nonlinear indices of liquid crystals (E7 and MLC2132) in the sub-ps regime (previously unknown). The nonlinear indices of KTA, MLN, and LGS were also measured in the crystal orientations adequate for type I difference frequency generation with a 1030 nm pump. This makes this study relevant for the development of mid-infrared OPCPA sources based on the Yb :YAG technology.

6.2.2 Perspectives

The sensitivity and overall performance of the interferometer could be pushed further by multiple scan acquisition, higher averaging, or extending the involved spectral bandwidth. Additionally, this work is not exhaustive as the phonon presence in KTA was noticed but barely investigated. This work could be extended by further investigating the phonon dynamics in different crystals. This could be done by increasing the pump pulse energy and scanning over longer time periods. The measurements realized so far show the existence of vibrational modes of the KTA lattice but do not allow the perfect retrieval of the phonon frequency. Additionally, the probing wavelength is limited to 1030 nm. The scope of this work could be extended by changing the working wavelength either by generating the second harmonic of the driving laser and measuring at the wavelength of 515 nm or by using an OPA as a source giving additional wavelength flexibility. A typical OPA at this driving wavelength would give a wavelength range between 500 nm and 2500 nm. Finally, another use of this setup would be to probe different nonlinear effects than the Kerr effect like third or fifth harmonic generation for example.

The interferometer was initially designed to be a phase measurement device with interferometric detection. On the first measurements we ran on the setup we noticed a transient variation of the relative group delay in the interferometric detection. The relative chirp between the reference and the probe was not a choice of design but a coincidence. After we measured the transient delay shift we investigated the potential reasons for the transcription of the nonlinear phase shift to optical group delay. We found out about the transcription of the frequency shift onto delay via chirped pulses and believed this was the main effect responsible for the relative group delay variation. To confirm this we developed the numerical model presented in this thesis and found that the order of magnitude did not match. Following this we investigated the literature more and found out that the chirp of the pump and probe pulses could cause the 2BC effect. As it turned out this effect is the main contributor to the measured signal. This technique ended up to be very robust due to the combination of both effects and the immediate future for the nonlinear chirped interferometry is the measurement of as many crystals in the femtosecond and picosecond reagimes as possible to enrich the literature with prescise measurements.

6.3 State-of-the-art CEP-stable sources

A review of the state-of-the-art CEP stable sources is presented. First, the measurement techniques are presented focusing on the most widespread one which is f-2f interferometry. It relies on the frequency beating between the frequency double red part and the blue part of an octave-spanning spectrum. Three types of CEP-stable sources are then detailed before focusing on the main considered sources which are OPCPAs.

— Frequency combs are widely used as a metrology tool in optical clocks for example.
— Fiber oscillators are the systems reaching the best overall stability due to the guided properties of fiber sources.
— Free space oscillators are the basis of plenty of optical systems including the later used CPA systems.

The main focus of this work is the development of CEP-stable OPCPA sources. CEP-stable Yb :YAG-based OPCPAs are mainly used as spectroscopy tools or as drivers for HHG sources for X-ray spectroscopy. Compared to the current Ti :Sa CPA systems, their main advantage is access to a higher average power. As an example of a CEP-stable Yb :YAG-based OPCPA the 800 nm Ti :Sa seeder is presented. Its architecture is detailed ranging from the seed generation through supercontinuum generation to the f-2f interferometer used to measure the CEP stability. The role of the WLG in the CEP noise is also emphasized motivating the study on the intrapulse coherence of WLG.

6.4 Spectral coherence in filamentation in bulk crystals

6.4.1 Summary

The spectral properties of supercontinuum generation are characterized by acquiring spectra for different crystal lengths and positions showing that placing the crystal before the beam waist yields a flatter and broader visible spectrum while the same thing is true for the infrared when the crystal is placed behind the beam waist. A modified version of the Bellini-Hänsch interferometer is presented. In this interferometer with a Mach-Zehnder geometry two identical supercontinuum are generated. Spectral interferometry is used to retrieve the spectrally resolved single-shot phase difference between the two supercontinua. The baseline stability of the interferometer was measured to be 6 mrad without any nonlinear effect. The decoherence added purely by the WLG process was shown to be of the order of a dozen mrad in the most stable case. The measurement on different pump lasers shows a decrease in intrapulse coherence with an increase in pulse energy. Additionally using the same laser while changing its operating mode shows the same tendency. This could be caused by many effects ranging from thermal effects in the amplifier to increased B-integral of the pulse. The lack of information on the internal design of the pump laser used makes drawing more conclusions from these measurements difficult.

A parametric study of WLG was conducted to quantify the impact of intrapulse coherence of three key parameters. First, the crystal size is studied by reproducing the measurements with 6 and 10-mm long YAG crystals. It is found that the infrared part of the spectrum is favored with a longer YAG crystal and the visible side of the continuum is favored when using shorter crystals. The spectral phase noise is indeed increased by a factor of 1.5 in the visible side of the spectrum when increasing the crystal size from 6 mm to 10 mm. The first experimental parameter extensively investigated is the crystal position. Two particular positions of the YAG crystal along the propagation axis were identified. If the crystal is placed 1.5 mm before the beam focus the generation favors the short-wavelength range with a better coherence. If the crystal is placed 1.5 mm after the focus the generation favors the long-wavelength range with a broader spectrum and a better coherence. The second experimental parameter investigated is pulse energy. In both particular positions, the impact of the pulse energy was quantified showing that the range of pulse energy leading to a minimum loss of intrapulse coherence is lenient (around 40% of the pulse energy). However, the fluctuations of energy can be directly transcribed into spectral phase fluctuations as the extraction of the spectrally resolved intensity to phase transfer coefficient. This transfer coefficient's value is lower for the visible side of the spectrum when the crystal is paced 1.5 mm before the beam focus and vice versa for the infrared part of the spectrum. This further confirms the two favorable regimes when generating infrared or visible light. This fact was also already existing experimental knowledge. The last investigated parameter is the wavefront aberrations of the driving beam. The wavefront of the driving beam can have a high aberration without the loss of coherence. Shot-to-shot wavefront variations are however very detrimental to the spectral phase stability of the

resulting supercontinuum. This conclusion highly motivates the development of wavefront sensors capable of measuring phase variations one order of magnitude more accurately than state-of-the-art sensors ideally at the laser repetition rate. Having access to such a wavefront sensor would allow the correlation of the wavefront variations with the phase rms of the WLG and more interestingly with the CEP of an OPCPA. The retrieval of the spatial phase to spectral phase transfer coefficients gives an alternative solution for the control of the absolute CEP value. Introducing an SLM in the WLG arm of an OPCPA would allow fine control of the CEP and could also be used in a stabilization feedback loop.

6.4.2 Perspectives

Despite quantifying the most relevant parameters for WLG this study is far from being complete as plenty of experimental parameters were not investigated at all. The change of pump laser was looked at but the physical origin of the noise as a function of energy is still unclear. Appendix D seems to indicate it is not strictly due to the increase in B integral. The influence of the spectral phase of the driving pulse was not studied at all and is expected to influence the intrapulse coherence. A non-exhaustive list of the missing parameters includes :

— The pump wavelength could be investigated simply by taking the second harmonic of the pump beam and conducting the same study at the wavelength of 515 nm. A more advanced scheme would be to use the output of an OPA to gain complete wavelength control in the 500-2500 nm range. Another option would be to change the pump laser technology and replace it with a Ti :Sa system or a fiber laser.

— The spectral phase of the driving beam can be investigated simply by tuning the compressor at the output of the driving laser. A more advanced scheme would be the use of an acousto-optic programmable dispersion filter in one of the interferometer arms to arbitrarily control the spectral phase.

— The driving pulse temporal contrast could also be modified to gain an insight into the impact of amplified spontaneous emission on the WLG process. This could be experimentally realized by manually tuning the seed level at the input of a laser amplifier. It would however be technically challenging to keep the experimental parameters identical and only affect the contrast of the pulse.

As a different starting point, the conditions of the WLG in the f-2f interferometer should also be considered as this work does not explore this side of the CEP measurement at all. The conclusions would likely be similar as the physical mechanisms at play would also be however the order of magnitude of the transfer coefficients extracted here could be completely different. This additional study would also be required to estimate the CEP noise added by the f-2f interferometer itself. The broadening mechanism could also be completely changed by replacing the bulk crystal with a nonlinear fiber for example. This would completely get rid of the plasma broadening suspected to be a source of decoherence.

As both a Ph.D. student and a member of Fastlite, I feel like my work was relevant to the field of OPCPAs. Outside of the commercial benefits and the competitive advantage provided to Fastlite by my work, this thesis started to answer some of the questions raised by the theory and experiments about the WLG process. It confirmed that this step is an essential contribution to the CEP drift of OPCPAs and raised a major question about the spatial variations of the driving pulse. Some of the unexplored parameters and unanswered questions are already listed above. In addition to these, the main weakness of the proposed interferometer is the relative nature of the measurement. An improvement on the existing setup would be the use of an achromatic reference with a fixed spectral phase to avoid the comparison of two identical WL. Another possible idea to circumvent this problem would be the addition of a third arm delayed by exactly one pulse. That would however add a lot of phase fluctuations due to the increased path length and make temporal overlap challenging at best. Finally, the missing piece of this thesis is the result attempted to be measured in appendix E. The experimental proof of the correlation with the double-WL measurement and the CEP drift of an OPCPA would completely legitimate this work in this context. Even better would be the quantification of the relation between the two quantities. It would make the double-WL interferometer a relevant measurement tool for OPCPA pump laser systems. Unfortunately, the short investigation of this particular problem was not satisfactory and needs to be properly explored.

6.5 SMART-X

The last aspect of the Ph.D. I would like to come back to is the European Marie Curie fellowship. This required the investment of a lot of time through symposiums, conferences, workshops, secondments, and various tutorials. I was able to spend three weeks in Milan in the group of Caterina Vozzi to get an introduction to HHG in solids. During this stay, I aligned an infrared OPA with a Ti :Sa CPA laser and was able to measure harmonics out of a tellurium crystal (previously unstudied). I personally believe being part of an ITN is very beneficial for a Ph.D. as it is a great opportunity to start building a professional network as well as to extend one's scientific knowledge beyond the scope of a Ph.D. I was able to learn a lot about X-ray spectroscopy, FEL and synchrotron experiments, sample preparation, and theory thanks to the ITN.

Annexe A

List of publications

A.1 Articles

— **Benjamin Maingot**, Gilles Chériaux, Nicolas Forget, and Aurélie Jullien. "Spectral coherence properties of continuum generation in bulk crystals." Optics Express 30, no. 12 (2022) : 20311-20320.

— Elizaveta Neradovskaia, **Benjamin Maingot**, Gilles Chériaux, Cyrille Claudet, Nicolas Forget, and Aurélie Jullien. "Nonlinear chirped interferometry for frequency-shift measurement and $\chi^{(3)}$ spectroscopy." APL Photonics 7, no. 11 (2022).

— **Benjamin Maingot**, Elizaveta Neradovskaia, Cyrille Claudet, Nicolas Forget, and Aurélie Jullien. "Measurement of nonlinear refractive indices of bulk and liquid crystals by nonlinear chirped interferometry." Optics Letters 48, no. 12 (2023) : 3243-3246.

— **Benjamin Maingot**, Nicolas Forget, and Aurélie Jullien. "Influence of wavefront perturbations on supercontinuum generation." To be submitted to Optics letters.

A.2 Conferences

— Virtual oral presentation for the Conference on Lasers and Electro Optics 2022 : Neradovskaia, Elizaveta, Benjamin Maingot, Gilles Chériaux, Cyrille Claudet, Nicolas Forget, and Aurélie Jullien. "Nonlinear chirped Doppler interferometry for ultrafast $\chi^{(3)}$ spectroscopy". In CLEO : Science and Innovations, pp. STh4L-5. Optica Publishing Group, 2022.

— Oral presentation for Ultrafast Optics 2023 (UFO) : Benjamin Maingot, Gilles Chériaux, Nicolas Forget, and Aurélie Jullien. "Spectral coherence properties of filamentation in bulk crystals".

— Invited oral presentation for the Conference on Lasers and Electro Optics 2023 : Benjamin Maingot, Gilles Chériaux, Nicolas Forget, and Aurélie Jullien. "Spectral coherence properties of filamentation in bulk crystals".

— Oral presentation for Conference on Lasers and Electro Optics Europe 2023 : Benjamin Maingot, Gilles Chériaux, Nicolas Forget, and Aurélie Jullien. "Spectral coherence properties of filamentation in bulk crystals".

— Virtual poster presentation for the Conference on Lasers and Electro Optics : Benjamin Maingot, Gilles Chériaux, Nicolas Forget, and Aurélie Jullien. "A study of stochastic phase noise in white light generation". In CLEO : Science and Innovations, pp. JW3B-149. Optica Publishing Group, 2022.
— Poster presentation in OPTIQUE Nice 2022 : Benjamin Maingot, Gilles Chériaux, Nicolas Forget, and Aurélie Jullien. "A study of stochastic phase noise in white light generation".

A.3 SMART-X

— SMART-X Stockholm network symposium : "CEP stability in OPCPAs".
— SMART-X second year symposium Trieste : "A study of stochastic phase noise in white light generation".
— Joint PERSEPHONE and SMART-X Bormio symposium : "Spectral coherence properties of filamentation in bulk crystals".
— SMART-X third year symposium Paris : "Nonlinear chirped Doppler interferometry for ultrafast $\chi^{(3)}$ spectroscopy".

Annexe B

Spectrometer Design

The measurements presented in section 4.6 on the DIRA500 and the Amphos 3102 require a fast spectrometer to measure single-shot spectra. The operating frequencies of these two lasers are indeed 10 and 50 kHz respectively. As the available spectrometers were not fast enough for this specific application I designed and assembled a homemade 80-kHz spectrometer. A diagram of the spectrometer is shown in figure B.1 (a).

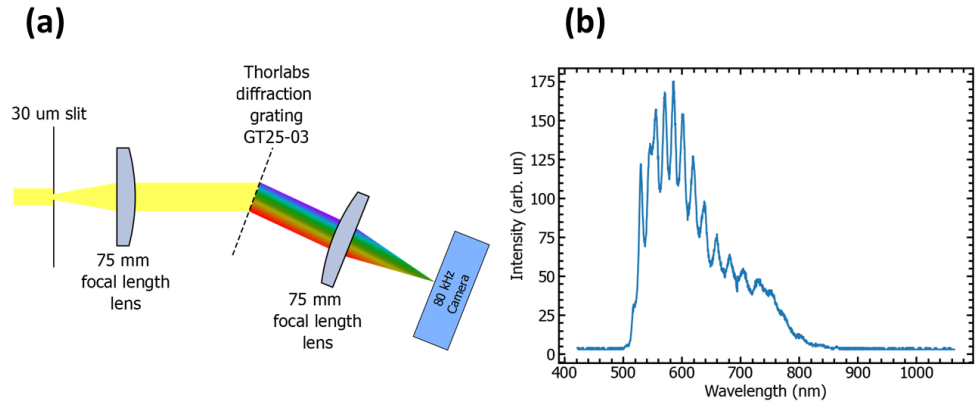

FIGURE B.1 – (a) : Diagram of the fast spectrometer. (b) : typical spectrum acquired with the fast spectrometer.

The design was realized using the spectrometer design tool of the company IBSEN offering a tool to pick the focal length of the different lenses as well as the grating period. The initial tries were made with a shorter focal length (30 mm) but the results were not satisfactory as the chromatic aberrations were too high in this case. The circular shape of the focal point resulted in two intense parts of the spectrum having a much larger signal than the rest. Figure B.1 (b) shows a typical experimental spectrum. The spectral resolution is 0.3 nm and the camera defines the maximal acquisition frequency at 80 kHz. The interfacing with the fast camera is also homemade with a C++ interface.

Annexe C

Spatial Light Modulator

This appendix gives additional information on the spatial light modulator used in section 5.4 as well as on the wavefront sensor used. The spatial light modulator is a homemade thermo-optically addressed liquid crystals device [64]. A diagram of the SLM is given in figure C.1.

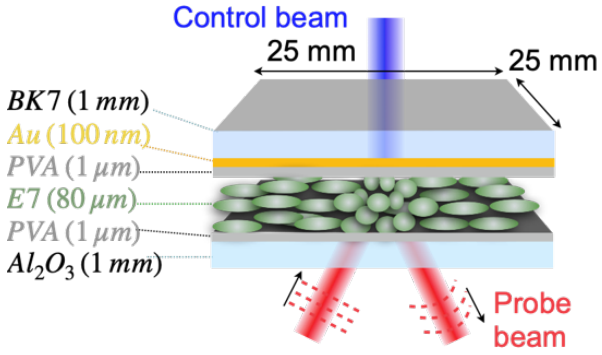

FIGURE C.1 – Diagram of the fast spectrometer.

The device comprises a thick BK7 window (6 mm) coated on one side with a 100-nm gold layer and an AR coating at 465 nm on the other side. This is the control beam size of the device used for the addressing. On the other side of the gold layer is a thin film of polyvinyl alcohol serving as an anchor for the liquid crystal orientation. A similar film is coated on the other side of the 80-μm layer of E7 liquid crystals, ensuring the crystals' orientation in the plane perpendicular to the device plane. Finally a sapphire window of 1 mm thickness serves as a window for the probe beam that will be addressed by the device. In the setup from section 5.4 the SLM is addressed using a blue laser diode (3 W) with a beam shaping setup detailed in figure C.2. As the refractive index of the LC layer varies with temperature adjusting the intensity of the blue writing beam modifies the spatial phase induced by the device.

The blue diode output is first coupled inside a multi-mode fiber to clean the spatial mode of the diode. It is then sent on a digital light processing (DLP) unit able to apply a spatial intensity mask to provide full control of the spatial profile of the writing beam. The DLP can apply an arbitrary intensity mask and is controlled via external software. It can convert grayscale images into a pattern then applied on the blue writing beam. The processing of grayscale images results in a tunable intensity in the spatial domain. It can apply a static pattern for a given duration or a sequence of patterns also with a tunable duration for each pattern as used in section 5.4.

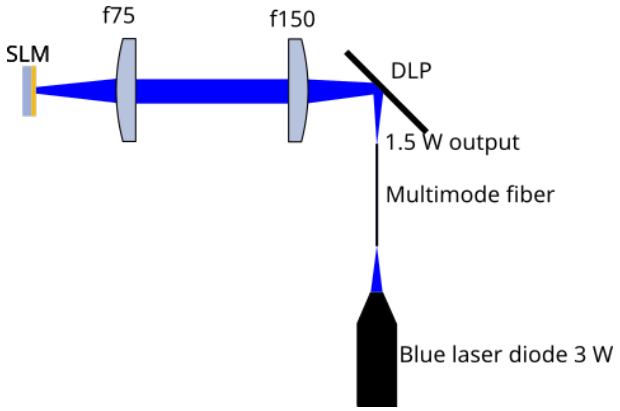

FIGURE C.2 – Beam shapin setup of the blue writing beam.

The plane of the DLP unit is then imaged on the SLM to reproduce the spatial intensity pattern applied by the DLP unit directly on the gold layer of the SLM. The blue light is absorbed by the gold, heating the LC layer.

The last part of the spatial light modulation in the setup is the measurement of the spatial phase induced by the SLM. It is realized by imaging the plane of the SLM (for the infrared beam) on a Shack-Hartmann wavefront sensor by Imagine optics as shown in figure C.3.

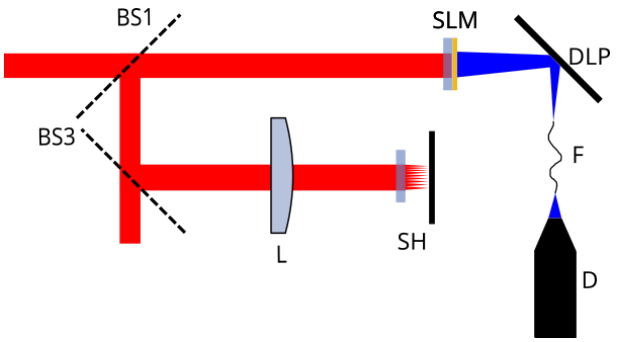

FIGURE C.3 – Imaging setup on the wavefront sensor. Partly extracted from figure 5.15 with the addition of FM (flip mirror) to pick up the driving laser and image it on SH (Shack-Hartmann wavefront sensor) using L (500 mm focal length lens).

Annexe D

B integral and polarization

D.1 B integral

Sections 4.6 and 4.7 showed a dependence of the intrapulse coherence of the WLG process on the pulse energy. Among the pulse characteristics affected by pulse energy, this section takes a look at the B integral of the driving pulse. B integral quantifies the accumulated nonlinear phase of a pulse [12]. A high amount of B integral degrades a pulse's temporal and spatial profile. The goal of this section is to investigate this parameter alone to discriminate it from the pulse energy and to assess if the energy dependence comes from the increased B integral of the driving laser.

A thick (80 mm) TeO_2 crystal is inserted in the beam path before the first beam splitter as indicated in figure D.1. As the TeO_2 crystal has a relatively high n_2 value ($6.1 * 10^{-16} cm^2/W$, 3 times higher than fused silica) they are adequate to add B integral to the driving pulse.

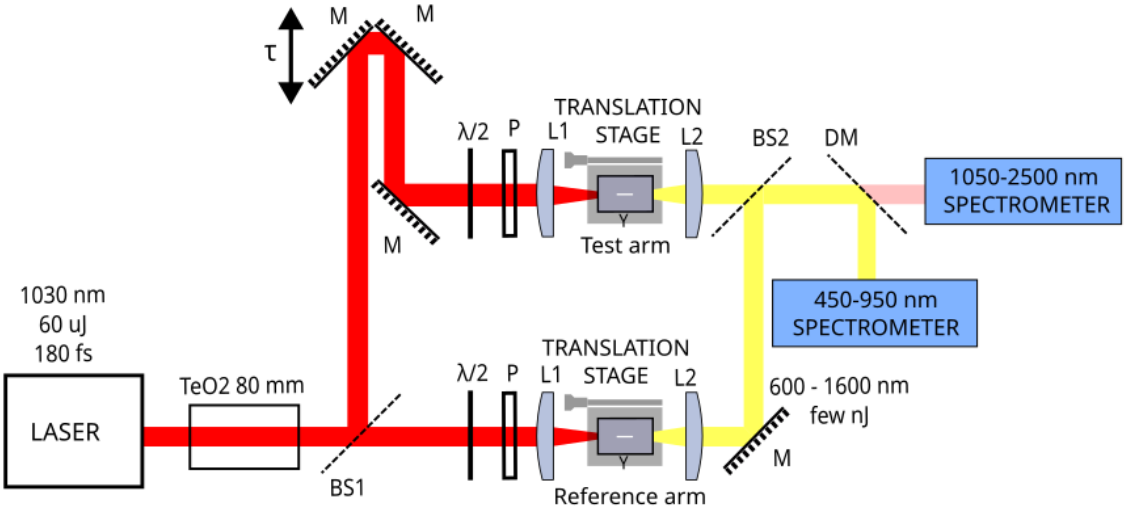

FIGURE D.1 – Experimental setup with the addition of a 80 mm bulk TeO_2 crystal before the first beam splitter.

The amount of B integral added to the pump pulse by the TeO_2 is estimated using a simple model with a square-shaped pulse both in time and space. This basic model aims to give an

idea of the amount of nonlinear phase induced to the pulse. The amount of B integral is given by :

$$B = \frac{2\pi}{\lambda} n_2 z I \tag{D.1}$$

where λ is the wavelength, z is the propagation distance inside the crystal and I is the intensity. As the B integral is proportional to the intensity it can be adjusted simply by changing the output power of the driving laser after the amplifier. The pulse energy is tuned from 9 μJ to 60 μJ giving a B integral measurement range from 1.2 rad to 7.8 rad. Removing the TeO_2 crystal gives a measurement without any nonlinear phase. The laser compressor is adjusted to compensate for the chirp the TeO_2 crystal added and generate the WL with a compressed pulse. As a consequence, the spectra are not broadened by the B integral but narrowed [281]. This is shown in figure D.3.

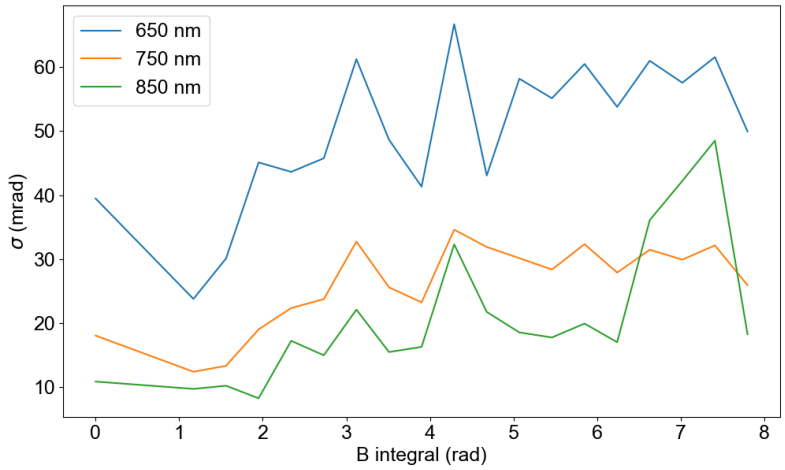

FIGURE D.2 – Phase stability as a function of B integral added to the input pulse for three different wavelengths.

The spectral bandwidth of the driving laser is 9 nm. The spectra shown in figure D.3 have a bandwidth of 8, 6.7, and 6.4 nm for respective values of B integral of 1.2, 3.9 and 7.8 rad.

Figure D.2 shows the phase stability of the WLG as a function of the B integral added to the pulse. Below the value of 2 rad the phase noise is constant with B integral. It shows a slight increase from the value of 2 rad to 8 rad of added B integral.

The phase noise does not show a drastic increase as a function of the B integral. At 750 nm the phase noise without any B integral is 18 mrad and 26 mrad at the maximum B integral value investigated. The global tendency is an increase in noise. The variation is however not monotonous and the minimum phase noise is reached for a B integral value of 2 rad for the wavelength of 850 nm. This measurement concludes that even with a B integral value above 2π the coherence of the WLG process is maintained. The decrease of the intrapulse coherence with increasing pulse energy is not shown in this study of the dependence on the B integral.

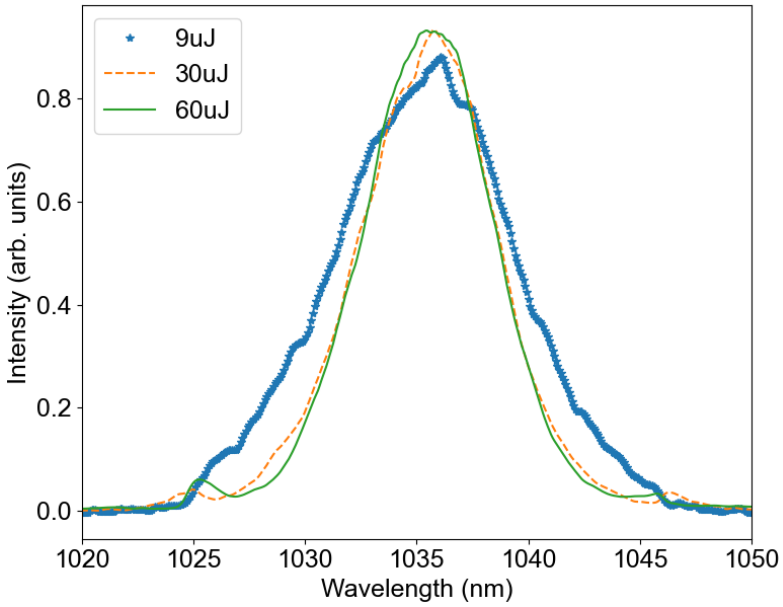

FIGURE D.3 – Spectra of the driving laser at different energies after propagating through 80 mm of TeO_2 crystal. The blue starred line has an input energy of 9 μJ, the orange dotted line has an input energy of 30 μJ and the green line has an input energy of 60 μJ. The calculated B integrals are 1.2, 3.9, and 7.8 rad respectively.

D.2 Polarization

The parameter of this subsection is the ellipticity of the polarization of the driving laser. The consequences of the driving pulse polarization on the filamentation process and vice versa have been extensively studied [282-284] although mostly in gases. It is for instance expected that the filamentation will be highly modified when the driving laser has an elliptical polarization [285]. The experimental setup is modified to incorporate quarter-wave plates in the beam paths. Two configurations are explored here. In the first one, a single quarter-wave plate is inserted in each arm and the ellipticity of the polarization is the same in each arm. The experimental setup is shown in figure D.4.

The wave plates are placed at 4 different angles relative to the laser polarization : 0° which does not have any impact on the polarization, 45° which turns the polarization from linear to circular and the two intermediate angles of 22.5 and 67.5° that give elliptical polarization. The phase noise at these 4 angles is displayed in figure D.5.

In this case, the minimum value of the phase noise is clearly reached when the angle is 0°. The noise value at this angle at 750 nm is 16 mrad. The noise seems slightly higher for an elliptical polarization than for a circular one. More in-depth measurements would however be required to understand the behavior of the noise with polarization.

Another experimental configuration was explored for polarization. Instead of keeping a balanced interferometer two quarter-wave plates are inserted in the same arm of the interferometer. One of them is inserted before the WLG and rotates the polarization and one is inserted after to restore the polarization to linear polarization. The experimental setup is shown in figure

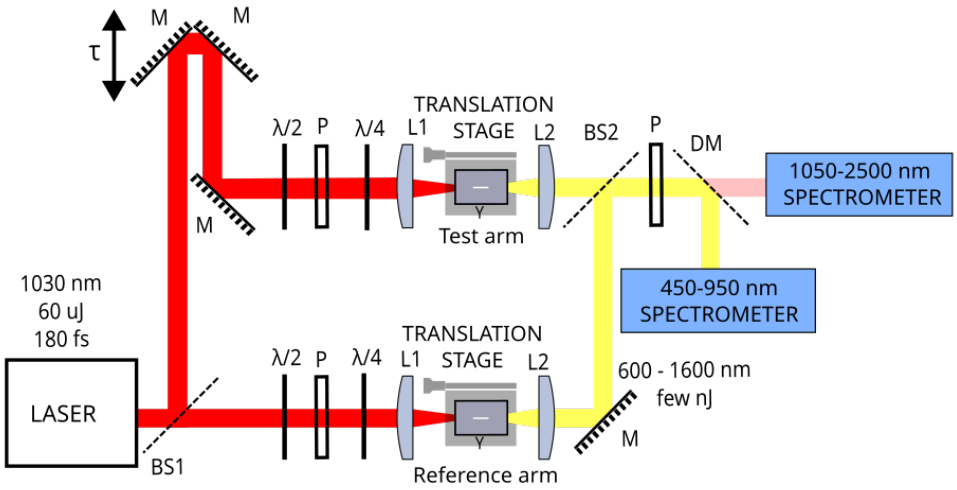

FIGURE D.4 – Experimental setup with the addition of a quarter-wave plate in each arm and a polarizer after the recombining beam splitter.

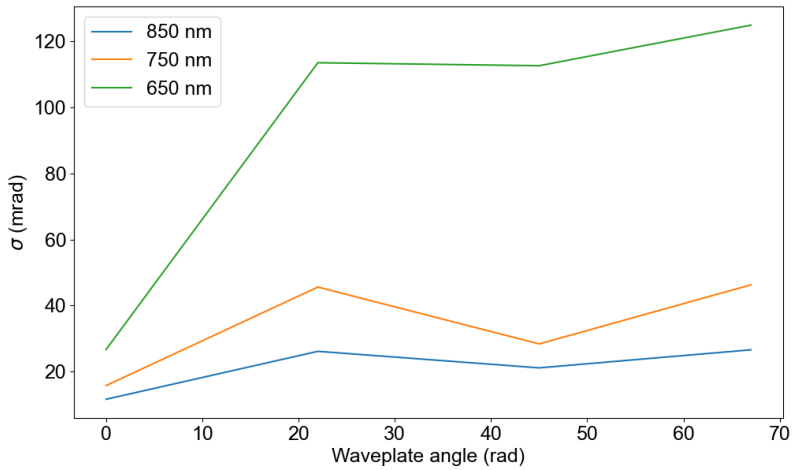

FIGURE D.5 – Phase noise at three different wavelengths as a function of the wave plate angles.

D.6

The wave plates are rotated from 0 to 90° in opposite directions with increments of 5°. The resulting phase noise for three different wavelengths is plotted in figure D.7.

Contrary to what is expected the noise curves are not symmetric around the 45° angle. At 650 nm the noise is lowest at 0° with an rms value of 25 mrad. It has two local maxima at 35 and 80° with respective rms noise values of 47 and 48 mrad and a local minimum at the angle of 55° with a noise rms value of 30 mrad. The expected shape of the noise would be the one observed with angle values of 22.5 and 67.7° for the maxima and 45° for the minimum. Although the first maximum is also present for the two higher wavelengths the second one is not visible in this measurement. Even though variations are observed here affecting the polarization of the beam does not significantly degrade the coherence of the WLG process. The worst value of the rms of the noise is always below 50 mrad.

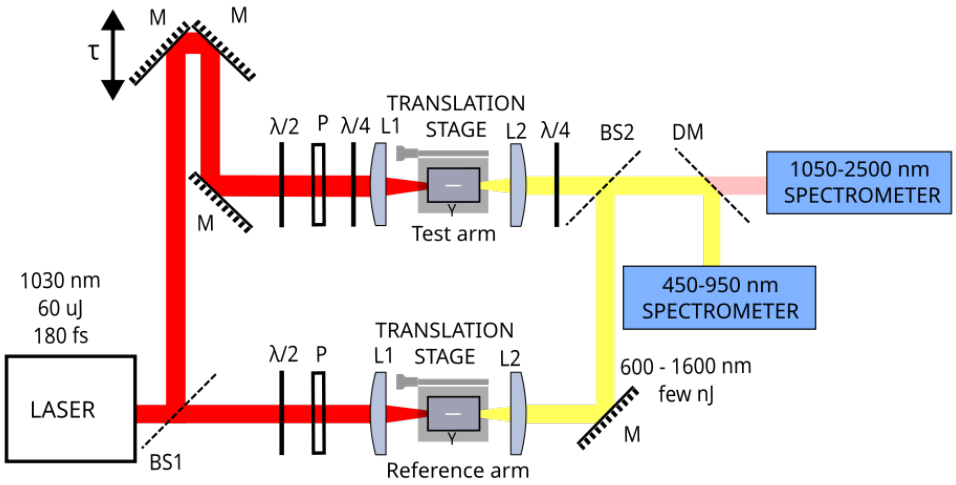

FIGURE D.6 – Experimental setup with the addition of two quarter-wave plates in the test arm.

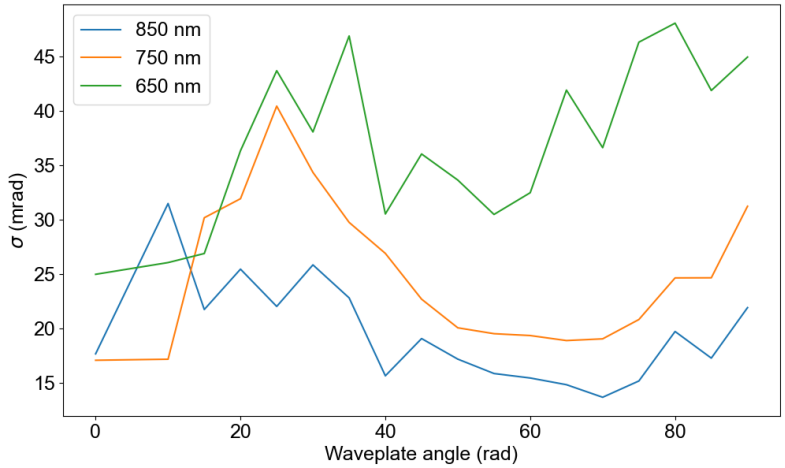

FIGURE D.7 – Phase noise at three different wavelengths as a function of the wave plate angles.

Annexe E

Correlations between CEP and double WL interferometer

This appendix presents the preliminary results obtained on the 800 nm seeder where an attempt at correlating the CEP noise of the OPCPA with the phase noise of the double WL interferometer is realized. The OPCPA presented in section 3.3 is used for this study. An f-2f similar to the one presented is used to measure the CEP variations at the output of the OPCPA. Contrary to what was presented the CEP value is not measured with the 800 nm output but with the 1600 nm output. The reason behind this choice is that as the 800 nm output is the second harmonic of the 1600 nm the CEP variations of the 1600 nm output are twice as low. The f-2f interferometer is almost identical to the one presented in figure 3.13. The only differences are the geometry that is switched to a fully reflective one and the spectrometer that is changed to a spectrometer centered around 1100 nm. With a driving wavelength at 1600 nm, the supercontinuum spectrum now spans indeed from 1000 to 2200 nm resulting in f-2f fringes around 1100 nm. In addition to the modified f-2f interferometer a small portion of the driving laser (10 μJ) is picked up before the OPCPA and sent to the double WL interferometer from chapter 4 (figure 4.7). The spectral phase at the wavelength of 700 nm is then recorded. The CEP value as well as the double WL measurement for the same laser shots are shown in figure E.1. The resulting standard deviations over 1000 laser shots are 100 mrad rms for the double WL measurement and 200 mrad rms for the CEP.

A correlation trace can be made out of this data simply by plotting the CEP as a function of the double WL phase for each shot. This is plotted in figure E.2. This trace shows that despite theoretical expectations no correlation appears between the two measurements.

The only evidence the two quantities are linked is the presence of peaks at similar frequencies in the power spectral density as showcased in figure E.3.

This is however far from experimental proof that the double WL measurement is directly linked to the CEP stability of the source. The current hypothesis to explain why no correlation was observed is that the noise in the CEP value was too high to draw any conclusion. A more extensive study would be required to discriminate whether the correlation exists and was not visible in this measurement.

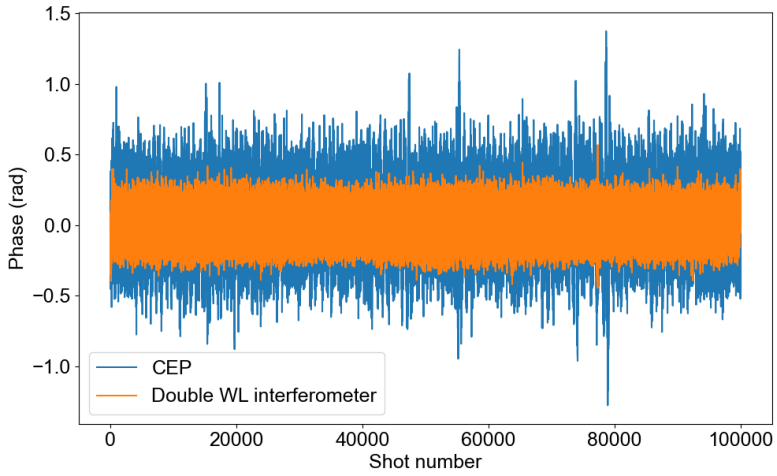

FIGURE E.1 – Raw phase acquired over 100000 laser shots for the double WL interferometer (orange) and the CEP (blue). A low-pass filter with a cut-off frequency of 10 Hz is applied to the data to remove slow drifts.

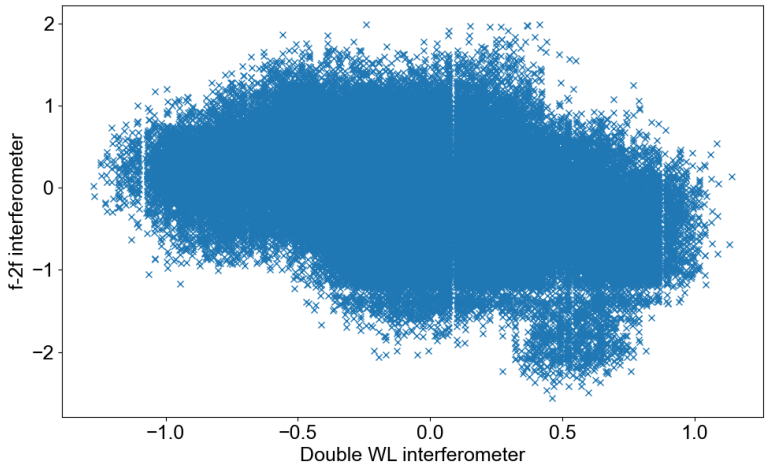

FIGURE E.2 – Correlation trace between the CEP value and the double WL interferometer measurement.

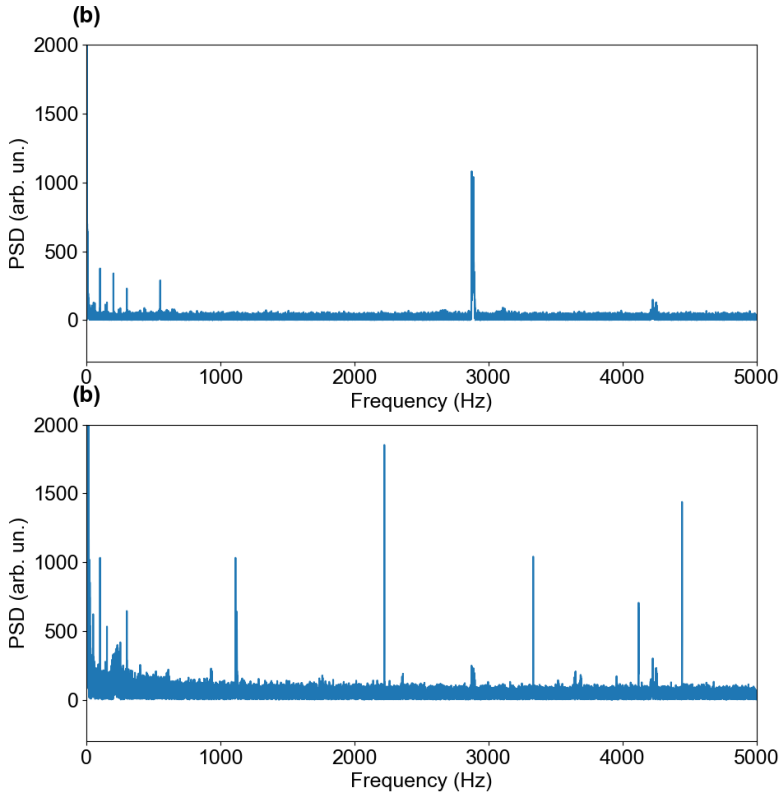

FIGURE E.3 – Power spectral densities of the double WL phase (figure (a)) and CEP (figure (b). The CEP shows a much more noisy PSD. The main frequency peak in the double WL measurement (at 2900 Hz) is also slightly visible in the CEP measurement.

Bibliographie

[1] Peter W SMITH. « Mode-locking of lasers ». In : *Proceedings of the IEEE* 58.9 (1970), p. 1342-1357.

[2] U KELLER, WH KNOX, JE CUNNINGHAM et al. « Femtosecond pulses from a continuously self-starting passively mode-locked Ti : sapphire laser ». In : *Optics letters* 16.13 (1991), p. 1022-1024.

[3] Harald R TELLE et al. « Carrier-envelope offset phase control : A novel concept for absolute optical frequency measurement and ultrashort pulse generation ». In : *Applied Physics B* 69.4 (1999), p. 327-332.

[4] Nathalie PICQUÉ et Theodor W HÄNSCH. « Frequency comb spectroscopy ». In : *Nature Photonics* 13.3 (2019), p. 146-157.

[5] Fangzheng ZHANG et al. « Flat optical frequency comb generation and its application for optical waveform generation ». In : *Optics Communications* 290 (2013), p. 37-42.

[6] Scott B PAPP et al. « Microresonator frequency comb optical clock ». In : *Optica* 1.1 (2014), p. 10-14.

[7] Samuel H CHUNG et Eric MAZUR. « Surgical applications of femtosecond lasers ». In : *Journal of biophotonics* 2.10 (2009), p. 557-572.

[8] George TURRELL et Jacques CORSET. *Raman microscopy : developments and applications*. Academic Press, 1996.

[9] Fritjof HELMCHEN et Winfried DENK. « Deep tissue two-photon microscopy ». In : *Nature methods* 2.12 (2005), p. 932-940.

[10] Nadeem H RIZVI et al. « Femtosecond laser micromachining : Current status and applications ». In : *Riken review* (2003), p. 107-112.

[11] Artem V KORZHIMANOV et al. « Horizons of petawatt laser technology ». In : *Physics-Uspekhi* 54.1 (2011), p. 9.

[12] Robert W BOYD. *Nonlinear optics*. Academic press, 2020.

[13] David A KLEINMAN. « Theory of second harmonic generation of light ». In : *Physical Review* 128.4 (1962), p. 1761.

[14] Charles C WANG et George W RACETTE. « Measurement of parametric gain accompanying optical difference frequency generation ». In : *Applied Physics Letters* 6.8 (1965), p. 169-171.

[15] PP HO et RR ALFANO. « Optical Kerr effect in liquids ». In : *Physical Review A* 20.5 (1979), p. 2170.

[16] Maciej LEWENSTEIN et al. « Theory of high-harmonic generation by low-frequency laser fields ». In : *Physical Review A* 49.3 (1994), p. 2117.

[17] Guang S HE et al. « Multiphoton absorbing materials : molecular designs, characterizations, and applications ». In : *Chemical reviews* 108.4 (2008), p. 1245-1330.

[18] Sonia BOSCOLO, Christophe FINOT et al. « Nonlinear pulse shaping in fibres for pulse generation and optical processing ». In : *International Journal of Optics* 2012 (2012).

[19] Daniel J KANE et Rick TREBINO. « Characterization of arbitrary femtosecond pulses using frequency-resolved optical gating ». In : *IEEE Journal of Quantum Electronics* 29.2 (1993), p. 571-579.

[20] Guozhen YANG et YR SHEN. « Spectral broadening of ultrashort pulses in a nonlinear medium ». In : *Optics letters* 9.11 (1984), p. 510-512.

[21] Donna STRICKLAND et Gerard MOUROU. « Compression of amplified chirped optical pulses ». In : *Optics communications* 56.3 (1985), p. 219-221.

[22] R BAUMGARTNER et R BYER. « Optical parametric amplification ». In : *IEEE Journal of Quantum Electronics* 15.6 (1979), p. 432-444.

[23] KF WALL et A SANCHEZ. « Titanium sapphire lasers, Lincoln Lab ». In : *J* 3.3 (1990), p. 447-462.

[24] Jan ROTHHARDT et al. « Octave-spanning OPCPA system delivering CEP-stable few-cycle pulses and 22 W of average power at 1 MHz repetition rate ». In : *Optics express* 20.10 (2012), p. 10870-10878.

[25] LC DINU et al. « Measurement of the subcycle timing of attosecond XUV bursts in high-harmonic generation ». In : *Physical review letters* 91.6 (2003), p. 063901.

[26] William P PUTNAM et al. « Optical-field-controlled photoemission from plasmonic nanoparticles ». In : *nature physics* 13.4 (2017), p. 335-339.

[27] Björn PIGLOSIEWICZ et al. « Carrier-envelope phase effects on the strong-field photoemission of electrons from metallic nanostructures ». In : *Nature Photonics* 8.1 (2014), p. 37-42.

[28] Tobias RYBKA et al. « Sub-cycle optical phase control of nanotunnelling in the single-electron regime ». In : *Nature Photonics* 10.10 (2016), p. 667.

[29] Andrius BALTUSKA et al. « Phase-controlled amplification of few-cycle laser pulses ». In : *IEEE Journal of Selected Topics in Quantum Electronics* 9.4 (2003), p. 972-989.

[30] David J JONES et al. « Carrier-envelope phase control of femtosecond mode-locked lasers and direct optical frequency synthesis ». In : *Science* 288.5466 (2000), p. 635-639.

[31] A GOLINELLI et al. « Original Ti : Sa 10 kHz front-end design delivering 17 fs, 170 mrad CEP stabilized pulses up to 5 W ». In : *Optics letters* 42.12 (2017), p. 2326-2329.

[32] Sebastian KOKE et al. « Direct frequency comb synthesis with arbitrary offset and shot-noise-limited phase noise ». In : *Nature Photonics* 4.7 (2010), p. 462-465.

[33] Jack HIRSCHMAN et al. « Long-term hybrid stabilization of the carrier-envelope phase ». In : *Optics Express* 28.23 (2020), p. 34093-34103.

[34] Giulio CERULLO et al. « Few-optical-cycle light pulses with passive carrier-envelope phase stabilization ». In : *Laser & Photonics Reviews* 5.3 (2011), p. 323-351.

[35] Nicolas THIRÉ et al. « Highly stable, 15 W, few-cycle, 65 mrad CEP-noise mid-IR OPCPA for statistical physics ». In : *Optics express* 26.21 (2018), p. 26907-26915.

[36] Audrius DUBIETIS et al. « Ultrafast supercontinuum generation in bulk condensed media (Invited Review) ». In : *arXiv preprint arXiv :1706.04356* (2017).

[37] Nils RAABE et al. « Role of intrapulse coherence in carrier-envelope phase stabilization ». In : *Physical Review Letters* 119.12 (2017), p. 123901.

[38] Bahaa EA SALEH et Malvin Carl TEICH. *Fundamentals of photonics*. john Wiley & sons, 2019.

[39] Charles FOURIER. *Fourier :'The Theory of the Four Movements'*. Cambridge University Press, 1996.

[40] Ronald Newbold BRACEWELL et Ronald N BRACEWELL. *The Fourier transform and its applications*. T. 31999. McGraw-Hill New York, 1986.

[41] Georgi P TOLSTOV. *Fourier series*. Courier Corporation, 2012.

[42] Javier Duoandikoetxea ZUAZO. *Fourier analysis*. T. 29. American Mathematical Soc., 2001.

[43] Joel L SCHIFF. *The Laplace transform : theory and applications*. Springer Science & Business Media, 1999.

[44] Valery SEROV et al. *Fourier series, Fourier transform and their applications to mathematical physics*. T. 197. Springer, 2017.

[45] Orhan AYTÜR et Haldun M OZAKTAS. « Non-orthogonal domains in phase space of quantum optics and their relation to fractional Fourier transforms ». In : *Optics Communications* 120.3-4 (1995), p. 166-170.

[46] Henry STARK. *Application of Optical Fourier Transforms*. Elsevier, 2012.

[47] Wenwei LIU et al. « Metasurface enabled wide-angle Fourier lens ». In : *Advanced Materials* 30.23 (2018), p. 1706368.

[48] Alexander SCHEELINE. « How to design a spectrometer ». In : *Applied spectroscopy* 71.10 (2017), p. 2237-2252.

[49] JW DEN HERDER et al. « The reflection grating spectrometer on board XMM-Newton ». In : *Astronomy & Astrophysics* 365.1 (2001), p. L7-L17.

[50] Adarsh B VASISTA, Deepak K SHARMA et GV KUMAR. « Fourier plane optical microscopy and spectroscopy ». In : *arXiv preprint arXiv :1806.08280* (2018).

[51] GIANCARLO RIPAMONTI et SERGIO COVA. « Carrier diffusion effects in the time-response of a fast photodiode ». In : *Solid-state electronics* 28.9 (1985), p. 925-931.

[52] P MAINE et al. « Generation of ultrahigh peak power pulses by chirped pulse amplification ». In : *IEEE Journal of Quantum electronics* 24.2 (1988), p. 398-403.

[53] Yasuhiro MATSUI et al. « Chirp-managed directly modulated laser (CML) ». In : *IEEE Photonics Technology Letters* 18.2 (2006), p. 385-387.

[54] Andrew M KOWALEVICZ JR et Frank BUCHOLTZ. *Beam divergence from an SMF-28 optical fiber*. Rapp. tech. NAVAL RESEARCH LAB WASHINGTON DC, 2006.

[55] Amit SINGH et al. « Temperature sensitivity of long period fiber grating in SMF-28 fiber ». In : *Optik* 125.1 (2014), p. 457-460.

[56] Michael L COOPER et al. « Waveguide dispersion effects in silicon-on-insulator coupled-resonator optical waveguides ». In : *Optics letters* 35.18 (2010), p. 3030-3032.

[57] Takashi MATSUI, Kazuhide NAKAJIMA et Izumi SANKAWA. « Dispersion compensation over all the telecommunication bands with double-cladding photonic-crystal fiber ». In : *Journal of lightwave technology* 25.3 (2007), p. 757-762.

[58] Linn F MOLLENAUER, Stephen G EVANGELIDES et Hermann A HAUS. « Long-distance soliton propagation using lumped amplifiers and dispersion shifted fiber ». In : *Journal of lightwave technology* 9.2 (1991), p. 194-197.

[59] Kyle FUERSCHBACH, Jannick P ROLLAND et Kevin P THOMPSON. « Theory of aberration fields for general optical systems with freeform surfaces ». In : *Optics express* 22.22 (2014), p. 26585-26606.

[60] Gregory N MCKAY, Faisal MAHMOOD et Nicholas J DURR. « Large dynamic range autorefraction with a low-cost diffuser wavefront sensor ». In : *Biomedical Optics Express* 10.4 (2019), p. 1718-1735.

[61] Ignacio IGLESIAS et al. « Extended source pyramid wave-front sensor for the human eye ». In : *Optics express* 10.9 (2002), p. 419-428.

[62] Marco LOMBARDO et Giuseppe LOMBARDO. « New methods and techniques for sensing the wave aberrations of human eyes ». In : *Clinical and Experimental Optometry* 92.3 (2009), p. 176-186.

[63] Martina VACALEBRE et al. « Advanced Optical Wavefront Technologies to Improve Patient Quality of Vision and Meet Clinical Requests ». In : *Polymers* 14.23 (2022), p. 5321.

[64] Vittorio Maria DI PIETRO et al. « Phase-only pulse shaper for multi-octave light sources ». In : *Optics Letters* 45.2 (2020), p. 543-546.

[65] Christian MAURER et al. « What spatial light modulators can do for optical microscopy ». In : *Laser & Photonics Reviews* 5.1 (2011), p. 81-101.

[66] Uzi EFRON. *Spatial light modulator technology : materials, devices, and applications*. T. 47. CRC press, 1994.

[67] Mariem GUESMI et Karel ŽÍDEK. « Calibration of the pixel crosstalk in spatial light modulators for 4f pulse shaping ». In : *Applied Optics* 60.25 (2021), p. 7648-7652.

[68] Hyeonseung YU et al. « Recent advances in wavefront shaping techniques for biomedical applications ». In : *Current Applied Physics* 15.5 (2015), p. 632-641.

[69] Robert S SHANKLAND. « Michelson-morley experiment ». In : *American Journal of Physics* 32.1 (1964), p. 16-35.

[70] P. H. SCHERRER et al. « The solar oscillations investigation—Michelson Doppler imager ». In : *The SOHO Mission* (1995), p. 129-188.

[71] Dimitry ROSCHDESTWENSKY. « Anomale dispersion im natriumdampf ». In : *Annalen der Physik* 344.12 (1912), p. 307-345.

[72] J-C CHANTELOUP. « Multiple-wave lateral shearing interferometry for wave-front sensing ». In : *Applied optics* 44.9 (2005), p. 1559-1571.

[73] A Gh PODOLEANU. « Optical coherence tomography ». In : *Journal of microscopy* 247.3 (2012), p. 209-219.

[74] John W PYHTILA, Robert N GRAF et Adam WAX. « Determining nuclear morphology using an improved angle-resolved low coherence interferometry system ». In : *Optics Express* 11.25 (2003), p. 3473-3484.

[75] L LEPETIT, G CHÉRIAUX et M JOFFRE. « Linear techniques of phase measurement by femtosecond spectral interferometry for applications in spectroscopy ». In : *JOSA B* 12.12 (1995), p. 2467-2474.

[76] Stéphanie GRABIELLE. « Manipulation et caractérisation du champ électrique optique : applications aux impulsions femtosecondes ». Thèse de doct. 2011.

[77] Adam BORZSONYI, Attila P KOVACS et Karoly OSVAY. « What we can learn about ultrashort pulses by linear optical methods ». In : *Applied Sciences* 3.2 (2013), p. 515-544.

[78] Juergen BAUER. « Die Dispersion des Phasensprungs bei der Lichtreflexion an dünnen Metallschichten ». In : *Annalen der Physik* 412.5 (1934), p. 481-501.

[79] AP KOVÁCS et al. « Group-delay measurement on laser mirrors by spectrally resolved white-light interferometry ». In : *Optics Letters* 20.7 (1995), p. 788-790.

[80] Pamela BOWLAN et al. « Crossed-beam spectral interferometry : a simple, high-spectral-resolution method for completely characterizing complex ultrashort pulses in real time ». In : *Optics express* 14.24 (2006), p. 11892-11900.

[81] Oren RAZ et al. « Vectorial phase retrieval for linear characterization of attosecond pulses ». In : *Physical review letters* 107.13 (2011), p. 133902.

[82] D MESHULACH, D YELIN et Yaron SILBERBERG. « White light dispersion measurements by one-and two-dimensional spectral interference ». In : *IEEE journal of quantum electronics* 33.11 (1997), p. 1969-1974.

[83] A BALTUŠKA et T KOBAYASHI. « Adaptive shaping of two-cycle visible pulses using a flexible mirror ». In : *Applied Physics B* 75 (2002), p. 427-443.

[84] Kazuhiko MISAWA et Takayoshi KOBAYASHI. « Femtosecond Sagnac interferometer for phase spectroscopy ». In : *Optics letters* 20.14 (1995), p. 1550-1552.

[85] AP KOVÁCS et al. « Dispersion control of a pulse stretcher–compressor system with two-dimensional spectral interferometry ». In : *Applied Physics B* 80 (2005), p. 165-170.

[86] Chris IACONIS et Ian A WALMSLEY. « Self-referencing spectral interferometry for measuring ultrashort optical pulses ». In : *IEEE Journal of quantum electronics* 35.4 (1999), p. 501-509.

[87] Thomas OKSENHENDLER et al. « Self-referenced spectral interferometry ». In : *Applied Physics B* 99.1-2 (2010), p. 7-12.

[88] eg PA FRANKEN et al. « Generation of optical harmonics ». In : *Physical Review Letters* 7.4 (1961), p. 118.

[89] IN ROSS, P MATOUSEK et JL COLLIER. « Optical parametric chirped pulse amplification ». In : *Conference on Lasers and Electro-Optics (CLEO 2000). Technical Digest. Postconference Edition. TOPS Vol. 39 (IEEE Cat. No. 00CH37088)*. IEEE. 2000, p. 249.

[90] Qiang LIU et al. « 103W high beam quality green laser with an extra-cavity second harmonic generation ». In : *Optics Express* 16.19 (2008), p. 14335-14340.

[91] Toshio KUROBORI, Yoshio CHO et Yukito MATSUO. « An intensity/phase autocorrelator for the use of ultrashort optical pulse measurements ». In : *Optics Communications* 40.2 (1981), p. 156-160.

[92] Joshua C BIENFANG et al. « 20W of continuous-wave sodium D 2 resonance radiation from sum-frequency generation with injection-locked lasers ». In : *Optics Letters* 28.22 (2003), p. 2219-2221.

[93] J ALNIS et al. « Sum-frequency generation with a blue diode laser for mercury spectroscopy at 254 nm ». In : *Applied Physics Letters* 76.10 (2000), p. 1234-1236.

[94] Franck VIDAL et Abderrahmane TADJEDDINE. « Sum-frequency generation spectroscopy of interfaces ». In : *Reports on Progress in Physics* 68.5 (2005), p. 1095.

[95] Guangyu FAN et al. « Hollow-core-waveguide compression of multi-millijoule CEP-stable 3.2 μm pulses ». In : *Optica* 3.12 (2016), p. 1308-1311.

[96] Anne-Lise VIOTTI et al. « Multi-pass cells for post-compression of ultrashort laser pulses ». In : *Optica* 9.2 (2022), p. 197-216.

[97] D ASHKENASI et al. « Application of self-focusing of ps laser pulses for three-dimensional microstructuring of transparent materials ». In : *Applied Physics Letters* 72.12 (1998), p. 1442-1444.

[98] Roger L FARROW et al. « Peak-power limits on fiber amplifiers imposed by self-focusing ». In : *Optics letters* 31.23 (2006), p. 3423-3425.

[99] Yaron SILBERBERG. « Collapse of optical pulses ». In : *Optics letters* 15.22 (1990), p. 1282-1284.

[100] Arnaud COUAIRON et André MYSYROWICZ. « Femtosecond filamentation in transparent media ». In : *Physics reports* 441.2-4 (2007), p. 47-189.

[101] Maximilian BRADLER. « Bulk continuum generation : the ultimate tool for laser applications and spectroscopy ». Thèse de doct. lmu, 2014.

[102] SL CHIN et al. « Advances in intense femtosecond laser filamentation in air ». In : *Laser Physics* 22 (2012), p. 1-53.

[103] AK DHARMADHIKARI et al. « Control of the onset of filamentation in condensed media ». In : *Physical Review A* 76.3 (2007), p. 033811.

[104] Olga KOSAREVA et al. « Arrest of self-focusing collapse in femtosecond air filaments : higher order Kerr or plasma defocusing ? » In : *Optics letters* 36.7 (2011), p. 1035-1037.

[105] Jinendra K RANKA, Robert W SCHIRMER et Alexander L GAETA. « Observation of pulse splitting in nonlinear dispersive media ». In : *Physical Review Letters* 77.18 (1996), p. 3783.

[106] A COUAIRON. « Dynamics of femtosecond filamentation from saturation of self-focusing laser pulses ». In : *Physical Review A* 68.1 (2003), p. 015801.

[107] A DUBIETIS et al. « Measurement and calculation of nonlinear absorption associated with femtosecond filaments in water ». In : *Applied Physics B* 84 (2006), p. 439-446.

[108] Ole BANG et al. « Collapse arrest and soliton stabilization in nonlocal nonlinear media ». In : *Physical Review E* 66.4 (2002), p. 046619.

[109] Alfred VOGEL et al. « Energy balance of optical breakdown in water at nanosecond to femtosecond time scales. » In : *Applied Physics B : Lasers & Optics* 68.2 (1999).

[110] Gadi FIBICH et Boaz ILAN. « Vectorial and random effects in self-focusing and in multiple filamentation ». In : *Physica D : Nonlinear Phenomena* 157.1-2 (2001), p. 112-146.

[111] M KOLESIK, EM WRIGHT et JV MOLONEY. « Femtosecond filamentation in air and higher-order nonlinearities ». In : *Optics letters* 35.15 (2010), p. 2550-2552.

[112] A TELEKI, EM WRIGHT et M KOLESIK. « Microscopic model for the higher-order nonlinearity in optical filaments ». In : *Physical Review A* 82.6 (2010), p. 065801.

[113] P CHERNEV et V PETROV. « Self-focusing of light pulses in the presence of normal group-velocity dispersion ». In : *Optics letters* 17.3 (1992), p. 172-174.

[114] Joshua E ROTHENBERG. « Pulse splitting during self-focusing in normally dispersive media ». In : *Optics letters* 17.8 (1992), p. 583-585.

[115] KD MOLL, Alexander L GAETA et Gadi FIBICH. « Self-similar optical wave collapse : observation of the Townes profile ». In : *Physical review letters* 90.20 (2003), p. 203902.

[116] A BRODEUR et al. « Moving focus in the propagation of ultrashort laser pulses in air ». In : *Optics Letters* 22.5 (1997), p. 304-306.

[117] Maik SCHELLER et al. « Externally refuelled optical filaments ». In : *Nature Photonics* 8.4 (2014), p. 297-301.

[118] Valeriy Petrovich KANDIDOV et al. « Intensity clamping in the filament of femtosecond laser radiation ». In : *Quantum Electronics* 41.4 (2011), p. 382.

[119] E ŽEROMSKIS et al. « Gain bandwidth broadening of the continuum-seeded optical parametric amplifier by use of two pump beams ». In : *Optics communications* 203.3-6 (2002), p. 435-440.

[120] Thomas BRABEC et Ferenc KRAUSZ. « Nonlinear optical pulse propagation in the single-cycle regime ». In : *Physical Review Letters* 78.17 (1997), p. 3282.

[121] Sergei V CHEKALIN et al. « Light bullets and supercontinuum spectrum during femtosecond pulse filamentation under conditions of anomalous group-velocity dispersion in fused silica ». In : *Quantum Electronics* 43.4 (2013), p. 326.

[122] Gadi FIBICH et George PAPANICOLAOU. « Self-focusing in the perturbed and unperturbed nonlinear Schrödinger equation in critical dimension ». In : *SIAM Journal on Applied Mathematics* 60.1 (1999), p. 183-240.

[123] V JUKNA et al. « Infrared extension of femtosecond supercontinuum generated by filamentation in solid-state media ». In : *Applied Physics B* 116 (2014), p. 477-483.

[124] A BRODEUR et SL CHIN. « Ultrafast white-light continuum generation and self-focusing in transparent condensed media ». In : *JOSA B* 16.4 (1999), p. 637-650.

[125] K Miura DAVIS et al. « Writing waveguides in glass with a femtosecond laser ». In : *Optics letters* 21.21 (1996), p. 1729-1731.

[126] Loic RAMOUSSE et al. « Femtosecond laser-induced damage threshold of nematic liquid crystals at 1030 nm ». In : *Applied optics* 60.26 (2021), p. 8050-8056.

[127] Stéphane BARLAND et al. « Reconfigurable design of a thermo-optically addressed liquid-crystal phase modulator by a neural network ». In : *Optics Express* 31.8 (2023), p. 12597-12608.

[128] Antonella TREGLIA et al. « Effect of electronic doping and traps on carrier dynamics in tin halide perovskites ». In : *Materials Horizons* 9.6 (2022), p. 1763-1773.

[129] Lorenzo RESTAINO, Deependra JADOUN et Markus KOWALEWSKI. « Probing nonadiabatic dynamics with attosecond pulse trains and soft x-ray Raman spectroscopy ». In : *Structural Dynamics* 9.3 (2022), p. 034101.

[130] Carlo KLEINE et al. « Electronic State Population Dynamics upon Ultrafast Strong Field Ionization and Fragmentation of Molecular Nitrogen ». In : *Physical Review Letters* 129.12 (2022), p. 123002.

[131] Marco BELLINI et Theodor W HÄNSCH. « Phase-locked white-light continuum pulses : toward a universal optical frequency-comb synthesizer ». In : *Optics Letters* 25.14 (2000), p. 1049-1051.

[132] Aurélie JULLIEN et al. « 10 ? 10 temporal contrast for femtosecond ultraintense lasers by cross-polarized wave generation ». In : *Optics letters* 30.8 (2005), p. 920-922.

[133] Elizaveta NERADOVSKAIA et al. « Nonlinear chirped Doppler interferometry for\c {hi}(3) spectroscopy ». In : *arXiv preprint arXiv :2204.02259* (2022).

[134] Benjamin MAINGOT et al. « Measurement of nonlinear refractive indices of bulk and liquid crystals by nonlinear chirped interferometry ». In : *Optics Letters* 48.12 (2023), p. 3243-3246.

[135] AA SAID et al. « z-scan : a simple sensitive technique for measuring refractive nonlinearities ». In : *OSA Annual Meeting*. Optica Publishing Group. 1989, TUY3.

[136] Mansoor SHEIK-BAHAE, Ali A SAID et Eric W VAN STRYLAND. « High-sensitivity, single-beam n 2 measurements ». In : *Optics letters* 14.17 (1989), p. 955-957.

[137] PD MAKER et RW TERHUNE. « Study of optical effects due to an induced polarization third order in the electric field strength ». In : *Physical Review* 137.3A (1965), A801.

[138] Adelbert OWYOUNG. « Ellipse rotation studies in laser host materials ». In : *IEEE Journal of Quantum Electronics* 9.11 (1973), p. 1064-1069.

[139] Y BAE, JJ SONG et YB KIM. « Photoacoustic study of two-photon absorption in hexagonal ZnS ». In : *Journal of Applied Physics* 53.1 (1982), p. 615-619.

[140] EJ CANTO-SAID et al. « Degenerate four-wave mixing measurements of high order nonlinearities in semiconductors ». In : *IEEE journal of quantum electronics* 27.10 (1991), p. 2274-2280.

[141] R DESALVO et al. « Z-scan measurements of the anisotropy of nonlinear refraction and absorption in crystals ». In : *Optics letters* 18.3 (1993), p. 194-196.

[142] T XIA et al. « Eclipsing Z-scan measurement of $\lambda/10$ 4 wave-front distortion ». In : *Optics letters* 19.5 (1994), p. 317-319.

[143] M SHEIK-BAHAE et al. « Measurement of nondegenerate nonlinearities using a two-color Z scan ». In : *Optics letters* 17.4 (1992), p. 258-260.

[144] Jiangwei WANG et al. « Time-resolved Z-scan measurements of optical nonlinearities ». In : *JOSA B* 11.6 (1994), p. 1009-1017.

[145] K MINOSHIMA, Makoto TAIJI et Takayoshi KOBAYASHI. « Femtosecond time-resolved interferometry for the determination of complex nonlinear susceptibility ». In : *Optics letters* 16.21 (1991), p. 1683-1685.

[146] KY KIM, I ALEXEEV et HM MILCHBERG. « Single-shot supercontinuum spectral interferometry ». In : *Applied physics letters* 81.22 (2002), p. 4124-4126.

[147] Inuk KANG, Todd KRAUSS et Frank WISE. « Sensitive measurement of nonlinear refraction and two-photon absorption by spectrally resolved two-beam coupling ». In : *Optics letters* 22.14 (1997), p. 1077-1079.

[148] Sylvia SMOLORZ, Frank WISE et NF BORRELLI. « Measurement of the nonlinear optical response of optical fiber materials by use of spectrally resolved two-beam coupling ». In : *Optics letters* 24.16 (1999), p. 1103-1105.

[149] Jean-Francois RIPOCHE et al. « Determination of the time dependence of n2 in air ». In : *Optics Communications* 135.4-6 (1997), p. 310-314.

[150] Jesse W WILSON, Philip SCHLUP et Randy BARTELS. « Phase measurement of coherent Raman vibrational spectroscopy with chirped spectral holography ». In : *Optics letters* 33.18 (2008), p. 2116-2118.

[151] Govind P AGRAWAL. « Nonlinear fiber optics ». In : *Nonlinear Science at the Dawn of the 21st Century*. Springer, 2000, p. 195-211.

[152] JK WAHLSTRAND et al. « Effect of two-beam coupling in strong-field optical pump-probe experiments ». In : *Physical Review A* 87.5 (2013), p. 053801.

[153] Ian H MALITSON. « Interspecimen comparison of the refractive index of fused silica ». In : *Josa* 55.10 (1965), p. 1205-1209.

[154] Sylvia SMOLORZ et Frank WISE. « Femtosecond two-beam coupling energy transfer from Raman and electronic nonlinearities ». In : *JOSA B* 17.9 (2000), p. 1636-1644.

[155] Piotr KABACIŃSKI et al. « Nonlinear refractive index measurement by SPM-induced phase regression ». In : *Optics express* 27.8 (2019), p. 11018-11028.

[156] Robert ADAIR, LL CHASE et Stephen A PAYNE. « Nonlinear refractive index of optical crystals ». In : *Physical Review B* 39.5 (1989), p. 3337.

[157] Arkady MAJOR et al. « Dispersion of the nonlinear refractive index in sapphire ». In : *Optics letters* 29.6 (2004), p. 602-604.

[158] Ulrich GUBLER et Christian BOSSHARD. « Optical third-harmonic generation of fused silica in gas atmosphere : Absolute value of the third-order nonlinear optical susceptibility χ (3) ». In : *Physical Review B* 61.16 (2000), p. 10702.

[159] Vittorio Maria DI PIETRO et Aurélie JULLIEN. « Broadband spectral domain interferometry for optical characterization of nematic liquid crystals ». In : *Applied Sciences* 10.14 (2020), p. 4701.

[160] HP LI et al. « Femtosecond Z-scan measurements of nonlinear refraction in nonlinear optical crystals ». In : *Optical materials* 15.4 (2001), p. 237-242.

[161] Mark MERO et al. « Laser-induced damage of nonlinear crystals in ultrafast, high-repetition-rate, mid-infrared optical parametric amplifiers pumped at 1 μm ». In : *Pacific Rim Laser Damage 2019 : Optical Materials for High-Power Lasers*. T. 11063. SPIE. 2019, p. 40-47.

[162] Marcus SEIDEL et al. « Multi-watt, multi-octave, mid-infrared femtosecond source ». In : *Science advances* 4.4 (2018), eaaq1526.

[163] Mahesh NAMBOODIRI et al. « Optical properties of Li-based nonlinear crystals for high power mid-IR OPCPA pumped at 1 μm under realistic operational conditions ». In : *Optical Materials Express* 11.2 (2021), p. 231-239.

[164] Gauri N PATWARDHAN et al. « Nonlinear refractive index of solids in mid-infrared ». In : *Optics Letters* 46.8 (2021), p. 1824-1827.

[165] Morten BACHE et Roland SCHIEK. « Review of measurements of Kerr nonlinearities in lithium niobate : the role of the delayed Raman response ». In : *arXiv preprint arXiv :1211.1721* (2012).

[166] Mansoor SHEIK-BAHAE et al. « Dispersion of bound electron nonlinear refraction in solids ». In : *IEEE Journal of quantum electronics* 27.6 (1991), p. 1296-1309.

[167] Chi-Shun TU et al. « Temperature dependent Raman scattering in KTiOPO4 and KTiOAsO4 single crystals ». In : *Journal of applied physics* 79.6 (1996), p. 3235-3240.

[168] Matthias LEZIUS et al. « Space-borne frequency comb metrology ». In : *Optica* 3.12 (2016), p. 1381-1387.

[169] Lin CHANG, Songtao LIU et John E BOWERS. « Integrated optical frequency comb technologies ». In : *Nature Photonics* 16.2 (2022), p. 95-108.

[170] Jacques MILLO et al. « Ultralow noise microwave generation with fiber-based optical frequency comb and application to atomic fountain clock ». In : *Applied Physics Letters* 94.14 (2009), p. 141105.

[171] Philip H BUCKSBAUM. « The future of attosecond spectroscopy ». In : *Science* 317.5839 (2007), p. 766-769.

[172] Adrian L CAVALIERI et al. « Attosecond spectroscopy in condensed matter ». In : *Nature* 449.7165 (2007), p. 1029-1032.

[173] Tibor WITTMANN et al. « Single-shot carrier–envelope phase measurement of few-cycle laser pulses ». In : *Nature Physics* 5.5 (2009), p. 357-362.

[174] Enrico RIDENTE et al. « Electro-optic characterization of synthesized infrared-visible light fields ». In : *Nature communications* 13.1 (2022), p. 1111.

[175] Theodor W HÄNSCH. « Nobel lecture : passion for precision ». In : *Reviews of Modern Physics* 78.4 (2006), p. 1297.

[176] KM EVENSON et al. « Speed of light from direct frequency and wavelength measurements of the methane-stabilized laser ». In : *Physical Review Letters* 29.19 (1972), p. 1346.

[177] Z BAY, GG LUTHER et JA WHITE. « Measurement of an optical frequency and the speed of light ». In : *Physical Review Letters* 29.3 (1972), p. 189.

[178] D LEE et NC WONG. « Tunable optical frequency division using a phase-locked optical parametric oscillator ». In : *Optics letters* 17.1 (1992), p. 13-15.

[179] DJ WINELAND. « Laser-to-microwave frequency division using synchrotron radiation ». In : *Journal of Applied Physics* 50.4 (1979), p. 2528-2532.

[180] Anthony E SIEGMAN. « Lasers university science books ». In : *Mill Valley, CA* 37.208 (1986), p. 169.

[181] James Neil ECKSTEIN. *High Resolution Spectroscopy Using Multiple Coherent Interactions.* Stanford University, 1978.

[182] Th UDEM, Ronald HOLZWARTH et Theodor W HÄNSCH. « Optical frequency metrology ». In : *Nature* 416.6877 (2002), p. 233-237.

[183] Jun YE et Steven T CUNDIFF. *Femtosecond optical frequency comb : principle, operation and applications*. Springer Science & Business Media, 2005.

[184] TA BIRKS et al. « Full 2D photonic band gaps in silica/air structures ». In : *Electronics letters* 31.22 (1995), p. 1941-1943.

[185] Jinendra K RANKA, Robert S WINDELER et Andrew J STENTZ. « Visible continuum generation in air–silica microstructure optical fibers with anomalous dispersion at 800 nm ». In : *Optics letters* 25.1 (2000), p. 25-27.

[186] Jun YE, Harald SCHNATZ et Leo W HOLLBERG. « Optical frequency combs : from frequency metrology to optical phase control ». In : *IEEE Journal of selected topics in quantum electronics* 9.4 (2003), p. 1041-1058.

[187] KR VOGEL et al. « Direct comparison of two cold-atom-based optical frequency standards by using a femtosecond-laser comb ». In : *Optics letters* 26.2 (2001), p. 102-104.

[188] Tobias J KIPPENBERG et al. « Dissipative Kerr solitons in optical microresonators ». In : *Science* 361.6402 (2018), eaan8083.

[189] David A LONG et al. « Multiheterodyne spectroscopy with optical frequency combs generated from a continuous-wave laser ». In : *Optics letters* 39.9 (2014), p. 2688-2690.

[190] L CONSOLINO et al. « Phase-locking to a free-space terahertz comb for metrological-grade terahertz lasers ». In : *Nature Communications* 3.1 (2012), p. 1040.

[191] Takeshi YASUI et al. « Terahertz frequency comb by multifrequency-heterodyning photoconductive detection for high-accuracy, high-resolution terahertz spectroscopy ». In : *Applied Physics Letters* 88.24 (2006), p. 241104.

[192] Albert SCHLIESSER, Nathalie PICQUÉ et Theodor W HÄNSCH. « Mid-infrared frequency combs ». In : *Nature photonics* 6.7 (2012), p. 440-449.

[193] Seok-Jeong LEE et al. « Ultrahigh scanning speed optical coherence tomography using optical frequency comb generators ». In : *Japanese Journal of Applied Physics* 40.8B (2001), p. L878.

[194] Jonas MORGENWEG, Itan BARMES et Kjeld SE EIKEMA. « Ramsey-comb spectroscopy with intense ultrashort laser pulses ». In : *Nature Physics* 10.1 (2014), p. 30-33.

[195] Scott A DIDDAMS, Leo HOLLBERG et Vela MBELE. « Molecular fingerprinting with the resolved modes of a femtosecond laser frequency comb ». In : *Nature* 445.7128 (2007), p. 627-630.

[196] Peter R GRIFFITHS. « The early days of commercial FT-IR spectrometry : a personal perspective ». In : *Applied spectroscopy* 71.3 (2017), p. 329-340.

[197] Patrick JACQUET et al. « Frequency comb Fourier transform spectroscopy with kHz optical resolution ». In : *Fourier Transform Spectroscopy*. Optica Publishing Group. 2009, FMB2.

[198] Yoonchan JEONG et al. « On the formation of noise-like pulses in fiber ring cavity configurations ». In : *Optical Fiber Technology* 20.6 (2014), p. 575-592.

[199] Daniele BRIDA et al. « Ultrabroadband Er : fiber lasers ». In : *Laser & Photonics Reviews* 8.3 (2014), p. 409-428.

[200] DC HANNA et al. « Active mode-locking of an yb : Er fibre laser ». In : *Electronics Letters* 2.25 (1989), p. 95-96.

[201] Irl N DULING. « All-fiber ring soliton laser mode locked with a nonlinear mirror ». In : *Optics letters* 16.8 (1991), p. 539-541.

[202] VJ MATSAS et al. « Self-starting, passively mode-locked fibre ring soliton laser exploiting non-linear polarisation rotation ». In : *Electronics Letters* 28.15 (1992), p. 1391-1393.

[203] Ursula KELLER et al. « Semiconductor saturable absorber mirrors (SESAM's) for femtosecond to nanosecond pulse generation in solid-state lasers ». In : *IEEE Journal of selected topics in QUANTUM ELECTRONICS* 2.3 (1996), p. 435-453.

[204] Paul W SMITH, Y SILBERBERG et DAB MILLER. « Mode locking of semiconductor diode lasers using saturable excitonic nonlinearities ». In : *JOSA B* 2.7 (1985), p. 1228-1236.

[205] Florian ADLER et al. « Phase-locked two-branch erbium-doped fiber laser system for long-term precision measurements of optical frequencies ». In : *Optics Express* 12.24 (2004), p. 5872-5880.

[206] Rupert HUBER et al. « Generation and field-resolved detection of femtosecond electromagnetic pulses tunable up to 41 THz ». In : *Applied Physics Letters* 76.22 (2000), p. 3191-3193.

[207] Günther KRAUSS et al. « All-passive phase locking of a compact Er : fiber laser system ». In : *Optics letters* 36.4 (2011), p. 540-542.

[208] Lihui PANG et al. « Ultra-stability Yb-doped fiber optical frequency comb with 2× 10-18/s stability in-loop ». In : *Optics Express* 24.25 (2016), p. 28993-29000.

[209] Shai YEFET et Avi PE'ER. « A review of cavity design for Kerr lens mode-locked solid-state lasers ». In : *Applied Sciences* 3.4 (2013), p. 694-724.

[210] David E SPENCE, P Np KEAN et Wilson SIBBETT. « 60-fsec pulse generation from a self-mode-locked Ti : sapphire laser ». In : *Optics letters* 16.1 (1991), p. 42-44.

[211] Peter W ROTH et al. « Directly diode-laser-pumped Ti : sapphire laser ». In : *Optics Letters* 34.21 (2009), p. 3334-3336.

[212] Pierre PICHON et al. « Light-emitting diodes : a new paradigm for Ti : sapphire pumping ». In : *Optica* 5.10 (2018), p. 1236-1239.

[213] Takao FUJI et al. « Monolithic carrier-envelope phase-stabilization scheme ». In : *Optics letters* 30.3 (2005), p. 332-334.

[214] Steven T CUNDIFF. « Phase stabilization of ultrashort optical pulses ». In : *Journal of Physics D : Applied Physics* 35.8 (2002), R43.

[215] Maciej KOWALCZYK et al. « CEP-stable Single-Cycle Pulses from a Cr : ZnS Laser ». In : *2022 Conference on Lasers and Electro-Optics (CLEO)*. IEEE. 2022, p. 1-2.

[216] Philip DIENSTBIER et al. « Generation of 1.5 cycle pulses at 780 nm at oscillator repetition rates with stable carrier-envelope phase ». In : *Optics Express* 27.17 (2019), p. 24105-24113.

[217] A GOLINELLI et al. « CEP-stabilized, sub-18 fs, 10 kHz and TW-class 1 kHz dual output Ti : Sa laser with wavelength tunability option ». In : *Optics Express* 27.10 (2019), p. 13624-13636.

[218] Marie OUILLÉ et al. « Relativistic-intensity near-single-cycle light waveforms at kHz repetition rate ». In : *Light : Science & Applications* 9.1 (2020), p. 47.

[219] O PRONIN et al. « Carrier-envelope phase stabilized thin-disk oscillator ». In : *Advanced Solid State Lasers*. Optica Publishing Group. 2013, AF3A-5.

[220] A DUBIETIS, G JONUŠAUSKAS et A PISKARSKAS. « Powerful femtosecond pulse generation by chirped and stretched pulse parametric amplification in BBO crystal ». In : *Optics Communications* 88.4-6 (1992), p. 437-440.

[221] Nicolas THIRÉ et al. « CEP-stable Infrared OPCPA Sources ». In : *Laser Science*. Optica Publishing Group. 2021, JTu1A-26.

[222] Mikayel MUSHEGHYAN et al. « Tunable, few-cycle, CEP-stable mid-IR optical parametric amplifier for strong field applications ». In : *Journal of Physics B : Atomic, Molecular and Optical Physics* 53.18 (2020), p. 185402.

[223] Wim VASSEN et al. « A frequency-stabilized titanium sapphire laser for high-resolution spectroscopy ». In : *Optics communications* 75.5-6 (1990), p. 435-440.

[224] TR SCHIBLI et al. « Frequency metrology with a turnkey all-fiber system ». In : *Optics letters* 29.21 (2004), p. 2467-2469.

[225] Christophe RADIER et al. « 10 PW peak power femtosecond laser pulses at ELI-NP ». In : *High Power Laser Science and Engineering* 10 (2022), e21.

[226] Murray K REED, Michael K STEINER-SHEPARD et Daniel K NEGUS. « Widely tunable femtosecond optical parametric amplifier at 250 kHz with a Ti : sapphire regenerative amplifier ». In : *Optics letters* 19.22 (1994), p. 1855-1857.

[227] TB NORRIS. « Femtosecond pulse amplification at 250 kHz with a Ti : sapphire regenerative amplifier and application to continuum generation ». In : *Optics letters* 17.14 (1992), p. 1009-1011.

[228] Samuel BOHMAN et al. « Generation of 5.0 fs, 5.0 mJ pulses at 1kHz using hollow-fiber pulse compression ». In : *Optics letters* 35.11 (2010), p. 1887-1889.

[229] Shihua CHEN et al. « Compression of high-energy ultrashort laser pulses through an argon-filled tapered planar waveguide ». In : *JOSA B* 28.5 (2011), p. 1009-1012.

[230] T AUGUSTE et al. « High-energy femtosecond laser pulse compression in single-and multi-ionization regime of rare gases : experiment versus theory ». In : *Applied Physics B* 111 (2013), p. 75-87.

[231] Frederik BÖHLE et al. « Compression of CEP-stable multi-mJ laser pulses down to 4 fs in long hollow fibers ». In : *Laser Physics Letters* 11.9 (2014), p. 095401.

[232] Stephan PRINZ et al. « CEP-stable, sub-6 fs, 300-kHz OPCPA system with more than 15 W of average power ». In : *Optics express* 23.2 (2015), p. 1388-1394.

[233] Rimantas BUDRIŪNAS, Tomas STANISLAUSKAS et Arūnas VARANAVIČIUS. « Passively CEP-stabilized frontend for few cycle terawatt OPCPA system ». In : *Journal of Optics* 17.9 (2015), p. 094008.

[234] Adolf GIESEN et al. « Scalable concept for diode-pumped high-power solid-state lasers ». In : *Applied Physics B* 58 (1994), p. 365-372.

[235] Clara J SARACENO et al. « The amazing progress of high-power ultrafast thin-disk lasers ». In : *Journal of the European Optical Society-Rapid Publications* 15.1 (2019), p. 1-7.

[236] Thomas NUBBEMEYER et al. « 1 kW, 200 mJ picosecond thin-disk laser system ». In : *Optics letters* 42.7 (2017), p. 1381-1384.

[237] Giulio CERULLO et Sandro DE SILVESTRI. « Ultrafast optical parametric amplifiers ». In : *Review of scientific instruments* 74.1 (2003), p. 1-18.

[238] Ines MARTIN et al. « Ultralow-Noise Optical Parametric Amplifier for Stimulated Raman Scattering Imaging ». In : *arXiv preprint arXiv :2305.07357* (2023).

[239] Tsuneto KANAI et al. « Supercontinuum-seeded, CEP-stable, high-power 4-micron KTA OPA driven by a 1.4-ps Yb : YAG thin-disk laser and its application to high harmonic generation ». In : *CLEO : Science and Innovations*. Optica Publishing Group. 2019, JM2E-4.

[240] Andrius BALTUŠKA, Takao FUJI et Takayoshi KOBAYASHI. « Controlling the carrier-envelope phase of ultrashort light pulses with optical parametric amplifiers ». In : *Physical review letters* 88.13 (2002), p. 133901.

[241] Gaetan JARGOT. « High-repetition rate CEP-stable few-cycle OPCPA sources in the short wavelength infrared/mid-infrared ». Thèse de doct. Université Paris-Saclay (ComUE), 2019.

[242] Lawrence E MYERS et Walter R BOSENBERG. « Periodically poled lithium niobate and quasi-phase-matched optical parametric oscillators ». In : *IEEE Journal of Quantum Electronics* 33.10 (1997), p. 1663-1672.

[243] Nicolas THIRÉ et al. « 4-W, 100-kHz, few-cycle mid-infrared source with sub-100-mrad carrier-envelope phase noise ». In : *Optics express* 25.2 (2017), p. 1505-1514.

[244] Frederic VERLUISE et al. « Amplitude and phase control of ultrashort pulses by use of an acousto-optic programmable dispersive filter : pulse compression and shaping ». In : *Optics letters* 25.8 (2000), p. 575-577.

[245] Fabian LÜCKING. « Carrier-envelope phase control for the advancement of attosecond pulse generation ». Thèse de doct. lmu, 2014.

[246] Nicolas FORGET et al. « Pump-noise transfer in optical parametric chirped-pulse amplification ». In : *Optics letters* 30.21 (2005), p. 2921-2923.

[247] IN ROSS, GHC NEW et PK BATES. « Contrast limitation due to pump noise in an optical parametric chirped pulse amplification system ». In : *Optics communications* 273.2 (2007), p. 510-514.

[248] Per KYLEMARK et al. « Noise characteristics of fiber optical parametric amplifiers ». In : *Journal of Lightwave Technology* 22.2 (2004), p. 409-416.

[249] Kyo INOUE et Takaaki MUKAI. « Experimental study on noise characteristics of a gain-saturated fiber optical parametric amplifier ». In : *Journal of lightwave technology* 20.6 (2002), p. 969.

[250] Zhi TONG et al. « Full characterization of the signal and idler noise figure spectra in single-pumped fiber optical parametric amplifiers ». In : *Optics Express* 18.3 (2010), p. 2884-2893.

[251] Xiaoming REN et al. « Single-shot carrier-envelope-phase tagging using an f–2f interferometer and a phase meter : a comparison ». In : *Journal of Optics* 19.12 (2017), p. 124017.

[252] Goëry GENTY, Stéphane COEN et John M DUDLEY. « Fiber supercontinuum sources ». In : *JOSA B* 24.8 (2007), p. 1771-1785.

[253] Darren D HUDSON et al. « Toward all-fiber supercontinuum spanning the mid-infrared ». In : *Optica* 4.10 (2017), p. 1163-1166.

[254] John M DUDLEY et James Roy TAYLOR. *Supercontinuum generation in optical fibers*. Cambridge University Press, 2010.

[255] John J MCFERRAN et al. « Suppression of pump-induced frequency noise in fiber-laser frequency combs leading to sub-radian f ceo phase excursions ». In : *Applied Physics B* 86 (2007), p. 219-227.

[256] J-L PENG et al. « Highly stable, frequency-controlled mode-locked erbium fiber laser comb ». In : *Applied Physics B* 86.1 (2007), p. 49-53.

[257] Gehui XIE et al. « Self-referenced frequency comb from a polarization-maintaining Er : Fiber laser based nonlinear polarization evolution ». In : *Results in Physics* 22 (2021), p. 103886.

[258] Aaron SCHWEINSBERG, Jerry KUPER et Robert W BOYD. « Loss of spatial coherence and limiting of focal plane intensity by small-scale laser-beam filamentation ». In : *Physical Review A* 84.5 (2011), p. 053837.

[259] C LABAUNE et al. « Filamentation in long scale length plasmas : Experimental evidence and effects of laser spatial incoherence ». In : *Physics of Fluids B : Plasma Physics* 4.7 (1992), p. 2224-2231.

[260] John R MARCIANTE et Govind P AGRAWAL. « Spatio-temporal characteristics of filamentation in broad-area semiconductor lasers ». In : *IEEE Journal of Quantum Electronics* 33.7 (1997), p. 1174-1179.

[261] L BERGÉ et al. « Ultrashort filaments of light in weakly ionized, optically transparent media ». In : *Reports on progress in physics* 70.10 (2007), p. 1633.

[262] Nobuhisa ISHII et al. « Optical parametric amplification of carrier-envelope phase-stabilized mid-infrared pulses generated by intra-pulse difference frequency generation ». In : *Optics Express* 27.8 (2019), p. 11447-11454.

[263] Ondřej NOVÁK et al. « Femtosecond 8.5 μm source based on intrapulse difference-frequency generation of 2.1 μm pulses ». In : *Optics letters* 43.6 (2018), p. 1335-1338.

[264] Hang-Dong HUANG et al. « Broadband mid-infrared pulse via intra-pulse difference frequency generation based on supercontinuum from multiple thin plates ». In : *Chinese Physics B* 28.11 (2019), p. 114203.

[265] Gunnar ARISHOLM. « Advanced numerical simulation models for second-order nonlinear interactions ». In : *Laser Optics' 98 : Fundamental Problems of Laser Optics*. T. 3685. International Society for Optics et Photonics. 1999, p. 86-97.

[266] Anne-Laure CALENDRON et al. « White-light generation with sub-ps pulses ». In : *Optics express* 23.11 (2015), p. 13866-13879.

[267] Audrius DUBIETIS et Arnaud COUAIRON. *Ultrafast supercontinuum generation in transparent solid-state media*. Springer, 2019.

[268] Aymeric Van de WALLE et al. « Spectral and spatial full-bandwidth correlation analysis of bulk-generated supercontinuum in the mid-infrared ». In : *Optics letters* 40.4 (2015), p. 673-676.

[269] N BLOEMBERGEN. « The influence of electron plasma formation on superbroadening in light filaments ». In : *Optics Communications* 8.4 (1973), p. 285-288.

[270] David W ALLAN et James A BARNES. « A) IWlDIFIED" ALLAN VARIANCE" WITH INCREASED OSCILLATOR CHARACTERIZATION ABILITY ». In : (1981).

[271] Ruoyu LIAO et al. « Spontaneous emission noise in mode-locked lasers and frequency combs ». In : *Physical Review A* 102.1 (2020), p. 013506.

[272] S LEGHMIZI et al. « On the different ways for defining the effective focal length of a Kerr lens effect ». In : *Laser Physics* 27.10 (2017), p. 106201.

[273] John H MARBURGER. « Self-focusing : theory ». In : *Progress in quantum electronics* 4 (1975), p. 35-110.

[274] Michele NATILE et al. « Simple carrier-envelope phase control and stabilization scheme for difference frequency generation-based systems ». In : *Optics Express* 29.11 (2021), p. 16261-16269.

[275] Selcuk AKTURK et al. « Spatio-temporal couplings in ultrashort laser pulses ». In : *Journal of Optics* 12.9 (2010), p. 093001.

[276] Hampus WIKMARK et al. « Spatiotemporal coupling of attosecond pulses ». In : *Proceedings of the National Academy of Sciences* 116.11 (2019), p. 4779-4787.

[277] Charles BOURASSIN-BOUCHET et al. « Duration of ultrashort pulses in the presence of spatio-temporal coupling ». In : *Optics express* 19.18 (2011), p. 17357-17371.

[278] Michelle RHODES et al. « Visualizing spatiotemporal pulse propagation : first-order spatiotemporal couplings in laser pulses ». In : *Applied Optics* 56.11 (2017), p. 3024-3034.

[279] F QUÉRÉ et al. « Applications of ultrafast wavefront rotation in highly nonlinear optics ». In : *Journal of Physics B : Atomic, Molecular and Optical Physics* 47.12 (2014), p. 124004.

[280] Yi-qiang QIN et al. « Wave-front engineering by Huygens-Fresnel principle for nonlinear optical interactions in domain engineered structures ». In : *Physical review letters* 100.6 (2008), p. 063902.

[281] SA PLANAS et al. « Spectral narrowing in the propagation of chirped pulses in single-mode fibers ». In : *Optics letters* 18.9 (1993), p. 699-701.

[282] Olga KOSAREVA et al. « Polarization rotation due to femtosecond filamentation in an atomic gas ». In : *Optics letters* 35.17 (2010), p. 2904-2906.

[283] Si-Min LI et al. « Unveiling stability of multiple filamentation caused by axial symmetry breaking of polarization ». In : *Photonics Research* 4.5 (2016), B29-B34.

[284] G FIBICH et B ILAN. « Multiple filamentation of circularly polarized beams ». In : *Physical review letters* 89.1 (2002), p. 013901.

[285] Shermineh ROSTAMI et al. « Dramatic enhancement of supercontinuum generation in elliptically-polarized laser filaments ». In : *Scientific Reports* 6.1 (2016), p. 20363.